COO-2245-44TR

COOLANT MIXING IN THE LMFBR OUTLET PLENUM

by

Yi Bin Chen

and

Michael W. Golay

June, 1977

DEPARTMENT OF NUCLEAR ENGINEERING

MASSACHUSETTS INSTITUTE OF TECHNOLOGY

Cambridge, Massachusetts

02139

ERDA Research and Development
Contract E(11-1)-2245
U.S. Energy Research and Development Administration

DISCLAIMER

"This report was prepared as an account of Government-sponsored work. Neither the United States, or the Energy Research and Development Administration nor any person acting on behalf of the Commission

A. Makes any warranty or representation, expressed or implied, with respect to the accuracy, completeness or usefulness of the information contained in this report, or that the use of any information, apparatus method, or process disclosed in this report may not infringe privately owned rights; or

B. Assumes any liabilities with respect to the use of, or for damages resulting from the use of, any information, apparatus, method, or process disclosed in this report.

As used in the above, 'person acting on behalf of the Commission' includes any employee or contractor of the Administration or employee of such contractor, to the extent that such employee or contractor prepares, disseminates, or provides access to, any information pursuant to his employment or contract with the Administration or his employment with such contractor."

Reports and Papers Published under MIT Coolant Mixing in LMFBR Rod Bundles Project

A. Quarterly Progress Reports (Available from National Technical Information Service, U.S. Department of Commerce, Springfield, VA 22151)

COO-2245-1	Period June 1, 1972 - November 30, 1972
COO-2245-2	Period December 1, 1972 - February 28, 1973
COO-2245-3	Period March 1, 1973 - May 31, 1973
COO-2245-6	Period June 1, 1973 - August 31, 1973
COO-2245-7	Period September 1, 1973 - November 30, 1973
COO-2245-8	Period December 1, 1973 - February 28, 1974
COO-2245-10	Period March 1, 1974 - May 31, 1974
COO-2245-13	Period June 1, 1974 - August 31, 1974
COO-2245-14	Period September 1, 1974 - November 31, 1974
COO-2245-15	Period December 1, 1974 - February 28, 1975
COO-2245-23	Period March 1, 1975 - May 31, 1975
COO-2245-25	Period June 1, 1975 - August 31, 1975
COO-2245-26	Period September 1, 1975 - November 30, 1975
COO-2245-28	Period December 1, 1975 - February 29, 1976
COO-2245-30	Period March 1, 1976 - May 31, 1976
COO-2245-31	Period June 1, 1976 - August 31, 1976
COO-2245-34	Period September 1, 1976 - November 30, 1976
COO-2245-38	Period December 1, 1976 - February 28, 1977

Reports Issued Under This Contract

B. Topical Reports (Available from National Technical Information Service, U.S. Department of Commerce, Springfield, VA 22151)

E. Khan and N. Todreas, "A Review of Recent Analytical and Experimental Studies Applicable to LMFBR Fuel and Blanket Assembly Design," COO-2245-4TR, MIT, Sept. 1973.

E. Khan, W. Rohsenow, A. Sonin and N. Todreas, "A Simplified Approach for Predicting Temperature Distribution in Wire Wrapped Assemblies," COO-2245-5TR, MIT, Sept. 1973.

T. Eaton and N. Todreas, "Instrumentation Methods for Interchannel Coolant Mixing Studies in Wire-Wrap Spaced Nuclear Fuel Assemblies," COO-2245-9TR, MIT, June 1974.

Y.B. Chen, K. Ip, N.E. Todreas, "Velocity Measurements in Edge Subchannels of Wire Wrapped LMFBR Fuel Assemblies," COO-2245-11TR, MIT, September 1974.

E. Khan, N. Todreas, W. Rohsenow, A.A. Sonin, "Analysis of Mixing Data Relevant to Wire-Wrapped Fuel Assembly Thermal-Hydraulic Design," COO-2245-12TR, MIT, September 1974.

E. Khan, W. Rohsenow, A. Sonin, N. Todreas, "A Porous Body Model for Predicting Temperature Distributions in Wire Wrapped Fuel and Blanket Assemblies of a LMFBR," COO-2245-16TR, MIT, March 1975.

E. Khan, W.M. Rohsenow, A. Sonin, N. Todreas, "Input Parameters to the ENERGY Code (To be used with the ENERGY Code Manual) COO-2245-17TR, MIT, May 1975.

E. Khan, W. Rohsenow, A. Sonin, N. Todreas, "Manual for ENERGY Codes I, II, III," COO-2245-18TR, MIT, May 1975.

E. Khan, W. Rohsenow, A. Sonin, N. Todreas, "Manual for ENERGY Codes I, II, III Computer Programs," COO-2245-18TR Revision 1, MIT, July 1976.

P. Carajilescov and N. Todreas, "Experimental and Analytical Study of Axial Turbulent Flows in an Interior Subchannel of a Bare Rod Bundle," COO-2245-19TR, MIT,

B. Chen and N. Todreas, "Prediction of Coolant Temperature Field in a Breeder Reactor Including Interassembly Heat Transfer," COO-2245-20TR, MIT, May 1975.

F. Carre and N. Todreas, "Development of Input Data to ENERGY Code for Analysis of Reactor Fuel Bundles," COO-2245-21TR, MIT, May 1975.

Reports Issued Under This Contract

B. Topical Reports (Available from National Technical Information Service, U.S. Department of Commerce, Springfield, VA 22151)

E. Khan and N. Todreas, "A Review of Recent Analytical and Experimental Studies Applicable to LMFBR Fuel and Blanket Assembly Design," COO-2245-4TR, MIT, Sept. 1973.

E. Khan, W. Rohsenow, A. Sonin and N. Todreas, "A Simplified Approach for Predicting Temperature Distribution in Wire Wrapped Assemblies," COO-2245-5TR, MIT, Sept. 1973.

T. Eaton and N. Todreas, "Instrumentation Methods for Interchannel Coolant Mixing Studies in Wire-Wrap Spaced Nuclear Fuel Assemblies," COO-2245-9TR, MIT, June 1974.

Y.B. Chen, K. Ip, N.E. Todreas, "Velocity Measurements in Edge Subchannels of Wire Wrapped LMFBR Fuel Assemblies," COO-2245-11TR, MIT, September 1974.

E. Khan, N. Todreas, W. Rohsenow, A.A. Sonin, "Analysis of Mixing Data Relevant to Wire-Wrapped Fuel Assembly Thermal-Hydraulic Design," COO-2245-12TR, MIT, September 1974.

E. Khan, W. Rohsenow, A. Sonin, N. Todreas, "A Porous Body Model for Predicting Temperature Distributions in Wire Wrapped Fuel and Blanket Assemblies of a LMFBR," COO-2245-16TR, MIT, March 1975.

E. Khan, W.M. Rohsenow, A. Sonin, N. Todreas, "Input Parameters to the ENERGY Code (To be used with the ENERGY Code Manual) COO-2245-17TR, MIT, May 1975.

E. Khan, W. Rohsenow, A. Sonin, N. Todreas, "Manual for ENERGY Codes I, II, III," COO-2245-18TR, MIT, May 1975.

E. Khan, W. Rohsenow, A. Sonin, N. Todreas, "Manual for ENERGY Codes I, II, III Computer Programs," COO-2245-18TR Revision 1, MIT, July 1976.

P. Carajilescov and N. Todreas, "Experimental and Analytical Study of Axial Turbulent Flows in an Interior Subchannel of a Bare Rod Bundle," COO-2245-19TR, MIT,

B. Chen and N. Todreas, "Prediction of Coolant Temperature Field in a Breeder Reactor Including Interassembly Heat Transfer," COO-2245-20TR, MIT, May 1975.

F. Carre and N. Todreas, "Development of Input Data to ENERGY Code for Analysis of Reactor Fuel Bundles," COO-2245-21TR, MIT, May 1975.

Reports Issued Under This Contract

B. Topical Reports, Continued

H. Ninokata and N.E. Todreas, "Turbulent Momentum Exchange Coefficients for Reactor Fuel Bundle Analysis," COO-2245-22TR, MIT, June 1975.

R. Anoba and N. Todreas, "Coolant Mixing in LMFBR Rod Bundles and Outlet Plenum Mixing Transients," COO-2245-24TR, August 1975.

B. Bosy, "Fabrication Details for Wire Wrapped Fuel Assembly Components," COO-2245-27TR, MIT, November 1975.

Ralph G. Bennett and Michael W. Golay, "Interferometric Investigation of Turbulently Fluctuating Temperature in an LMFBR Outlet Plenum Geometry," COO-2245-29TR, MIT, June 1976.

N.E. Todreas, "Analysis Methods for LMFBR Wire Wrapped Bundles," COO-2245-32TR, MIT, November 1976.

K.L. Basehore and N.E. Todreas, "Development of Stability Criteria and an Interassembly Conduction Model for the Thermal-Hydraulics Code SUPERENERGY," COO-2245-33TR, MIT December 1976.

Robert Masterson and Neil E. Todreas, "Analysis of the Feasibility of Implementing an Implicit Temporal Differencing Scheme in the SUPERENERGY Code," COO-2245-35TR, MIT, February 1977.

S. Glazer, C. Chiu and N. Todreas, "Collection and Evaluation of Salt Mixing Data with the Real Time Data Acquisition System," COO-2245-36TR, MIT, April 1977.

B. Mikic, E.U. Khan and N.E. Todreas "An Approximate Method for Predicting Temperature Distribution in Wire Wrapped Fuel Assemblies of a LMFBR," COO-2245-37TR, MIT, April 1977.

Reports Issued under this Contract

C. Papers and Summaries

Yi Bin Chen, Ka-Lam Ip, Neil E. Todreas, "Velocity Measurements in Edge Channels of Wire-Wrapped LMFBR Fuel Assemblies," American Nuclear Society Transactions Vol. 19, 1974, pp. 323-324.

P. Carajilescov, N. Todreas, "Experimental and Analytical Study of Axial Turbulent Flows in an Interior Subchannel of a Bare Rod Bundle," J. of Heat Transfer, Vol. 98, No. 2, May 1976, pp. 262-268 (Included as Appendix to Quarterly Progress Report, COO-2245-15).

E. Khan, W. Rohsenow, A. Sonin, N. Todreas, "A Porous Body Model for Predicting Temperature Distribution in Wire-Wrapped Fuel Rod Assemblies," Nuclear Engineering and Design, 35 (1975) 1-12.

E. Khan, W. Rohsenow, A. Sonin, N. Todreas, "A Porous Body Model for Predicting Temperature Distribution in Wire-Wrapped Rod Assemblies Operating in Combined Forced and Free Convection," Nuclear Engineering and Design, 35 (1975) 199-211.

Ralph G. Bennett and Michael W. Golay, "Development of an Optical Method for Measurement of Temperature Fluctuation in Turbulent Flows," American Nuclear Society Transactions, Vol. 22, 1975, p. 581.

B. Chen and N. Todreas, "Prediction of the Coolant Temperature Field in a Breeder Reactor Including Interassembly Heat Transfer," Nuclear Engineering and Design 35, (1975) 423-440 (Included as Appendix to Quarterly Progress Report, COO-2245-23).

R. Bennett and M.W. Golay, "Interferometric Investigation of Turbulently Fluctuating Temperature in an LMFBR Outlet Plenum Geometry," Accepted for the ASME Winter Annual Meeting, Dec., 1976, (Included as Appendix in Quarterly Progress Report, COO-2245-30).

B.B. Mikic, E.U. Khan, N.E. Todreas, "An Approximate Method for Predicting Temperature Distribution in Wire Wrapped Fuel Assemblies of a Liquid Metal Fast Breeder Reactor," Mech. Res. Comm., Vol. 3, 353-360 (1976).

Reports Issued Under this Contract

C. Papers and Summaries (Continued)

L. Wolf, R. Karimi, I.Y. Kim, C.N. Wong, M.K, Yeung "2-D Thermoelastic Analysis of LMFBR Fuel Rod Claddings," Paper C4/d, 4th International Conf. Structural Mechanics in Reactor Technology, San Francisco, August 1977.

M. Yeung, L. Wolf, "Effective Conduction Mixing Lengths for Subchannel Analysis of Finite Hexagonal LMFBR Bundles," ANS Meeting, New York, June 1977.

C. Chiu and N. Todreas,"Flow Split Measurements In An LMFBR Radial Blanket Assembly," ANS Meeting, New York, June 1977.

ABSTRACT

Small scale experiments involving water flows are used to provide mean flow and turbulence field data for LMFBR outlet plenum flows. Measurements are performed at Reynolds Number (Re) values of 33000 and 70000 in a 1/15-scale FFTF geometry and at Re = 35000 in a 3/80-scale CRBR geometry. The experimental behavior is predicted using two different turbulence model computer programs, TEACH-T and VARR-II. It is found that the qualitative nature of the flow field within the plenum depends strongly upon the distribution of the mean inlet velocity field, upon the degree of inlet turbulence, and upon the turbulence momentum exchange model used in the calculations. It is found in the FFTF geometry that the TEACH-T predictions are better than that of VARR-II, and in the CRBR geometry neither codes provides a good prediction of the observed behavior.

From the sensitivity analysis, it is found that the production and dissipation of turbulence are the dominant terms in the transport equations for turbulent kinetic energy and turbulent energy dissipation rate, and the diffusion terms are relatively small. From the same study a new set of empirical constants for the turbulence model is evolved for the prediction of plenum flows.

ACKNOWLEDGEMENTS

The authors wish to express their sincere gratitude to all people who assisted them during the preparation of this report, and the research that supported it. In particular, to the following people:

Professor Neil E. Todreas who has given us much valuable advice and has kindly lent us the Laser Doppler Anemometer with great patience.

To Professor Lothar Wolf and Mr. John Bartzis for their helpful suggestions on our problems.

To Mr. Ralph Bennett who carefully proofread the draft of this report.

To Ms. Marsha Myles for her typing of this report.

Financial support by the United States Energy Research and Development Administration under contract No. E(11-1)-2245 is also sincerely acknowledged.

TABLE OF CONTENTS

LIST OF TABLES

LIST OF FIGURES

No.

No.

No.

No.

NOMENCLATURE

B	constant appearing in Bradshaw's turbulence model
C_1, C_2, C_μ	constants appearing in transport equations of K-ε model
$C_D, C_S, C_B, C_{K\ell}$	constants appearing in transport equations of K-Kℓ model
CQ	amount of heat transfer from boundary to the surrounding fluid
E_{10}, E_{20}	electric field intensity
f_D	Doppler frequency
f_o	reference frequency
g_X, g_Z	gravitational forces in X and Z direction
G	generation terms of turbulent kinetic energy
I	internal energy
K	turbulent kinetic energy
K_i, K_s	wave numbers of incident and scattered light respectively
ℓ	length scale or Prandtl's mixing length
N_{pf}	number of fringes in the measuring volume
y^j	coordinate in cross-stream direction where j is zero for plane flows and is 1 for axisymmetric flows
σ	turbulent kinematic viscosity
$\sigma_K, \sigma_\varepsilon$	effective turbulent Prandtl number for transport of K and ε
$\sigma_{K\ell}$	constants appearing in transport equation of K - Kℓ model
ρ	density of the fluid

ρ_o	reference density
Γ, Γ_1, α, α_1, γ_1, γ_2, γ_3, γ_4	constants appearing in transport equations of K - σ model
γ_T	reciprocal of the turbulent Prandtl number
ν	kinematic viscosity
ν_t	turbulent kinematic viscosity
μ	molecular viscosity
μ_t	turbulent viscosity
μ_{eff}	effective viscosity
ε	turbulent energy dissipation rate
P	pressure
P'	fluctuating pressure component
Re	Reynolds number, defined with respect to inlet duct width
RX,RZ	resistance terms in VARR-II
γ	radial coordinate
S	source terms
t	time
U	mean velocity
U*	friction velocity
$\overline{U'V'}$	kinematic shear stress
$\overline{Ui'Uj'}$	kinematic Reynolds stresses
Ui,Uj	velocity component in Appendix A but mean velocity for other chapters and appendices
Ui',Uj'	fluctuating velocity component
W	mean velocity in Z direction
X_i,X_j	general Cartesian coordinate

τ	wall shear stress or turbulent shear stress
λ	wavelength of laser light
θ	half angle of the beam intersection
β_o	relaxation factor
W_D	Doppler frequency
ψ_1, ψ_2, ψ_3	phase shifts
δf	broadening due to finite transit time, optical imperfection, or velocity gradient
$\delta_{i,j}$	Kronecker delta

CHAPTER 1

INTRODUCTION

In the liquid metal-cooled fast breeder reactor (LMFBR), sodium is the coolant that removes heat from the reactor core. Since sodium is a good heat transfer medium and has a low heat capacity, the temperature difference between the inlet and outlet of the core is much greater than that of the current design light water reactor (LWR). A typical temperature rise is approximately 300°F. During a reactor scram, with or without flow coastdown, the cold sodium will issue from the reactor core, and will mix with the hot sodium that had previously filled the reactor outlet plenum. Predicting the transient thermal response of the sodium in the outlet plenum is an important problem, since this transient will dictate the thermal fatigue environment for the outlet nozzles, instrument trees, and other mechanical components which will be exposed to the reactor coolant flow.

A detailed analytical treatment of the coolant mixing in the outlet plenum is hampered by the complex nature of the resulting turbulent flow. The Navier-Stokes equation cannot be solved numerically because of the small scale of turbulence, and due to the limited storage capacity and speed of existing computers. Therefore, most problems in turbulent flow are solved by using the time-averaged Navier-Stokes equation (or Reynolds equation). Due to the nonlinearity of the Navier-Stokes equations, one additional term, known as the Reynolds stress, appears in the Reynolds equation. Much of the attention

has been concentrated on how to model this stress in terms of known quantities. This is the so-called turbulence model approach. In general, the LMFBR outlet plenum will display a recirculating flow pattern. The simplest models (e.g., Prandtl's mixing length theory) have been found to be inadequate in providing accurate predictions of this behavior. Therefore, current design work has adopted the use of a two-equation turbulence model. This decision is based on the need for accuracy with reasonably short computing times.

In this work,two computer codes, namely TEACH-T[1] and VARR-II[2], are used. TEACH-T is a steady-state two-dimensional code which models turbulent kinetic energy and turbulent energy dissipation rate as two additional dependent variables. VARR-II is a time-dependent two-dimensional thermal-hydraulic code. Different from TEACH-T, it solves transport equations for turbulent kinetic energy and turbulent viscosity. In addition, an energy conservation equation is incorporated into the code for temperature prediction, and it provides a buoyant force feedback to the momentum equation. The code TEACH-T has been modified to calculate flows in the reactor plenum geometry, and used to generate predictions for the experimental part of this work. The code VARR-II is currently in use as a design tool in the Clinch River Breeder Reactor Program. Its predictions have not been verified experimentally in the flow geometry of interest. It is also being used in this work to predict the flow in an experimental test cell.

In the experimental part of this work, a small scale

Cartesian geometry test model of a diametrical section of the prototypic outlet plenum geometries are used. The experiments consist of measurements of velocity, turbulent kinetic energy, and Reynolds stresses in the two perpendicular directions by a Laser Doppler Anemometer. These data are compared to predictions of the behavior of the experiment by each of the two-equation turbulence model codes.

In order to provide some rational explanation of the two-equation model, a survey of existing turbulence models is included in Chapter 2. Chapter 3 describes the analytical model used in the VARR-II and TEACH-T. A detailed description of experimental apparatus is in Chapter 4. The rest of the chapters discuss the results.

CHAPTER 2

REVIEW OF LITERATURE

Most fluid problems encountered in the real world are turbulent. Turbulence is characterized by its irregularity, high diffusivity, and dissipative nature. The design engineer demands high heat output from his heat exchanger which requires a high mass flow rate, and therefore, entails a high Reynolds number and turbulent flow. Flows in heat exchangers, gas furnaces, turbines, etc., are all turbulent to take advantage of the highly diffusive (strongly mixed) nature of the turbulence. Therefore, a good prediction of the mean turbulent fluid behavior, such as pressure drop, velocity distribution, and heat flux is of great value to the designer.

Although turbulent flows exhibit randomness, we have no doubt that they still obey the Navier-Stokes equation and continuity equation. Since the number of unknowns is exactly equal to the number of equations, and since computer methods of solving these differential equations of fluid dynamics are well advanced even for three-dimensional time-dependent flow, in principle we should be able to solve it. Unfortunately, some of the important processes of turbulent phenomena take place in small eddies of the order of a millimeter in size, while the whole domain of the flow field might extend to meters or kilometers. A fine mesh to allow an accurate description of a turbulent flow would definitely exceed the existing computer storage by many orders of magnitude, to say nothing of the computer time.

Fortunately, there is no need to predict all of the details of turbulent motions. Generally, we are concerned with its time-averaged effects. This escapes the requirement of an excessively fine-mesh grid, unavoidable for the Navier-Stokes equation approach, because the time-averaged properties of a turbulent fluid vary much more slowly than do the time-dependent ones. Therefore, it is entirely possible to solve the time-averaged Navier-Stokes equation for most engineering problems with today's computers.

The transport equation for momentum, known as Reynolds equation, is derived (in Appendix A) from the Navier-Stokes equation by suitable averaging procedures. Due to the non-linearity of the Navier-Stokes equation, the resulting equation contains a new unknown correlation (Reynolds stresses) which must be replaced by functions of the model variables. This is the well-known closure problem. The "turbulence model" approach has been invented to solve this problem.

The following section gives a detailed description of some existing turbulence models.

2.1 Survey of Existing Turbulence Models

All of the turbulence models have a common goal, i.e., to calculate the Reynolds stresses which appear in the momentum equation. The models are customarily classified in order by reference to the number of differential equations that are solved beyond those governing the transport equation of mean velocities, temperature, and concentrations.

2.1.1 Zero Equation Models

The models of this group relate the turbulent shear stress (or Reynolds stress) uniquely to the mean flow properties at each location. Since they require only algebraic expressions, these simple models have enjoyed much popularity.

All of the zero equation models use the Boussinesq concept of eddy viscosity, i.e.,

$$\overline{U'V'} = -\nu_t \frac{\partial U}{\partial y}$$

where ν_t is the turbulent kinematic viscosity.

The task is thus reduced to determining the ν_t. The most popular method used by researchers is Prandtl's mixing length hypothesis.[3]

In 1925, Prandtl proposed that turbulent shear stresses and velocity gradients are related by formulas of the same type as for laminar fluids. The effective (or turbulent) viscosity entering the formula is proportional to the product of the local density, a local turbulence length scale, and a local velocity of a random motion; the random velocity is proportional to the length scale multiplied by a local velocity gradient, i.e.,

$$-\overline{\rho U'V'} = \mu_t \frac{\partial U}{\partial y}$$

$$\mu_t = \rho \ell V_{random}$$

$$V_{random} = \ell \left| \frac{\partial U}{\partial y} \right|$$

$$\text{hence } -\rho\overline{U'V'} = \rho \ell^2 \left| \frac{\partial U}{\partial y} \right| \frac{\partial U}{\partial y}$$

The length scale ℓ, known as Prandtl's mixing length, is proportional to the distance of a nearby wall, or the width of the region of the turbulent shear flow.

For many boundary-layer flows, Prandtl's mixing length theory gives remarkable results. However, the constants involved must vary with the problem considered. This lack of universality is an indication that this model fails to describe some important features of the turbulent flows.

As mentioned above, the algebraic models are based upon the assumption that turbulent shear stresses are uniquely dependent on the local mean field, i.e., the generation and dissipation of turbulent energy are in balance everywhere, and the convection and diffusion of turbulent energy are ignored. Such models might be expected to be realistic only when the turbulence is influenced by the local properties of the velocity field or changes only slowly in the direction of the flow. In many cases (e.g., recirculating flows[4]) turbulence is not in local equilibrium with its immediate neighborhood, but depends on processes and events which happen at a considerable distance from the point in question, i.e., the convection and diffusion of turbulence are significant for such flows. In such a situation, we must consider the transport of the turbulence by means of differential equations.

2.1.2 One Equation Model

2.1.2.1 Transport Equation for Turbulent Kinetic Energy

Since turbulence is characterized by its random velocity

and length scale, Kolmogorov[5] and Prandtl[6] independently proposed the use of a transport equation for turbulent kinetic energy (derived in Appendix A) to describe the random velocity scale. Prandtl retained his assumption that the length scale could be taken as proportional to the distance from wall. They both adopted the eddy viscosity concept, and ν_t is proposed to be

$$\nu_t = C_\mu \, K^{1/2} \ell$$

The quality of the prediction of this model depends, of course, on the appropriate prescription of the length scale. But whenever the diffusion and convection of turbulence play a significant role, the prediction is expected to be better than zero equation model.

Bradshaw et al.[7] have proposed a different equation for eddy viscosity. They postulated that the turbulent shear stress is proportional to the turbulent kinetic energy, thus

$$\tau = B\rho K$$

where B is supposedly a universal constant.

This model also needs to incorporate a length scale expression for the dissipation terms. They applied the model to a turbulent boundary level near a wall and obtained good agreement with experimental data. For many flows this assumption is unrealistic, since the shear stress may be zero while K is finite as in the case of a jet.

2.1.2.2 Transport Equation for Eddy Viscosity

Nee and Kovasznay[8] have proposed a transport equation for eddy viscosity itself, based on a phenomenological theory

of turbulence. A length scale distribution is also needed as input. They were successful in making predictions in the turbulent wall boundary layer.

All the models discussed so far have necessitated the use of an algebraic length scale specification, and experience has shown that this may vary with the boundary conditions. There is little hope of achieving universality for these length scales, unless they are also solved by transport equations.

2.1.3 Two-Equation Models

As a fluctuating phenomenon, turbulence is characterized by its random velocity and length scale. Hence, if we want to describe the turbulence closure in terms of two parameters, the turbulent kinetic energy and length scale are appropriate ones. This leads to the two-equation turbulence model approach.

In a two-equation model, the selection of the main variables is a matter of convenience as long as the turbulence kinetic energy and length scale can be represented by the two chosen variables. Many pairs of variables are suitable, the criteria being the simplicity of the governing equation and its associated boundary conditions. A turbulent kinetic energy equation is incorporated in all the models. However, the second model-equation governs either the length scale, dissipation, turbulent vorticity, or the frequency.

2.1.3.1 K - ε Model

A form of a K - ε Model was first proposed by Harlow and Nakayama,[9] and then pursued by researchers at the Imperial

College [1]. The turbulent energy dissipation rate, ε, is defined as $\overline{\nu(\partial U_i'/\partial x_j)^2}$. The differential equation for ε can be derived easily from the Navier-Stokes equation (see Appendix A). This model has shown great success for large variety of flows and will be discussed in detail in Chapter 3.

2.1.3.2 K - Kℓ Model

Rodi and Spalding[10] using Rotta's[11] equation for ℓ derived the differential equation for Kℓ. The equations for K and Kℓ are

$$U\frac{\partial K}{\partial x} + V\frac{\partial K}{\partial y} = \frac{1}{y^i}\frac{\partial}{\partial y}\left(y^j \frac{\nu_t}{\sigma_k}\frac{\partial K}{\partial y}\right) + \nu_t\left(\frac{\partial U}{\partial y}\right)^2 - C_D\frac{K^{3/2}}{\ell}$$

$$U\frac{\partial K\ell}{\partial x} + V\frac{\partial K\ell}{\partial y} = \frac{1}{y^i}\frac{\partial}{\partial y}\left[y^j \frac{\nu_t}{\sigma_{K\ell}}\left(\frac{\partial K\ell}{\partial y} + C_{K\ell}\,\ell\frac{\partial K}{\partial y}\right)\right]$$

$$+ C_B\,\nu_t\,\ell\left(\frac{\partial U}{\partial y}\right)^2 - C_s\cdot K^{3/2}$$

where C_D, C_s, C_B, σ_k, $\sigma_{K\ell}$, and $C_{K\ell}$ are constants.

This model has reported great success in predicting the behavior of free jets, mixing layers, plane jets, and radial jets. Becuase of a lack of universality, no further progress has been made.

2.1.3.3 K - σ Model

Stuhmiller[12] using a heuristic argument about turbulence derived the differential equations for turbulent kinetic energy, K and eddy viscosity, σ. This model is adopted in the computer code VARR-II and is discussed in Chapter 3.

All the models discussed here use the Boussinesq formula to relate the turbulent shear stress to the local velocity gradient. There are engineering problems for which this formula is not adequate. For example, in an annulus having one rough and one smooth wall, the shear stress is often finite when the velocity gradient is zero, and there is a significant region of flow in which the shear stress and velocity gradient have opposite signs. These failures naturally lead to multi-equation models.

2.1.4 Multi-Equation Model (Reynolds Stress Model)

The most direct way to determine $\overline{U'V'}$ is, of course, to solve a transport equation for this quantity. It is expected that the use of the Reynolds stress model will increase the universality of the prediction methods, because in contrast to the above method, it is unnecessary to introduce an approximate shear stress relation, whose validity is in question for certain flow conditions. However, the Reynolds stress equation (derived in Appendix A) involves new unknowns, such as triple correlations and pressure-velocity correlations. These quantities are either difficult to measure or hard to simulate. Since this model is still in an early stage, we will not go into further details.

As discussed above, a good turbulence model is universal and is not too complex to use. Universality implies that a single set of empirical constants or functions inserted into the equations provides close simulations of all varieties of flows. Complexity is measured by the number of differential equations

which the model contains, and the number of the empirical constants and functions which are required to complete them.

Now it should be clear that the main obstacles to model development are the difficulty of selecting the set of differential equations that are capable of providing universality, and then the difficulty of providing, from experiments and knowledge, the required constants and functions.

CHAPTER 3

DESCRIPTION OF THE ANALYTICAL MODEL ADOPTED IN THE STUDY

One major task of this study is to select appropriate turbulence model codes, generate predictions, and compare them with the experimental results.

There are two codes used in this investigation. They are discussed in the following two sections.

3.1 TEACH-T Code

TEACH-T is a steady state two-dimensional two-equation turbulence model code[1]. It was developed by the staff in the Mechanical Engineering Department at the Imperical College of Science and Technology in England.

3.1.1 Basic Assumptions

Generally, turbulence is nonisotropic and three-dimensional, and thus turbulence parameters have directional properties. Any description of turbulence by scalar parameters implies an isotropy of the mean flow properties. Therefore, in a two-equation turbulence model, the nonisotropy of the turbulence can only be dependent upon the nonisotropy of the mean flow field, usually through an eddy viscosity, ν_t. On the basis of the above discussion, the Reynolds stresses can be expressed as

$$\overline{U_i' U_j'} = \frac{2}{3} K \delta_{ij} - \nu_t \left(\frac{\partial U_i}{\partial x_j} + \frac{\partial U_j}{\partial x_i} \right)$$

where the first term on the right hand side has been added in order to make the equation applicable to homogeneous and isotropic

turbulence. With this formulation, the equations of motion will retain their original form with a variable viscosity. From dimensional analysis, the turbulent viscosity, ν_t, is related to turbulence kinetic energy, K, and a length scale, ℓ, by

$$\nu_t = C_\mu K^{1/2} \ell$$

where C_μ is supposedly a constant.

3.1.2 Model Equations

The quantities K and ε serve as the model variables. As stated in section 2.1.3 these are not the only possible variables, and in fact many other pairs of variables are more attractive. The criterion of the selection is just the simplicity of the governing equations and associated boundary conditions.

The TEACH-T code has adopted the K-ε turbulence model, first proposed by Harlow and NaKayama[9]. The reason for this selection lies partly in the relative ease with which the exact equations for K and ε can be derived and partly in the fact that ε appears directly as an unknown in the equation for K.

The derivation of the turbulence kinetic energy equation is included in Appendix A. The resulting equation follows:

$$\frac{\partial K}{\partial t} + U_k \frac{\partial K}{\partial x_k} = - \frac{\partial}{\partial x_k} \left(\frac{1}{2} \overline{U'_k U'_i U'_i} + \frac{1}{\rho} \overline{P' U'_k} \right) - \overline{U'_i U'_k} \frac{\partial U_i}{\partial x_k}$$

$$- \nu \left(\overline{\frac{\partial U'_i}{\partial x_k} \frac{\partial U'_i}{\partial x_k}} - \frac{\partial^2}{\partial x_k} K \right)$$

The most disappointing feature it exhibits, which is common to

all turbulence equations is that it contains terms involving an unknown correlation of the velocity and pressure, and therefore cannot be solved. The physical meaning of the individual terms is easily recognized as convection, diffusion, generation, and dissipation.

The generation term poses very few problems, since it contains only the products of Reynolds stresses and velocity gradients. They can be measured experimentally or found by calculation. The physical meaning of this term is also easily understood. The mean flow performs work on the turbulent eddies, and thus energy is transferred from the mean motion into the fluctuating motion.

Towsend[13] has proposed an energy cascade process in turbulent flows, by which energy is transferred from the big eddies to the small eddies. At the end of the cascade, the viscous stresses perform deformation work against the fluctuating strain rate, and all the energy is dissipated into heat. The last term describes this process.

The diffusion terms are the most difficult ones to tackle. The triple correlation, $\frac{1}{2}\frac{\partial}{\partial x_k}\overline{U'U'U'}$, represents the energy transport by the turbulent eddies, and the pressure-velocity correlation represents the transport of energy by pressure fluctuations. The last process is not yet properly understood and its measurement is hampered by severe difficulties[4]. The triple correlation can be measured, but two-equation theory is not advanced enough to model it. The escape is to recognize that both terms do not generate or absorb turbulence energy,

and act only as agents to change the spatial distribution of the energy. This process is similar in nature to laminar diffusion, and it is suggestive to model it by a second order diffusion equation with a diffusion coefficient that is related to the turbulent viscosity, i.e.,

$$-\frac{\partial}{\partial x_k}\left(\frac{1}{2}\overline{U_k'U_i'U_i'} + \overline{U_k'P'}\right) = \frac{\partial}{\partial x_k}\left(\frac{\nu_t}{\sigma_k}\frac{\partial}{\partial x_k}K\right)$$

Thus, the resulting equation for turbulence kinetic energy is

$$\frac{DK}{Dt} = \frac{\partial}{\partial x_k}\left(\frac{\nu_t}{\sigma_k}\frac{\partial}{\partial x_k}K\right) + G - \varepsilon$$

$$\text{where } G \equiv -\overline{U_i'U_j'}\frac{\partial U_i}{\partial x_j} = \nu_t\left(\frac{\partial U_i}{\partial x_j} + \frac{\partial U_j}{\partial x_i}\right)^2$$

$$\varepsilon \equiv \nu\left(\overline{\frac{\partial U_i'}{\partial x_k}\frac{\partial U_i'}{\partial x_k}}\right)$$

σ_k is a model constant.

Algebraic manipulation of the Navier-Stokes equation yields a transport equation for the turbulence energy dissipation rate (see Appendix A for a derivation).

$$\frac{\partial \varepsilon}{\partial t} + U_k\frac{\partial}{\partial x_k}\varepsilon = -2\nu\frac{\partial U_i}{\partial x_k}\left(\overline{\frac{\partial U_i'}{\partial x_l}\frac{\partial U_k'}{\partial x_l}} + \overline{\frac{\partial U_i'}{\partial x_i}\frac{\partial U_l'}{\partial x_k}}\right)$$

$$-2\nu\overline{\frac{\partial U_i'}{\partial x_k}\frac{\partial U_i'}{\partial x_k}\frac{\partial U_k'}{\partial x_k}} - 2\overline{\left(\nu\frac{\partial^2 U_i'}{\partial x_k \partial x_l}\right)^2}$$

$$-\frac{\partial}{\partial x_k}\left(\overline{U_k'\varepsilon'} + \frac{2\nu}{\rho}\overline{\frac{\partial P'}{\partial x_l}\frac{\partial U_k'}{\partial x_l}}\right)$$

$$-2\nu\,\overline{u_k'\,\frac{\partial u_i'}{\partial x_1}}\;\frac{\partial^2 u'_i}{\partial x_1 \partial x_k} + \nu^2\;\frac{\partial^2}{\partial x_k^2}\,\overline{\left(\frac{\partial u_i'}{\partial x_1}\right)^2}$$

None of the terms on the right hand side of the equation are accessible to measurement. According to Launder[4], at a high Reynolds number the equation can be simplified to

$$\frac{D\varepsilon}{Dt} = \frac{1}{\rho}\,\frac{\partial}{\partial x_k}\left(\frac{\mu_t}{\sigma_\varepsilon}\,\frac{\partial \varepsilon}{\partial x_k}\right) + \frac{C_1}{\rho}\,\frac{\mu_t \varepsilon}{K}\left(\frac{\partial U_i}{\partial x_k} + \frac{\partial U_k}{\partial x_i}\right)\frac{\partial U_i}{\partial x_k} - C_2\,\frac{\varepsilon^2}{K}$$

where σ_ε, C_1, and C_2 are model constants.

The physical meaning of these terms is easily recognized as convection, diffusion, production, and decay.

3.1.3 Model Constants

In the transport equations for K and ε, several empirical constants still need to be determined. Launder et al.[1] obtained the value of C_2 from the decay of grid turbulence, C_μ and C_1 from near wall turbulence, and σ_k and σ_ε from an optimization of theory and data. The recommended values are

C_μ	C_1	C_2	σ_k	σ_ε
0.09	1.44	1.92	1.0	1.3

Now the only remaining problems are a solution algorithm and boundary conditions. These are quite lengthy and are described in detail in Appendix C.

The TEACH-T code has been applied to many turbulent flow problems, including recirculating flow, free shear flow, pipe flow, and boundary layer flow. The agreement with experimental

data is generally very good.

3.2 VARR-II Code

VARR-II is a time-dependent two-dimensional thermal-hydraulic code[2]. It solves turbulence kinetic energy and turbulent viscosity equations. Hence, it is a two-equation turbulence model code. In addition, an energy conservation equation is included to account for small density variations due to temperature changes, and in this way, it provides a buoyant force feedback into the momentum equation. This code was developed by Science Applications Inc. for the Westinghouse Advanced Reactor Division to aid in the design of the LMFBR outlet plenum.

3.2.1 Basic Assumptions

Stuhmiller [12] used a plausible explanation of the turbulence transport phenomena to derive the two turbulence model equations. His arguments may be summarized as follows. In a fully developed turbulent flow, fluctuations exist on every spatial scale from the largest allowed by the geometry of the boundaries to the smallest allowed by molecular viscosity. However, it is often possible to distinguish two spatial regimes: one that is primarily responsible for the diffusivity of the flow, and a second for the viscous dissipation of energy. Based on these assumptions, the turbulence spectrum may be simplified to one in which there are only two eddy sizes: the production scale, which interacts strongly with the mean flow by transferring energy from the mean motion to the large eddies,

and the dissipation scale, which represents the small scale motion leading ultimately to the creation of heat. Since only large eddies have direct importance to the mean flow, a single wavenumber of the turbulence frequency spectrum is considered. Physical interpretation of the interaction with other wavenumbers is made so that the equation of motion for the fluctuating quantities can be linearized. From the dynamics of the simulated fluctuation, the equations of turbulence kinetic energy, turbulent viscosity, and Newtonian stress-strain are derived.

Different from other work, the closure of the equations for the fluctuating quantities, rather than their correlations, leads to the introduction of new parameters and reveals several interconnections between measurable quantities.

3.2.2 Model Equations

The final form of the equations for mean motion, U_i, turbulence kinetic energy, q, and turbulent viscosity, σ, is as follows:

$$\frac{\partial U_i}{\partial t} + U_k \frac{\partial U_i}{\partial x_k} = - \frac{\partial P}{\partial x_i} + \frac{\partial}{\partial x_k}(\sigma+\nu)\left(\frac{\partial U_i}{\partial x_k} + \frac{\partial U_k}{\partial x_i}\right)$$

$$\frac{\partial q}{\partial t} + U_k \frac{\partial q}{\partial x_k} = \frac{1}{2}\sigma \left(\frac{\partial U_i}{\partial x_k} + \frac{\partial U_k}{\partial x_i}\right)^2 + \frac{\partial}{\partial x_k}\Gamma\sigma \frac{\partial q}{\partial x_k} - \alpha\frac{(2q)^2}{\sigma}$$

$$\frac{\partial \sigma}{\partial t} + U_k \frac{\partial \sigma}{\partial x_k} = \frac{\sigma^2}{4q} \left(\frac{\partial U_i}{\partial x_k} + \frac{\partial U_k}{\partial x_i}\right)^2 + \frac{\sigma}{q} \frac{\partial}{\partial x_k}\Gamma\sigma\frac{\partial q}{\partial x_k}$$

$$-\frac{\sigma^3}{q^2}\frac{\partial}{\partial x_k}\Gamma q\frac{\partial}{\partial x_k}\left(\frac{q}{\sigma}\right) - 4\alpha_1 q$$

where $\Gamma = 3\frac{\gamma_1}{\gamma_2}(1 + \gamma_2^2)$

$$\alpha = \frac{1}{3}\frac{\gamma_2^2}{\gamma_2^2 + 1}$$

$$\Gamma_1 = (\gamma_3/\gamma_1)\Gamma$$

$$\alpha_1 = (1 - \frac{\gamma_4}{2\gamma_2})\alpha$$

3.2.3 Model Constants

The first section has described briefly the development of a two-equation turbulence model of turbulent flow, which introduces four empirical constants: either the set γ_1, γ_2, γ_3 and γ_4 or Γ, α, Γ_1, α_1. They are determined from experiments on the decay of turbulence, a consideration of near-wall turbulence, of turbulent pipe flow, and of boundary-layer flow.

The recommended values are

Γ	α	Γ_1	α_1
1.5	0.045	0.75	0.01125

Finally, the description of the numerical solution algorithm and boundary conditions is found in Appendix B.

The author has applied the model to turbulent pipe flow and turbulent wake flow; the agreement is good except near a solid wall. But this code has not been tested against enough data, and the free parameters are also just tentative values. Hence, more testing is urgently needed, and the experiments in this work are aimed at supporting this code.

The code TEACH-T has been modified to calculate flows in the reactor plenum geometry, and used to generate predictions for the experimental part of this work. The code VARR-II is currently in use as a design tool in the Clinch River Breeder Reactor Program. Its predictions have not been verified experimentally in the flow geometry of interest. It is also being used in this work to predict the flow in an experimental test cell. Thus, by intercomparison of the results from these two competing turbulence model codes and the observed experimental data, one may identify sources of error in the predictions and make appropriate improvements in the turbulence models for the outlet plenum application.

CHAPTER 4

DESCRIPTION OF THE EXPERIMENTAL APPARATUS

This chapter describes the hydraulic facilities and instruments used in the experiments.

4.1 Hydraulic Facilities

A schematic diagram of the hydraulic loop is shown in Fig. 4.1. The 50 gallon aluminum tank is filled with distilled water. All the pipes, valves, and fittings are made of copper or brass to prevent corrosion. Polystyrene latex particles with sizes between 0.46 μ and 0.54 μ are added to the water to increase the intensity of the scattered light. A 1 HP pump and a 5 HP pump are connected in parallel to deliver the flow. In order to increase the Reynolds numbers, a heat exchanger is included in the loop to increase the temperature. To measure flow rates, two different flowmeters are used in order to assure the accuracy of the flowmeter readings. Flow rates ranging from 0.7 to 37.8 GPM can be obtained.

A variable geometry outlet plenum test section which can simulate two reactor cases, namely those of the Fast Flux Test Facility (FFTF) and the Clinch River Breeder Reactor (CRBR), has been fabricated. It is composed of one 2" thick machined aluminum piece and two 1" thick plexiglass faceplates which when bolted together define the rectangular internal geometry shown in Fig. 4.2. By moving the internal plexiglass blocks it can change from a 1/15-scale FFTF geometry to a 3/80-scale CRBR geometry, and vice versa.

4.2 Instrumentation

A complete list of the instruments for the experiments is given in Table 4.1. The functions of the individual instruments are described in the following sections. A detailed discussion of the Laser Doppler Anemometer is found in Appendix D.

4.2.1 Optical System[14]

The optical arrangement for the experiments, a two channel reference beam mode, is shown in Fig. 4.3. The laser beam from a Spectra-Physics Model 164 2 watt Argon Laser enters axially into the DISA Model 55L83 Beam Splitter and Modular section through a small window. It then passes through a beam splitting prism which splits the beam in either a 50/50 or 90/10 intensity ratio. One beam passes through a Bragg cell, where it is diffracted and is shifted in frequency by $\pm$ 40MHz depending on the orientation of the Bragg cell with respect to the incident laser beam. It then passes through a neutral density filter which is continuously adjustable between 0% and 100% transmission. This shifted beam then passes through a DISA 55L85 Two-Channel section which further splits the beam. Three beams come out of this two-channel section. They enter the DISA Model 55L87 beam separator which focusses the beam to a point within the flow channel with a 30 cm focal length lens. The two DISA Model 55L12 photomultipliers are aligned with the two reference (shifted) beams to pick up the signal. Each photomultiplier is powered from its own high voltage supply. The anode currents of the photomultipliers are monitored by two Simpson current meters.

The laser, optical unit, and photomultiplier are mounted on the aluminum plate shown in Fig. 4.4. The plate is supported by a table whose carriage provides three dimensional travel of the entire system. The measuring point is positioned within the flow channel by moving the carriage containing the laser, optical unit, and photomultipliers as an integral unit.

4.2.2 Signal Processing System

The signal from the photomultiplier is downshifted electronically by either a TSI Model 985 Frequency Shifter or DISA Model 55L70 Control Unit. The amount of frequency downshift is adjustable and can be selected to fit the best tracking range of the signal processor. Then the signal is fed into either the DISA Model 55L20 Signal Processor or the TSI Model 980 Signal Processor. Both trackers contain a frequency lock loop which can track the Doppler signal continuously and provide an electric analog of the instantaneous Doppler frequency of the flow velocity.

The analog outputs of each tracker are connected to the DISA Model 52B25 Turbulence Processor which makes the cross-correlation of the two velocity components.

An HP Model 141B oscilloscope monitors the output of the preamplifier. This is very helpful during optical alignment to optimize the signal and to provide a constant check on the quality of the Doppler signal.

4.2.3 Signal Recording System

Two digital voltmeters and two True RMS Voltmeters (with

integrating circuits) are connected to the output of the tracker to obtain the average voltage and rms voltage respectively. These voltages correspond to the average velocity and the rms velocity in the flow.

One more digital voltmeter is connected to the Turbulence Processor to get the value of the two-component voltage cross-correlation, which in turn corresponds to the Reynolds stress.

The complete layout of the instrumentation is shown in Fig. 4.3.

Table 4.1
Description of Equipment

Unit	Manufacturer	Model No.
Argon Laser	Spectra-Physics	164
Laser Exciter	Spectra-Physics	265
Optical Unit	DISA	55L88
Photomultiplier	DISA	55L12
High Voltage Supplier	Baird-Atomic	312A
Anode Current Meter	Simpson	N/A
LDA Control Unit	DISA	55L70
LDA Frequency Shifter	TSI	985
Doppler Signal Processor	DISA	55L22
Doppler Signal Processor	TSI	980
Turbulence Processor	DISA	52B25
Digital Voltmeter	TSI	1076
Digital Voltmeter	Hewlett-Packard	3456A
RMS Voltmeter	DISA	55D35
Oscilloscope	Hewlett-Packard	141B

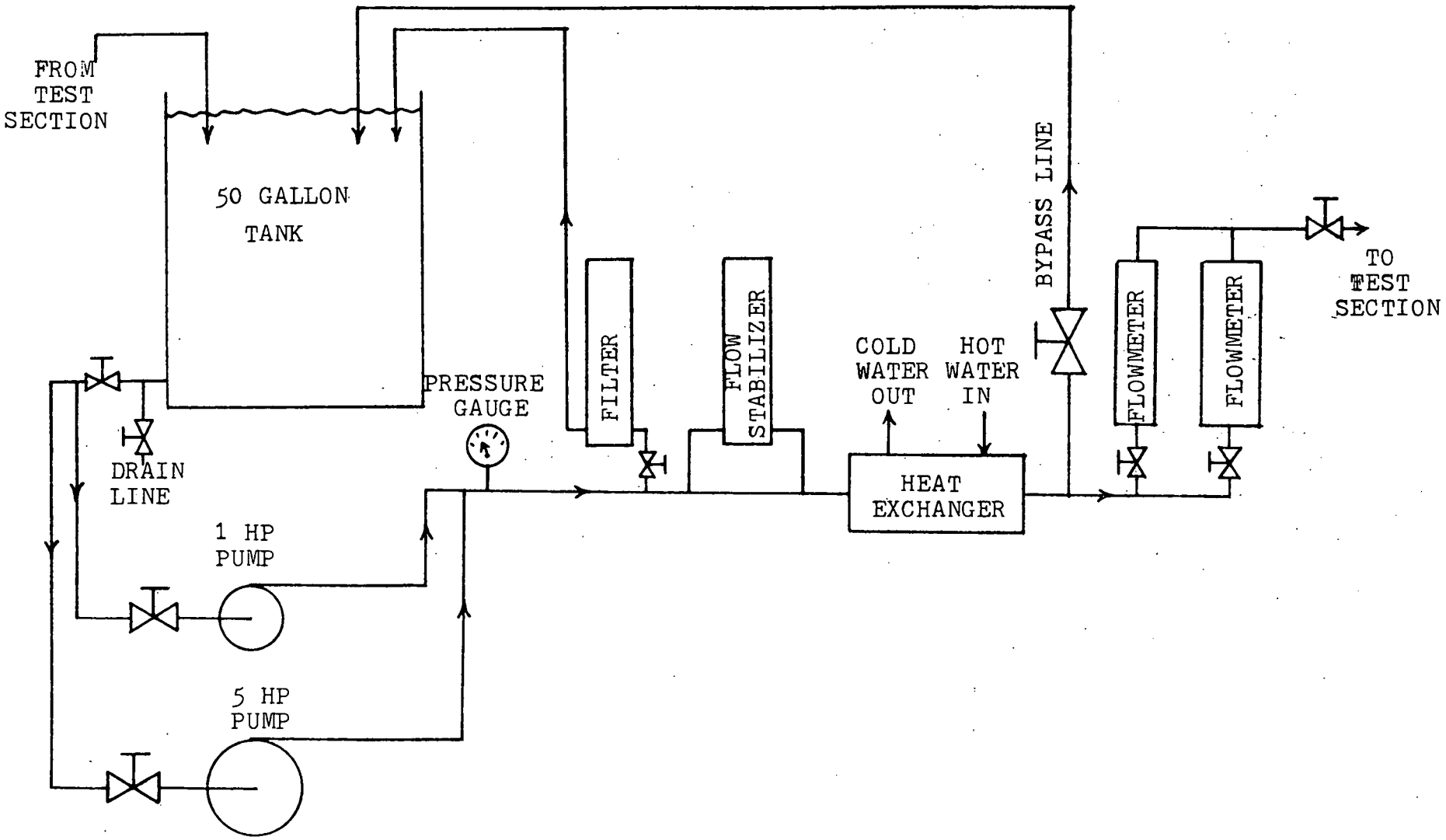

Fig. 4.1 The Hydraulic Loop

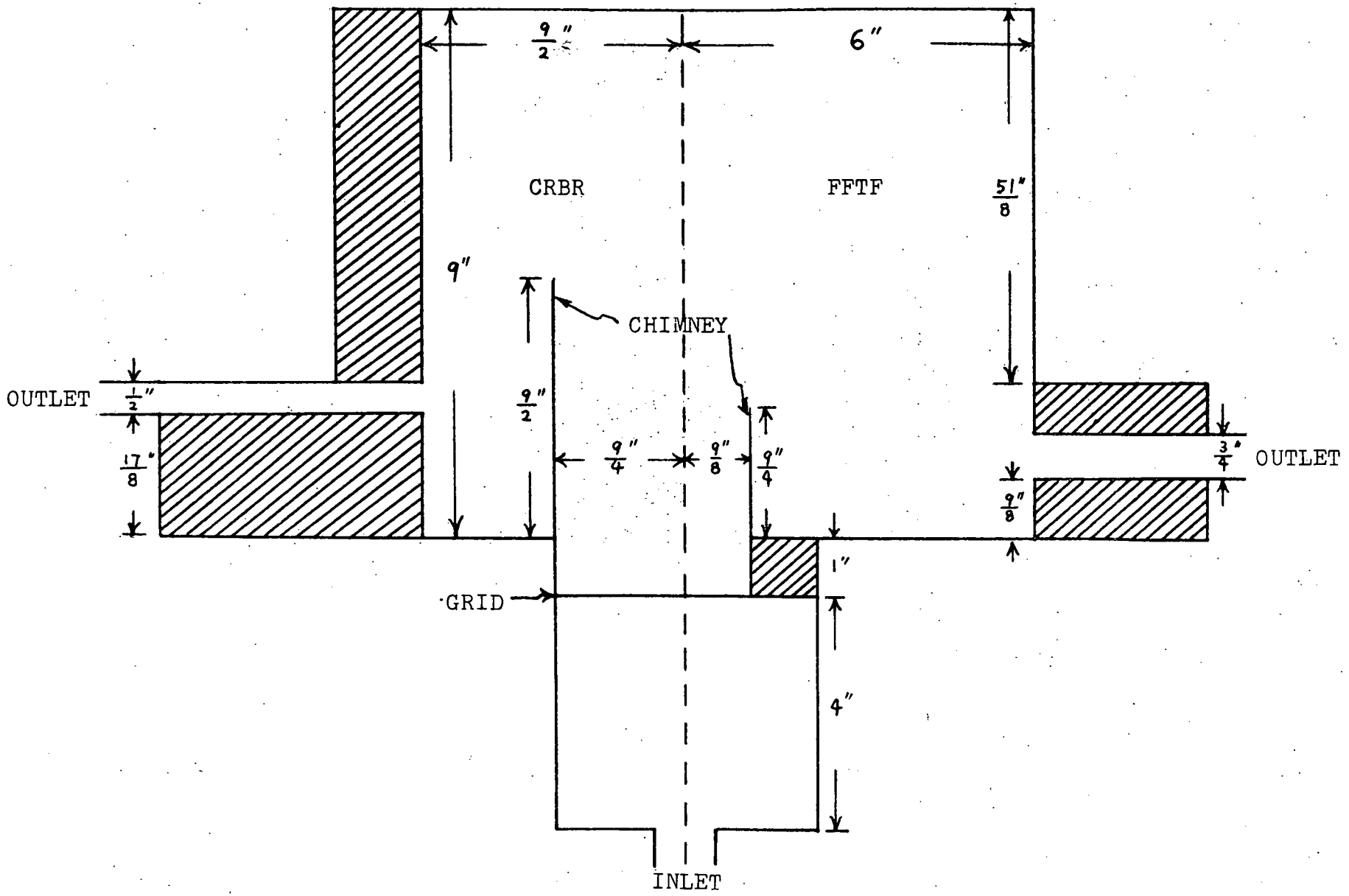

Fig. 4.2 Test Section

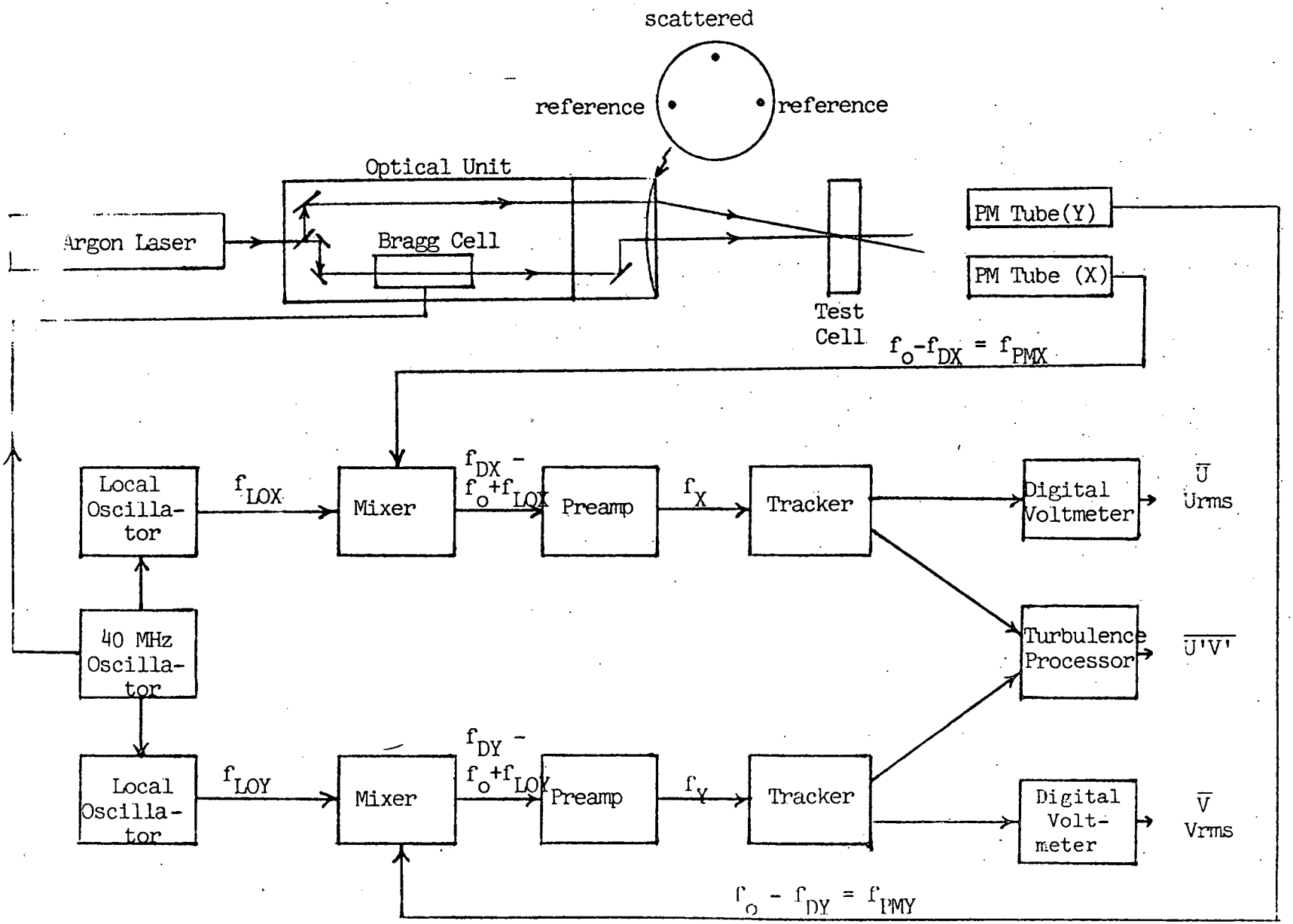

Fig. 4.3 Layout of Instruments

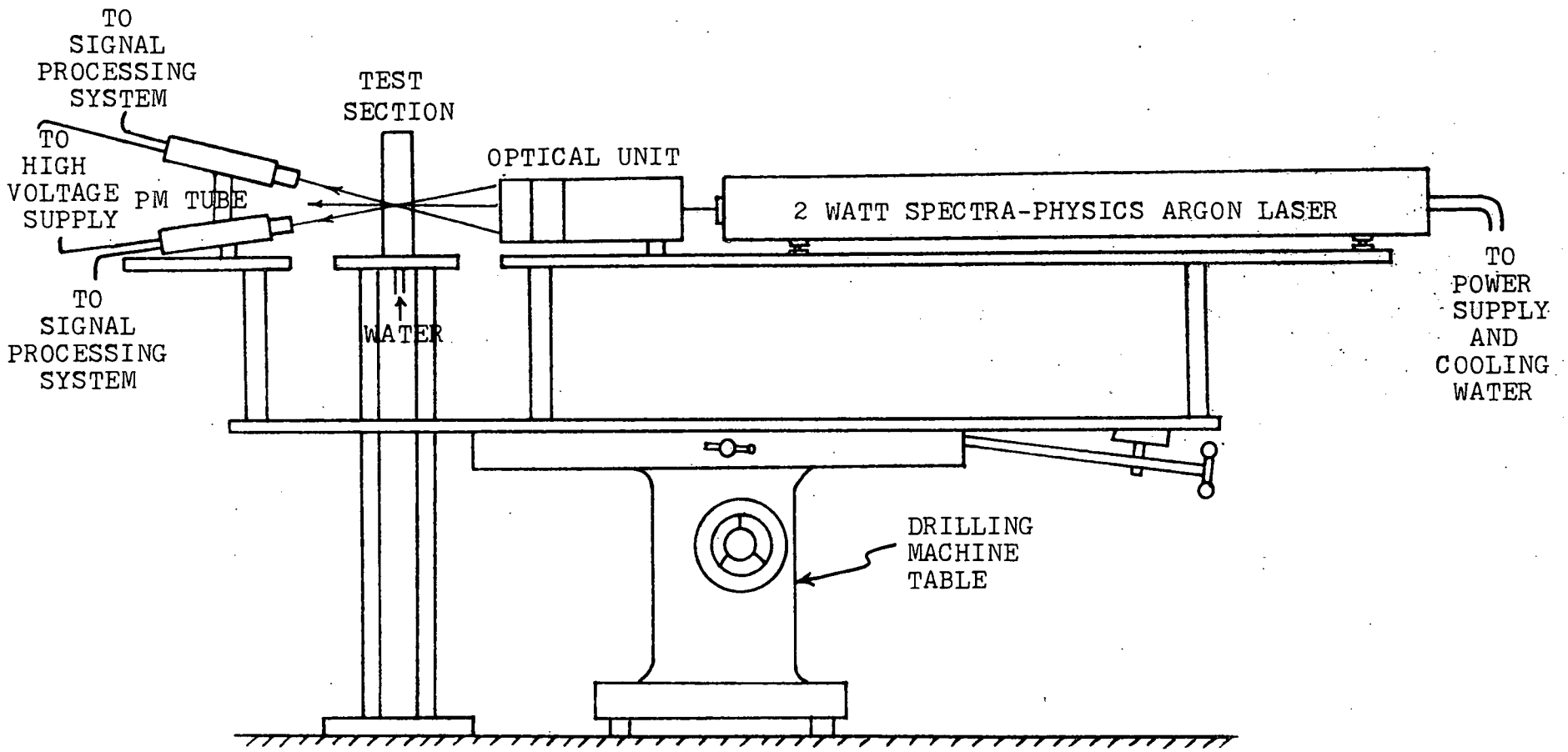

Fig. 4.4 Experimental Setup

CHAPTER 5

DISCUSSION OF EXPERIMENTAL RESULTS AND COMPUTER CODE PREDICTIONS

5.1 Description of Experiments

Water flow tests were performed with Cartesian geometry 1/15-scale model of FFTF geometry and 3/80-scale model of CRBR geometry as shown in Fig. 4.2. A summary of tests for which comparisons will be made is given in Table 5.1. The Reynolds number is defined with respect to the inlet duct width and inlet flow rate. The normal inlet condition implies that no inlet blockage arise to reshape the flow distribution. In the distorted case,a partial inlet blockage is used to provide a velocity distribution which has a maximum near the outside edge of the inlet orifice. The experimental errors are typically 3 percent for the mean velocity, 7 percent for the turbulent kinetic energy, and 20 percent for the Reynolds stress (see Appendix F for error analysis). The data reduction method is included in Appendix E. The reduced data are tabulated in Appendix G.

5.2 Computer Code Calculations

For the computer prediction, the inlet velocity distribution is provided by the experimental data. Inlet turbulence parameters, such as turbulent kinetic energy, turbulent energy dissipation rate, and turbulent kinematic viscosity, either are matched to the experimental data or are built-in values in the codes. Uniform mesh in both directions is used

to improve numerical stability and accuracy. Due to the mesh size and geometry of the test section, the minimum mesh points requirements are 18 x 26 and 14 x 20 for FFTF and CRBR geometry, respectively (see Figs.G.1 and G.2). The number of mesh points could be increased to improve the accuracy, but they are limited by computer storage capacity and computing time. A typical computation time for FFTF geometry at IBM 360/65 computer is 20 and 180 minutes for TEACH-T and VARR-II respectively.

5.3 Comparison of Code Predictions with Experimental Data

5.3.1 FFTF Geometry

The measured and predicted velocity field data are shown in Figs.5.1 through 5.22 for the FFTF geometry. In each of the velocity maps the local velocities are normalized to the maximim inlet velocity. It is not surprising that all the figures show the recirculating flow pattern, which is consistent with flow visualization during the experiment in which a torroidal flow pattern is observed.

It is seen from the data that both the measured and predicted flow fields depend strongly on the inlet flow conditions, such as the velocity distribution and turbulence parameters.

5.3.1.1 FFTF Geometry, Re=33,000, Normal Inlet Velocity Distribution Case

From Figs. 5.1 to 5.3, it is seen that both codes predict velocity fields with inlet jets which persist spatially with greater momentum than are observed experimentally.

Similarly the predicted vortex centers are significantly displaced from the observed vortex location and the predicted mean velocity values near the wall boundary are greater than those observed experimentally. The predicted shape of the velocity contours near the top wall is also different from experiment. The agreement with the experiment of the TEACH-T prediction is generally superior to that of VARR-II prediction. This is thought to be so because the former calculations are performed by matching the turbulent kinetic energy values to those obtained from the experiment. It is seen in Fig. 5.4 that the turbulent kinetic energy prediction by TEACH-T agrees reasonably well at most positions with experimental values (i.e., within the same order of magnitude) and those predicted by VARR-II are generally lower than the measured values by as much as an order of magnitude, typically. From Fig. 5.5, it is seen that the Reynolds stress agreement is poorer for both codes than is that for the turbulent kinetic energy. This is thought to occur because in neither calculation are the inlet Reynolds stress value matched to the experimental values. The generally better agreement of the TEACH-T prediction reflects the value of specifying accurately the inlet velocity and turbulent kinetic energy, while the VARR-II calculation employs built-in turbulent kinetic energy and turbulent kinematic viscosity functions.

5.3.1.2 FFTF Geometry, Re=70,000 Normal Inlet Velocity Distribution Case

The measured and predicted velocity and turbulent field data are shown in Figs. 5.6 through 5.14. It is seen from Figs. 5.6 through 5.8 that the velocity field comparison between TEACH-T, VARR-II, and the experiment is reasonably good reflecting the expected improvement in turbulence model prediction at high Reynolds number. As in the case of Re=33,000

the calculation tends to predict different shape and higher velocities of near-wall flows and with the overall vortex shape being distorted from that observed experimentally. In Figs. 5.11 and 5.12, a series of calculations is presented which is identical to the cases of Figs. 5.7 and 5.8 except that the inlet turbulence parameters are matched with the experimental data. It is seen that the mean flow field predictions are virtually identical in all cases. In the TEACH-T case the overall predictions of the turbulent kinetic energy and Reynolds stress fields are improved by matching the inlet turbulent energy dissipation rate. In the VARR-II case the mean velocity, turbulent kinetic energy and Reynolds stress field are almost unaffected by matching the inlet turbulence parameters, and the quality of the prediction is generally poorer than that by TEACH-T. The inability of both codes to predict the near-wall velocities is thought to be due to use of an insufficient number of mesh points to resolve the important details of turbulence and the failure of all the turbulence models to describe the non-isotropic turbulent flow close to the wall.

It is seen in Fig. 5.9 that the measured turbulent kinetic energy is quite uniform over the entire flow field except near the inlet jet region. Hence, one expects that the diffusion of the turbulent kinetic energy is relatively small. Code predictions confirm this argument. In the later sensitivity analysis (Section 5.4), when we change the value of diffusion coefficients, the velocity fields are seen to remain almost unchanged. This also indicates that the diffusion terms in the transport equations are small compared to other terms. The TEACH-T code also indicates that convection is

not a small term compared to generation and dissipation, but the local equilibrium of generation and dissipation is seen to be not a bad assumption for most parts of the flow region.

From the experimental data it is also suggested that the Reynolds stress is proportional to the local mean flow speed. Hence, a test is made in Section 5.3.1.4 to check the adequacy of this conclusion.

5.3.1.3 FFTF Geometry, Re=70,000, Distorted Inlet Velocity Distribution Case

The qualitative dependence of the observed and predicted flow fields on the inlet mean velocity distribution is shown in Figs. 5.15 through 5.17. In this case the inlet flow rate is maintained at Re=70,000; however, a partial inlet flow blockage is used to provide a velocity distribution which has a maximum near the outside edge of the inlet duct. This results in a mean flow map which is qualitatively different from that observed in the previous cases. The main flow is observed to split into two parts, one of which passes through the center portion of the plenum, and another of which reaches the top wall and forms a rotating secondary flow. This is due to the high shear stress above the inlet orifice which results in rapid entrainment of inlet fluid in the main plenum flow. The high near-wall velocity causes this secondary flow to move counter-clockwise as with the main flow.

It is notable that both codes are barely able to predict the qualitative features of this flow, and neither code is

successful in describing the experimentally observed flow field in detail, particularly in regard to the location and rate of circulation of the secondary flow vortex. Unfortunately, in this case, the inlet velocity and turbulent parameters measurements are not detailed enough to calculate the turbulent energy dissipation rate and turbulent viscosity. Consequently, no exactly matched predictions can be presented here. However, comparison of experimental data and predictions suggests that a lower value for the dissipation rate should apply. Hence, the TEACH-T code is rerun for a new dissipation rate. The resulting velocity field is shown in Fig. 5.18. It is seen that the predictions of velocity field are of somewhat better quality in terms of magnitude but the second vortex disappears. This is due to the low inlet dissipation rate which causes the inlet jet to persist with greater momentum than in the previous case. In the later sensitivity analysis, an effort is made to adjust the inlet turbulence parameters, and to use the best set of empirical constants, but all the predictions are unable to reproduce the experimental results.

As with the previous cases, the diffusion of turbulent kinetic energy is small, Reynolds stress is proportional to the local velocity, and the TEACH-T prediction of the turbulence parameters is much more successful than that of VARR-II.

The importance of this case lies in the fact that the qualitative nature of the mean flow field is strongly dependent not only upon the inlet mean velocity field but also the inlet turbulence parameters.

5.3.1.4 Zero-Equation Model

In a separate calculation, a simple Reynolds stress relationship $\overline{U'V'} = C|\underline{U}|^2$ rather than a two-equation model is used in TEACH-T, where C is the average value of proportional constants between Reynolds stress and square of mean flow speed in the measured flow field. The resulting velocity maps are shown in Figs. 5.21 and 5.22 for normal and distorted inlet velocity distribution respectively. It is seen that the simple model yields results which are approximately equivalent in quality to those obtained from two-equation models (see Figs. 5.11 and 5.16) except the overestimation of near-wall velocities. The results are weakly sensitive to the value of C. This indicates that the turbulence model used to describe the turbulent momentum transfers within the flow may be less important than an accurate knowledge of the detailed inlet mean flow field.

5.3.2 CRBR Geometry

Data similar to those obtained in the 1/15-scale FFTF test cell have also been obtained for steady state water flows in a 3/80-scale CRBR outlet plenum geometry. In this geometry, the inlet orifice is much wider and the chimney penetrates much deeper into the plenum than in the FFTF case, so that relative to the inlet duct the outlet plenum is much shorter and narrower than in the FFTF case. Because of the wider inlet orifice, the maximum attainable Reynolds number decreases to 35,000. As with FFTF geometry, normal and distorted inlet

mean velocity distributions were investigated. Due to uncertainties in the accuracy of the measured data, the distorted mean flow distribution case is removed from this section and is included in Appendix H. The striking feature of the distorted inlet flow distribution case is that both codes are unable to predict the mean flow anywhere qualitatively.

5.3.2.1 CRBR Geometry, Re=35,000, Normal Inlet Velocity Distribution Case

The measured and predicted velocity fields are shown in Figs. 5.23 through 5.25. Because of the shorter distance between the inlet orifice and the top wall, the inlet jet moves perpendicularly upward and turns only in the vicinity of the wall, while in the FFTF case the mean flow is able to follow streamlines very nicely from the entrance to the exit in a fashion as would be predicted by intuition.

This greater mean flow chaos is seen in the comparison of the measured flow field to the TEACH-T and VARR-II predictions. It is seen in the lower half of the plenum that the measurements and code predictions agree reasonably well. While in the upper half of the plenum, both codes do not have good agreement with the measurement.

Due to the large discrepancy in the prediction of the mean flow field with the normal inlet flow distribution, TEACH-T is rerun with the mesh size reduced by half. The resulting velocity distribution is shown in Fig. 5.28.

Comparing to Fig. 5.24, it is concluded that reducing the mesh size does not improve the quality of the result.

It is seen from Fig. 5.26 that the turbulent kinetic energy increases very rapidly as inlet jet approaches the top wall. This region is characterized by conversion of mean flow kinetic energy into stagnation pressure, and turbulent kinetic energy at a rate exceeding that of dissipation. It would be expected that the pressure and velocity correlation would be large in this region and would have a complicated spatial variation, although a measurement of this quantity is unavailable. These phenomena result in complex turbulence transport processes. In addition, because of more tortuous flow path in the CRBR geometry, the number of significant length-scale determining the nature of the flow in any region of the plenum would be greater than in the FFTF case; the magnitude and complexity of each term in the turbulent transport equations would be increased greatly as well as the degree of departure from turbulent isotropy. The net result is that the closure assumptions for the turbulence models examined here are too simple to describe adequately the complicated nature of the CRBR flow field.

Several investigators used either a lumped parameter approach[15,16] (i.e., the outlet plenum is divided into several characteristic regions), or zero-equation models[17] to study the transient thermal behavior in the outlet plenum. They all have found that the predictions for the CRBR geometry are of poorer quality than those of the FFTF geometry. This also confirms that flows in the CRBR geometry are too complicated for available models to treat with reasonable accuracy.

5.4 Sensitivity Study

Due to the unsatisfactory results predicted by both the TEACH-T and VARR-II models, a sensitivity study of the empirical constants was judged to be the next step to improve the results of the computer code predictions. For convenience, the turbulence transport equations for both codes are reported here:

TEACH-T:

$$\frac{\partial K}{\partial t} + U_K \frac{\partial K}{\partial X_K} = \frac{\partial}{\partial X_K}\left(\frac{\nu_t}{\sigma_K}\frac{\partial}{\partial X_K} K\right) + \nu_t\left(\frac{\partial U_i}{\partial X_j} + \frac{\partial U_j}{\partial X_i}\right)^2 + \varepsilon$$

$$\frac{\partial \varepsilon}{\partial t} + U_K \frac{\partial \varepsilon}{\partial X_K} = \frac{\partial}{\partial X_K}\left(\frac{\nu_t}{\sigma_\varepsilon}\frac{\partial}{\partial X_K}\varepsilon\right) + \frac{C_1 \nu_t \varepsilon}{K}\left(\frac{\partial U_i}{\partial X_K} + \frac{\partial U_K}{\partial X_i}\right)\frac{\partial U_i}{\partial X_K}$$

$$- C_2\left(\frac{\varepsilon^2}{K}\right)$$

where $\nu_t = C_\mu K^2/\varepsilon$ and C_μ, C_1, C_2, σ_K, σ_ε are model constants.

VARR-II:

$$\frac{\partial q}{\partial t} + U_K \frac{\partial q}{\partial X_K} = \frac{\sigma}{2}\left(\frac{\partial U_i}{\partial X_K} + \frac{\partial U_K}{\partial X_i}\right)^2 + \frac{\partial}{\partial X_K}\Gamma\sigma \frac{\partial q}{\partial X_K} - \alpha\frac{(2q)^2}{\sigma}$$

$$\frac{\partial \sigma}{\partial t} + U_K \frac{\partial \sigma}{\partial X_K} = \frac{\sigma^2}{4q}\left(\frac{\partial U_i}{\partial X_K} + \frac{\partial U_K}{\partial X_i}\right)^2 + \frac{\sigma}{q}\frac{\partial}{\partial X_K}\Gamma\sigma \frac{\partial q}{\partial X_K}$$

$$- \frac{\sigma^3}{q^2}\frac{\partial}{\partial X_K}\Gamma_1 q \frac{\partial}{\partial X_K}\left(\frac{q}{\sigma}\right) - 4\alpha_1 q$$

where Γ, Γ_1, α, and α_1 are model constants.

Since the running time for VARR-II is extremely long, sensitivity analyses have been concentrated on the TEACH-T model. From the comparison of two pairs of transport equations, it is seen that some of the parameters in the TEACH-T model apply also to VARR-II model.

The TEACH-T model has five free parameters in the transport equations for K and ε. It was decided to change each at a time in order to examine the changes in computed results especially in the mean velocity and turbulent kinetic energy fields.

5.4.1 Case of FFTF Geometry with Normal Inlet Velocity Distribution

A FFTF test run with normal inlet velocity distribution and a Reynolds number of 70000 was selected as a starting case. A complete list of the range of variables examined in the sensitivity study is shown in Table 5.2.

As discussed before, the diffusion terms are expected to make a small contribution to the turbulence transport processes. It is seen from Table 5.2 that the velocity field is indeed insensitive to the change of diffusion parameters σ_K and σ_ε, although the turbulent kinetic energy field does change significantly as these parameters change. Increasing the value of C_μ which results in an increase of turbulent viscosity or momentum exchange is seen to improve the predicted and measured velocity field agreement, but the turbulent kinetic energy is also increased relative to the experimental results. Hence a second energy dissipation parameter, C_2, is decreased to

increase the turbulent kinetic energy dissipation rate and move the turbulent kinetic energy back to the origianl value without changing too much the magnitude of the velocity field. From many tests, the best values of these parameters are found to be $C_\mu = 0.25$ and $C_2=0.16$, where all the other variables are unchaged. The predicted velocity distribution and turbulent kinetic energy distribution are shown in Figs. 5. 29 and 5. 30. As is seen from these Figures, the quality of the predictions is improved by these changes. The data of Appendix I shows the calculated velocity and turbulent kinetic energy fields for the cases examined.

5.4.2 Case of FFTF Geometry with Distorted Inlet Velocity Distribution

The next step is to apply this new set of parameters to the case of FFTF geometry with distorted inlet velocity distribution. Because of complicated turbulent transport phenomena we are unable to reproduce the experimentally-observed double vortex velocity distribution, although the quality of the turbulent kinetic energy distribution prediction is improved.

Due to the resource limitations, no CRBR and VARR-II cases have been tested. But for the VARR-II model, by comparing and manipulating the transport equations, the turbulence equation parameters are found to be related to corresponding turbulence parameters in the TEACH-T model as follows: $\Gamma = 1/\sigma_K$, $\alpha = C_\mu/4$, and $\alpha_1 = C_\mu (2-C_2)/4$. The improved values of these parameters are $\Gamma = 1.0$, $\alpha = 0.00625$, and $\alpha_1 = 0.025$ which are different from the values recommended by the authors of

the model: $\Gamma = 1.5$, $\alpha = 0.045$, $\alpha_1 = 0.01125$.

5.5 Summary

It is found that the qualitative nature of the flow field within the plenum depends strongly upon the distribution of mean inlet velocity field, upon the values of the inlet turbulence parameters, and upon the turbulence momentum exchange model used in the calculations. It is found in the FFTF geometry that the TEACH-T predictions are better than that of VARR-II, and in the CRBR geometry neither codes provides a good prediction of the observed behavior.

From the sensitivity analysis, it is found that the production and dissipation of turbulence are the dominant terms in the transport equations for turbulent kinetic energy and turbulent energy dissipation rate, and the diffusion terms are relatively small. A new set of empirical constants is evolved from the study for the prediction of plenum flows.

5.6 Explanation of Discrepancies

Since this is probably the first attempt to compare the turbulence model codes prediction with large scale recirculating flow experimental data, some discrepancies are expected. Efforts are made to outline the possible reasons why the two-equation turbulence models fail to give good predictions in terms of either comparison of predictions and experiments, or of other similar types of flows. Among the important reasons for these discrepancies are the following:

1. The present closure does not take account of the intermittent nature of the turbulence (i.e., in some regions the flows can alternate in time between being laminar or turbulent) which independent measurement[18] shows to be present in the outer edge regions of the jet. A similar jet is found in the plenum which could exhibit the same behavior although the measurement is beyond our capability. The averaging of the equation of motion, which is an essential part of the present approach, tends to smooth out this time dependence. The validity of the concepts of turbulent kinetic energy and Reynolds stress is questionable when a flow field is alternating between laminar and turbulent since the statistical ensemble in terms of which these parameters are defined is not unique. Hence, it is possible that this intermittency effect will introduce some disagreements between predictions and measurements.

2. Due to the small velocity in the central region of the recirculating flow, it is possible that relaminarization could occur in this region. Hence, the accuracy of the turbulence transport equations to describe the momentum transport in this region is questionable.

3. In the present models, the closure assumption implies that a single length scale will suffice to represent motion of all the eddies with different sizes and shapes. From Chapter 3, the appropriate length scales are seen to be $K^{3/2}/\varepsilon$ and $\sigma/K^{1/2}$ for TEACH-T and VARR-II, respectively. Yet in recirculating flows the dimensions of turbulent eddies are much different in different directions and their shapes will alter appreciably during their lifetime. A multi-length scale closure in turbulence modeling is necessary to describe adequately this process.

4. In the calculated prediction, two dimensional flows are assumed to exist. But the flows in the test section are actually three-dimensional. Although the transverse boundary layer is calculated to be small, the presence of the walls tends to change the flow pattern and turbulent energy transport processes. Hence, some disagreements are expected to arise from this source.

5. In the CRBR case, the region close to the top wall is characterized by conversion of momentum and turbulent kinetic energy into stagnation pressure. Consequently, the velocity and pressure correlation $\overline{U'P'}$ would be expected to be large and

the diffusion of turbulent kinetic energy would also be significant. The experimental results indicate the existence of large gradients of turbulent kinetic energy in that region which confirms this argument. But the parameter $\overline{U'P'}$ is generally not available for measurement and hence, the modeling of this term is difficult and inadequate. So whenever the $\overline{U'P'}$ value is significant, the accuracy of the prediction is expected to be questionable.

6. As flow moves close to the wall, the degree of departure from isotropy increases. The present models are inadequate to describe turbulent transport phenomena in the near-wall region because the flow there is much more complicated than in the far field. The large disagreement of mean flow and turbulence parameters field supports this finding. Hence, the highly anisotropic flow near a solid wall is not described adequately by a two-equation model.

Table 5.1 List of Test Runs

Geometry		FFTF			CRBR	
Re		33,000	70,000		35,000	
Inlet Velocity Distribution		NORMAL	NORMAL	DISTORTED	NORMAL	DISTORTED
Fig.NO.	TEACH	5.2	5.7, 5.11	5.16, 5.18	5.24, 5.28, 5.29	H.2
	VARR	5.3	5.8, 5.12	5.17	5.25	H.3

Table 5.2 List of Test Cases in Sensitivity Analysis

	C_μ	σ_K	σ_ε	C_1	C_2	Velocity	Turbulent Kinetic Energy
ORIGINAL	0.09	1.0	1.3	1.44	1.92	N/A	N/A
TEST CASE	0.18	1.0	1.3	1.44	1.92	D-Moderate	I-Moderate
	0.27					D-Moderate	I-Moderate
	0.90					D-Moderate	I-Moderate
TEST CASE	0.09	0.5	1.3	1.44	1.92	No	D-Small
		0.1				I-Small	D-Moderate
		1.5				No	I-Small
TEST CASE	0.09	1.0	0.65	1.44	1.92	No	D-Moderate
			2.60			D-Small	I-Moderate
			3.90			D-Small	I-Moderate
TEST CASE	0.09	1.0	1.3	2.88	1.92	I-Moderate	D-Large
				4.32		I-Moderate	D-Large
				0.72		Different Flow Pattern	I-Large
TEST CASE	0.09	1.0	1.3	1.44	0.96	I-Moderate	D-Large
					0.64	I-Moderate	D-Large
					3.84	Different Flow Pattern	I-Large
FINAL RESULT	0.25	1.0	1.3	1.44	1.60	N/A	N/A

Note: D or I means that prediction is decreased or increased relative to prediction by original set of free parameters

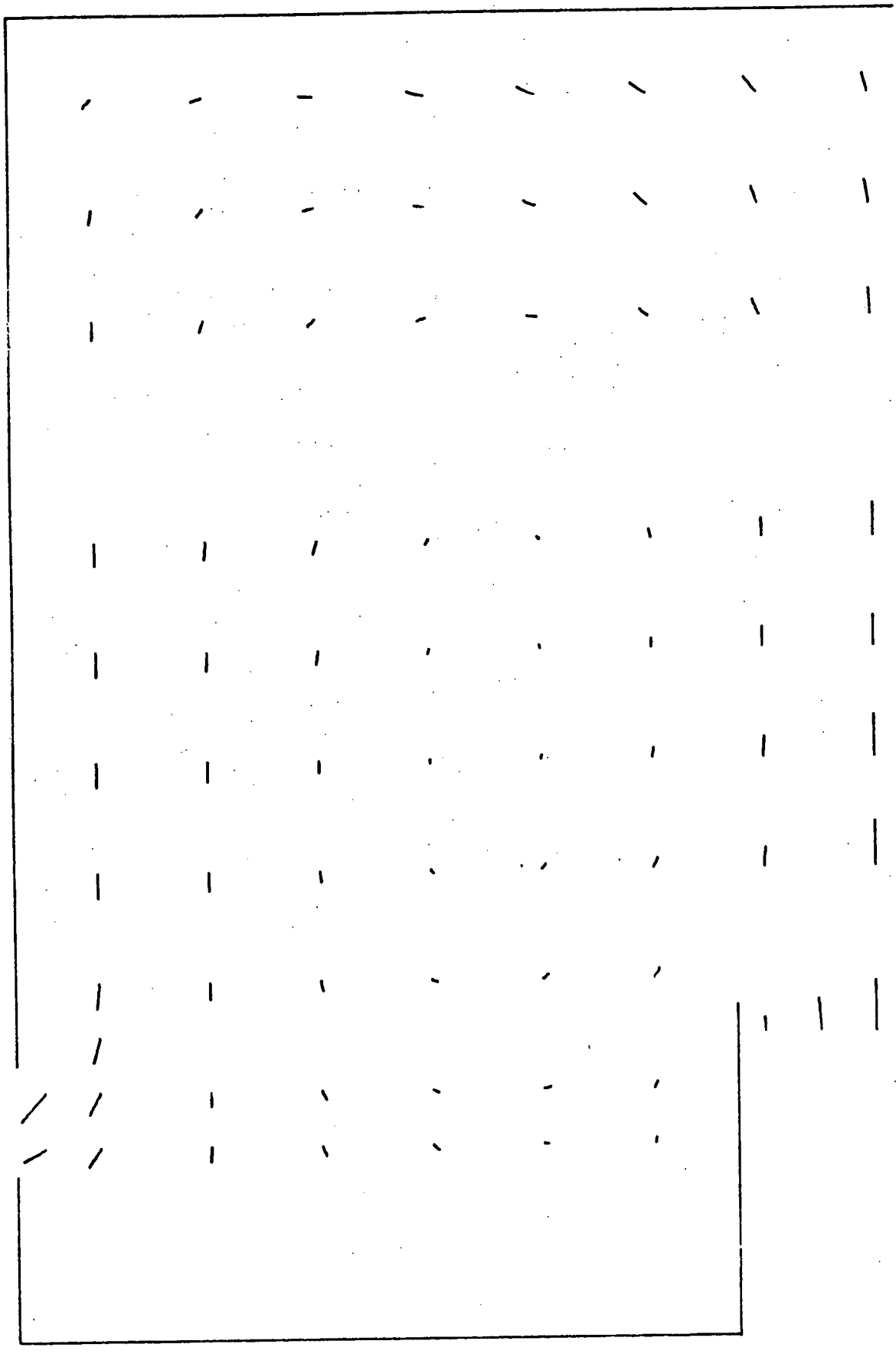

Fig. 5.1 Measured Mean Flow Field, FFTF Geometry, Re=33000, Normal Inlet Velocity Distribution

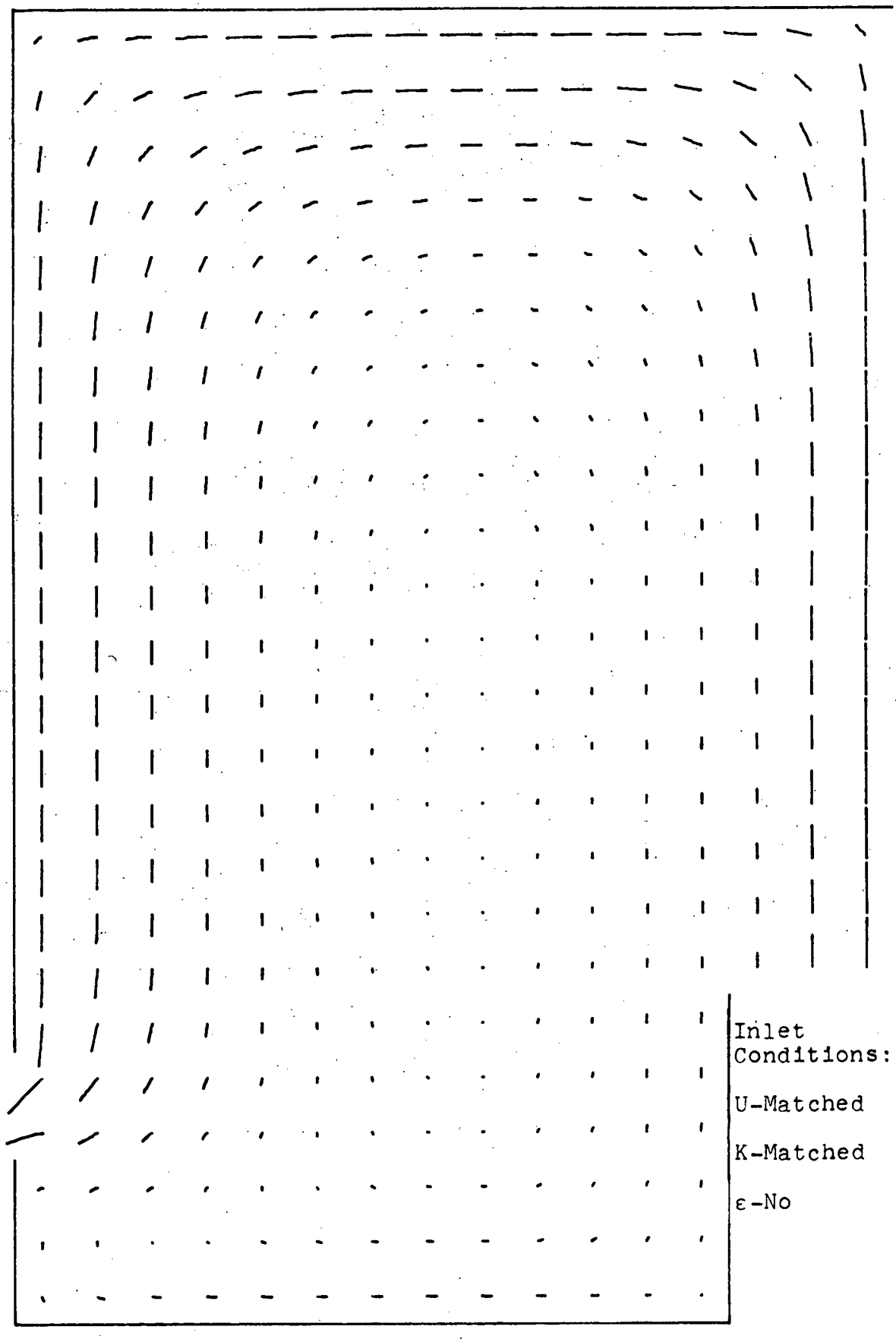

Fig. 5.2 TEACH-T Prediction, FFTF Geometry, Re=33000, Normal Inlet Velocity Distribution

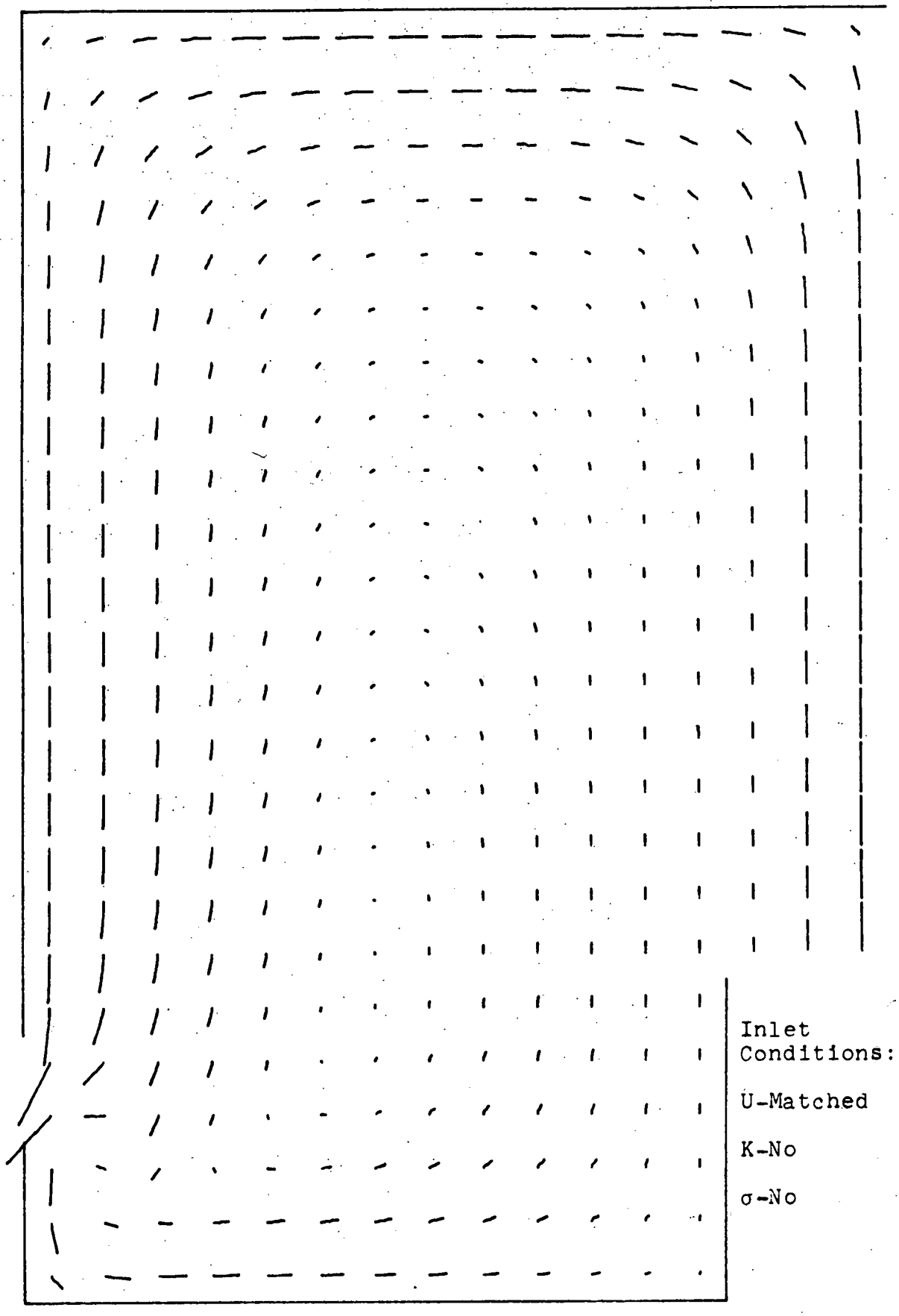

Fig. 5.3 VARR-II Prediction, FFTF Geometry, Re=33000, Normal Inlet Velocity Distribution

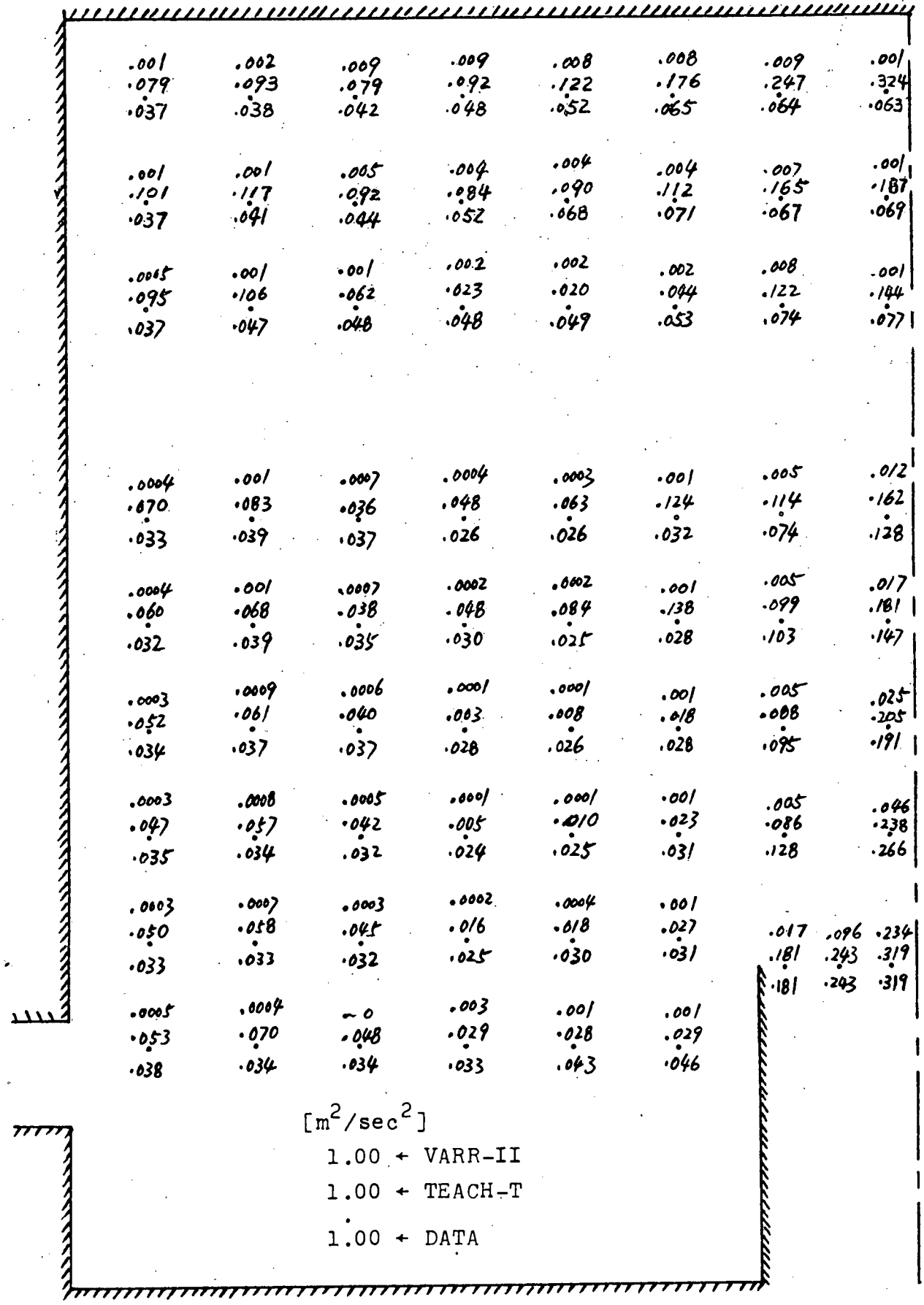

Fig. 5.4 Compared Calculated and Measured Turbulence Kinetic Energy Fields, FFTF Geometry, Re=33000, Normal Inlet Velocity Distribution

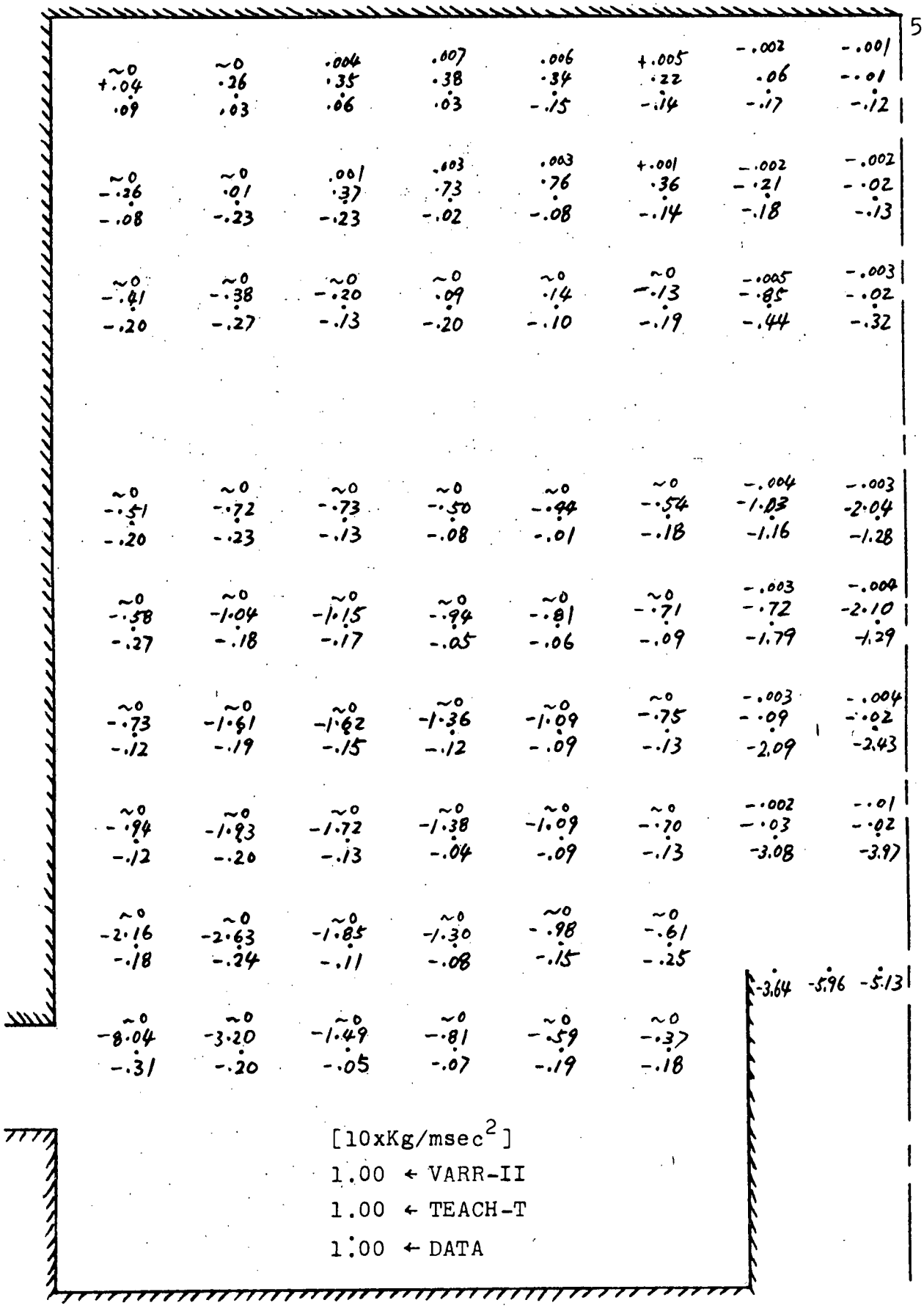

Fig. 5.5 Compared Calculated and Measured Reynolds Stress Fields, FFTF Geometry, Re=30000, Normal Inlet Velocity Distribution

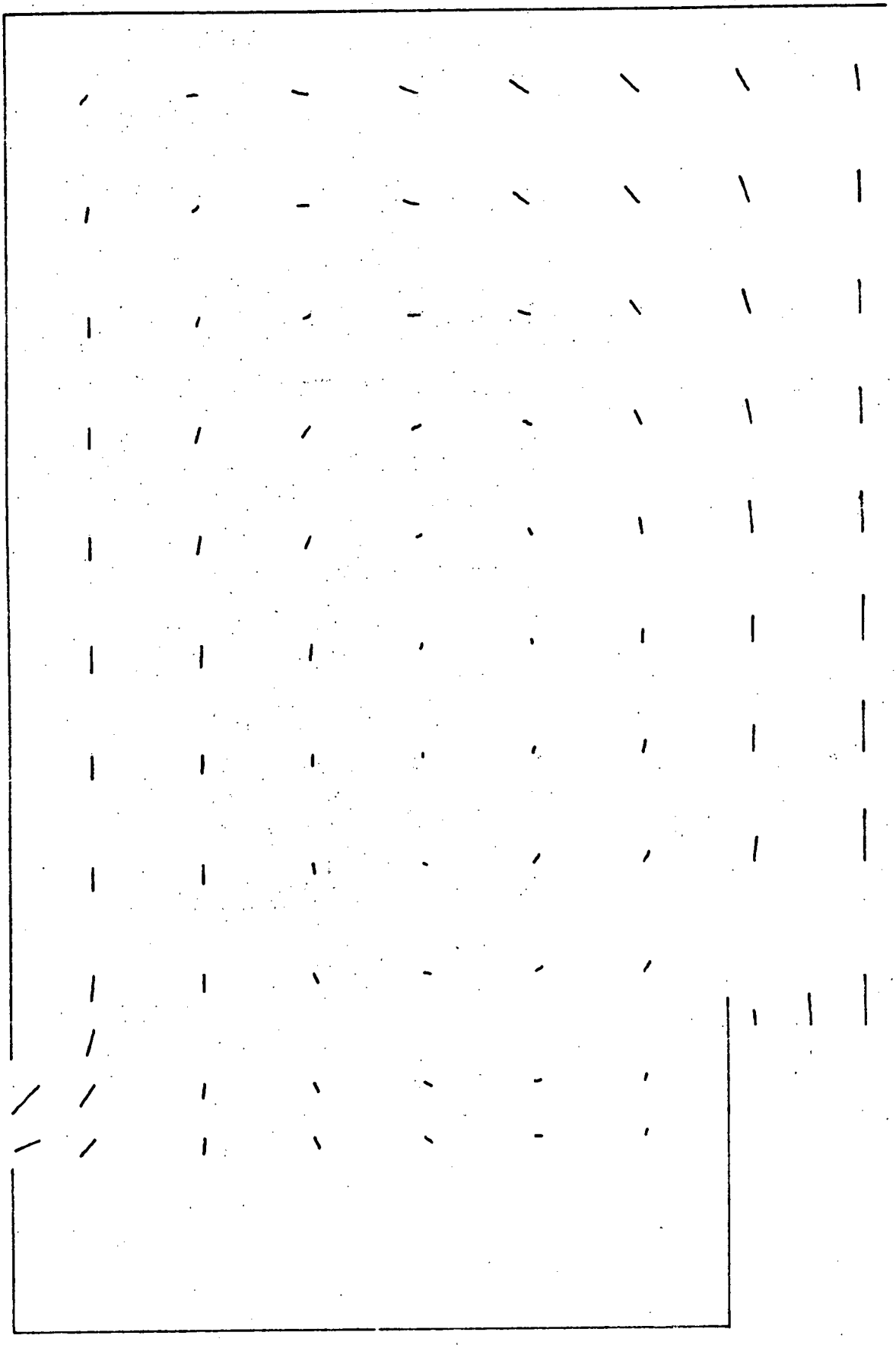

Fig. 5.6 Measured Mean Flow Field, FFTF Geometry, Re=70000, Normal Inlet Velocity Distribution

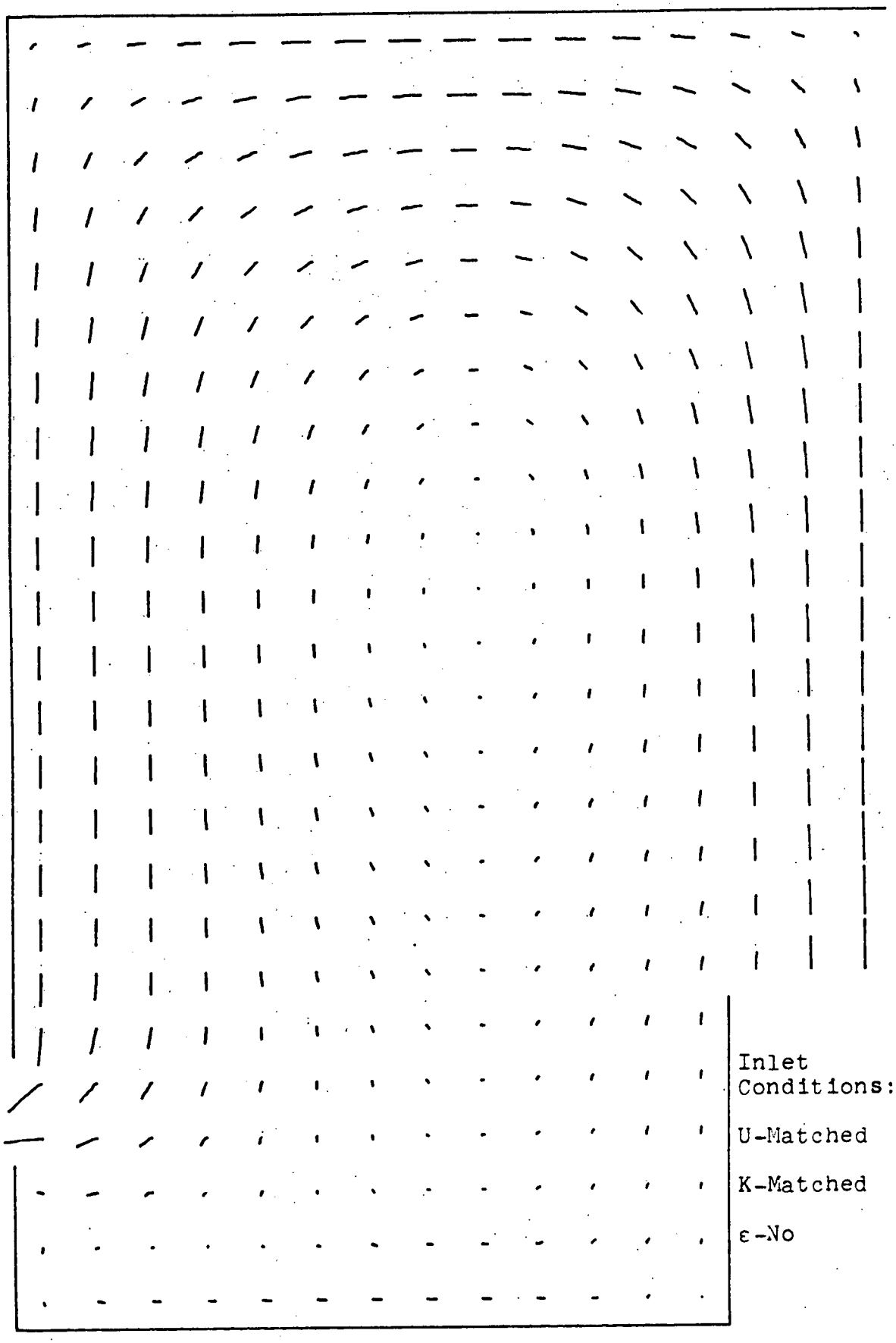

Fig. 5.7 TEACH-T Prediction, FFTF Geometry, Re=70000, Normal Inlet Velocity Distribution

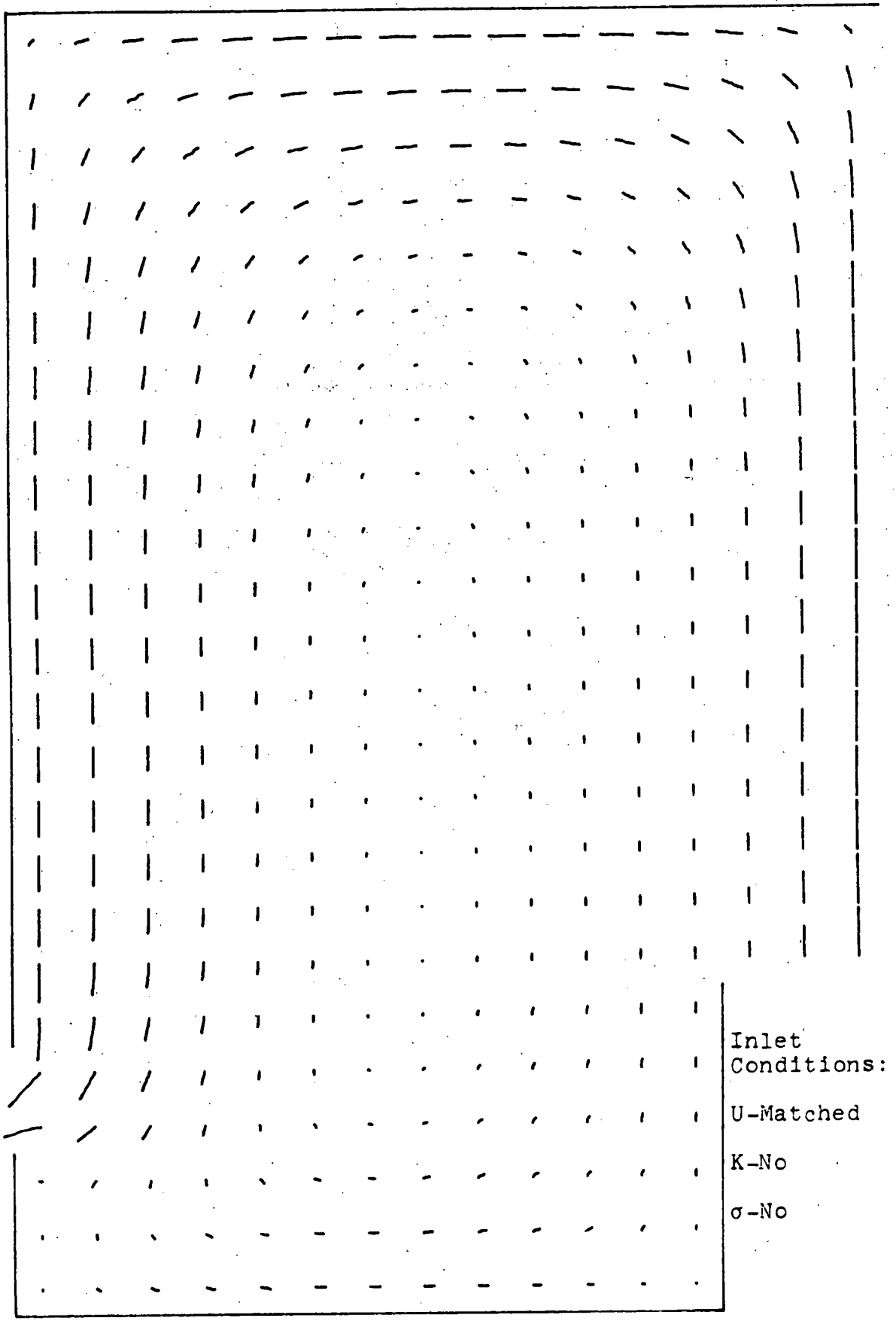

Fig. 5.8 VARR-II Prediction, FFTF Geometry, Re=70000, Normal Inlet Velocity Distribution

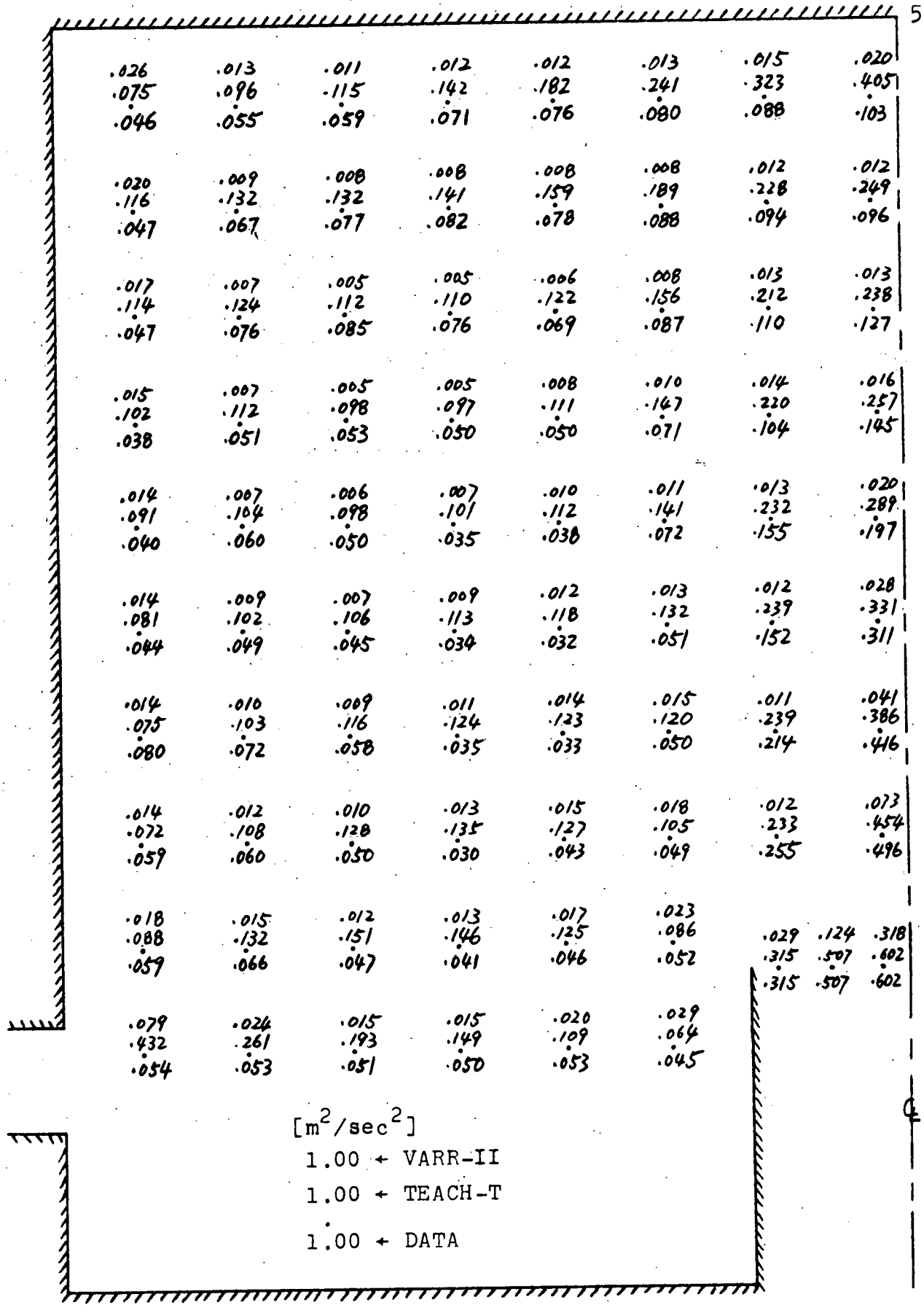

Fig. 5.9 Compared Calculated and Measured Turbulent Kinetic Energy Fields, FFTF Geometry, Re=70000, Normal Inlet Velocity Distribution

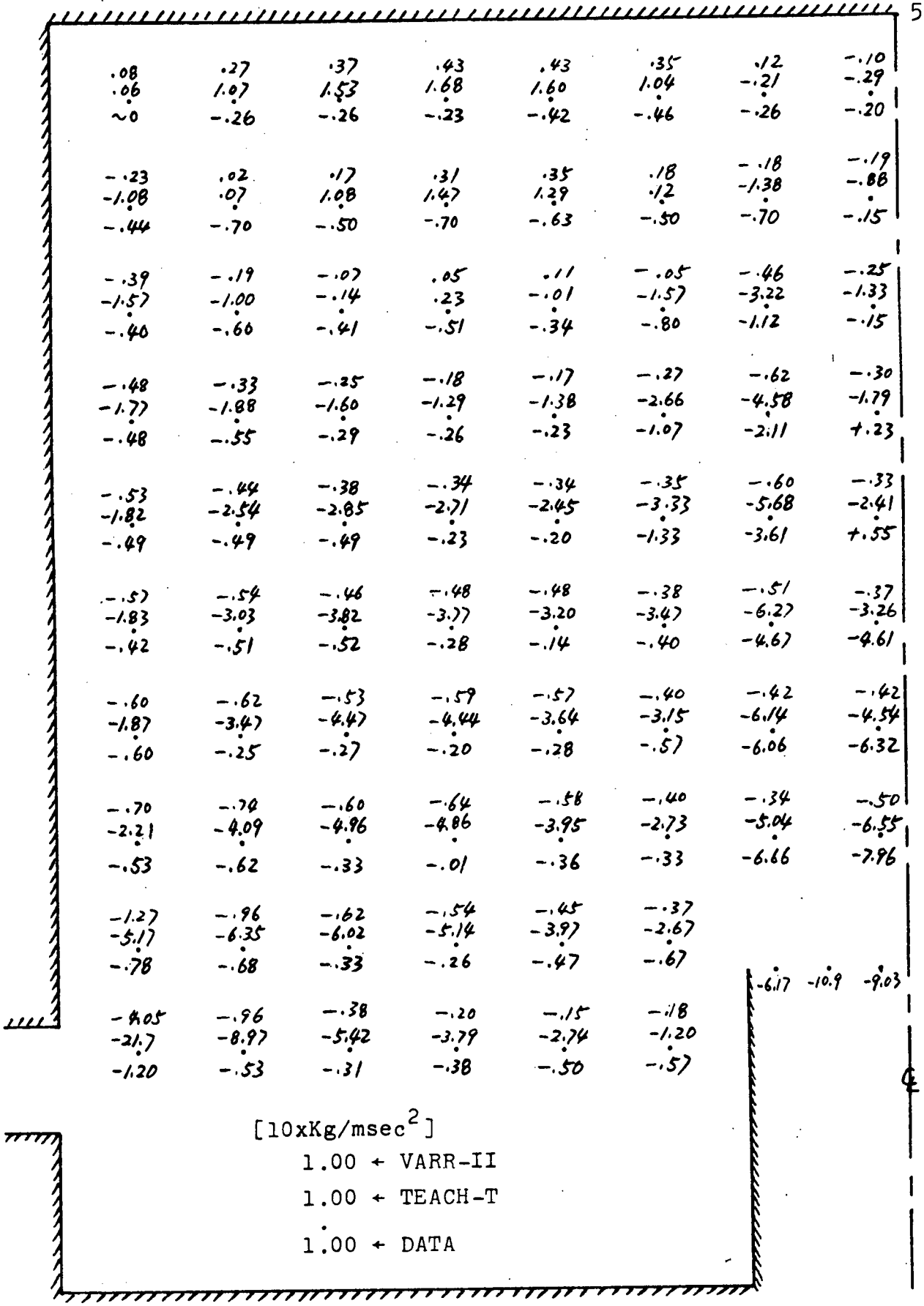

Fig. 5.10 Compared Calculated and Measured Reynolds Stress Fields, FFTF Geometry, Re=70000, Normal Inlet Velocity Distribution

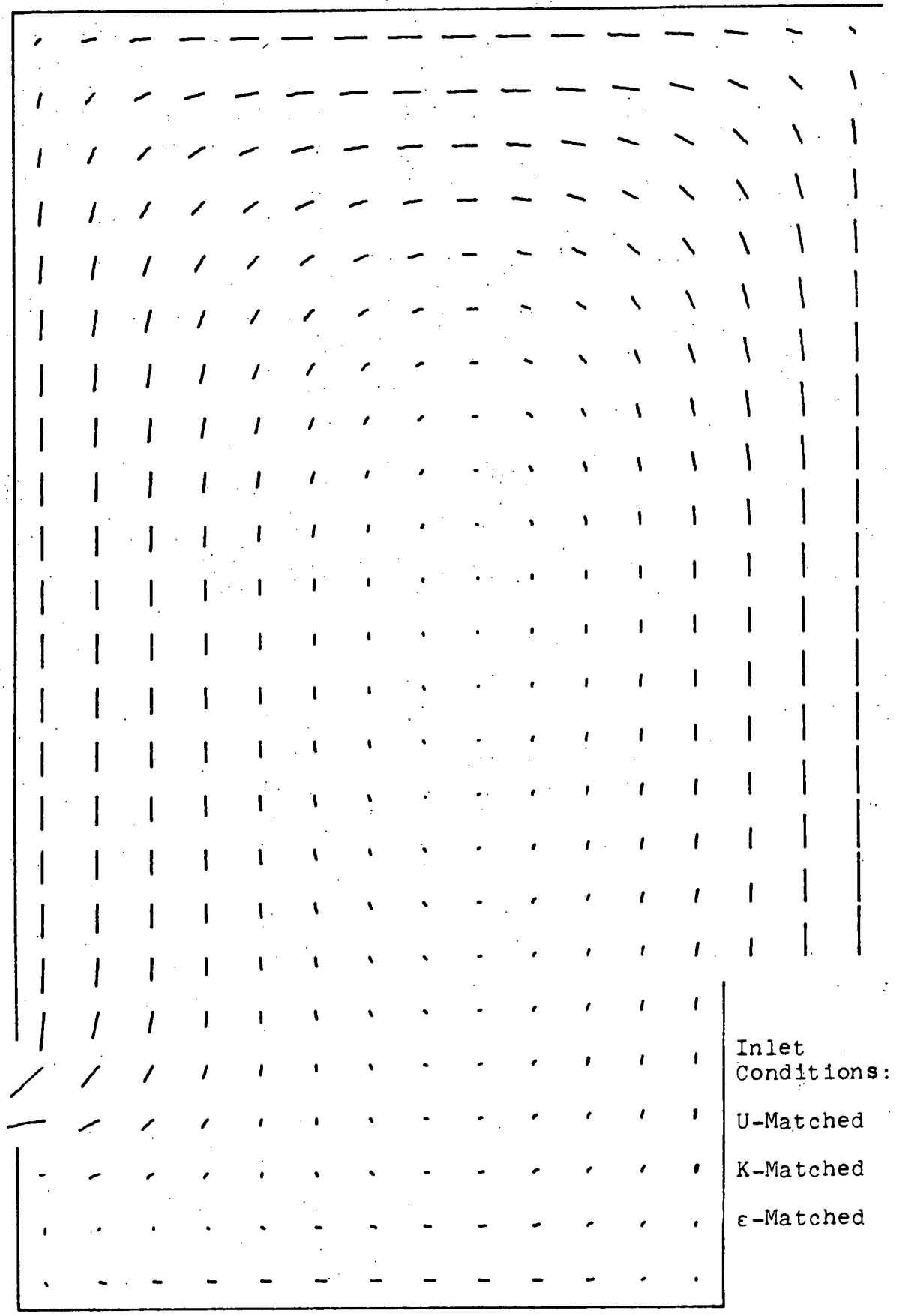

Fig. 5.11 TEACH-T Prediction, FFTF Geometry, Re=70000, Normal Inlet Velocity Distribution

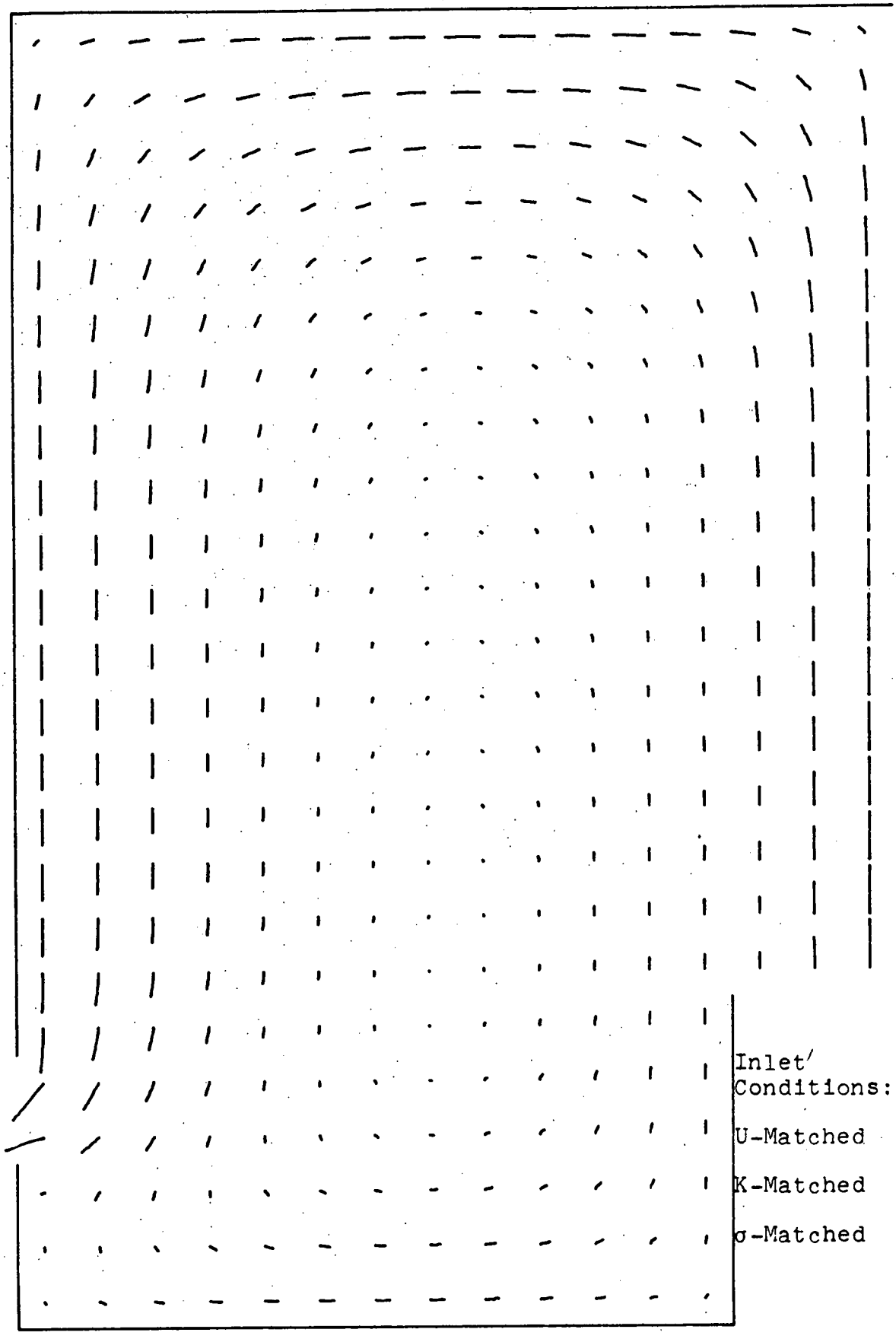

Fig. 5.12 VARR-II Prediction, FFTF Geometry, Re=70000, Normal Inlet Velocity Distribution

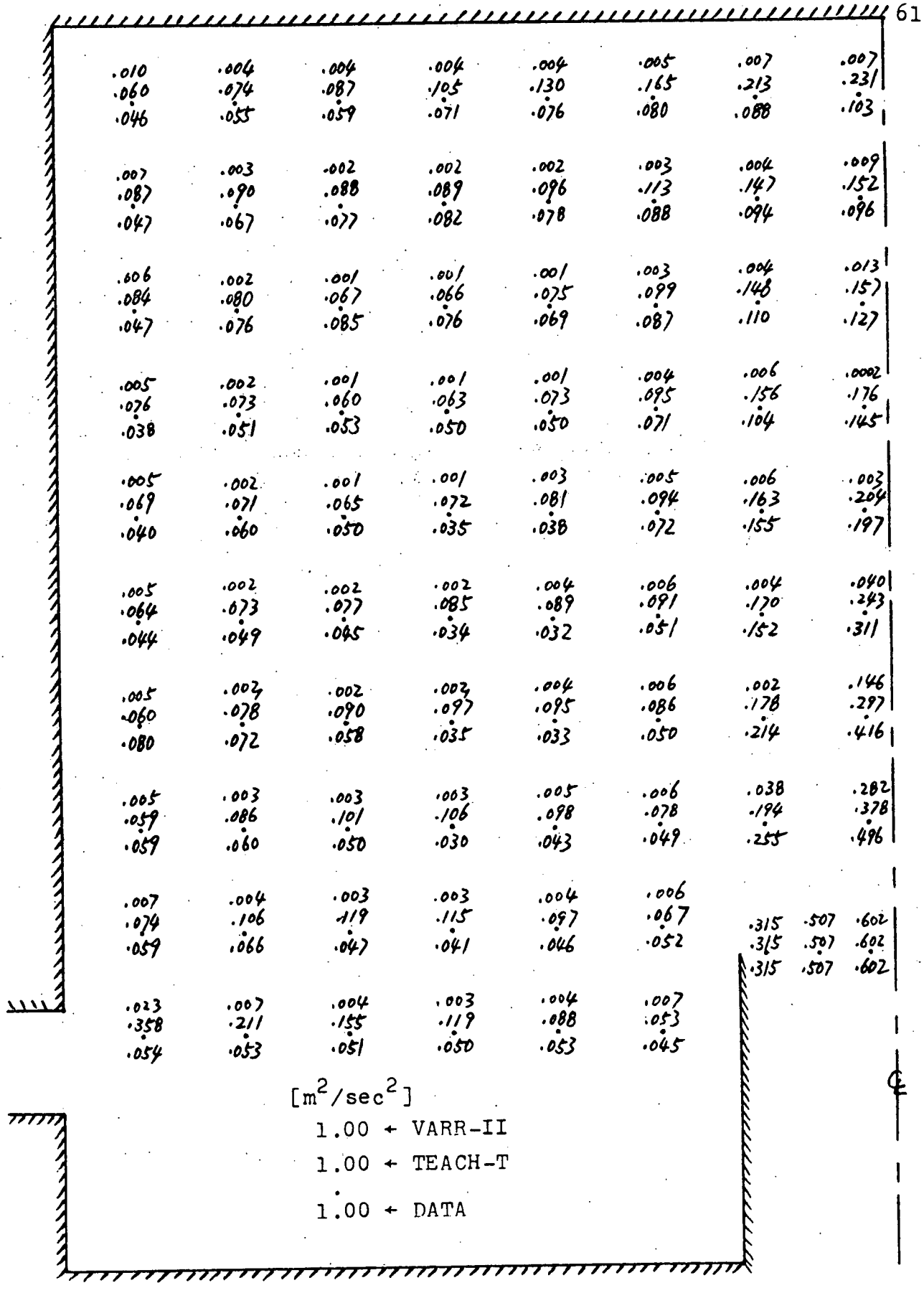

Fig. 5.13 Compared Calculated and Measured Turbulent Kinetic Energy Fields, FFTF Geometry, Re=70000, Normal Inlet Velocity Distribution

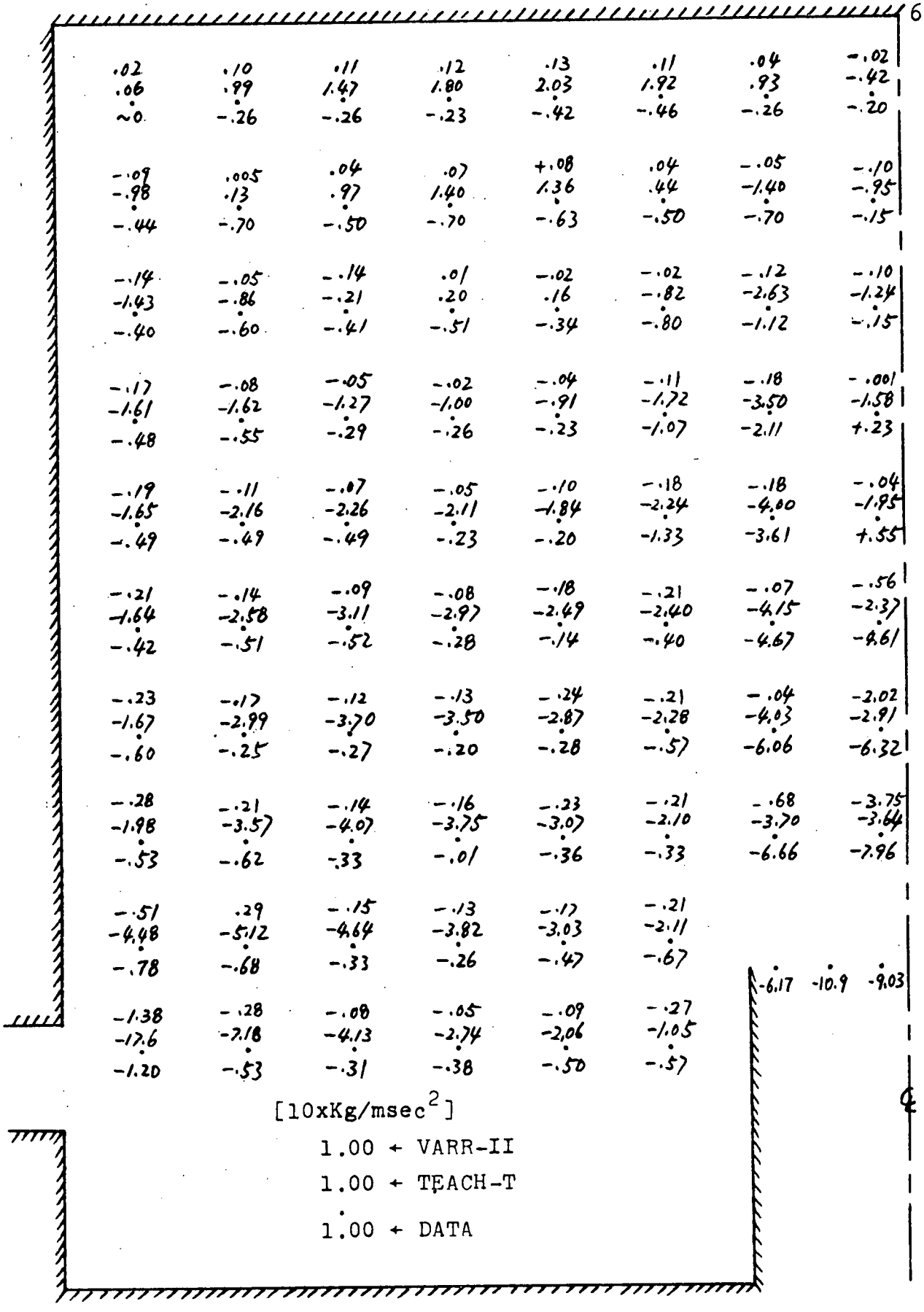

Fig. 5.14 Compared Calculated and Measured Reynolds Stress Fields, FFTF Geometry, Re=70000, Normal Inlet Velocity Distribution

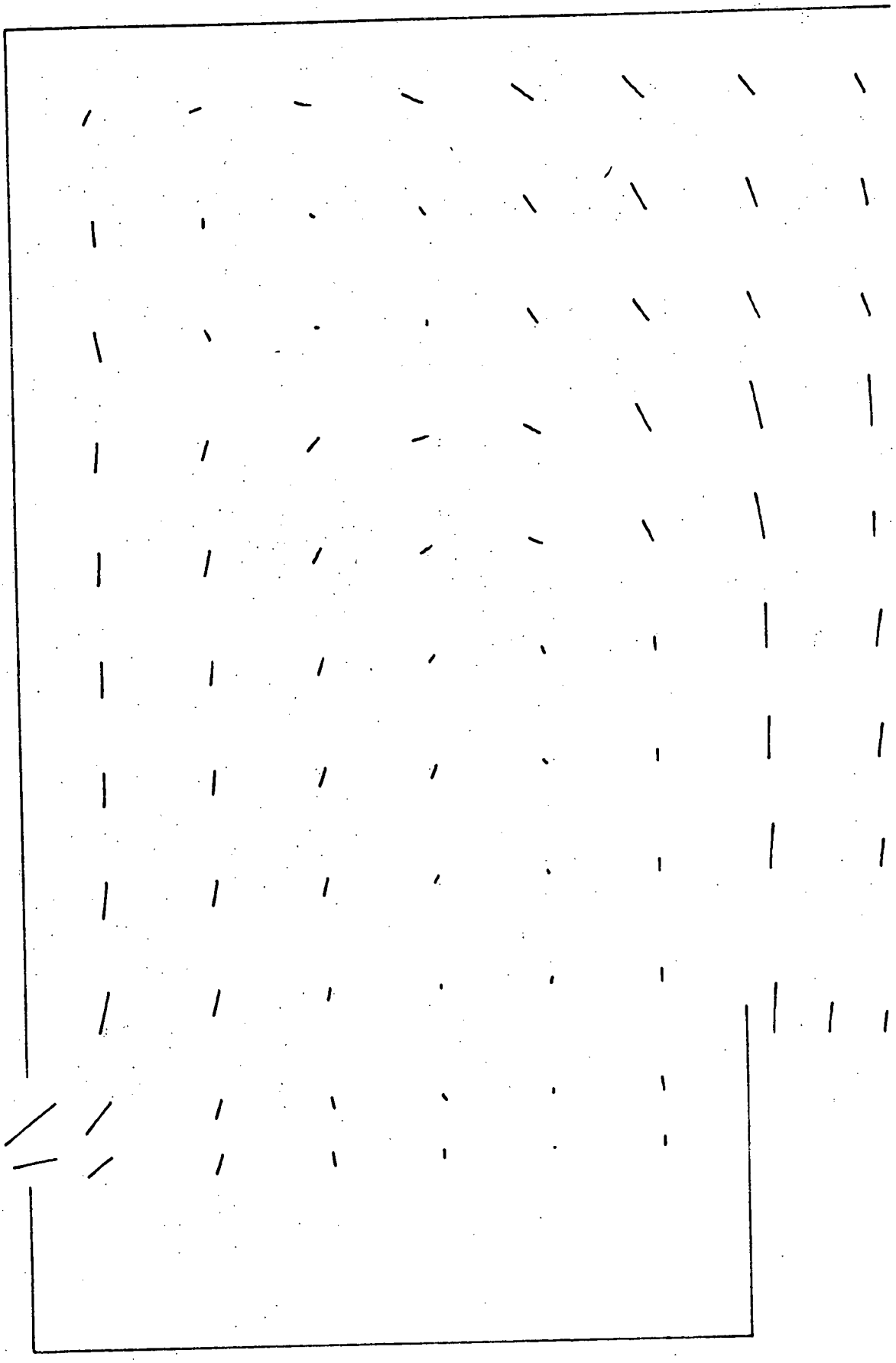

Fig. 5.15 Measured Mean Flow Field, FFTF Geometry, Re=70000, Distorted Inlet Velocity Distribution

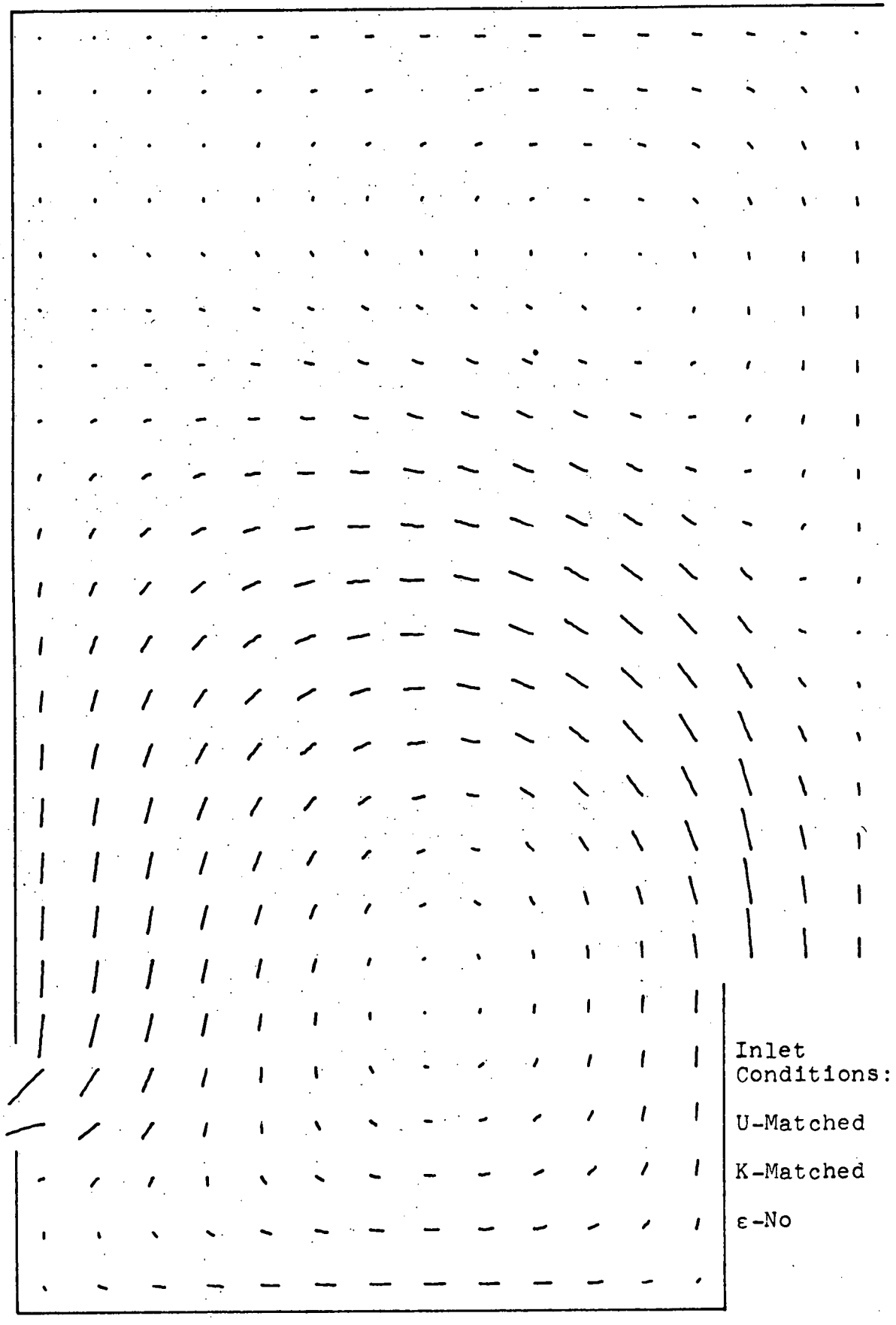

Fig. 5.16 TEACH-T Prediction, FFTF Geometry, Re=70000, Distorted Inlet Velocity Distribution

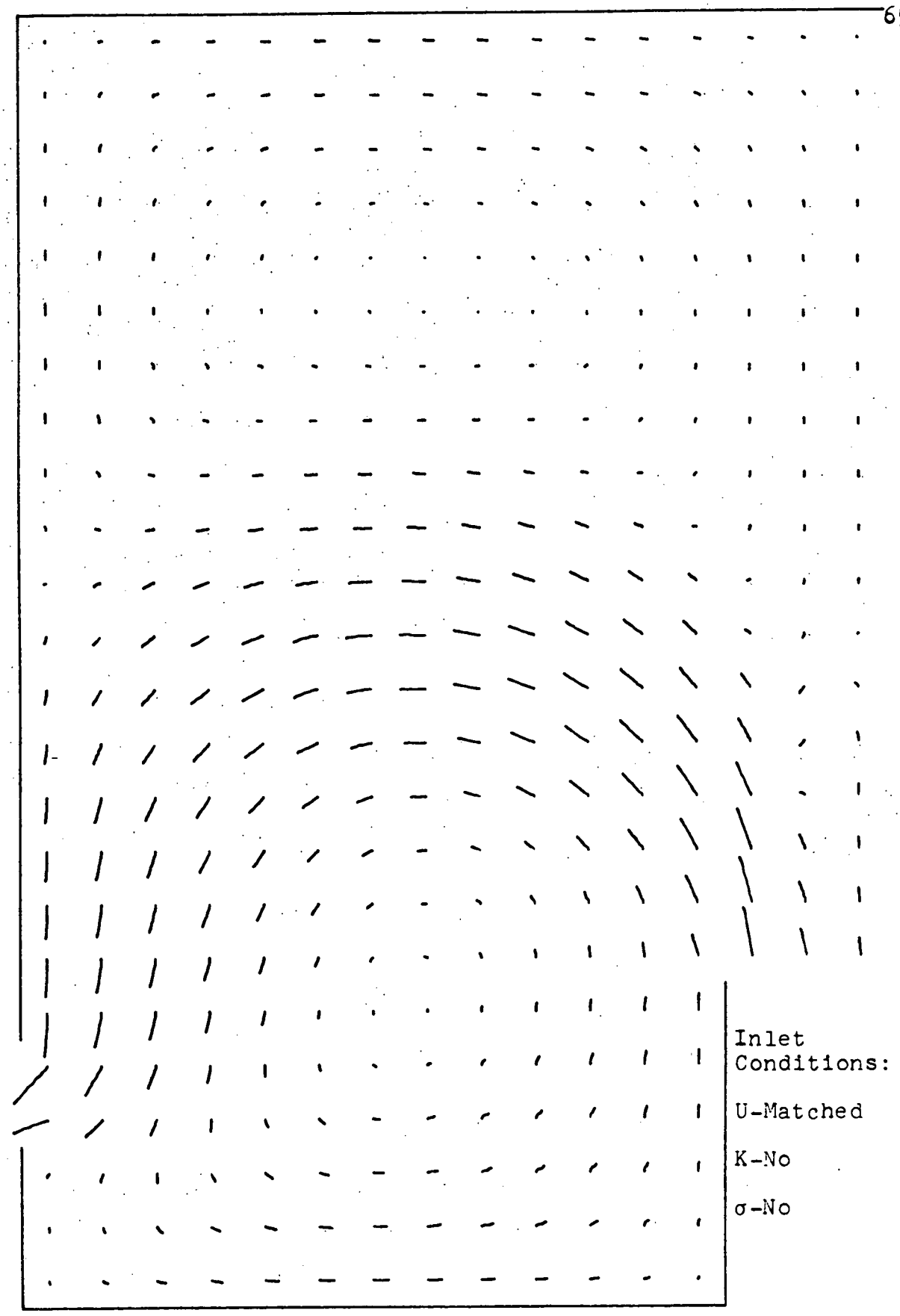

Fig. 5.17 VARR-II Prediction, FFTF Geometry, Re=70000,
Distorted Inlet Velocity Distribution

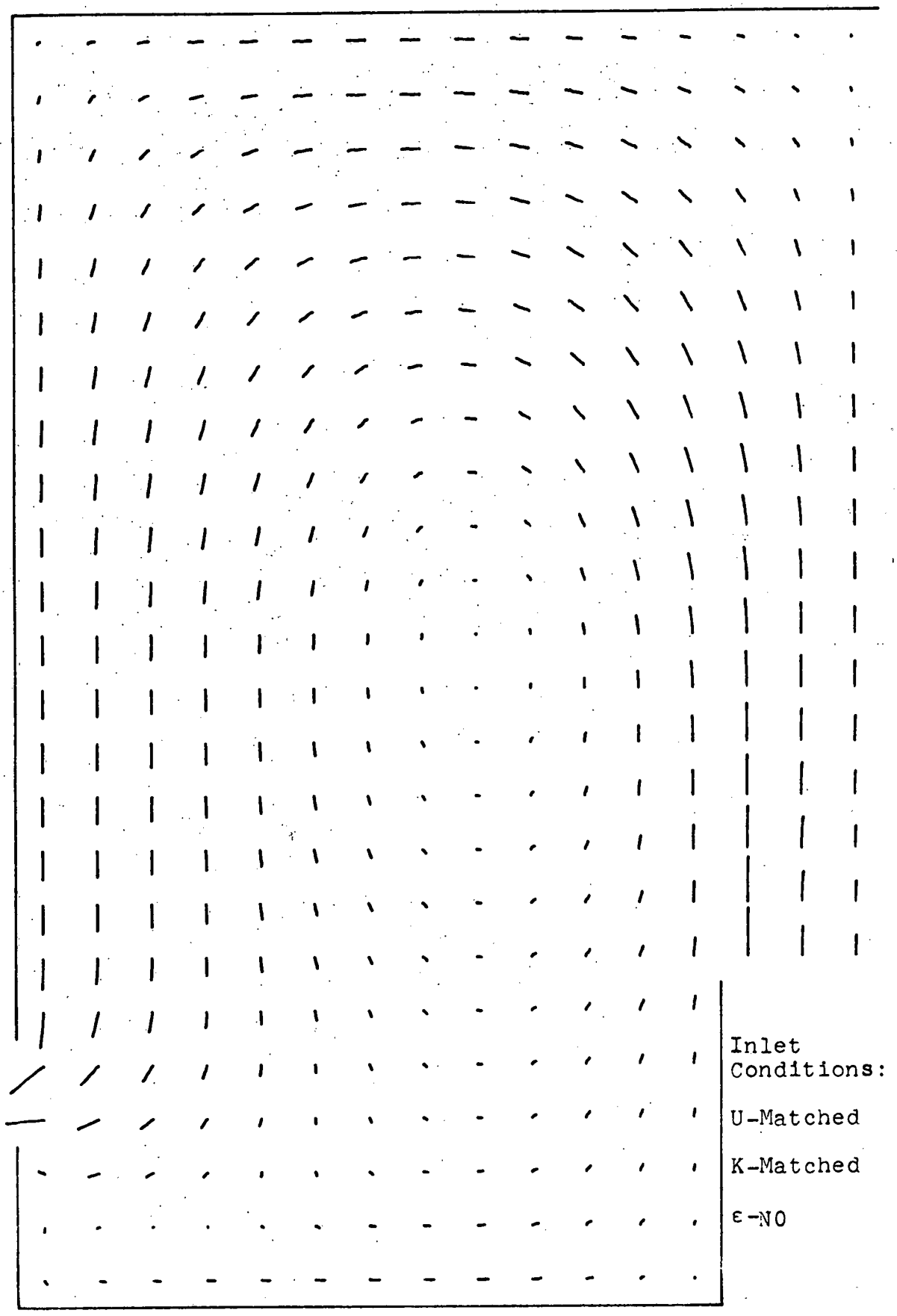

Fig. 5.18 TEACH-T Prediction, FFTF Geometry, Re=70000, Distorted Inlet Velocity Distribution

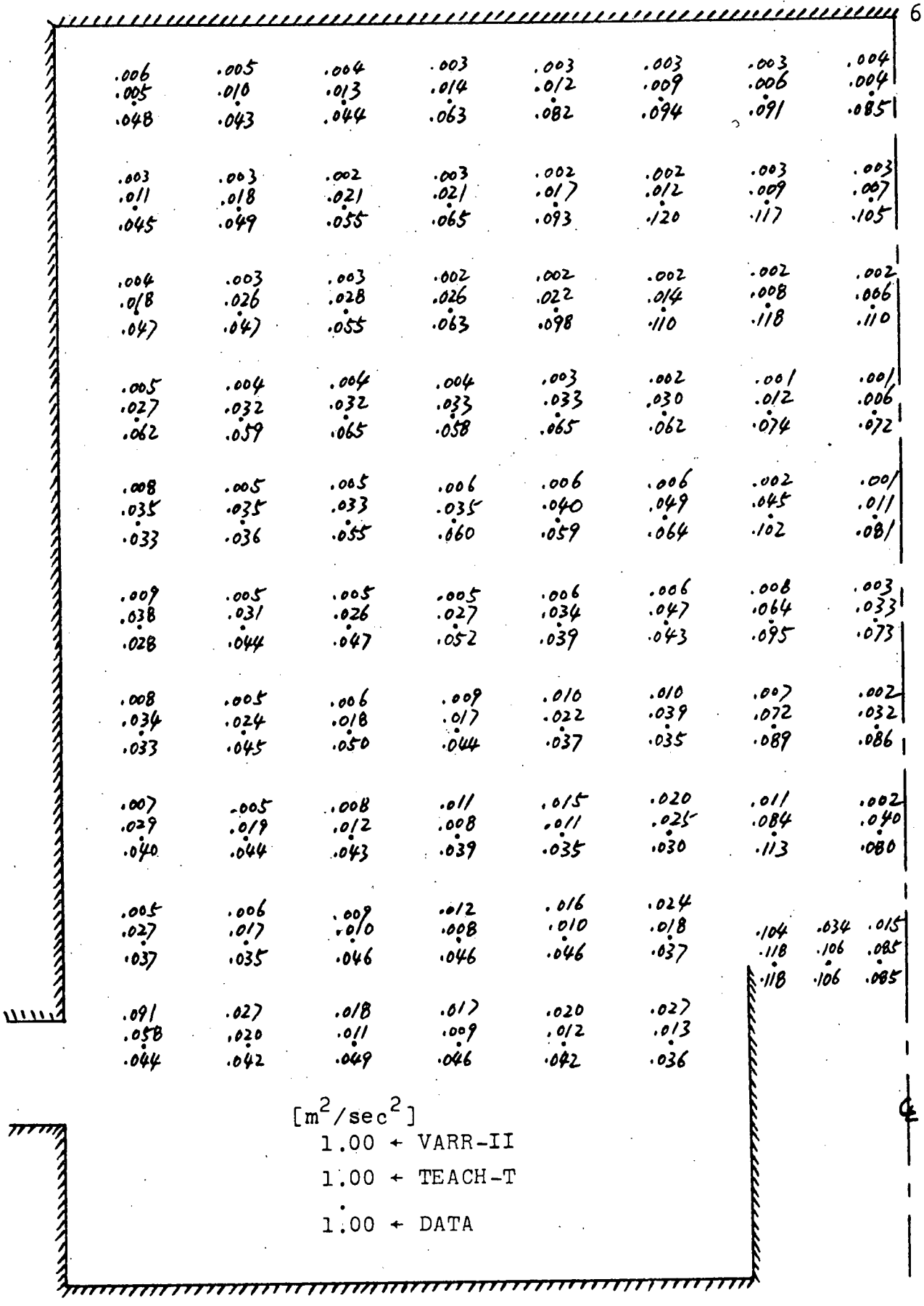

Fig. 5.19 Compared Calculated and Measured Turbulent Kinetic Energy Fields, FFTF Geometry, Re=70000, Distorted Inlet Velocity Distribution

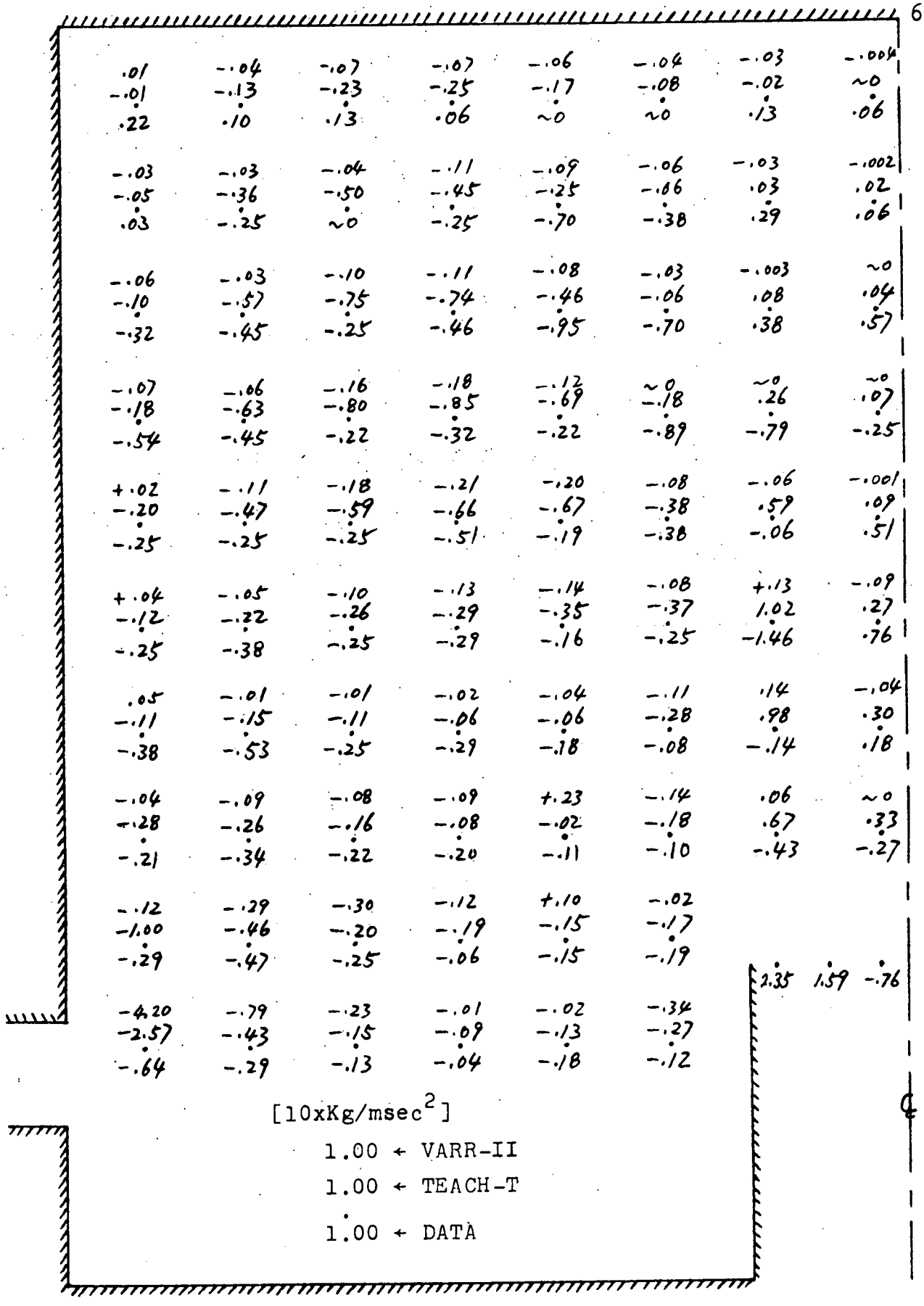

Fig. 5.20 Compared Calculated and Measured Reynolds Stress Fields, FFTF Geometry, Re=70000, Distorted Inlet Velocity Distribution

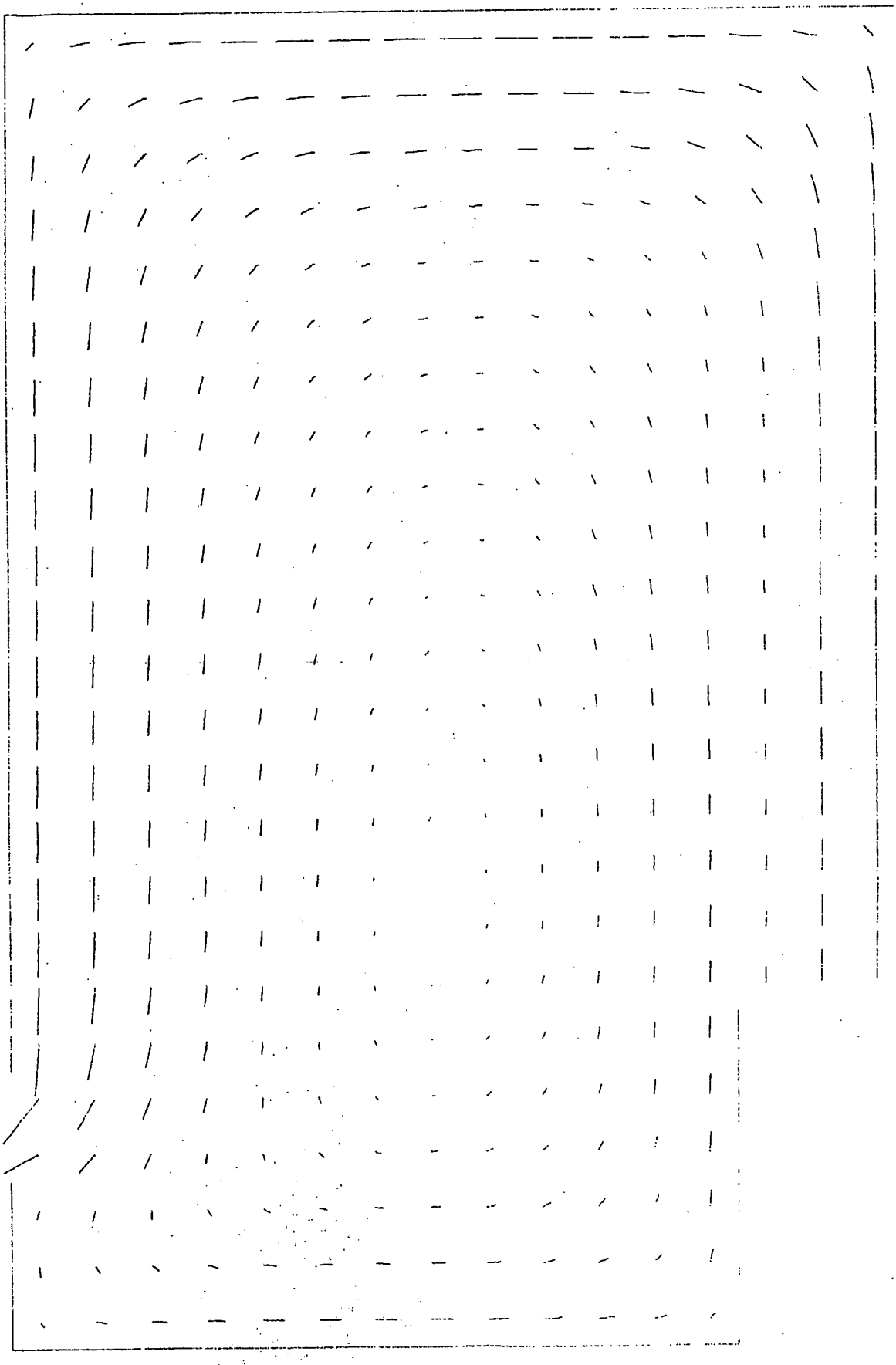

Fig. 5.21 TEACH-T Prediction with Reynolds Stress = $-20|\underline{U}|^2$, FFTF Geometry, Re=70000, Normal Inlet Velocity Distribution

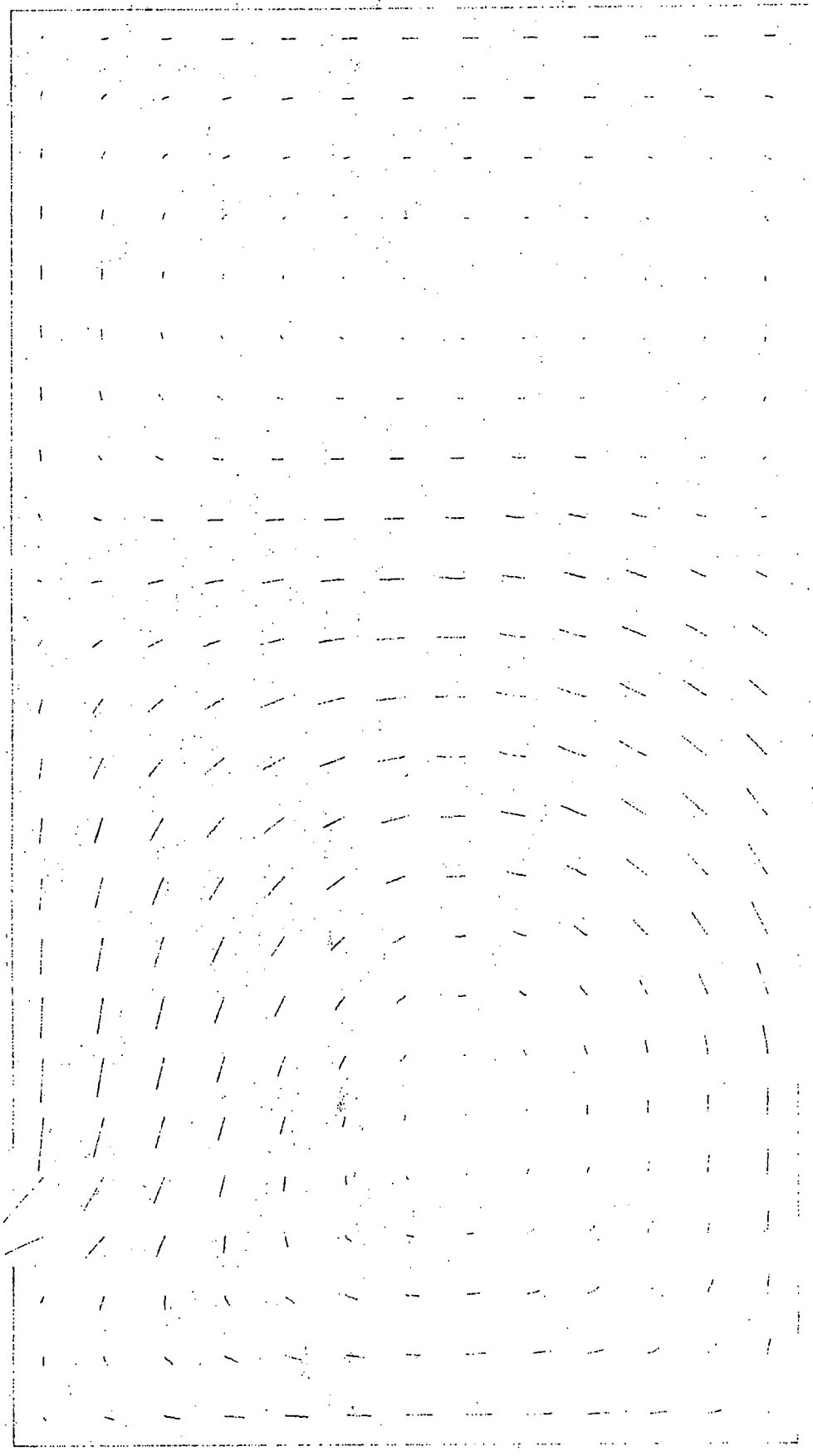

Fig. 5.22 TEACH-T Prediction with Reynolds stress = $-20|U|^2$, FFTF Geometry, Re=70000, Distorted Inlet Velocity Distribution

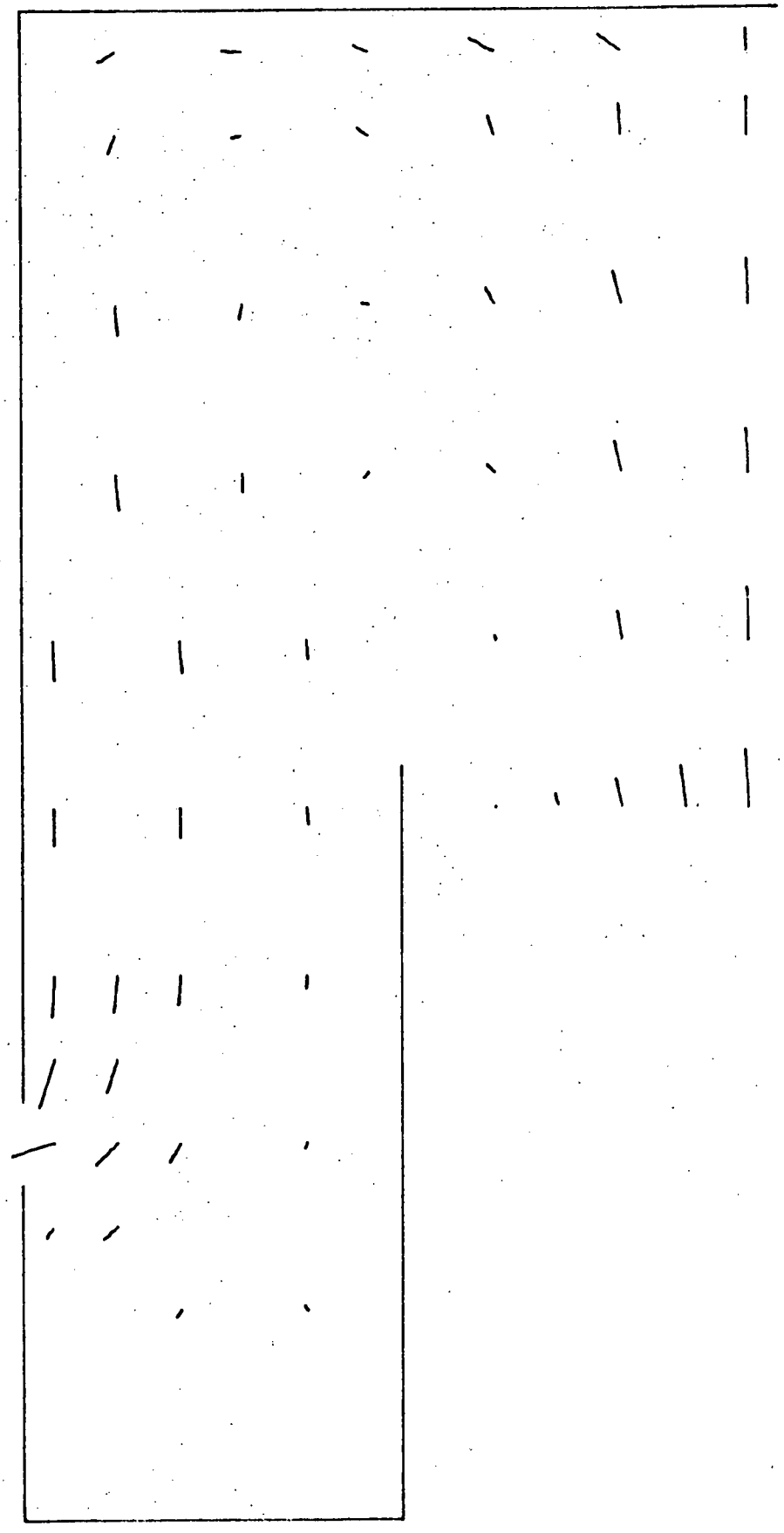

Fig. 5.23 Measured Mean Flow Field, CRBR Geometry, Re=35000, Normal Inlet Velocity Distribution

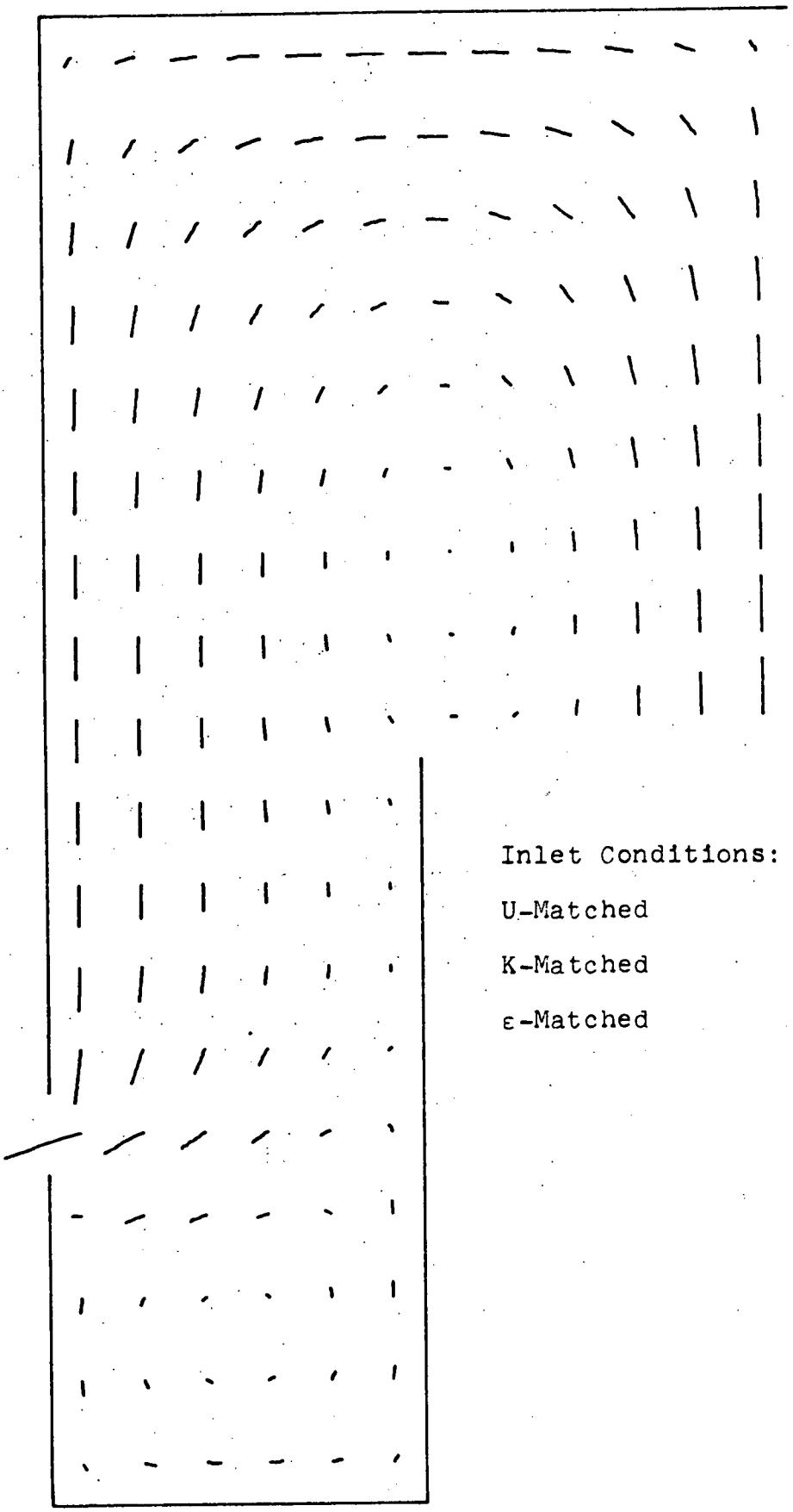

Fig. 5.24 TEACH-T Prediction, CRBR Geometry, Re=35000, Normal Inlet Velocity Distribution

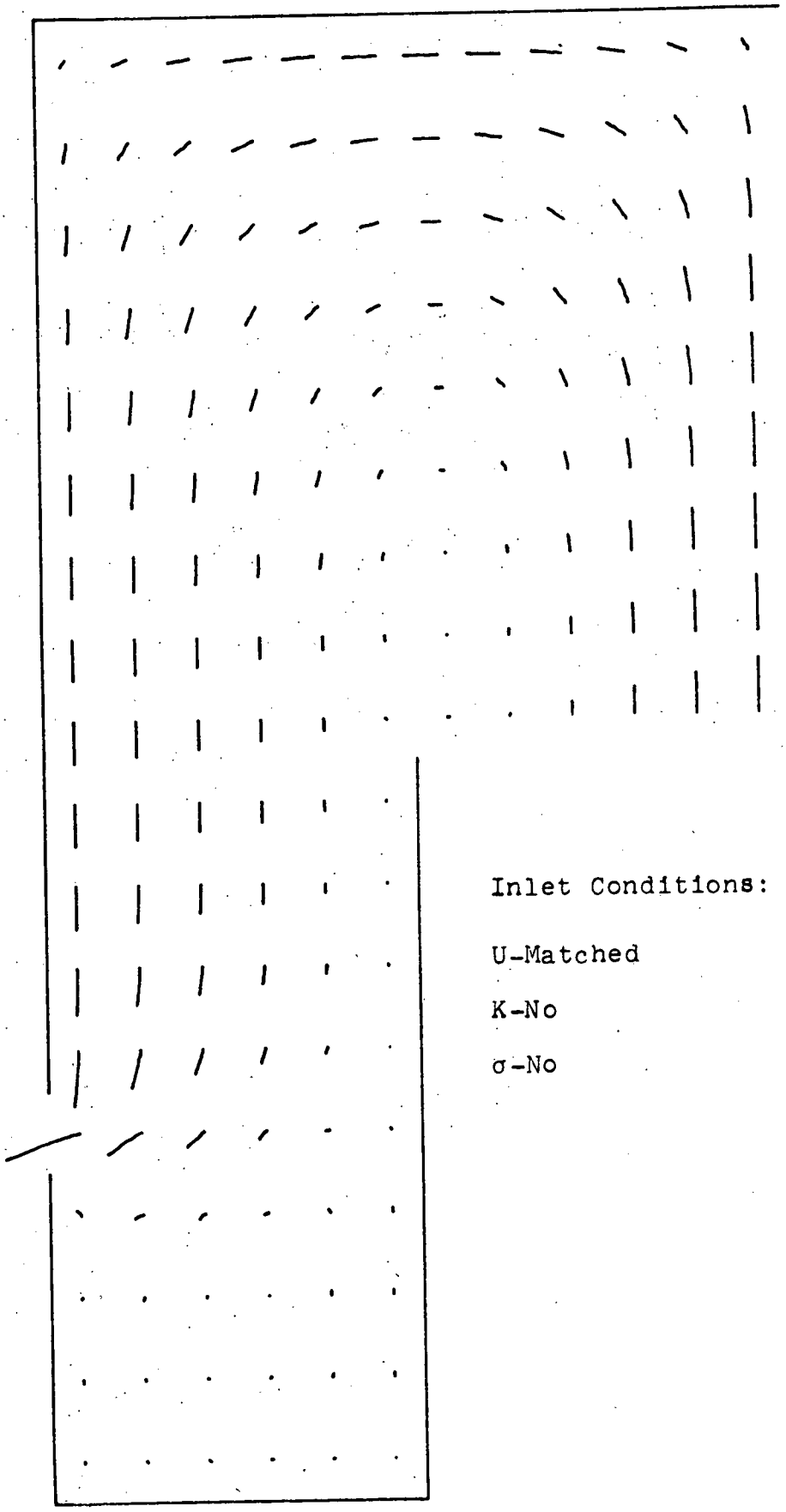

Fig. 5.25 VARR-II Prediction, CRBR Geometry, Re=35000, Normal Inlet Velocity Distribution

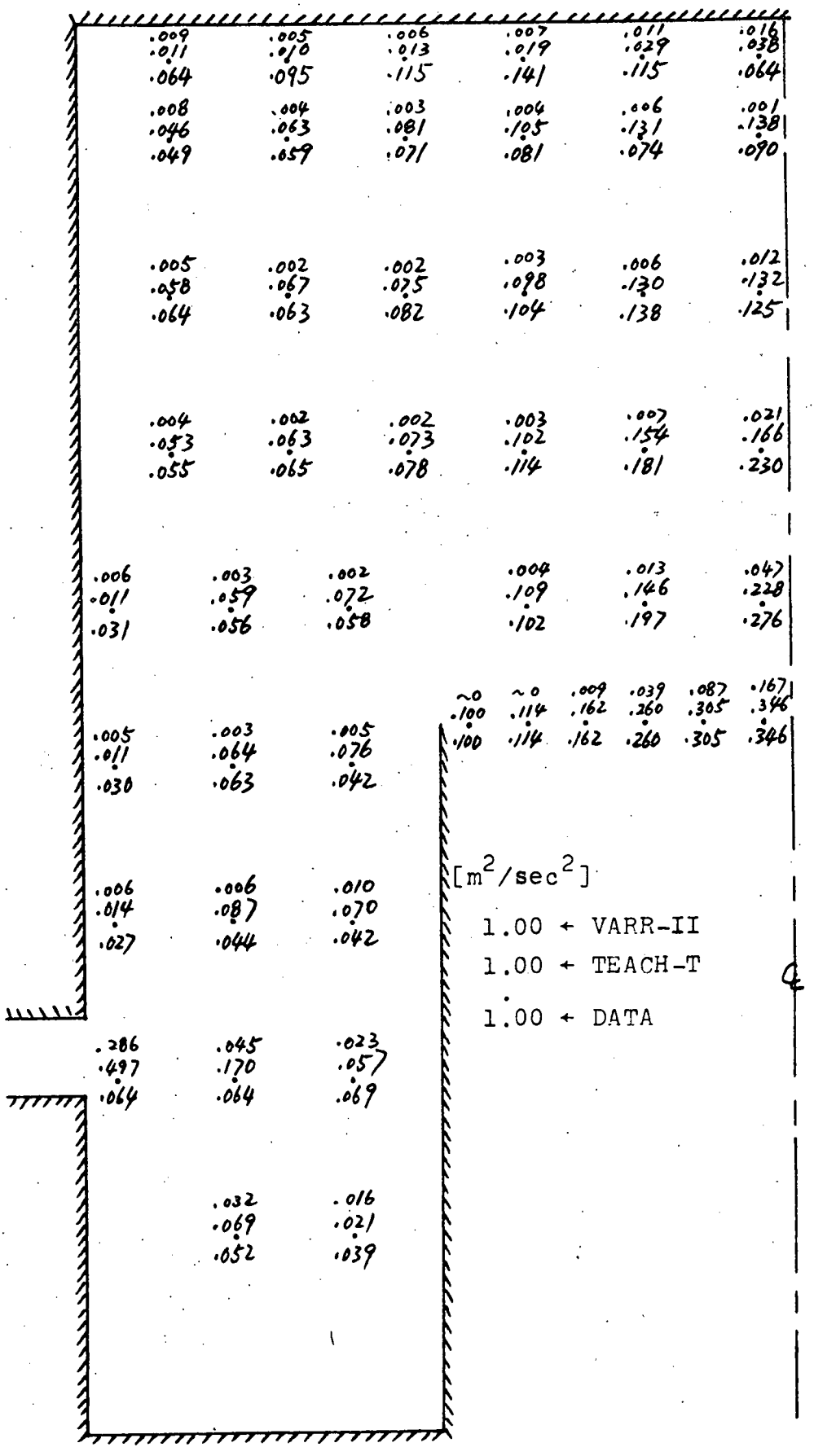

Fig. 5.26 Compared Calculated and Measured Turbulent Kinetic Energy Fields, CRBR Geometry, Re=35000, Normal Inlet Velocity Distribution

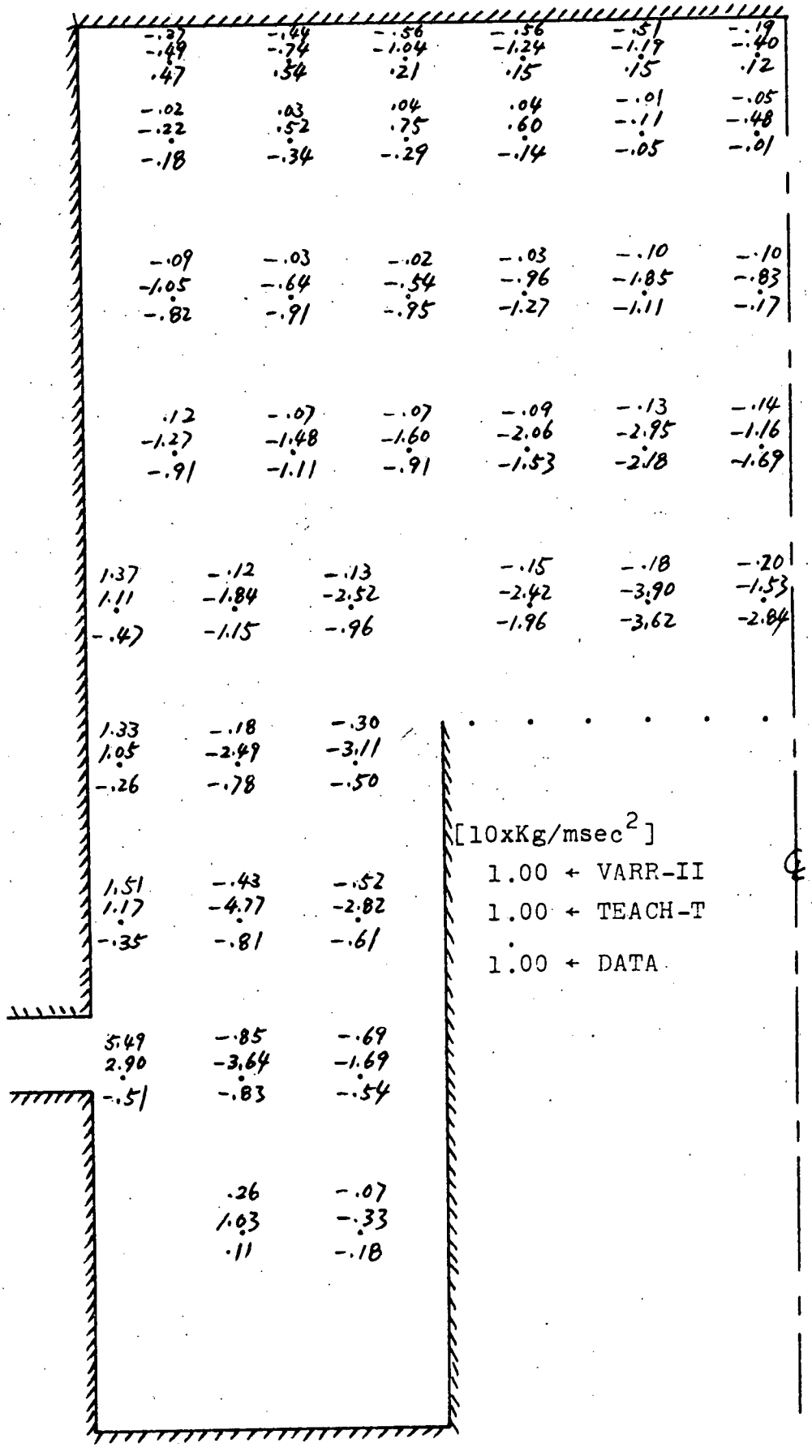

Fig. 5.27 Compared Calculated and Measured Turbulent Reynolds Stress Fields, CRBR Geometry, Re=35000, Normal Inlet Velocity Distribution

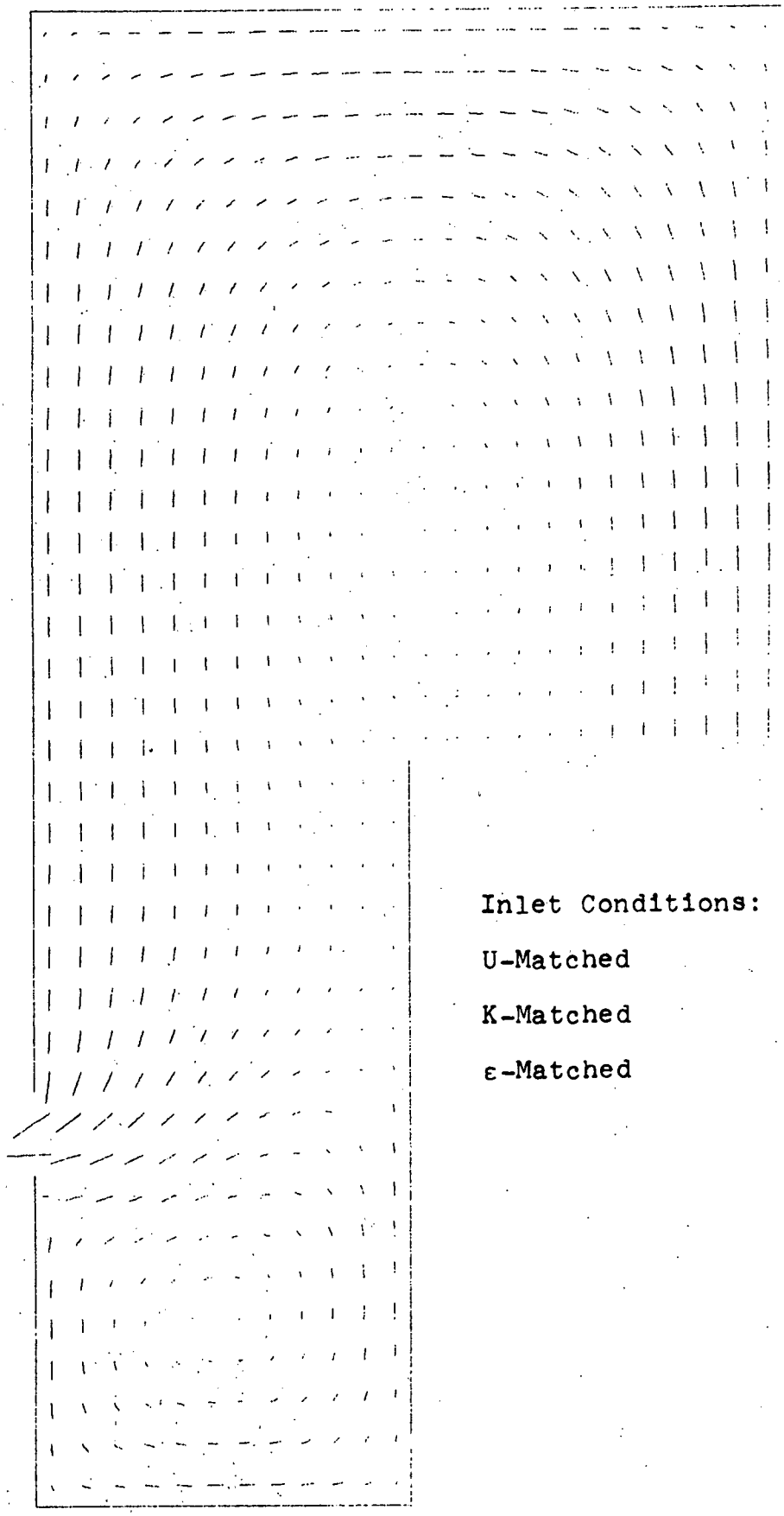

Fig. 5.28 TEACH-T Prediction, CRBR Geometry, Re=35000, Normal Inlet Velocity Distribution

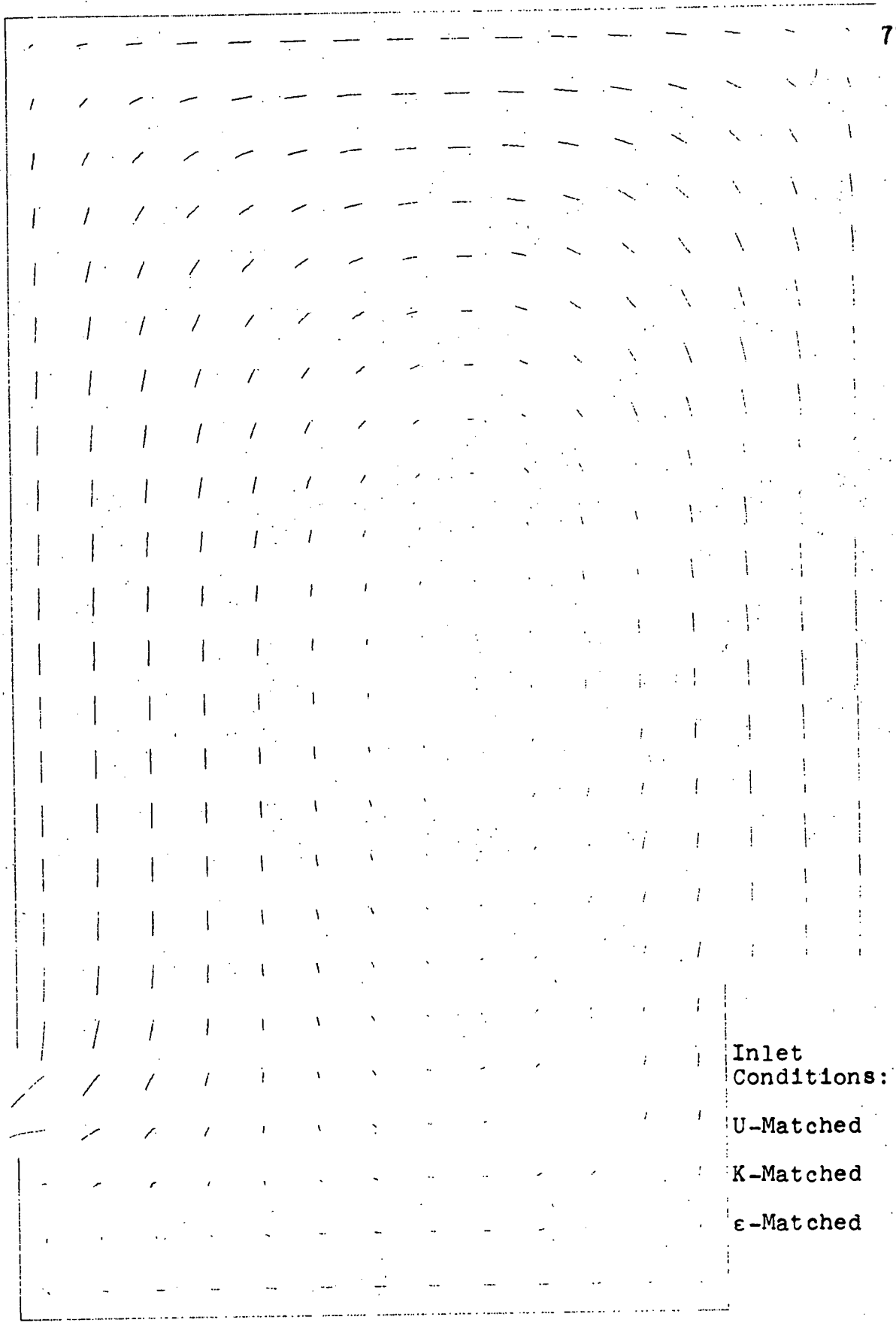

Fig. 5.29 TEACH-T Prediction with New Set of Constants, FFTF Geometry, Re=70000, Normal Inlet Velocity Distribution

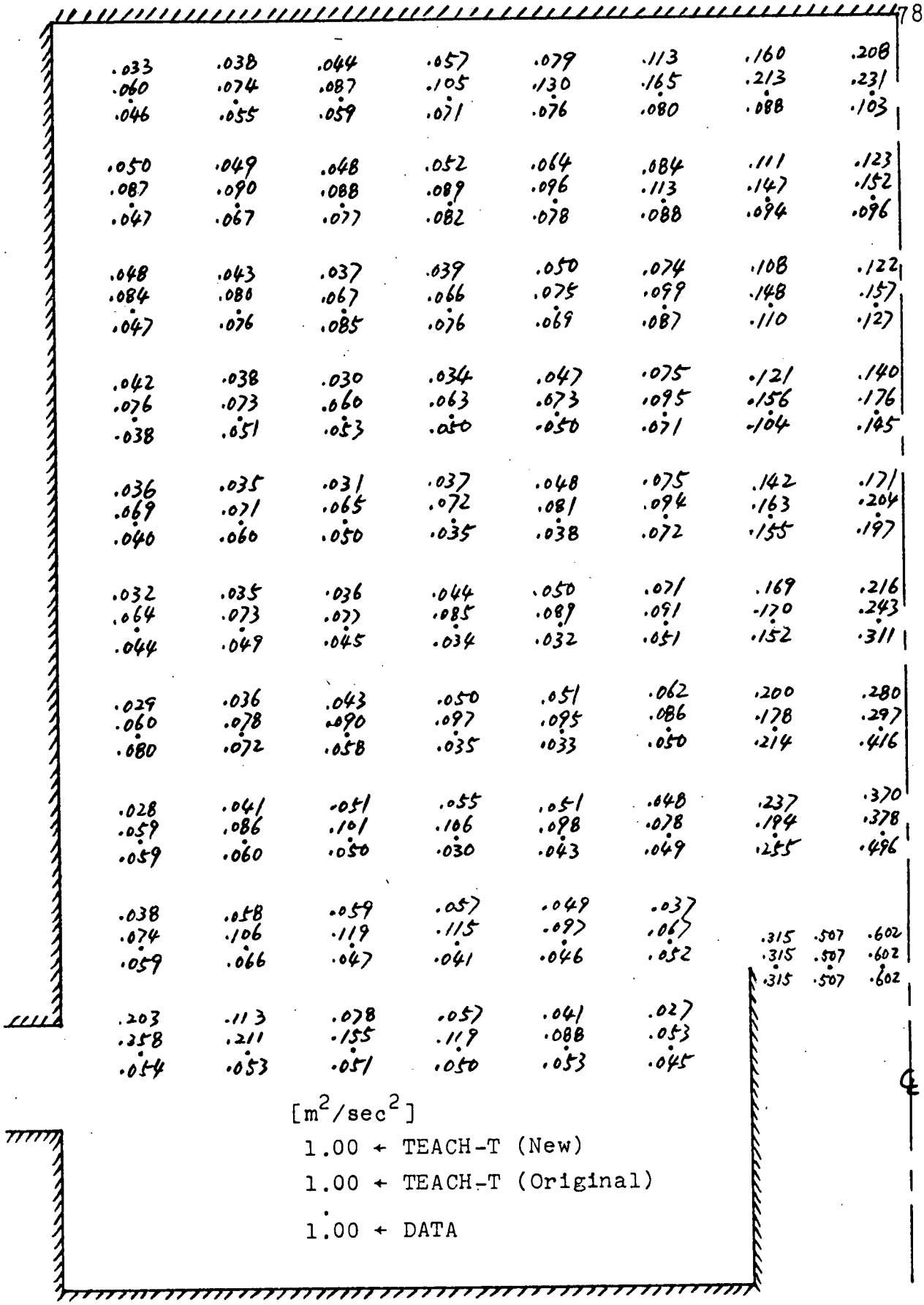

Fig. 5.30 Compared Calculated and Measured Turbulent Kinetic Energy Fields, FFTF Geometry, Re=70000, Normal Inlet Velocity Distribution

CHAPTER 6

CONCLUSIONS AND RECOMMENDATIONS

6.1 Conclusions

From the FFTF case having normal inlet flow condition, it is seen that good agreement is obtained between the measurements and the TEACH-T prediction. The inferior quality of the VARR-II predictions of the turbulence quantities is attributable to use of a poorly tested turbulence model, and use of built-in rather than experimental inlet turbulence parameters.

By contrast, in the CRBR geometry it is seen that the turbulence model calculations are much less accurate than in the FFTF case in the prediction of mean flow fields. The predictions of turbulence quantities fields are hopelessly poor. The cause for this may be due to the fact that in CRBR geometry, the tortuous flow path increases the complexity of the turbulence model equations as well as the degree of departure from isotropy. The net result is that the closure assumptions for the turbulence models examined are too simple to describe adequately the complicated nature of the CRBR flow field.

From the sensitivity analysis, it is found that the production and dissipation of turbulence are the dominant terms in the transport equations for turbulent kinetic energy and turbulent energy dissipation rate over the whole flow field except near the inlet jet region, and the diffusion

terms are relatively small. From the same study a new set of empirical constants for the turbulence model is evolved for the prediction of plenum flows.

The inability of either program to predict the nature of the flow under distorted inlet conditions indicates that the choice of a turbulence model is not as important as an accurate knowledge of inlet velocity and turbulence fields. It also implies that models such as those used in this study should be used with great caution in situations in which abrupt changes in shape arise or in which strong mean flow gradients are imposed. Within these limitations, codes of the type used in this work can provide predictions which are useful for design purposes.

6.2 Recommendations

6.2.1 Turbulence Models

Further research work is needed to incorporate the intermittency, relaminarization, and multi-length scale effects into the turbulence model equations or to develop a calculation strategy to compensate for these effects.

6.2.2 Experiments

For future work more measuring points in the inlet orifice are necessary in order to calculate accurately the turbulent energy dissipation rate or turbulent viscosity for the computer input.

REFERENCES

1. Notes on "Turbulent Recirculating Flow - Prediction and Measurement," College of Engineering, The Pennsylvania State University, July 28-August 1, 1975.

2. Cook, J.L., P.I. Nakayama, "VARR-II. A Computer Program for Calculating Time Dependent Turbulent Fluid Flows with Slight Density Variation," WARD-D-0106, July 1975.

3. Prandtl, L., "Uber die ausgebildete turbulenz," ZAMM 5, 1925, p. 136.

4. Launder, B.E., "Progress in the Modeling of Turbulence Transport," College of Engineering, The Pennsylvania State University, July 28-August 1, 1975.

5. Kolmogorov, A.N., "Equations of Turbulent Motion of an Incompressible Fluid," Itv. AK. Nauk. SSR, Seria fizicheska VI, 1942, pp. 56-58.

6. Prandtl, L., K. Wiegkardt, "Uber ein neues formelsystem fur die ausgebildete turbulenz," Nachr. Akad. Wiss. Gottingen, Math.-Phys. Kl., 1945, p. 6.

7. Bradshaw, P., D.H. Ferriss, N.P. Atwell, "Calculation of Boundary-layer Development using the Turbulent Energy Equation," J. Fluid Mech., Vol. 28, part 3, 1967, pp. 593-616.

8. Nee, V.W., L.S.G. Kovasznay, "Simple Phenomenological Theory of Turbulent Shear Flows," The Phys. of Fluids, Vol. 12, No. 3, March 1969, pp. 473-484.

9. Harlow, F.H., P.I. Nakayama, "Transport of Turbulence Energy Decay Rate," Los Alamos Sci. Lab. Rep. LA-3854, 1968.

10. Rodi, W., D.B. Spalding, "A Two-Parameter Model of Turbulence, and its Application to Free Jets," Warme - und Stoffubertragung, Vol. 3, 1970, pp. 85-95.

11. Rota, J., "Statistiche Theorie nichthomogener Turbulenz," Zeitsch. f. Physik, 129, pp. 547-572, and 131, pp. 51-77, 1951.

12. Stuhmiller, J.H., "Development and Validation of a Two-Variable Turbulence Model," SAI-74-509-LJ, January 1974, Science Application, Inc., La Jolla, Calif.

13. Townsend, A.A., The Structure of Turbulent Shear Flow, Cambridge University Press, 1956.

14. The DISA Type 55L Laser Doppler Anemometer Mark II Instruction Manual, DISA Electronics, Franklin Lakes, N.J. 1974.

15. Yang, J.W., A.K. Agrawal, "An Analytical Model for Transient Fluid Mixing in Upper Outlet Plenum of an LMFBR," International Meeting on Fast Reactor Safety and Related Physics, Chicago, Ill., Oct. 5-8, 1976.

16. Howard, P.A., "PLENUM-3: A Lumped Parameter LMFBR Outlet Plenum Mixing Code," ANL-CT-76-32, March 1976.

17. Lorentz, J.J., "MIX - A Computer Code for Transient Thermal - Hydraulic Analysis of LMFBR Outlet Plenums," ANL-CT-75-41, May 1975.

18. Hinze, J.O., Turbulence, Second Edition, McGraw-Hill Book Company, 1975.

19. Amsden, A.A., F.H. Halow, "The SMAC Method: A Numerical Technique for Calculating Incompressible Fluid Flows," Los Alamos Sci. Lab. Rep. LA-4370, May 1970.

20. Novendstern, E.H., "Description of VARR-II Changes," Private Communication.

21. Caretto, L.S., A.D. Gosman, S.V. Patanker, D.B. Spalding, "Two Calculations Procedures for Steady, Three-Dimensional Flows with Recirculation," Imperial College, Mechanical Engineering Department, Rep. No. HTS/72/5.

22. Yeh, Y., H. Cummins, "Localized Fluid Flow Measurement with a He-Ne Laser Spectrometer," Appl. Phys. Letters, 4, 176, 1964.

23. Goldstein, R.J., D.K. Kreid, "Fluid Velocity Measurement from the Doppler Shift of Scattered Laser Radiation," University of Minnesota Heat Transfer Lab. Rep. No. 85, 1968.

24. Durst, F., J.H. Whitelaw, "Theoretical Considerations of Significance to the Design of Optical Anemometer," Impirical College, Mechanical Engineering Department Rep. No. ET/TN/A/15, 1972.

25. George, W.K., Jr., "Limitations to Measuring Accuracy Inherent in the Laser Doppler Signal," proceedings of the LDA Symposium Copenhagen, 1975.

26. Durst, F., J.H. Whitelaw, "Light Source and Geometrical Requirements for the Optimization of Optical Anemometry Signals," Opto-electronics, 5, 137, 1973.

27. Melling, A., J.H. Whitelaw, "Optical and Flow Aspects of Particles," Proceedings of the LDA Symposium, Copenhagen, 1975.

28. Wilson, E.B.Jr., An Introduction to Scientific Research, McGraw-Hill, New York, 1952.

APPENDIX A
TRANSPORT EQUATIONS FOR MOMENTUM, TURBULENT KINETIC ENERGY, AND TURBULENT ENERGY DISSIPATION RATE

We assume that the Navier-Stokes equation is a valid description for turbulent and incompressible fluids. Accordingly, the derivations here are based on the following set of equations (in tensor form):

$$\frac{\partial U_j}{\partial t} + U_k \frac{\partial U_j}{\partial X_k} = g_j - \frac{1}{\rho} \frac{\partial P}{\partial X_j} + \frac{\partial}{\partial X_k} \left(\nu \frac{\partial U_j}{\partial x_k}\right) \qquad (A.1)$$

$$\frac{\partial U_k}{\partial x_k} = 0 \qquad (A.2)$$

where U_j is the velocity component, g_j is the externally applied body acceleration, P is the pressure, and ν is the molecular kinematic viscosity.

1.1 Transport Equations for Momentum

In describing a turbulent flow in mathematical terms, it is convenient to separate it into a mean motion and a fluctuating motion. Hence the field variables, U_j and P_j can be expressed as

$$U_j \equiv \overline{U}_j + U_j'$$

$$P_j \equiv \overline{P}_j + P_j' \qquad (A.3)$$

so that, by definition, the time-average of all quantities describing the fluctuations are equal to zero:

$$\overline{U_j'} = 0, \quad \overline{P_j'} = 0 \qquad (A.4)$$

Upon introducing relations A.3 into Eq. A.1 and forming

By definition, the turbulent kinetic energy, K, is defined as $K \equiv (1/2)\ \overline{U_i'^2}$. Tensor contraction of the indices i and j yields the transport equation for the turbulent kinetic energy:

$$\frac{\partial K}{\partial t} + \overline{U}_k \frac{\partial K}{\partial x_k} = -\frac{\partial}{\partial x_k}\left(\overline{K'U_k'} + \frac{1}{\rho}\overline{U_k'P'}\right) - \overline{U_i'U_k'}\frac{\partial \overline{U}_i}{\partial x_k} - \overline{\left(\frac{\partial U_i'}{\partial x_k}\right)\left(\frac{\partial U_i'}{\partial x_k}\right)} + \frac{1}{2}\nu\overline{\frac{\partial^2}{\partial x_k^2} U_i'^2} \qquad (A.9)$$

1.3 Transport Equation for the Turbulence Energy Dissipation Rate

Taking the derivative of Eq. A.7 for U_i' with respect to x_l, multiplying throughout by $2\nu\partial U_i/\partial x_l$ and forming averages, we get the transport equation for the turbulence energy dissipation rate:

$$\frac{\partial \varepsilon}{\partial t} + \overline{U}_k \frac{\partial}{\partial x_k}\varepsilon = -2\nu\frac{\partial \overline{U}_i}{\partial x_k}\left(\overline{\frac{\partial U_i'}{\partial x_l}\frac{\partial U_k'}{\partial x_l}} + \overline{\frac{\partial U_l'}{\partial x_i}\frac{\partial U_l'}{\partial x_k}}\right) - 2\nu\overline{U_k'\frac{\partial U_i'}{\partial x_l}}\frac{\partial^2 \overline{U}_i}{\partial x_l \partial x_k}$$

$$-2\nu\overline{\frac{\partial Ui'}{\partial x_k}\frac{\partial Ui'}{\partial x_l}\frac{\partial Uk'}{\partial x_l}} - \overline{2\left(\nu\frac{\partial^2 U_i'}{\partial x_k \partial x_l}\right)^2} + \nu^2\overline{\frac{\partial^2}{\partial x_k^2}\left(\frac{\partial U_i'}{\partial x_l}\right)^2}$$

$$-\frac{\partial}{\partial x_k}\left(\overline{U_k'\varepsilon'} + \frac{2\nu}{\rho}\overline{\frac{\partial P'}{\partial x_l}\frac{\partial U_k'}{\partial x_l}}\right) \qquad (A.10)$$

Where the turbulence energy dissipation rate, ε, is defined as

$$\varepsilon \equiv \nu\overline{\left(\frac{\partial U_i'}{\partial x_j}\right)\left(\frac{\partial U_i'}{\partial x_j}\right)}\ .$$

APPENDIX B
DESCRIPTION OF THE VARR-II CODE

The detailed structure of the code is described in the VARR-II user's manual[2]. Here we state briefly the solution algorithm in VARR-II, and changes which have been made in order to run VARR-II on an IBM computer.

1. Equations of Motion

In Varr-II, the q - σ (identical to K - σ) two equation model is adopted[12]. Six differential equations are solved by this code in cyclindrical coordinates:

$$\frac{\partial U}{\partial t} + \frac{1}{r}\frac{\partial}{\partial r} rU^2 + \frac{\partial}{\partial z} UW = -\frac{\partial P}{\partial r} + \frac{(\rho-\rho_o)}{\rho} g_x - RX(U)$$

$$+ \frac{\partial}{\partial r}\left[\left(\frac{\sigma}{r}\right)\frac{\partial}{\partial r}(ru)\right] + \frac{\partial}{\partial z}\left[(\sigma)\frac{\partial U}{\partial z}\right] \qquad (B.1)$$

$$\frac{\partial W}{\partial t} + \frac{1}{r}\frac{\partial}{\partial r} rUW + \frac{\partial}{\partial z} W^2 = -\frac{\partial P}{\partial z} + \frac{(\rho-\rho_o)}{\rho} g_z - RZ(W)$$

$$+ \frac{1}{r}\frac{\partial}{\partial r}\left[(r\sigma)\frac{\partial W}{\partial r}\right] + \frac{\partial}{\partial z}\left[(\sigma)\frac{\partial W}{\partial z}\right] \qquad (B.2)$$

$$\frac{\partial q}{\partial t} + \frac{1}{r}\frac{\partial}{\partial r}(rUq) + \frac{\partial}{\partial z}(Wq) = +2\sigma\,(SIJ)$$

$$+ \Gamma\left\{\frac{1}{r}\frac{\partial}{\partial r}\left[(r\sigma)\frac{\partial q}{\partial r}\right] + \frac{\partial}{\partial z}\left[(\sigma)\frac{\partial q}{\partial z}\right]\right\} - 4\alpha\, q^2/\sigma \qquad (B.3)$$

$$\frac{\partial \sigma}{\partial t} + \frac{1}{r}\frac{\partial}{\partial r}(rU\sigma) + \frac{\partial}{\partial z}(W\sigma) = +\frac{\sigma^2}{q}(SIJ) + \Gamma(\sigma/q)\left\{\frac{1}{r}\right.$$

$$\left.\frac{\partial}{\partial r}\left[(r\sigma)\frac{\partial q}{\partial r}\right] + \frac{\partial}{\partial z}\left[(\sigma)\frac{\partial q}{\partial z}\right]\right\} - \Gamma_1\left(\frac{\sigma^3}{q^2}\right)\left\{\frac{1}{r}\frac{\partial}{\partial r}(r\sigma)\right.$$

$$\left.\frac{\partial}{\partial r}(q/\sigma)\right] + \frac{\partial}{\partial z}\left[(q)\frac{\partial}{\partial z}(q/\sigma)\right]\right\} - \alpha(q/\sigma)\sigma \qquad (B.4)$$

$$\frac{\partial I}{\partial t}+\frac{1}{r}\frac{\partial}{\partial r}(rUI) + \frac{\partial}{\partial z}(WI) = -CQ + \frac{1}{r}\frac{\partial}{\partial r}[(r\gamma_t\sigma)\frac{\partial I}{\partial r}]$$
$$+ \frac{\partial}{\partial z}[(\gamma_T\sigma)\frac{\partial I}{\partial z}] \qquad (B.5)$$

$$\frac{1}{r}\frac{\partial}{\partial r}(rU) + \frac{\partial W}{\partial z} = 0 \qquad (B.6)$$

where $SIJ=(\frac{\partial U}{\partial r})^2 + (\frac{\partial W}{\partial z})^2 + (1/2)(\frac{\partial U}{\partial z} + \frac{\partial W}{\partial r})^2 + \frac{U^2}{r^2}$

In the above equations, U and W are mean velocities, P is the pressure normalized by the reference density, ρ is the density of the fluid, ρ_o is the reference density, g_x and g_y are components of gravitational acceleration, RX and RZ are the model resistance terms, q is the turbulence kinetic energy, σ is the turbulence kinematic viscosity, and I is the specific internal energy. γ_T is the reciprocal of the turbulent Prandtl number, and -CQ is the amount of heat transfer from an obstacle subregion to the surrounding fluid. The constants α, Γ, and Γ_1 are parameters whose values were chosen by considering the decay of isotropic turbulence, turbulent pipe flow, and turbulent wakes.

2. Analysis

2.1 Finite Difference Formualtion

The finite difference mesh for numerically solving the above equations consists of a rectangular cell with edges δx and δY. Fluid properties are located at the cell positions shown in Fig. B.1. The velocities are defined at the middle of the cell faces to facilitate the finite difference formulation.

The complete finite difference equations can be found in the VARR-II user's manual. Except for the treatment of the convection terms, the equations can be easily derived. Due

to a stability problem, the authors adopt the donor cell approach to treat the convection terms. For instance, consider the following one dimensional equation,

$$\frac{\partial Q}{\partial t} + \frac{\partial}{\partial x}(UQ) = 0.$$

Using central differencing in space and forward differencing in time, the finite difference equation is (see Fig. B.2)

$$(Q_i^{n+1} - Q_i^n)/\delta t = -[U_R(Q_i + Q_{i+1})/2 - U_L(Q_i + Q_{i-1})/2]/\delta x$$

$$= -\frac{1}{2\delta x}[U_R(Q_i + Q_{i+1}) - U_L(Q_i + Q_{i-1})]$$

We now assume that U_R and U_L are greater than zero, and that fluid with a velocity U_R or U_L carries the property Q_i or Q_{i-1} respectively. The new formulation under the donor cell approach is

$$\frac{Q_i^{n+1} - Q_i^n}{\delta t} = -\frac{U_R Q_i - U_L Q_{i-1}}{\delta x} \qquad U_R, U_L > 0$$

Similarly, for $U_R, U_L < 0$ we have

$$\frac{Q_i^{n+1} - Q_i^n}{\delta t} = \frac{U_R Q_{i+1} - U_L Q_i}{\delta x} \qquad U_R, U_L < 0$$

These can be put into a general form that encompasses both cases,

$$\frac{Q_i^{n+1} - Q_i^n}{\delta t} = -(1/2\delta x)[U_R(Q_i + Q_{i+1}) + \alpha_x|U_R|(Q_i - Q_{i+1}) - U_L(Q_{i-1} + Q_i) - \alpha_x|U_L|(Q_{i-1} - Q_i)]$$

If α_x equals 0 or 1, the above form reduces to the central difference or donor cell methods respectively. In general, the donor cell treatment improves the numerical stability and convergence rate.

2.2 Solution Procedures

The velocities computed from Eq.'s B.1 and B.2 will not, in general, satisfy the continuity equation (Eq. B.6). VARR-II adopts the simplified Marker-and-Cell (SMAC) method[19]. The continuity constraint is imposed by adjusting the cell pressure. For example, if the divergence of a cell, $\nabla \cdot D \equiv \frac{\partial U}{\partial r} + \frac{\partial V}{\partial z} + \frac{U}{r}$, is negative corresponding to a net flow of mass into the cell, the cell pressure is increased to counteract the inflow. Likewise, when there is a net flow out of the cell, the cell pressure is decreased to draw the flow back. Because there is one pressure variable for each cell, the divergence for each cell can be driven to zero in this way. However, the pressure adjustment must be done iteratively, since the adjustment in one cell will affect its neighbors.

The new cell pressure is $P_{ij} + \delta P$, and the new velocities are

$$\begin{aligned} U_{ik} &\longrightarrow U_{ik} + (1/\delta x)\delta P\, \delta t \\ U_{i-1,k} &\longrightarrow U_{i-1,k} - (1/\delta x)\delta P\, \delta t \\ W_{i,k} &\longrightarrow W_{i,k} + (1/\delta z)\delta P\, \delta t \\ W_{i,k-1} &\longrightarrow W_{i,k-1} - (1/\delta z)\delta P \delta t \end{aligned} \qquad \text{(B.7)}$$

$$\delta P = -\beta D/\delta t \quad , \text{ where } \beta = \frac{1}{2}\beta_o \left[\frac{1}{(1/\delta x)^2 + (1/\delta z)^2}\right] \qquad \text{(B.8)}$$

Eq. B.8 is derived by substituting the right side of Eq. B.7 into the divergence condition, Eq. B.6, and solving for δP. The term β_o is a relaxation factor.

The convergence rate will be improved by using this relaxation factor. β_o is usually bounded between 1.2 and 2.0.

2.3 Boundary Conditions

Four types of boundary conditions can be simulated in VARR-II.

2.3.1 Rigid Boundary Conditions

Following the example in Fig. B.3(a), if the left boundary is to be a rigid free-slip wall, then the normal velocity there must be zero and the tangential velocity should have no normal gradient, i.e., $U_{1,k} = 0$, and $W_{1,k} = W_{2,k}$.

If the left boundary is a no-slip rigid wall, then the tangential velocity component at the wall should also be zero, i.e., $U_{1,k} = 0$, and $W_{1,k} = -W_{2,k}$.

2.3.2 Continuative Boundary Conditions

This boundary condition allows for an outflow of fluid. For a top wall with a free-slip wall boundary condition, as shown in Fig. B.3(b), the outside tangential velocities are $U_{i,k+2} = U_{i,k+1}$ and $U_{i-1,k+2} = U_{i-1,k+1}$. For the no-slip wall boundary condition, the opposite signs are used. The normal velocity is determined by satisfying the divergence free condition in the unit cell.

2.3.3 Periodic Boundary Conditions

The periodic boundary condition allows the setting up of a mesh boundary configuration that approximates an infinitly long mesh in which periodic flows exist one after another. It is shown in Fig. B.3(c). This boundary condition is very useful for calculating fully developed flows.

2.3.4 Derived Boundary Conditions

This boundary condition insures the correct turbulent shear stress at the wall when the mesh size is too large to properly resolve the velocity distribution near the wall. This is done by analytically prescribing a logarithmic velocity profile between the computational cell next to the wall and the wall itself. This profile is: $W = U^* (A \ln\frac{U^* x}{\nu} + B)$, where $U^* = \sqrt{\frac{\tau}{\rho}}$, and A and B are universal constants. The above equation can be put into the following form:

$$U^* = \frac{W}{A \ln(U^* x/\nu) + B}$$

An iteration scheme determines U^*, W, q and σ.

The complete solution scheme in VARR-II is shown in Fig. B.4. One calculational cycle is composed of four steps:

(1) Compute guesses for the new velocities for the entire mesh from Eq.'s B.1 and B.2 which involve only the values at previous times.

(2) Match the boundary conditions and adjust the new velocities to satisfy the continuity equation (Eq.B.6) by making appropriate changes in the cell pressures. In the iteration, each cell is considered successively and is given a pressure change that drives its velocity divergence to zero.

(3) When convergence has been achieved, the velocity and pressure fields are used to compute the turbulent kinetic energy, kinematic viscosity, and internal energy.

(4) Finally, all of the field properties are at the advanced time level and are used as the starting values for the

next cycle.

3. Changes made in VARR-II

The original version of VARR-II was developed to run on a CDC 7600 computer. The Westinghouse Advanced Reactor Division has made several small modifications[20]. The changes discussed below are from the Westinghouse version of the code. Due to the different assembly language and plotting subroutines used by different computer facilities, the following changes were made in order to run VARR-II on an IBM computer:

(1) An overlay structure was removed, due to the large active memory of the IBM machine.

(2) All the plotting subroutines were removed, and a new routine was inserted.

(3) An assembly language subroutine, BITPIC, for bit manipulation was removed, and appropriate actions were taken to ensure the correctness of the remaining statements.

(4) All of the seven-character names were reduced to six by removing either the first or the last character.

(5) Programming errors in the derived boundary condition were corrected.

The correctness of the new version was tested by running a sample problem.

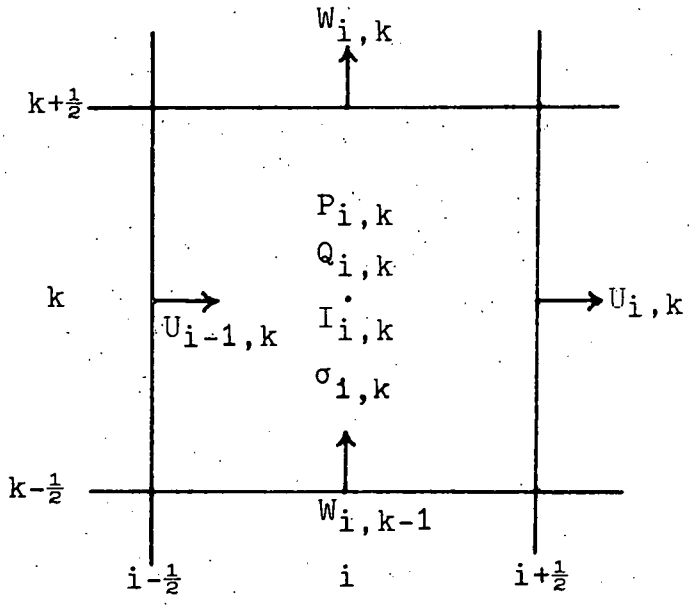

Fig. B.1 A typical cell showing the locations of the principle variables

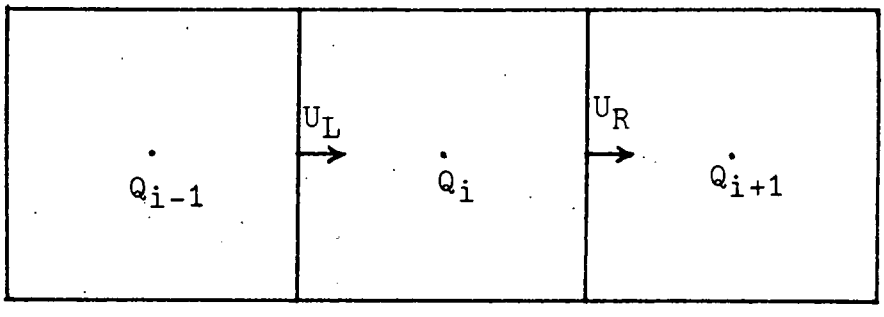

Fig. B.2 A typical cell showing the donor cell treatment of the convection terms

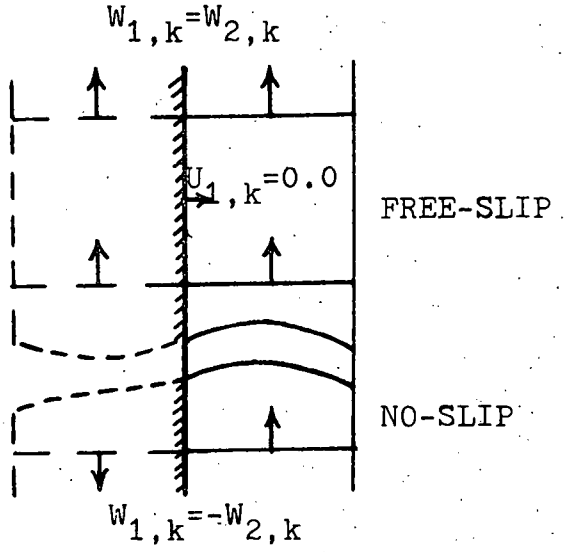

(a) RIGID BOUNDARY-LEFT WALL

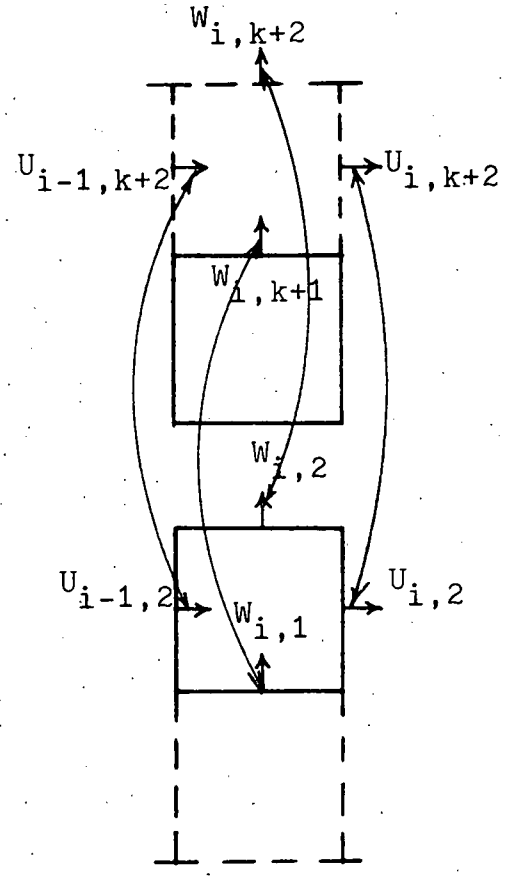

(c) PERIODIC BOUNDARY-TOP AND BOTTOM

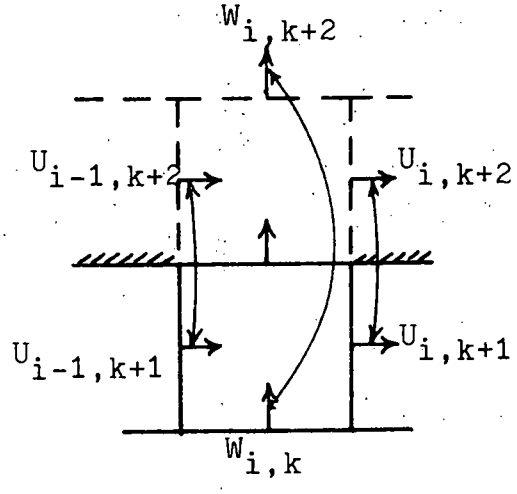

(b) CONTINUATIVE BOUNDARY
- TOP WALL

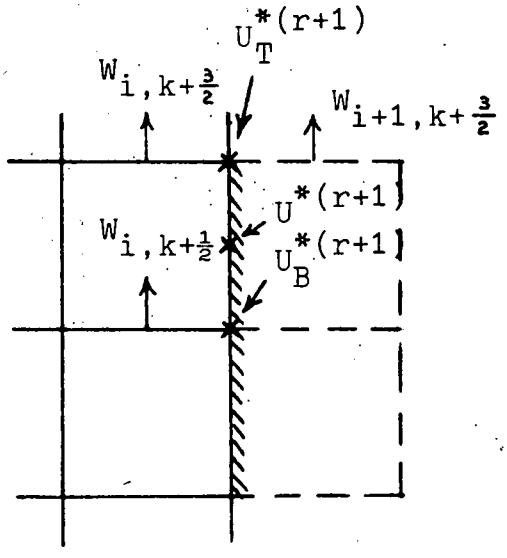

(d) DERIVED BOUNDARY CONDITION
- RIGHT WALL

Fig. B.3 Details of VARR-II Boundary Conditions

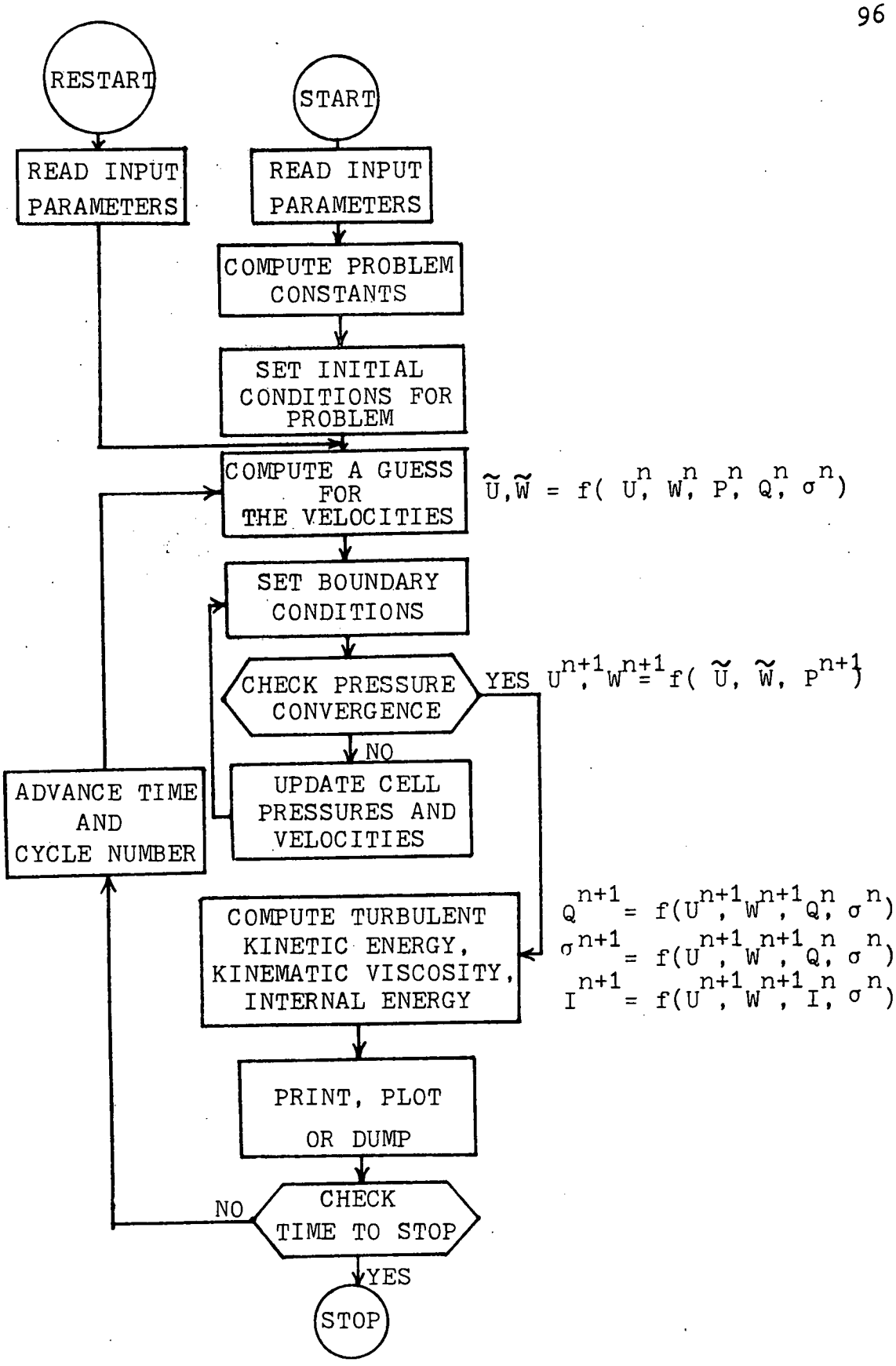

Fig. B.4. Flow Diagram of Solution Scheme

APPENDIX C
DESCRIPTION OF THE TEACH-T CODE

The TEACH-T code[1] was developed in the Mechanical Engineering Department at the Imperial College of Science and Technology in England.

1. Equation of Motion

This code adopts a K-ε two-equation turbulence model. Four differential equations are solved by the code:

$$\frac{\partial}{\partial x_j}(\rho U_j U_i) - \frac{\partial}{\partial x_j}(\mu\frac{\partial U_i}{\partial x_j} - \rho\overline{U_i'U_j'}) - \frac{\partial P}{\partial x_i} = 0 \qquad (C.1)$$

$$\frac{\partial}{\partial x_i}(\rho U_i) = 0 \qquad (C.2)$$

$$U_j\frac{\partial}{\partial x_j}\rho K - \frac{\partial}{\partial x_j}(\frac{\mu_t}{\sigma_K}\frac{\partial K}{\partial x_j}) - \mu_t G + \rho\varepsilon = 0 \qquad (C.3)$$

$$U_j\frac{\partial}{\partial x_j}\rho\varepsilon - \frac{\partial}{\partial x_j}(\frac{\mu_t}{\sigma_\varepsilon}\frac{\partial \varepsilon}{\partial x_j}) - \frac{C_1\varepsilon}{K}\mu_t G + C_2\rho\frac{\varepsilon^2}{K} = 0 \qquad (C.4)$$

where $$-\rho\overline{U_i'U_j'} = \mu_t(\frac{\partial U_i}{\partial x_j} + \frac{\partial U_j}{\partial x_i})$$

$$\mu_t = C_\mu \rho K^2/\varepsilon$$

$$G \equiv (\frac{\partial U_i}{\partial x_j} + \frac{\partial U_j}{\partial x_i})\frac{\partial U_i}{\partial x_j}$$

In the above equations, U_i is the mean velocity, P is the mean pressure, ρ is the density of the fluid, K is the turbulent kinetic energy, ε is the turbulent energy disspation rate, μ is the viscosity, μ_t is the turbulence viscosity, and σ_K, σ_ε, C_1, C_2, and C_μ are constants determined by experiments.

2. Analysis

2.1 Finite Difference Formulation[21]

In the previous section, all of the differential equations except the continuity equation can be expressed in terms of the following general transport equation in cyclindrical coordinates:

$$\frac{1}{r}\left[\frac{\partial}{\partial x}(\rho r U\phi) + \frac{\partial}{\partial r}(\rho r V\phi) - \frac{\partial}{\partial x}\left(r\Gamma\frac{\partial\phi}{\partial x}\right) - \frac{\partial}{\partial r}\left(r\Gamma\frac{\partial\phi}{\partial r}\right)\right] - S_\phi = 0 \qquad (C.5)$$

The finite difference grid is shown in Fig. C.1. Scalar quantities are defined at the intersections of grid lines, and the velocities are defined at control volume boundaries (dashed lines).

A finite difference equation for the scalar ϕ_p is obtained by integrating Eq. C.5 over the control volume, and then by using Gauss's theorem to replace volume integrals by surface integrals. The resulting equation is

$$\int_s^n\left[\left(\rho r U\phi - r\Gamma\frac{\partial\phi}{\partial x}\right)_E - \left(\rho r U\phi - r\Gamma\frac{\partial\phi}{\partial x}\right)_W\right]dr +$$

$$\int_W^E\left[\left(\rho r V\phi - r\Gamma\frac{\partial\phi}{\partial r}\right)_N - \left(\rho r V\phi - r\Gamma\frac{\partial\phi}{\partial r}\right)_S\right]dx - \int_V S_\phi dV = 0, \qquad (C.6)$$

Assume that the net x-direction convection and diffusion of ϕ through the control volume are given by

$$a_E(\phi_E-\phi_p) + a_W(\phi_W-\phi_p), \qquad (C.7)$$

where

$$a_E = \begin{cases} 0 & \text{when } F_E > D_E \\ -2F_E & \text{when } F_E < -D_E \\ D_E - F_E & \text{when } -D_E \leq F_E \leq D_E \end{cases}$$

$$F_E = \dot{m}''_E A_E/2, \quad D_E = \Gamma_E A_E/\delta x_E$$

The terms $\dot{m}''_E$, A_E, and Γ_E stand for the mass flux, cross-sectional area, and average exchange coefficient at the boundary respectively.

The above scheme is a hybrid of central and upwind (donor cell) difference schemes. As $|F/D|$ is less than or greater than unity, it reduces to central or upwind difference schemes respectively. This hybrid scheme has the advantage of being more accurate and stable over a wide range of F/D.

The resultant difference equation from Eq.'s C.6 and C.7 is $a_p \phi_p = \sum_n a_n \phi_n + S_\phi$,

where $\sum_n$ is a summation over all neighbors, and

$$a_p = \sum_n a_n .$$

The treatment of the momentum equation is essentially the same as the above. The control volume for the velocities are, of course, displaced from those of ϕ. Interpolation is sometimes necessary to obtain velocities, densities, viscosities, etc. The difference equations are,

$$a_p U_p = \sum_n a_n U_n + A_W(P_W - P_p) + S_u$$

$$a_p V_p = \sum_n a_n V_n + A_s(P_s - P_p) + S_v$$

where S_u and S_v are integral source terms, that are discussed in Sec. 2.2.1 below.

Finally, the finite difference equation for the continuity equation is

$$(\rho UA)_E - (\rho UA)_W + (\rho VA)_N - (\rho VA)_S = 0$$

2.2 Treatment of Source Terms

2.2.1 Momentum

In the momentum equation, the source terms are

$$S_u = \frac{\partial}{\partial x}(\mu_{eff}\frac{\partial U}{\partial x}) + \frac{1}{r}\frac{\partial}{\partial r}(r\mu_{eff}\frac{\partial U}{\partial r}), \text{ and}$$

$$S_v = \frac{\partial}{\partial x}(\mu_{eff}\frac{\partial V}{\partial x}) + \frac{1}{r}\frac{\partial}{\partial r}(r\mu_{eff}\frac{\partial V}{\partial r}) - \mu_{eff}\frac{V}{r^2} \quad .$$

The integral source terms in Eq. C.6 can be simply derived by integrating the above equation over the control volume.

2.2.2 Turbulence Kinetic Energy

The source term in the K equation is,

$$S_K = \mu_t G + C_D\rho\varepsilon$$

$$= -2\mu_t\left[\left(\frac{\partial U}{\partial x}\right)^2 + \left(\frac{\partial V}{\partial r}\right)^2 + \left(\frac{V}{r}\right)^2\right] + \left(\frac{\partial U}{\partial r} + \frac{\partial V}{\partial x}\right)^2 + C_D\rho\varepsilon \quad .$$

The integral source can be calculated by assuming that the source term is uniform over the control volume, i.e.,

$$\int_V S_K dV = -\int_V (\mu_t G - C_D\rho\varepsilon)dV = \int [C_D\rho(\frac{C_\mu\rho K^2}{\mu_t}) - \mu_t G]dV$$

$$\approx bK_p + C$$

where $b \equiv -C_\mu C_D \rho_p^2 K_p^* \delta V/\mu_t$, $C \equiv \mu_t G \delta V$, and

K_p^* is the previous value of K_p.

2.2.3 Turbulence Kinetic Energy Dissipation Rate

The source terms in the equation are,

$$S_\varepsilon = C_1\varepsilon\frac{\mu_t G}{K} + \frac{C_2\rho\varepsilon^2}{K}$$

Assuming S_ε is uniform over the control volume, the integral source term is

$$\int_V S_\varepsilon dV = \int (C_1 \frac{\mu_t G\varepsilon}{K} - \frac{C_2 \rho \varepsilon^2}{K}) dV$$

$$\approx b\varepsilon_p + C.$$

Where $$b \approx -C_2 \frac{\rho \varepsilon^* \delta V}{K_p}$$

$$C \approx C_1 \frac{\mu_t G \varepsilon^*_p}{K^*_p}$$

2.3 Boundary Conditions

Fig. C.2 illustrates the boundary conditions discussed below.

2.3.1 Velocity

In order to assure the correct shear stress on the wall, the shear stress is calculated as

$$\tau_s = - \frac{\rho_p (C_\mu C_D)^{\frac{1}{4}} K_{pw}^{\frac{1}{2}} (U_p - U_s)}{U^+}$$

where $K_{pw} \equiv (K_p + K_w)/2$

$$U^+ = \frac{1}{K} \ln (Ey^+)$$

$$K = 0.4, \quad E = 9.793, \quad y^+ \equiv \rho (C_\mu C_D)^{\frac{1}{4}} K_{pw}^{\frac{1}{2}} y_p / \mu$$

For laminar flow ($y^+ < 11.63$), a laminar law is employed:

$$\tau_s = - \mu \frac{(U_p - U_s)}{y_p}$$

The usual shear force expression is suppressed by setting $a_{outside} = 0$.

2.3.2 Turbulent Kinetic Energy

Calculation of G is altered by

$$\int_V \mu_t \left(\frac{\partial U}{\partial r} + \frac{\partial V}{\partial x} \right)^2 dV \approx \tau_s \, (U_p - U_s) \, \delta V / y_p$$

where τ_s, U_s and U_p are nearby average values. Contributions from the outside are suppressed by setting $a_{outside} = 0$.

2.3.3 Turbulent Energy Dissipation Rate

The finite difference equation at the near wall node is replaced by a log-law based relation:

$$\varepsilon_p = \frac{(C_\mu C_D)^{3/4}}{C_D \; K} \; \frac{K_p^{3/2}}{y_p}$$

In order to utilize the above formulation, the source coefficients are replaced by,

$$b = -10^{30} \; , \; C = 10^{30} \varepsilon_p$$

2.4 The Solution Procedures

The solution technique is a series of guess and correct operations. First, the guessed pressures P* and velocities U* and V* (which may be initial guesses, or values from the previous cycle) are substituted into the momentum equations. This yields an intermediate U* and V*. In general, these velocities will not satisfy the continuity equation.

The pressures are then adjusted to satisfy continuity. The relations between velocities and pressures are

$$U_w = U_w^* + \frac{\partial U_w}{\partial (P_w - P_p)} (P'_w - P'_p),$$

where P' is the pressure correction.

The velocity and pressure relations can be deduced from the momentum equation as

$$D_w = \frac{\partial U_w}{\partial (P_w - P_p)} = \frac{A_w}{a_p - b} .$$

Substituting this into the momentum equation, we obtain

$$(a_p - b)\, P'_p = \sum_n a_n P'_n + M_p + C ,$$

where $M_p = (\rho U^* A)_w - (\rho U^* A)_E + (\rho V^* A)_s - (\rho V^* A)_N$

$$S_u = b\, U_p + C$$

$$a_w = \rho_w D_w A_W$$

$$a_p \equiv \sum_n a_n .$$

Once the P' field has been obtained, it is a straightforward matter to update the pressures and velocities. In general, it is not necessary to satisfy the continuity equation for each cycle, since the subsequent calculation for ϕ (e.g., K,ε) will affect the velocities. The procedures adopted by TEACH-T are, for each cycle, U, V, K and ε, iterated three times, and P five times. The convergence criterion is that residual sources for mass and velocities are below certain values.

This solution algorithm obviates the need to approach the steady state via the time evolution of the flow, as is required by the conventional method (such as the SMAC method in VARR-II). In the plenum considered in this work, the computation time for TEACH-T is approximately one order of magnitude less than that of VARR-II.

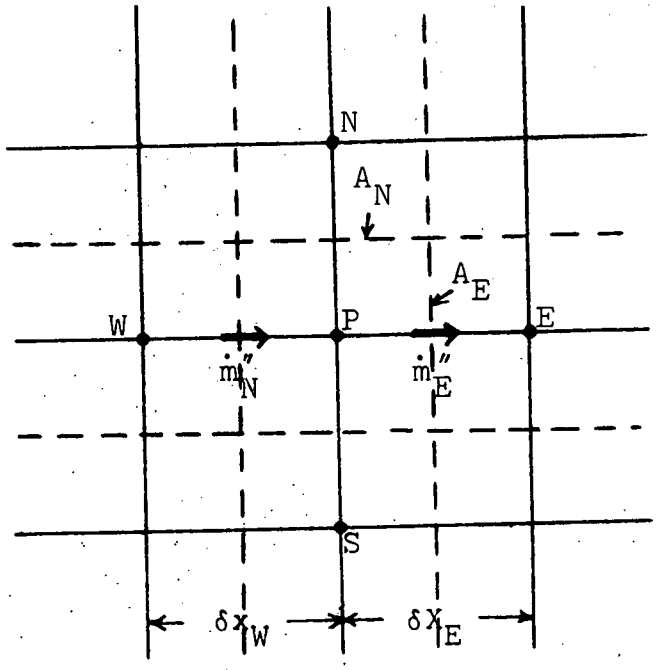

Fig. C.1 Finite Difference Grid for TEACH-T

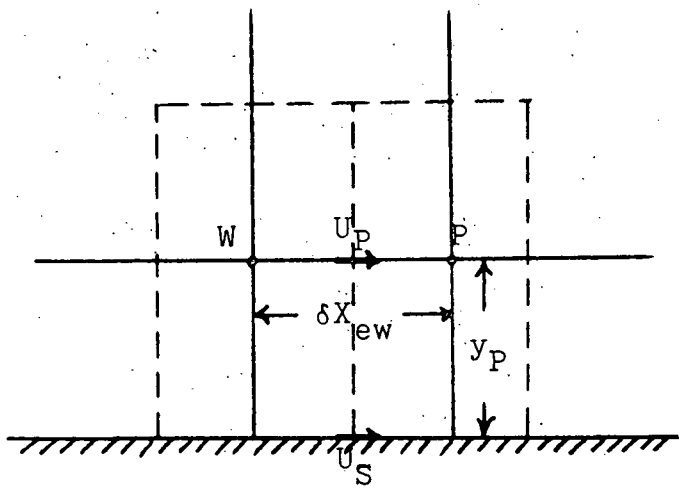

(a) Velocity Boundary Conditions

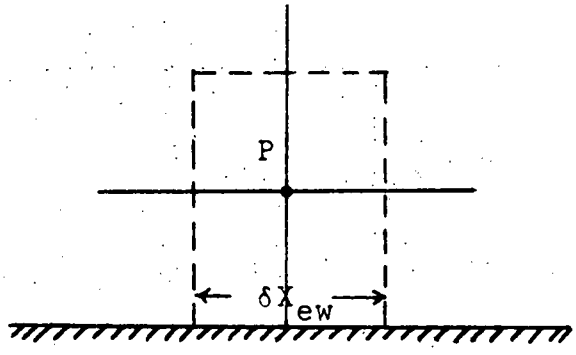

(b) Turbulent Kinetic Energy and Dissipation Rate Boundary Condition

Fig. C.2 Boundary Conditions in TEACH-T

APPENDIX D
LASER DOPPLER ANEMOMETER

1. Introduction

The Laser Doppler Anemometer (LDA) was developed in 1964 by Yeh and Cummins[22] who first demonstrated that the Doppler shift of light scattered by moving particles could be detected by heterodyning the scattered light with a laser source on a photocell. Since then, a tremendous effort has been made by many researchers around the world toward making the LDA a reliable fluid velocity measuring instrument.

The major advantages of the LDA over conventional hot wire or pitot tube probes are:

1. The measurement is performed with laser beams; no probes disturb the flow.
2. The measuring (or scattering) volume is very small, which allows a high spatial resolution.
3. No calibration of the equipment is required.
4. The fluid velocity is linearly proportional to the Doppler shift.
5. The directional sensitivity is ideal for two or three-dimensional measurements.

2. Principle of the Laser Doppler Anemometer

If a source of sound or electromagnetic waves of constant frequency is put into motion, a fixed observer will receive a different frequency. This is the well-known Doppler effect.

A similar phenomenon is also observed when the source is fixed but the wave is scattered by a moving body before reaching a fixed observer. The Doppler shift of an electromagnetic wave is usually very small compared to the source frequency and very difficult to detect. Conventional light sources have a bandwidth larger than the Doppler shift and this change in frequency could not be detected in the broad signal. It is the introduction of the laser that permits the measurement of a Doppler shift at optical frequencies. The laser is a source monochromatic light with a very small bandwidth. For example, a single axial mode of the He-Ne laser operating at 6328 Å ($f \sim 10^{14}$Hz) has a bandwidth of 10 Hz. The Doppler shift is usually larger than one KiloHertz. Although this is still small compared to the source frequency, it is large compared to the source bandwidth and thus is detectable with a heterodyne technique.

As illustrated in Fig. D.1, light incident on a scattering particle is scattered at a different wave number. If $\underline{K}_i$ and $\underline{K}_s$ are the wave numbers of the incident and scattered light respectively, the difference in wave number is given by $\underline{K} = \underline{K}_i - \underline{K}_s$.

If $\underline{U}$ is the velocity vector of the scattering particle, the frequency shift between incident and scattered light as seen by a fixed observer is[23]

$$W_D = 2\pi f_D = \underline{K} \cdot \underline{U}, \text{ or } f_D = \frac{1}{\lambda_i} \underline{U} \cdot (\hat{K}_i - \hat{K}_s) \qquad (D.1)$$

where λ_i is the wavelength of the incident beam, and $\hat{K}_i$ and

$\hat{K}_s$ are unit vectors.

Note that the Doppler shift is linearly proportional to the component of velocity in the direction of $\underline{U} \cdot (\hat{K}_i - \hat{K}_s)$. This result permits us to measure components of velocity in any direction by properly orienting the difference vector, $(\hat{K}_i - \hat{K}_s)$. Secondly, the LDA has an ambiguity of the flow direction, i.e., the LDA system is unable to distinguish whether the velocity is positive or negative. Unless a frequency shift device is used, the LDA will give erroneous results for small and possibly reverse flows.

The Doppler shift can be detected by a square law detector, such as photomultiplier or photodiode. Considering the reference beam system shown in Fig. D.2, the two light beams may be represented by

$$E_1 = E_{10} \sin 2\pi f_o t$$

$$E_2 = E_{20} \sin 2\pi (f_o + f_D) t$$

The output current, i, is proportional to the square of the total electric field incident on it:

$$i \alpha (E_1 + E_2)^2$$

$$= E_{10}^2 \sin^2 2\pi f_o t + E_{20}^2 \sin^2 2\pi (f_o + f_D) t$$

$$+ E_{10} E_{20} [\cos 2\pi f_D t - \cos 2\pi (2f_o + f_D)]$$

Since the detector cannot follow frequencies greater than several hundred megahertz, terms in the expansion involving f_o, $f_o + f_D$, and $2f_o + f_D$ will give rise only to a D.C. current proportional to the time average of those terms. If

f_D is below the frequency cutoff of the detector, there will be a signal

$$i\alpha \frac{E_{10}^2 + E_{20}^2}{2} + E_{10}E_{20}\cos 2\pi f_D t$$

The first term is the D.C. current and the second term is the A.C. or Doppler current. In order to know the velocity, a proper frequency analysis instrument (such as spectrum analyzer, frequency tracker, or frequency counter) may be used to determine the Doppler frequency.

3. Modes of Operation

There are several different optical arrangements for the experimenter. The two most popular schemes are discussed here.

3.1 Reference Beam Mode

As shown in Fig. D.2, the incident light is first split into two beams. After passing through the focusing lens, they intersect within the fluid to form the measuring volume. A photodetector is aligned with the reference beam to pick up the signal. In order to reduce the intensity of the reference beam and optimize the signal, a neutral density filter must be used.

This mode is preferred for measurement in flows with high particle concentrations.

3.2 Dual Scatter (or Fringe) Mode

In the dual scatter mode, two beams intersect to form the fringes illustrated in Fig. D.3. The Doppler frequency

is shown to be proportional to the rate at which fringes are crossed by the scattering particles. Note that this result is identical to Eq. D.1. Consequently, the Doppler shift is independent of the direction of detection. The immediate advantage of this result is that scattered light can be collected over a wide solid angle with relatively low intensity scattered light. In general, this mode requires a low particle concentration for a good signal to noise ratio.

4. Limitations on Accuracy

The Laser Doppler Anemometer provides an absolute measurement of velocity and does not require any calibration. Its frequency and spatial resolution are excellent. Also, this technique allows the scattering volume to be easily positioned in the flow channel by traversing the optical components. In spite of these advantages over other types of anemometers, the LDA still has many limitations.

4.1 Frequency Broadening

The term "frequency broadening" refers to the finite width of the frequency probability density distribution of the optical signals resulting from effects other than the variation of local velocity with time. There are several contributions to the frequency broadening, and these are subdivided into three different classes for discussion.

4.1.1 Finite Transit Time Broadening

A typical signal generated by a particle passing through the measuring volume is shown in Fig. D.4. The small size of the measuring volume and the finite velocity of the scattering particles result in a finite signal burst. Since the coherent information only exists for a time interval $\Delta\tau$, it limits the resolution of the magnitude of the local velocity variations with time. If an electronic data processing system is used, it gives not only the signal frequency but also the envelope of the signal burst. From detailed frequency analysis[24], it can be deduced that the finite spectral width, δf, is inverseley proportional to the duration, $\Delta\tau$, i.e.,

$$\delta f \sim \frac{1}{\Delta\tau}$$

$$\text{since } \Delta\tau = \frac{d_m}{U} = \frac{N_{pf}}{f}$$

$$\frac{\delta f}{f} \sim \frac{1}{N_{pf}}$$

where d_m is the fringe spacing, and N_{pf} is the number of fringes in the measuring volume. From the above equation, it is concluded that in order to ensure this broadening is less than 1%, N_{pf} must be greater than 100.

4.1.2 Broadening due to Optical Imperfections

From Eq. D.1, the Doppler frequency is

$$f = \frac{1}{\lambda} \underline{U} \cdot (\hat{K}_i - \hat{K}_s)$$

Due to the finite size of the laser beam, imperfections of the optical components, and possible optical alignment errors, the

$\underline{U}\cdot(\hat{K}_i - \hat{K}_s)$ term will not be uniform over the transit time of particles.

4.1.3 Broadening Due to Spatial Variations in Velocity

If a velocity gradient exists over the finite size of the measuring volume, particles crossing the control volume at different positions will have different velocities. These velocity differences cannot be distinguished from velocity variations with time, and have to be considered as a broadening. This can be represented by

$$\frac{\delta f}{f} \sim \frac{1}{2U}\left[\frac{\partial U}{\partial x}\right]\delta x$$

where δx is the dimension of the scattering volume perpendicular to the direction of the velocity gradient measurement.

4.2 Velocity Biasing

The number of particles which arrive having a particular velocity is, in general, dependent on the velocity. If the particle distribution is uniform in space, the rate of particles arriving in the scattering volume will be higher for fast particles (cf. a high volume flow rate for fast particles). Consequently, the average value of the measured velocity component will tend to be higher than the statistical mean value. The degree of biasing depends not only on the signal processors used, but also on the averaging mode employed. For example, consider two different averaging modes for the frequency tracker:

Mode 1 - the analog voltage is integrated over all time, no matter whether the Doppler signal is present or not.

Mode 2 - the analog voltage is integrated only over the time that the Doppler signal is present.

It is no surprise that these two modes give different average values, and mode 2 tends to give better results. Unfortunately, most of the commercial trackers adopt the first scheme. The ideal signal processor for decreasing the velocity biasing is the random sampling circuit, i.e., it observes the scattering volume at random instants of time, so that there is an equal probability to detect either fast or slow particles.

4.3 Random Phase Fluctuation due to Many Scattering Particles

So far only the signal produced by single particle has been discussed. While more than one particle is in the volume, not only the signal amplitude changes, but also the phase changes abruptly.[25] For example, in Fig. D.5(a) there is only one particle in the volume, and the Doppler current is given by

$$i_D \alpha \begin{cases} A\cos(\omega_D t + \theta) & \text{particle in volume} \\ 0 & \text{particle not in volume} \end{cases}$$

Considering Fig. D.5(b), there are two particles in the volume which entered at different times. The Doppler current is given by

$$i_D \alpha \begin{cases} A \cos(\omega_D t + \psi_1), & \text{particle 1 in volume} \\ A \cos(\omega_D t + \psi_1) + A \cos(\omega_D t + \psi_2), & \text{Both particles in volume} \\ = 2A \cos(\omega_D t + \psi) & \\ \text{where } \psi = \tan^{-1} \dfrac{\sin\psi_1 + \sin\psi_2}{\cos\psi_1 + \cos\psi_2} & \\ A \cos(\omega_D t + \psi_2), & \text{particle 2 in volume.} \end{cases}$$

As shown in the figure, each of the abrupt changes of phase amounts to an anomalous zero crossing. A tracker cannot distinguish these crossings from velocity fluctuations.

The second example of a phase fluctuation is shown in Fig. D.5(c). There are two particles with different velocities which entered at the same time. The output is given by

$$i_D \alpha A \cos(\omega_{D_1} t) + A \cos(\omega_{D_2} t)$$

$$= 2A \cos\left(\frac{\omega_{D_1} + \omega_{D_2}}{2}\right) t \cos\left(\frac{\omega_{D_1} + \omega_{D_2}}{2} t\right)$$

The first term gives a frequency proportional to the mean velocity. The second term is an envelope of the signal. As shown in the figure, extra zero crossings will be detected as velocity fluctuations.

In summary, a phase fluctuation will result from

(a) a velocity difference across the control volume,

(b) a particle population change in the control volume, and

(c) a Doppler envelope crossing a zero, even when particles are present.

5. Optimization of the Doppler Signal

Some optimization procedures are followed to improve the signal to noise ratio, and to increase the accuracy of the measurement.

5.1 Laser Power Requirements

When light strikes a particle, it scatters in every direction. The resulting distribution depends on several factors such as the properties of the light (e.g., wavelength), and the properties of the scattering particles (e.g., size, shape, refractive index). The intensity of light scattered backward is about three orders of magnitude less than the intensity of light scattered forward. Since only part of the total laser power scattered by a particle is collected by the photomultiplier and several photons per unit time are required to insure a good signal, the laser power requirement varies with the scattering direction. For forward scattering, the suggested laser power[26] is .05mw/(m/sec). For backward scattering, the requirement is a thousand times greater. In this experiment, a 2 Watt laser is used, and is well above this limit for flows of water.

5.2 Optical Path Length Difference

The requirement here is that the optical path length difference of the two beams should be zero or differ by integral multiple of 2L, where L is the laser resonator cavity length. In practice, the commercially available integrated optical unit is designed so that the difference will cause only a small

decrease in the amplitude of the signal. For the DISA Optic Unit with a two-channel section, the path length difference is about 5.7 cm, and is small compared to the 1 m. laser cavity length.

5.3 Measuring Volume

As discussed in section 4.1, a small scattering volume is desirable for high spatial resolution and to minimize broadening due to velocity gradients. But a small scattering volume can cause a large transit time broadening. Hence, there exists an optimum size for minimum broadening. The measuring volume can be adjusted by changing the focal length of the lens or the beam separation distance. In practice, as long as one percent spatial resolution and 100 fringe lines are assured, no optimization is necessary.

5.4 Scattering Particles

Since the scattered light comes from the interaction of the laser beam with the particles suspended on the fluid, it is very important to choose the particle properly for accurate results. In this experiment, polystyrene latex particles are used.

5.4.1 Relative Density of the Particles and the Fluid

The LDA system measures the particle velocity in the fluid instead of fluid velocity itself. It is very important to know whether the particles suspended in the fluid will follow the fluid. It has been shown[27] that particles with a density close to that of the fluid will follow the fluid

within a broad velocity range. In this experiment, polystyrene latex particles with density of 1.05 are used, which is very close to the density of water.

5.4.2 Particle Concentration

As discussed in section 4.3, if several particles are simultaneously passing through the measuring volume, the mixed signal will lead to less accurate results in the fringe mode. Thus the best concentration is that which results in only one particle being within the measuring volume at any time. This condition can be obtained by properly seeding the fluid and adjusting the size of measuring volume. In contrast, the reference beam mode usually requires a high particle concentration in order to get a better signal to noise ratio.

5.4.3 Particle Size

In the fringe mode, if the size of the particles is larger than the fringe spacing, then no signal can be detected. In practice, the size of the particles should be smaller than one quarter of a fringe spacing. But the size should not be too small, because the scattering intensity decreases with the area of the particles. In this experiment, polystyrene latex particles with size ranging from 0.46 to 0.54 micron are used.

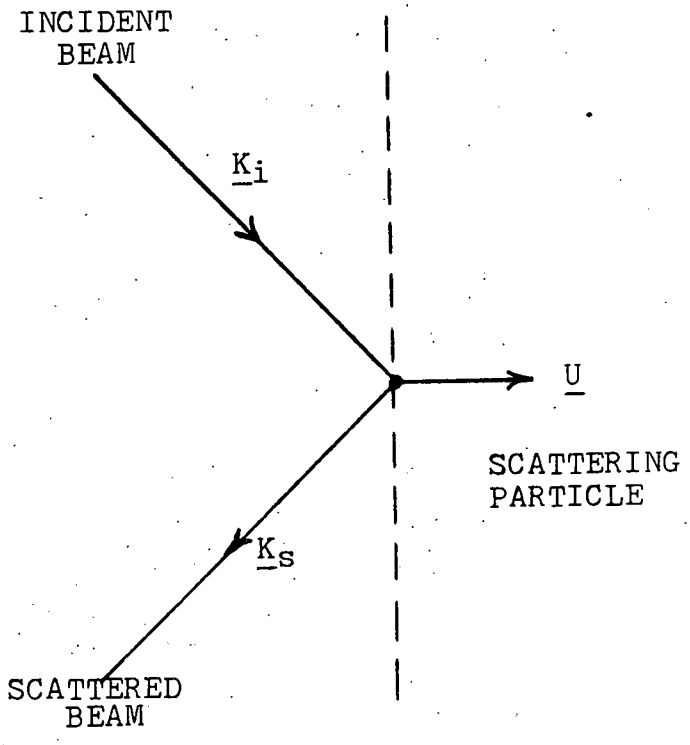

Fig. D.1 Frequency Shift for Light Scattered from a Moving Particle

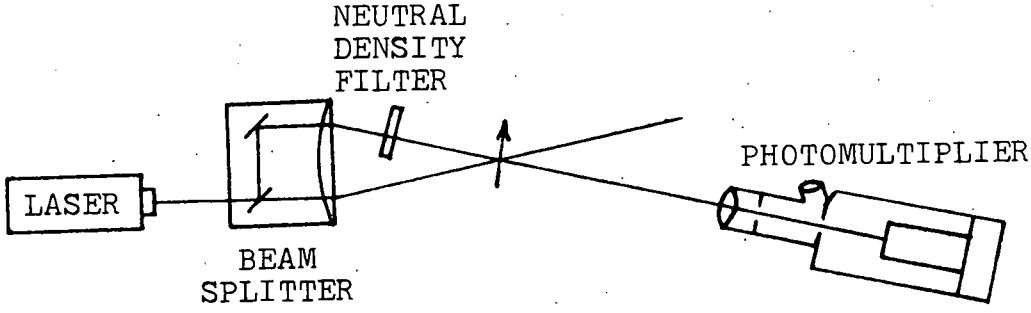

REFERENCE BEAM MODE

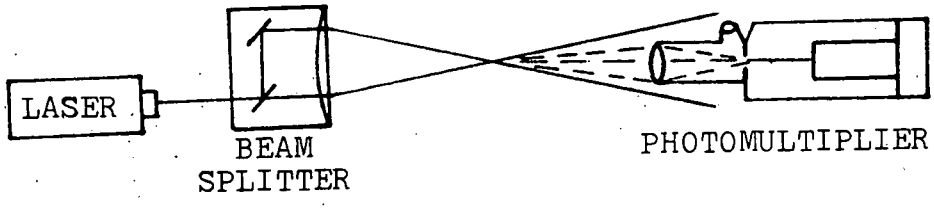

DUAL SCATTER (FRINGE) MODE

Fig. D.2 Modes of Operation

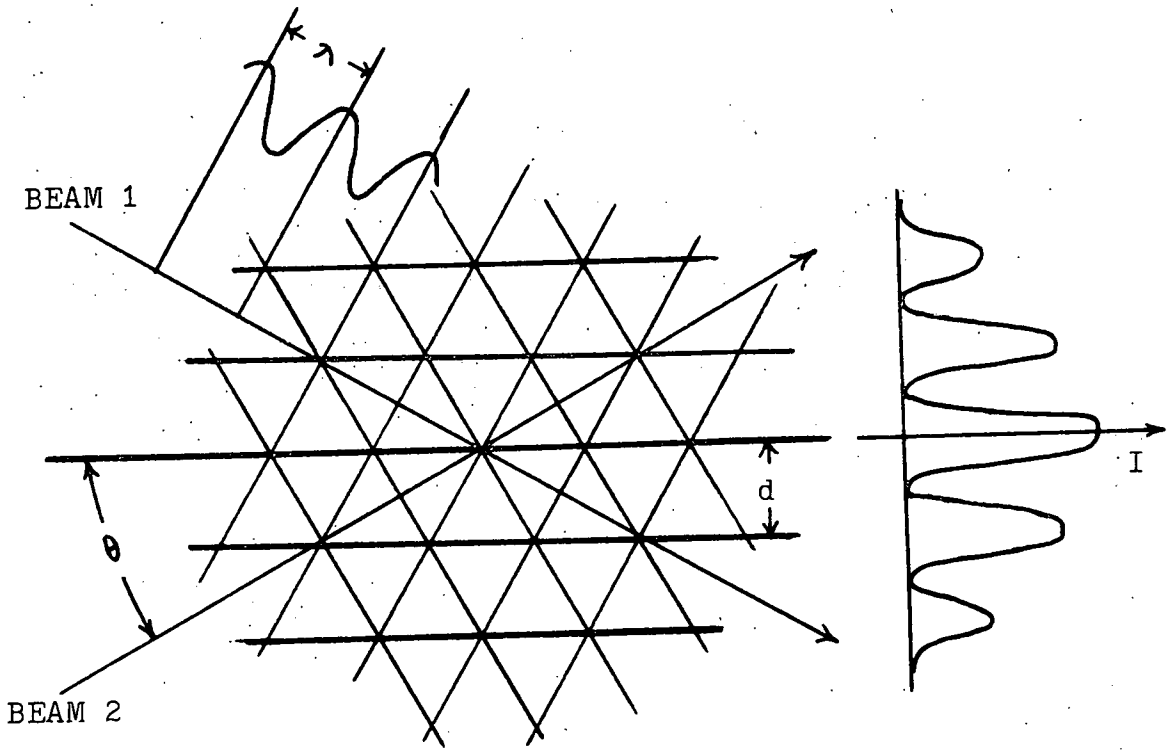

Fig. D.3 Fringe Pattern at Beam Crossing Point

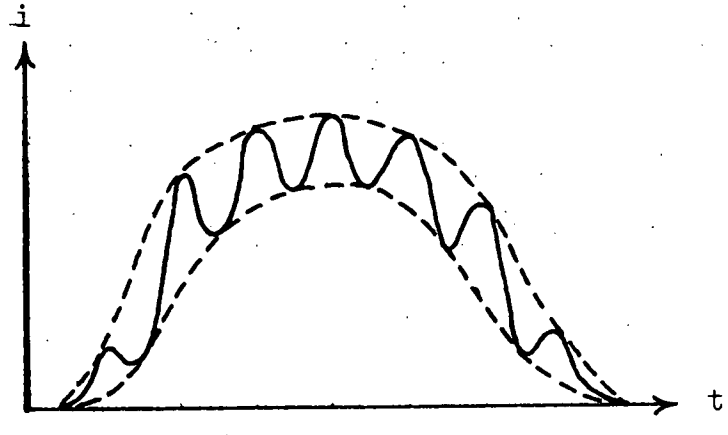

Fig. D.4 Typical Doppler Signal from Photomultiplier

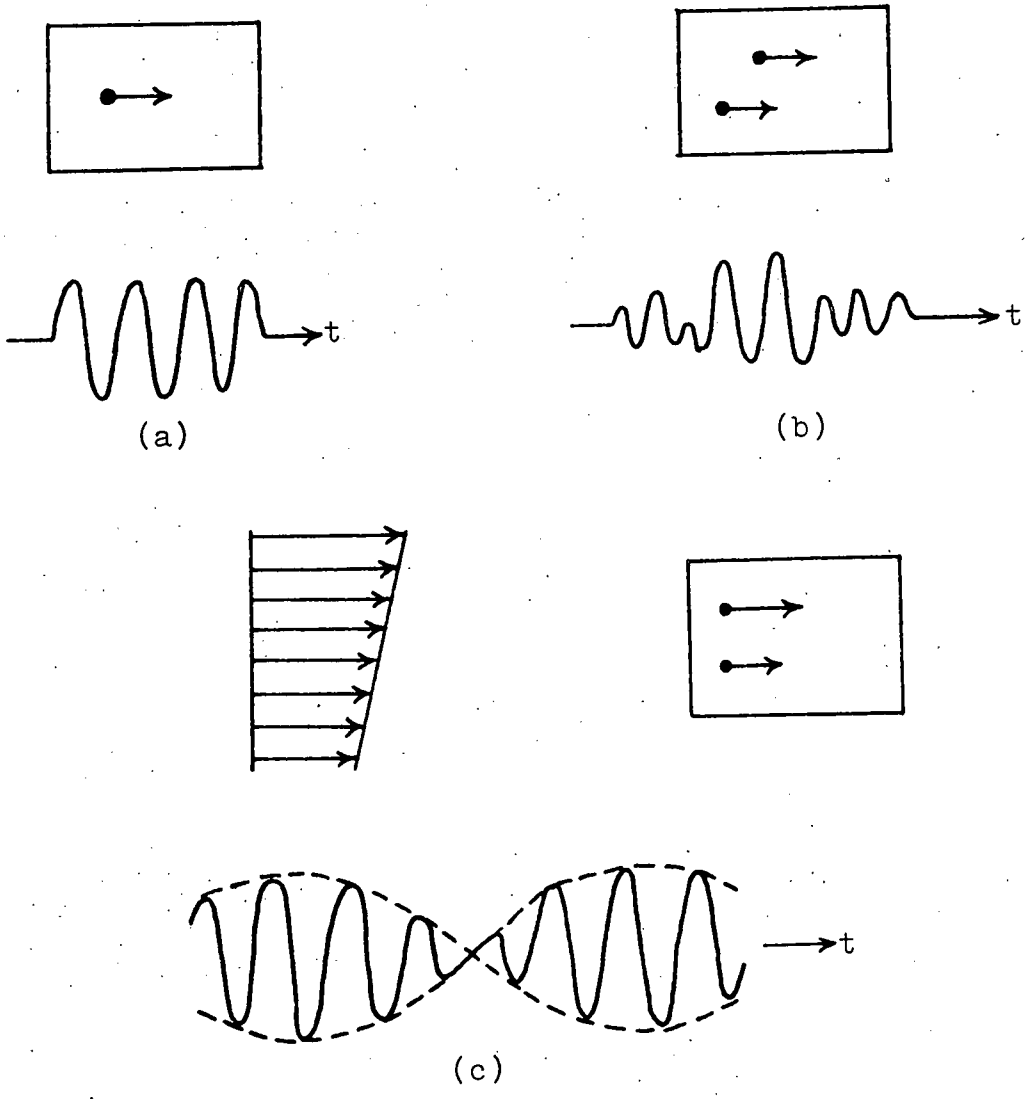

Fig. D.5 a) Signal generated by passage of single particle in steady, uniform flow

b) Signal generated by two particles which entered the flow at different times

c) Signal generated by two particles having different velocities

APPENDIX E
DATA REDUCTION

1. Average Velocities, Root Mean Square Velocities, and Reynolds Stresses

From Eq. D.1 in Appendix D, the Doppler (or frequency) shift is

$$f_D = \frac{1}{\lambda} \underline{U} \cdot (\hat{K}_i - \hat{K}_s)$$

It can be shown that when two intersecting beams are used, this vector equation can be rewritten as

$$U = \frac{f_D \lambda}{2 \sin \theta} \qquad (E.1)$$

where U = the component of local flow velocity which is normal to the bisector of the beam intersection angle,

θ = the half angle of the beam intersection,

λ = the wavelength of laser light.

In this experiment, $\lambda = 5145 \times 10^{-10}$ m, and $\theta = 4.047^\circ$, hence, U (m/sec) $= 3.645 \times 10^{-3} f_D$ (KHz).

1.1 Average Velocity

Since analog output of the tracker is linearly proportional to the Doppler frequency in the range selected, and since 10 Volts corresponds to the maximum frequency, f_{MAX}, in that range, the average velocity can be expressed as

$$U\ (m/sec) = 3.645 \times 10^{-3} \times \left[\frac{V_x - V_{shift}}{10}\right] \times f_{MAX}\ (KHz)$$

$$= 3.645 \times 10^{-4} \times (V_x - V_{shift}) \times f_{MAX}\ (KHz) \quad (E.2)$$

where V_x = the average analog voltage reading in the digital voltmeter,

V_{shift} = the voltage corresponding to the shifted frequency.

1.2 Root Mean Square Velocity

From Eq. 2, the rms velocity is simply

$$\sqrt{\overline{U'^2}}(m/sec) \equiv \sqrt{\frac{1}{T}\int_o^T U'^2 dt} = 3.645 \times 10^{-4} \times f_{MAX}(KHz) \times \sqrt{\overline{V'^2}}$$

1.3 Reynolds Stress

The velocity cross-correlation can be expressed as

$$\overline{U'_x U'_y}(m^2/sec^2) = [(3.645 \times 10^{-4}) \times f_{xMAX} \times V'_x]\ [(3.645 \times 10^{-4}) \times f_{yMAX} \times V'_y] = 1.329 \times 10^{-7} \times f_{xMAX} \times f_{yMAX} \times \overline{V'_x V'_y}$$

where subscripts x and y stand for velocity components in the x and y directions respectively.

The Reynolds stress is given simply as $-\rho\overline{U'_x U'_y}$.

2. Reynolds Numbers

The Reynolds number of the test cell is based on the inlet geometry and average inlet velocity.

2.1 FFTF Geometry

Flow Rate (GPM) = Area (m^2) x U_{INLET}(m/sec) x

.01585 x 10^6 (GPM/m^3sec)

= 46.02 x U_{INLET}(m/sec)

or U_{INLET}(m/sec) = .02173 x Flow Rate (GPM)

The Reynolds number is defined as

$$Re \equiv \frac{\rho U_{INLET} D_e}{\mu}$$

where D_e, hydraulic diameter, is defined with respect to inlet duct width.

At 110°F, Re = 1909 x Flow Rate (GPM)

2.2 CRBR Geometry

Similarly, U_{INLET} and Re in the CRBR geometry are

U_{INLET}(m/sec) = 0.01087 x Flow Rate (GPM)

At 110°F, Re = 1248 x Flow Rate (GPM)

APPENDIX F
ERROR ANALYSIS

The purpose of this appendix is to estimate the errors in the velocities, root mean square velocities, turbulent kinetic energies, and double velocity correlations from the uncertainties in the LDA measurement technique and the accuracy of the instrument.

1. General Principle

Since the errors come from many sources, the method of compounding errors suggested by Wilson[28] was used here.

Suppose that the final result, y, is related to the components, Xi, by the relation

$$Y = F(X_1, X_2, \ldots X_n)$$

where F is a known functional form. The small variation in X_i will alter y by the amount

$$dy = \frac{\partial F}{\partial X_1} dX_1 + \frac{\partial F}{\partial X_2} dX_2 + \ldots + \frac{\partial F}{\partial X_n} dX_n$$

$$= \sum_{i=1}^{n} \frac{\partial F}{\partial X_i} dX_i$$

The square of the error will be

$$(dy)^2 = \sum_{i,j} \frac{\partial F}{\partial X_i} \frac{\partial F}{\partial X_j} dX_i \, dX_j$$

If the components dX_1, dX_2,..., dX_n are independently distributed and symmetrical with respect to positive and negative values, then the products, $dX_i \, dX_j$ $(i \neq j)$, will vanish on the average so that

$$(dy)^2 = \sum_{i=1}^{n} \left(\frac{\partial F}{\partial X_i}\right)^2 (dX_i)^2$$

This may also be written in terms of the variance, σ, as

$$\sigma^2 = \sum_{i=1}^{n} \left(\frac{\partial F}{\partial X_i}\right)^2 \sigma_i^2 \qquad (F.1)$$

2. Calculation of the Error in Velocity

The velocity is calculated by the expression

$$V = \frac{f\,\lambda}{2\sin\theta} \qquad (F.2)$$

where f = the Doppler shift

λ = the wavelength of laser light

θ = the half angle of the beam intersection

Hence, there are three quantities, f, λ, and θ which will make a contribution to the errors. The error in λ is negligibly small. The errors associated with f and θ are discussed below.

2.1 Error due to the Uncertainty in θ

The uncertainty in θ comes from the following sources:

1. the beam separation distance
2. the focal length of the optical lens

Factor one, the accuracy of the beam separation distance was judged to be 1% which results in a 1% error in θ.
Factor two, the error in the focal length of the optical lens was judged to be very small.

In Eq. F.2, differentiate V with respect to θ:

$$\frac{\partial V}{\partial \theta} = -f \lambda \cos\theta / 2\sin^2\theta \qquad (F.3)$$

From Eq. F.1, the error (normalized by the velocity) is

$$\frac{1}{V^2} \left(\frac{\partial V}{\partial \theta}\right)^2 (\Delta\theta)^2 = \left(\frac{\Delta\theta}{\tan\theta}\right)^2$$

$$\simeq \left(\frac{\Delta\theta}{\theta}\right)^2 \qquad (F.4)$$

where $\tan\theta \simeq \theta$ ($\theta = 4.047°$ in this experiment)

2.2 Error Due to the Uncertainty in f

The uncertainty in the frequency comes from the following sources:

1. the accuracy of the frequency tracker
2. the accuracy of the digital voltmeter
3. the accuracy of the frequency shifter
4. signal broadening
5. phase fluctuations
6. velocity biasing

Factor one, the overall accuracy of the tracker as specified by the manufacturer is 1% of the full scale deflection. For this experiment, the measured frequency was close to 40% of the full scale reading, hence the accuracy is 2.5%.
Factor two, the accuracy of the digital voltmeter is 0.1%. It is small compared to other errors, and thus will be neglected in the calculation.

For factor three, the manufacturers do not specify the accuracy of their frequency shifter. It involves both frequency upshifting and downshifting,and errors might occur during these processes. A 1% error is assigned for this factor.

Factor four, signal broadening, is discussed in Appendix D. Since the average frequency (or voltage) was obtained by taking the time average of the Doppler signal, the values should be very accurate and not be affected by broadening.

Factors five and six, phase fluctuations and velocity biasing, are also discussed in Appendix D. These errors depend on the particular setup of the experiment, e.g., the concentration of the scattering particles; only very delicate experiments can determine the magnitude of this error. But these two factors were judged to have small contribution, and a 1% total error is assigned to these factors.

In Eq. F.2, differentiate V with respect to f:

$$\frac{\partial V}{\partial f} = \frac{\lambda}{2 \sin \theta} \qquad (F.5)$$

Hence the error is

$$\sum_i \frac{1}{V^2} \left(\frac{\partial V}{\partial f_i}\right)^2 (\Delta f_i)^2 = \sum_i \left(\frac{\Delta f_i}{f}\right)^2 \qquad (F.6)$$

where i = all six factors discussed above.

2.3 Other Errors

In the above sections, only errors associated with Eq. F.2 were discussed. The other possible errors are listed here:

1. Position errors, i.e., the measuring points are not exactly the desired positions. In this experiment the test section is relatively large compared to the measuring volume, hence this error is judged to be neglibly small.
2. Erros in the measurement angle, i.e., the laser beam is not perpendicular to the test section, so that the measured velocity component is not the correct one. A 1% error in velocity is assigned to this factor.

2.4 Sample Calculation for the Error in the Velocity

The total error for the velocity measurement can be calculated by combining Eqs. F.1, F.4, F.5 and other errors from the previous sections:

$$\left(\frac{\Delta V}{V}\right)^2 = \left(\frac{\Delta\theta}{\theta}\right)^2 + \sum_i \left(\frac{\Delta f_i}{f}\right)^2 + \left(\frac{\Delta Vo}{V}\right)^2$$

$$= (.01)^2 + (.025)^2 + (.01)^2 + (.01)^2 + (.01)^2$$

$$= 0.001025$$

$$\frac{\Delta V}{V} = 3.2\%$$

Hence, the error in the velocity measurement is 3.2%.

3. Calculation of the Error in the Root Mean Square Velocity

The root mean square velocity is calculated by an expression similar to that for the velccity:

$$V_{rms} = \frac{f_{rms}\lambda}{2\sin\theta} \qquad (F.7)$$

where f_{rms} is the fluctuating component of the Doppler frequency. The errors in V_{rms} are also from f_{rms} and θ.

3.1 Error due to the Uncertainty in θ

Since the source of the error is the same as that for the velocity, we can use Eq. F.4 for V_{rms}:

$$\frac{1}{V_{rms}^2}\left(\frac{\partial Vrms}{\partial \theta}\right)(\Delta\theta)^2 \approx \left(\frac{\Delta\theta}{\theta}\right)^2 \qquad (F.8)$$

3.2 Error due to the Uncertainty in f_{rms}

The uncertainty comes from the following sources:

1. The accuracy of the frequency tracker
2. The Accuracy of the RMS voltmeter
3. Signal broadening
4. Phase fluctuations

Factor one is discussed in section 2.2. The accuracy is 2.5%.

Factor two, the accuracy of the RMS voltmeter, is specified by the manufacturer to be 2%, for frequencies below 10 KHz which is the upper bound for water flows.

Factor three, signal broadening is, no longer small. Since it is difficult to separate it from the much larger broadening due to the turbulent fluctuations, an error of 1% is assigned to this factor.

Factor four, phase fluctuations, is also very difficult to determine. An error of 1% is assigned to this factor.

Hence, the total error is

$$\sum_i \frac{1}{V_{rms}^2} \left(\frac{\partial V_{rms}}{\partial f_{rms,i}}\right)^2 (\Delta f_{rms,i}) = \sum_i \left(\frac{\Delta f_{rms,i}}{f_{rms}}\right)^2 \qquad (F.9)$$

3.3 Sample Calculation for the Error in the Root Mean Square Velocity

The total error is calculated by combining Eqs. F.8 and F.9:

$$\left(\frac{\Delta V_{rms}}{V_{rms}}\right)^2 = \left(\frac{\Delta\theta}{\theta}\right)^2 + \sum_i \left(\frac{\Delta frms,i}{frms}\right)^2$$

$$= (.01)^2 + (.025)^2 + (.02)^2 + (.01)^2 + (.01)^2$$

$$= 0.001325$$

$$\frac{\Delta V_{rms}}{V_{rms}} = 3.6\%$$

Hence, the error in the root mean square velocity measurement is 3.6%.

4. Calculation of the Error in the Turbulent Kinetic Energy

The turbulent kinetic energy, K, is calculated with the expression

$$K = \frac{1}{2}\left(U_{rms}^2 + V_{rms}^2\right) \qquad (F.10)$$

where U_{rms} and V_{rms} are the root mean square values of the velocity components U and V respectively.

The error comes from the following two sources:

1. Eq. F.10 should include all three velocity fluctuation components, i.e., $K \equiv \frac{1}{2}\left(U_{rms}^2 + V_{rms}^2 + W_{rms}^2\right)$.

Since no measurement was made of W_{rms}, and since W_{rms} was not in the main flow direction, the neglect of this term was judged to have approximately 5% error.

2. Accuracy of U_{rms} and V_{rms}. From Section 3.3, these were determined to be 3.6%. In Eq. F.10, differentiate K with respect to U_{rms} and V_{rms},

$$\frac{\partial K}{\partial U_{rms}} = U_{rms}, \quad \frac{\partial K}{\partial V_{rms}} = V_{rms}$$

Hence, the error (normalized by the turbulent kinetic energy) is

$$\frac{1}{K^2}\left[\left(\frac{\partial K}{\partial U_{rms}}\right)^2 (\Delta U_{rms})^2 + \left(\frac{\partial K}{\partial V_{rms}}\right)^2 (\Delta V_{rms})^2\right]$$

$$= \frac{1}{K^2}\left[(U_{rms})^2 (\Delta U_{rms})^2 + (V_{rms})^2 (\Delta V_{rms})^2\right]$$

$$= 4\left[\frac{(U_{rms})^2(\Delta U_{rms})^2 + (V_{rms})(\Delta V_{rms})^2}{(U_{rms}{}^2 + V_{rms}{}^2)}\right]$$

$$\approx \left(\frac{\Delta U_{rms}}{U_{rms}}\right)^2 + \left(\frac{\Delta V_{rms}}{V_{rms}}\right)^2 \quad \text{if } U_{rms} \approx V_{rms}$$

In this measurement, U_{rms} was very close to V_{rms}, so U_{rms} is assumed to be approximately equal to V_{rms} to simplify the analysis.

The total error in turbulent kinetic energy is the sum of parts one and two above:

$$\left(\frac{\Delta K}{K}\right)^2 = (.036)^2 + (.036)^2 + (.05)^2$$

$= 0.005092$

$\frac{\Delta K}{K} = 7.1\%$

Hence, the error in the turbulent kinetic energy is 7.1%.

5. Calculation of the Error in the Velocity Correlation

The velocity correlation is represented by $\overline{U'V'}$. The error comes from the following four sources:

1. Errors in U' and V'
2. The accuracy of the turbulence processor
3. The accuracy of the digital voltmeter
4. Errors in visual reading

In the first factor, since the errors associated with U' and V' are not expected to be correlated, they will not make a contribution to the error in the velocity correlation measurement. Factor two, the accuracy of the turbulence processor which does the multiplication, is specified by the manufacturer as 2% $\pm$ 10 mV. Since a constant calibration was used, the possible $\pm$ 10 mV electronic drift error was eliminated. Factor three, the accuracy of the digital voltmeter, is negligibly small.

Factor four, the visual reading error, is common to visually recorded data if the reading is not a constant. Although an integrating circuit with a 30 second time constant was used, the reading of the digital voltmeter was still not a constant. For the experiments, a visual averaging method was used. Since

the fluctuation was typically 20%, this value is assumed to be the error.

Hence, the total error in the velocity correlation measurement is 20%.

APPENDIX G
TABULATION OF DATA

The reduced data from the experiments is presented in Tables G.1. through G.4. The measurement locations are shown in Figs. G.1 and G.2 for the FFTF and CRBR geometries, respectively.

Table G.1

FFTF Geometry, Re=70,000, Normal
Inlet Mean Flow Distribution

Location (I,J)	U (m/sec)	V (m/sec)	Urms (m/sec)	Vrms (m/sec)	$\overline{U'V'}$ ($10^{-3}m^2/sec^2$)	K (m^2/sec^2)
24,2	.867	.121	.371	.260	1.97	.103
24,4	.778	.441	.336	.250	2.62	0.878
24,6	.619	.608	.311	.250	4.59	.0798
24,8	.442	.675	.297	.250	4.26	.0755
24,10	.265	.645	.283	.250	2.29	.0714
24,12	.149	.543	.255	.232	2.62	0.593
24,14	-.0177	.380	.255	.213	2.62	.0552
24,16	-.276	.256	.234	.195	~0	.0462
22,2	1.079	.0519	.347	.269	1.50	.0962
22,4	.920	.321	.340	.269	7.015	.0938
22,6	.584	.497	.329	.260	5.05	.0878
22,8	.407	.571	.297	.260	6.36	.0778
22,10	.177	.552	.276	.297	7.015	.0821
22,12	0	.404	.265	.287	5.05	.0765
22,14	-.195	.219	.265	.250	7.015	.0665
22,16	-.499	.0797	.237	.195	4.39	.0470
20,2	1.150	.0575	.407	.297	1.50	.127
20,4	.849	.256	.371	.287	11.305	.110
20,6	.478	.358	.318	.269	8.065	.0868
20,8	.159	.441	.276	.250	3.47	.0694
20,10	0	.423	.255	.297	5.12	.0764
20,12	-.092	.219	.276	.306	4.13	.0849
20,14	-.294	.108	.297	.250	6.10	.0755

Location (I,J)	U (m/sec)	V (m/sec)	Urms (m/sec)	Vrms (m/sec)	$\overline{U'V'}$ ($10^{-3}m^2/sec^2$)	K (m^2/sec^2)
20,16	-.672	.0056	.230	.204	4.07	.0472
18,2	1.274	.0519	.407	.352	-2.29	.145
18,4	.849	.163	.347	.297	21.30	.104
18,6	.478	.219	.290	.241	10.80	.0711
18,8	.159	.284	.255	.185	2.29	.0496
18,10	-.127	.311	.248	.195	2.62	.0496
18,12	-.389	.284	.230	.232	2.95	.0533
18,14	-.548	.163	.219	.232	5.57	.0509
18,16	-.718	.0148	.205	.185	4.855	.0382
16,2	1.486	.063	.478	.408	-5.57	.197
16,4	1.150	.108	.425	.362	36.44	.155
16,6	.563	.0871	.301	.232	13.42	.0721
16,8	.251	.117	.234	.148	1.97	.0383
16,10	-.088	.163	.216	.152	2.29	.0348
16,12	-.421	.191	.234	.213	4.916	.050
16,14	-.619	.108	.248	.241	4.916	.0597
16,16	-.814	.020	.198	.204	4.916	.0404
14,2	1.698	-.022	.601	.510	46.53	.311
14,4	.938	-.0315	.425	.352	47.14	.152
14,6	.478	-.022	.255	.195	4.068	.0514
14,8	.156	.033	.212	.137	1.44	.0319
14,10	-.177	.0612	.212	.148	2.816	.0335
14,12	-.538	.0630	.226	.195	5.25	.0446
14,14	-.796	.0389	.212	.232	5.12	.0494
14,16	-.945	-.0185	.205	.213	4.20	.0438

Location (I,J)	U (m/sec)	V (m/sec)	Urms (m/sec)	Vrms (m/sec)	$\overline{U'V'}$ ($10^{-3}m^2/sec^2$)	K (m^2/sec^2)
12,2	1.840	.0148	.708	.575	63.79	.416
12,4	.938	-.0408	.495	.426	61.17	.214
12,6	.442	-.106	.248	.195	5.77	.0496
12,8	.230	-.050	.216	.139	2.816	.0330
12,10	-.106	.0056	.219	.148	2.03	.0351
12,12	-.393	.0148	.290	.176	2.685	.0576
12,14	-.637	.0241	.318	.204	2.49	.0715
12,16	-.828	.0148	.354	.185	6.097	.0798
10,2	1.886	-.022	.814	.575	80.35	.496
10,4	.870	-.124	.566	.436	67.225	.255
10,6	.386	-.208	.251	.185	3.28	.0487
10,8	.287	-.191	.248	.158	3.60	.0431
10,10	-.0354	-.128	.202	.139	.979	.030
10,12	-.333	-.0723	.269	.163	3.28	.0495
10,14	-.686	-.020	.297	.176	6.23	.0597
10,16	-.899	-.0185	.304	.158	5.31	.0587
8,6	.357	-.208	.241	.213	6.75	.0517
8,8	.198	-.282	.234	.195	4.78	.0462
8,10	-.0318	-.226	.241	.152	2.624	.0405
8,12	-.315	-.152	.262	.158	3.28	.0467
8,14	-.616	-.0093	.333	.148	6.88	.0663
8,16	-.934	.089	.283	.195	7.87	.0590
7,16	-.899	.256	.283	.185	9.51	.0572
7.5,2	1.843	.024	.885	.649	91.15	.602
7.5,3	1.153	.0742	.814	.593	110.225	.507

Location (I,J)	U (m/sec)	V (m/sec)	Urms (m/sec)	Vrms (m/sec)	$\overline{U'V'}$ ($10^{-3}m^2/sec^2$)	K (m^2/sec^2)
7.5,4	.552	.0519	.637	.473	62.28	.315
6,6	.265	-.059	.230	.195	5.70	.0454
6,8	.0637	-.208	.230	.232	5.05	.0533
6,10	-.120	-.245	.248	.195	3.866	.0496
6,12	-.287	-.152	.265	.176	3.08	.0507
6,14	-.492	.0742	.283	.158	5.38	.0525
6,16	-.757	.515	.290	.152	12.07	.0536
6,17	-1.005	1.029	.290	.222	13.24	.0668
5,6	.237	-.0686	.244	.195	4.916	.0487
5,8	.0142	-.226	.241	.222	4.72	.0537
5,10	-.191	-.245	.244	.213	3.866	.0525
5,12	-.350	-.182	.248	.176	2.89	.0462
5,14	-.531	.0538	.276	.204	4.72	.0589
5,16	-.563	.515	.297	.167	5.097	.0581
5,17	-.350	.921	.311	.156	4.72	.0609

Table G.2
FFTF Geometry, Re=70,000, Distorted
Inlet Mean Flow Distribution

Location (I,J)	U (m/sec)	V (m/sec)	Urms (m/sec)	Vrms (m/sec)	$\overline{U'V'}$ ($10^{-3}m^2/sec^2$)	K (m^2/sec^2)
24,2	.338	.166	.338	.234	-.642	.0847
24,4	.374	.285	.338	.261	-1.28	.0914
24,6	.417	.388	.338	.270	∿0	.0938
24,8	.313	.406	.303	.270	∿0	.0824
24,10	.182	.388	.249	.252	-.642	.0629
24,12	.0784	.315	.214	.207	-1.284	.0443
24,14	-.0712	.216	.214	.198	-.963	.0425
24,16	-.267	.142	.232	.207	-2.25	.0483
22,2	.474	.099	.356	.2-8	-.642	.105
22,4	.552	.189	.374	.306	-2.89	.117
22,6	.509	.279	.374	.315	3.85	.120
22,8	.313	.207	.321	.288	7.06	.0930
22,10	.153	.0991	.267	.243	2.57	.0653
22,12	.0534	.0631	.249	.216	∿0	.0545
22,14	-.157	.009	.249	.189	2.57	.0490
22,16	-.470	-.0451	.232	.189	-.321	.0447
20,2	.417	.153	.356	.306	-5.78	.110
20,4	.509	.225	.392	.288	-3.85	.118
20,6	.410	.279	.356	.306	7.06	.110
20,8	.267	.180	.321	.306	9.63	.0983
20,10	.0997	.00901	.267	.234	4.62	.0631
20,12	-.00356	-.0487	.249	.216	2.57	.0545
20,14	-.178	-.0901	.249	.180	4.49	.0473

Location (I,J)	U (m/sec)	V (m/sec)	Urms (m/sec)	Vrms (m/sec)	$\overline{U'V'}$ ($10^{-3}m^2/sec^2$)	K (m^2/sec^2)
20,16	-.552	-.114	.249	.180	3.21	.0473
18,2	.994	.0519	.313	.216	2.56	.0723
18,4	.920	.200	.313	.225	7.96	.0743
18,6	.520	.274	.285	.207	8.99	.0620
18,8	.180	.311	.274	.234	2.25	.0649
18,10	-.0991	.330	.256	.225	3.31	.0581
18,12	-.230	.219	.256	.252	2.25	.0645
18,14	-.357	.108	.253	.234	4.49	.0594
18,16	-.559	.0426	.278	.216	5.46	.0620
16,2	.463	.00901	.338	.216	-5.136	.0806
16,4	.883	.157	.374	.252	.642	.102
16,6	.399	.189	.285	.216	3.85	.0640
16,8	.107	.256	.285	.189	1.926	.0585
16,10	-.142	.225	.285	.198	+5.136	.0603
16,12	-.274	.115	.249	.216	2.57	.0545
16,14	-.484	.117	.214	.162	2.57	.0360
16,16	-.627	.027	.214	.144	2.57	.0332
14,2	.695	-.112	.303	.234	-7.70	.0733
14,4	.873	.00901	.356	.252	14.765	.0953
14,6	.274	.0252	.232	.180	2.57	.0430
14,8	.142	.0631	.249	.126	1.60	.0390
14,10	-.125	.0991	.267	.180	2.89	.0519
14,12	-.317	.110	.249	.180	2.57	.0473
14,14	-.463	.0451	.249	.162	3.85	.0442
14,16	-.673	.00901	.196	.135	2.57	.0283

Location (I,J)	U (m/sec)	V (m/sec)	Urms (m/sec)	Vrms (m/sec)	$\overline{U'V'}$ ($10^{-3}m^2/sec^2$)	K (m^2/sec^2)
12,2	.623	-.0775	.321	.261	-1.80	.0855
12,4	.816	-.0379	.338	.252	1.41	.0891
12,6	.232	.00901	.214	.153	.770	.0346
12,8	.0677	.0649	.232	.144	1.80	.0372
12,10	-.232	.0991	.249	.162	2.89	.0442
12,12	-.346	.123	.232	.216	2.50	.0502
12,14	-.452	.0469	.232	.189	5.39	.0447
12,16	-.655	.0180	.214	.144	3.852	.0332
10,2	.516	-.0631	.303	.261	2.696	.0800
10,4	.873	-.0811	.392	.270	4.30	.113
10,6	.256	.0108	.214	.117	1.03	.0297
10,8	.0606	.0306	.232	.126	1.156	.0348
10,10	-.128	.0811	.232	.153	2.05	.0385
10,12	-.331	.0901	.249	.153	2.25	.0428
10,14	-.484	.0847	.249	.162	3.40	.0442
10,16	-.695	.0775	.249	.135	2.12	.0402
8,6	.235	.00901	.232	.144	1.93	.0372
8,8	.125	-.0270	.249	.171	1.54	.0457
8,10	-.0499	-.00361	.249	.171	.578	.0457
8,12	-.232	.0451	.249	.171	2.50	.0457
8,14	-.484	.126	.232	.126	4.75	.0348
8,16	-.787	.186	.232	.144	2.89	.0372
7.5,2	.374	-.0559	.338	.234	7.70	.0847
7.5,3	.563	-.0811	.374	.270	-16.05	.106
7.5,4	.976	-.0631	.410	.261	-23.75	.118

Location (I,J)	U (m/sec)	V (m/sec)	Urms (m/sec)	Vrms (m/sec)	$\overline{U'V'}$ ($10^{-3}m^2/sec^2$)	K (m^2/sec^2)
6,6	.271	.0451	.232	.135	1.22	.0359
6,8	.0784	0	.232	.171	1.86	.0415
6,10	-.0891	-.0631	.249	.171	.3852	.0457
6,12	-.196	-.0451	.267	.162	1.28	.0488
6,14	-.346	.108	.249	.144	2.89	.0415
6,16	-.591	.496	.249	.162	6.42	.0442
6,17	-.784	1.009	.232	.180	4.17	.0430
5,6	.178	.0108	.214	.180	.706	.0391
5,8	.0178	.00901	.214	.189	.770	.0407
5,10	-.142	-.00901	.232	.180	1.48	.0430
5,12	-.249	-.0451	.249	.189	1.80	.0490
5,14	-.356	.115	.249	.198	2.44	.0507
5,16	-.367	.487	.338	.216	2.82	.0806
5,17	-.153	.856	.338	.279	.770	.0963

Table G.3
CRBR Geometry, Re=35,000, Normal Inlet Mean Flow Distribution

Location (I,J)	U (m/sec)	V (m/sec)	Urms (m/sec)	Vrms (m/sec)	$\overline{U'V'}$ ($10^{-3}m^2/sec^2$)	K (m^2/sec^2)
19,2	.478	.0315	.336	.121	-1.18	.0637
19,4	.363	.528	.292	.380	-1.51	.115
19,6	.292	.575	.274	.454	-1.51	.141
19,8	.150	.324	.221	.426	-2.165	.115
19,10	.0265	.445	.195	.389	-5.45	.0947
19,12	-.221	.389	.168	.315	-4.79	.0638
18,2	.858	.0093	.425	.015	+.131	.090
18,4	.699	.0519	.354	.148	+.459	.0736
18,6	.433	.139	.292	.278	+1.44	.0813
18,8	.195	.260	.221	.306	+2.92	.0712
18,10	-.044	.241	.186	.287	+3.41	.0585
18,12	-.380	.158	.177	.260	+1.77	.0493
16,2	1.053	.046	.442	.232	+1.676	.125
16,4	.752	.204	.389	.352	+11.18	.138
16,6	.380	.204	.301	.343	+12.83	.104
16,8	.265	.167	.230	.334	+9.55	.0821
16,10	-.310	.074	.195	.297	+9.216	.0629
16,12	-.681	-.074	.186	.306	+8.24	.0640
14,2	.999	.0556	.495	.464	+17.06	.230
14,4	.716	.167	.425	.426	+22.00	.181
14,6	.186	.185	.301	.371	+15.44	.114
14,8	-.0973	.111	.212	.334	+9.185	.0782
14,10	-.433	-.0093	.203	.297	+11.15	.0647
14,12	-.840	-.093	.195	.269	+9.185	.0551
12,2	1.229	.0371	.531	.519	+28.68	.276

Location (I,J)	U (m/sec)	V (m/sec)	Urms (m/sec)	Vrms (m/sec)	$\overline{U'V'}$ ($10^{-3}m^2/sec^2$)	K (m^2/sec^2)
12,4	.663	.111	.433	.454	+36.55	.197
12,6	.0973	.0185	.283	.352	+19.81	.102
12,9	-.416	-.037	.195	.278	+ 9.65	.0576
12,11	-.734	-.074	.212	.260	+11.62	.0562
12,13	-.911	-.037	.195	.156	+ 4.72	.0311
10.5,2	1.336	.0927	.619	.556	+30.79	.346
10.5,3	.964	.130	.584	.519	+42.90	.305
10.5,4	.646	.148	.460	.556	+45.22	.260
10.5,5	.310	.0927	.354	.445	+40.97	.162
10.5,6	.0265	0	.248	.408	+27.15	.114
10,9	-.363	-.0371	.186	.222	+ 5.06	.0420
10,11	-.681	-.00927	.195	.297	+ 7.84	.0629
10,13	-.858	0	.177	.167	+ 2.59	.0296
8,9	-.301	.0185	.186	.222	+ 6.20	.0420
8,11	-.681	.0556	.195	.222	+ 8.166	.0437
8,12	-.840	.0927	.173	.222	+ 5.976	.0398
8,13	-.946	.0556	.159	.167	+ 3.48	.0266
7,12	-.770	.260	.212	.250	+10.80	.0539
7,13	-1.123	.371	.248	.241	+ 5.22	.0597
6,9	-.133	.0556	.195	.315	+ 5.45	.0686
6,11	-.433	.260	.248	.260	+ 8.40	.0644
6,12	-.504	.501	.248	.260	+ 7.74	.0644
6,13	-.310	1.010	.265	.241	+ 5.12	.0643
5,12	-.292	.334	.265	.315	- 1.78	.0849
5,13	-.239	.185	.230	.297	- 4.72	.0704

Location (I,J)	U (m/sec)	V (m/sec)	Urms (m/sec)	Vrms (m/sec)	$\overline{U'V'}$ ($10^{-3}m^2/sec^2$)	K (m^2/sec^2)
4,9	.115	.0742	.142	.241	+ 1.84	.0391
4,11	-.150	.111	.212	.241	- 1.12	.0516

Table G.4

CRBR Geometry, Re=35,000, Distorted Inlet Mean Flow Distribution

Location (I,J)	U (m/sec)	V (m/sec)	Urms (m/sec)	Vrms (m/sec)	$\overline{U'V'}$ ($10^{-3}m^2/sec^2$)	K (m^2/sec^2)
19,2	.255	-.046	.265	.241	.919	.0643
19,4	.251	.161	.248	.250	+1.24	.0620
19,6	.234	.297	.248	.297	-.722	.0747
19,8	.163	.399	.212	.297	-2.03	.0665
19,10	.0743	.399	.195	.315	-2.03	.0686
19,12	-.156	.269	.177	.241	-3.67	.0445
18,12	.340	.0093	.336	.352	+2.23	.119
18,4	.357	.083	.318	.315	+.262	.100
18,6	.340	.195	.283	.315	+1.24	.0897
18,8	.225	.139	.248	.241	+2.23	.0597
18,10	.0566	.139	.195	.204	+4.855	.0397
18,12	-.333	.0278	.186	.185	+6.82	.0344
16,2	.375	-.0278	.318	.352	+5.64	.113
16,4	.340	-.0278	.318	.352	+1.37	.113
16,6	.340	-.0278	.318	.334	-.262	.106
16,8	.216	.0093	.301	.324	+5.64	.0979
16,10	-.0495	-.0278	.230	.315	9.246	.0761
16,12	-.280	-.0742	.230	.204	5.15	.0472
14,2	.251	-.0278	.265	.111	.656	.0414
14,4	.198	-.121	.283	.334	-.328	.0957
14,6	.287	-.0927	.318	.371	-4.59	.119
14,8	.198	-.0093	.283	.278	10.50	.0787
14,10	-.191	-.0649	.248	.278	10.50	.0693

Location (I,J)	U (m/sec)	V (m/sec)	Urms (m/sec)	Vrms (m/sec)	$\overline{U'V'}$ ($10^{-3}m^2/sec^2$)	K (m^2/sec^2)
14,12	-.563	-.121	.230	.222	10.19	.0512
12,2	.340	0	.354	.352	1.94	.125
12,4	.322	-.0649	.336	.315	2.59	.106
12,6	.340	-.102	.301	.297	-2.00	.0892
12,9	-.209	-.083	.212	.222	8.50	.0473
12,11	-.545	-.139	.230	.204	12.415	.0472
12,13	-.846	-.083	.212	.185	4.39	.0397
10.5,2	.163	0	.371	.334	3.94	.125
10.5,3	.172	0	.354	.352	3.12	.125
10.5,4	.163	-.0278	.336	.352	1.635	.119
10.5,5	.198	-.0556	.354	.371	-4.26	.131
10.5,6	.340	-.0278	.336	.352	-8.20	.119
10.5,7	.534	-.0278	.336	.241	-6.56	.0855
10,9	-.315	-.121	.195	.185	6.56	.0361
10,11	-.580	-.083	.230	.241	9.185	.0555
10,13	-.775	-.0556	.212	.148	3.94	.0335
8,9	-.315	-.0742	.195	.167	4.59	.0329
8,11	-.580	-.020	.195	.185	7.87	.0361
8,12	-.722	.00927	.195	.185	9.185	.0361
8,13	-.846	0	.212	.185	5.25	.0397
7,12	-.704	.232	.212	.185	11.51	.0397
7,13	-1.04	.334	.212	.167	7.87	.0365
7,9	-.315	-.0185	.195	.185	5.57	.0361
7,11	-.527	.0927	.212	.222	9.51	.0473
6,9	-.191	.0464	.195	.204	3.15	.0397

Location (I,J)	U (m/sec)	V (m/sec)	Urms (m/sec)	Vrms (m/sec)	$\overline{U'V'}$ ($10^{-3}m^2/sec^2$)	K (m^2/sec^2)
6,11	-.386	.213	.212	.222	7.25	.0473
6,12	.421	.399	.248	.222	7.90	.0554
6,13	-.191	.881	.301	.260	5.935	.0789
5,12	-.191	.250	.212	.204	-2.26	.0433
5,13	-.156	.145	.230	.222	-.391	.0512
4,9	.0566	.0093	.133	.111	.525	.0150
4,11	-.129	.0834	.177	.241	.360	.0447

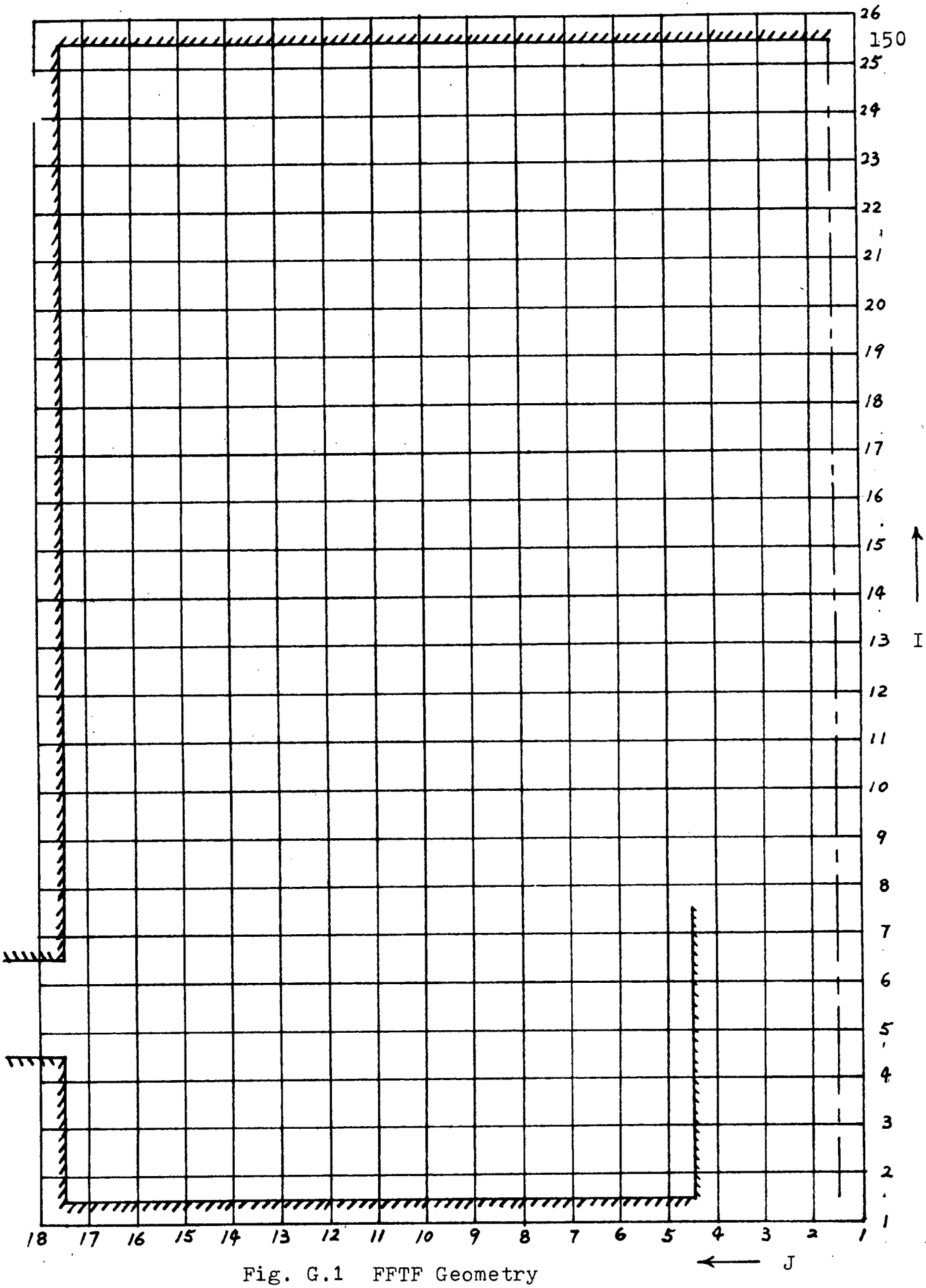

Fig. G.1 FFTF Geometry

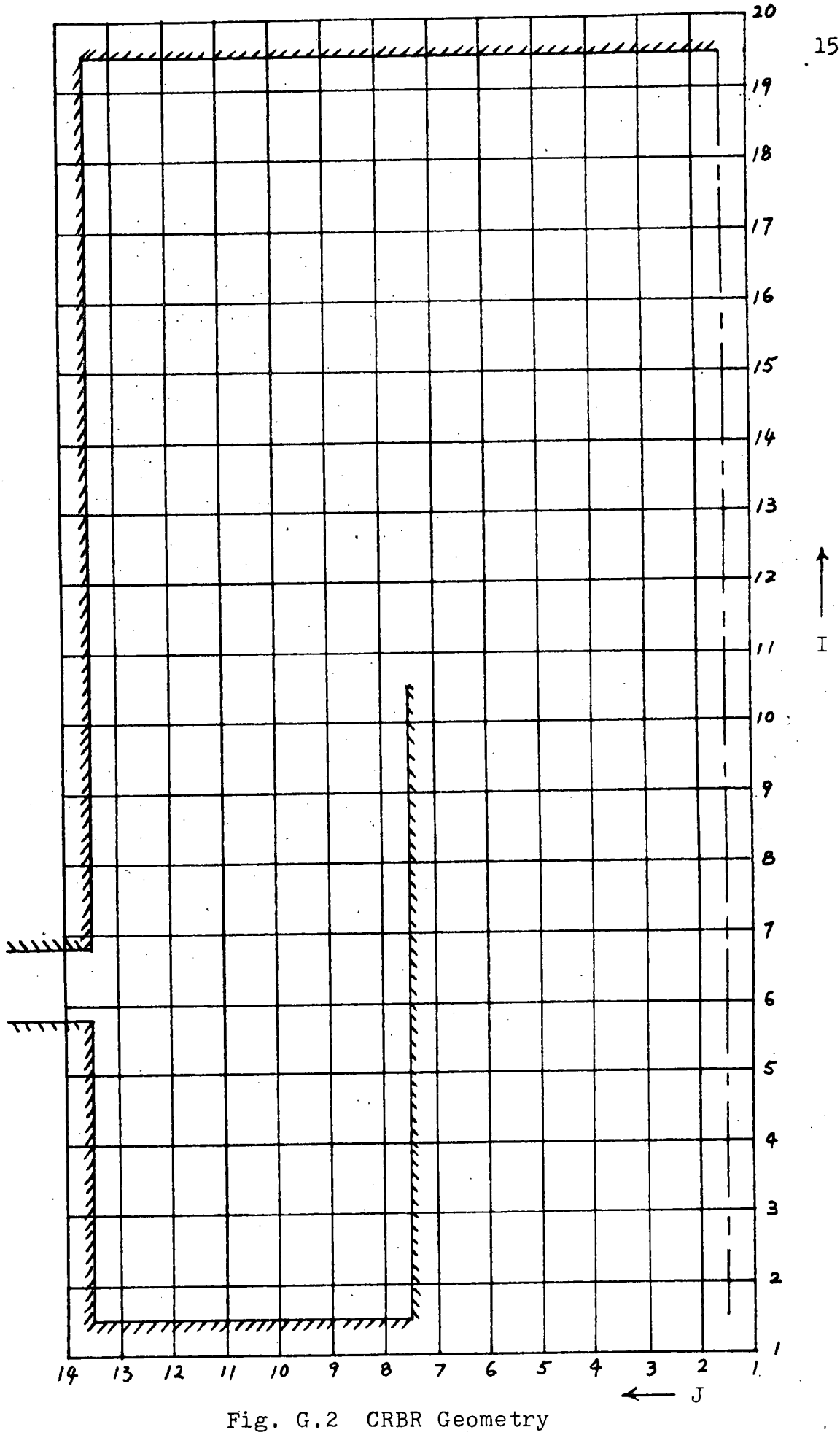

Fig. G.2 CRBR Geometry

APPENDIX H

CRBR GEOMETRY, Re=35,000, DISTORTED INLET VELOCITY DISTRIBUTION CASE

In Figs. H.1 through H.5 CRBR flow data are shown for the case with a partial inlet flow blockage which results in a distorted inlet velocity distribution. The striking feature is that neither code is able to predict the mean flow anywhere qualitatively except in the vicinity of the oulet orifice. Both codes predict that there is a stagnant flow region in the upper part of the plenum and that the inlet jet is unable to reach the top wall. It contradicts the measured mean flow field. As stated in section 5.3.2, the highly complex turbulent transport processes in the CRBR geometry which results in great difficulties to predict the mean flow field even in the normal inlet velocity distribution case. Hence, in a highly chaotic mean flow field in CRBR geometry, the computer codes fail completely.

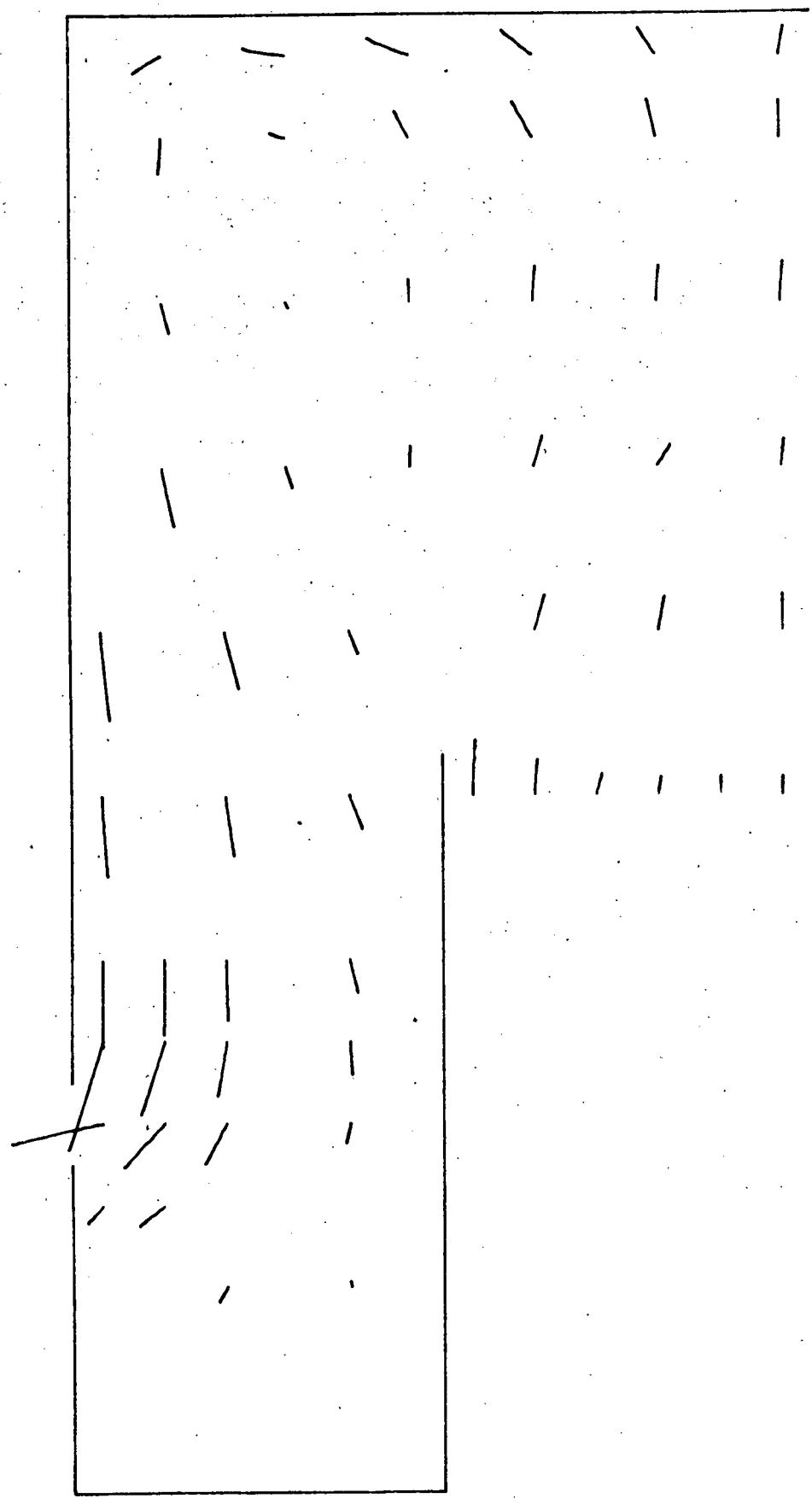

Fig. H.1 Measured Mean Flow Field, CRBR Geometry, Distorted Inlet Velocity Distribution

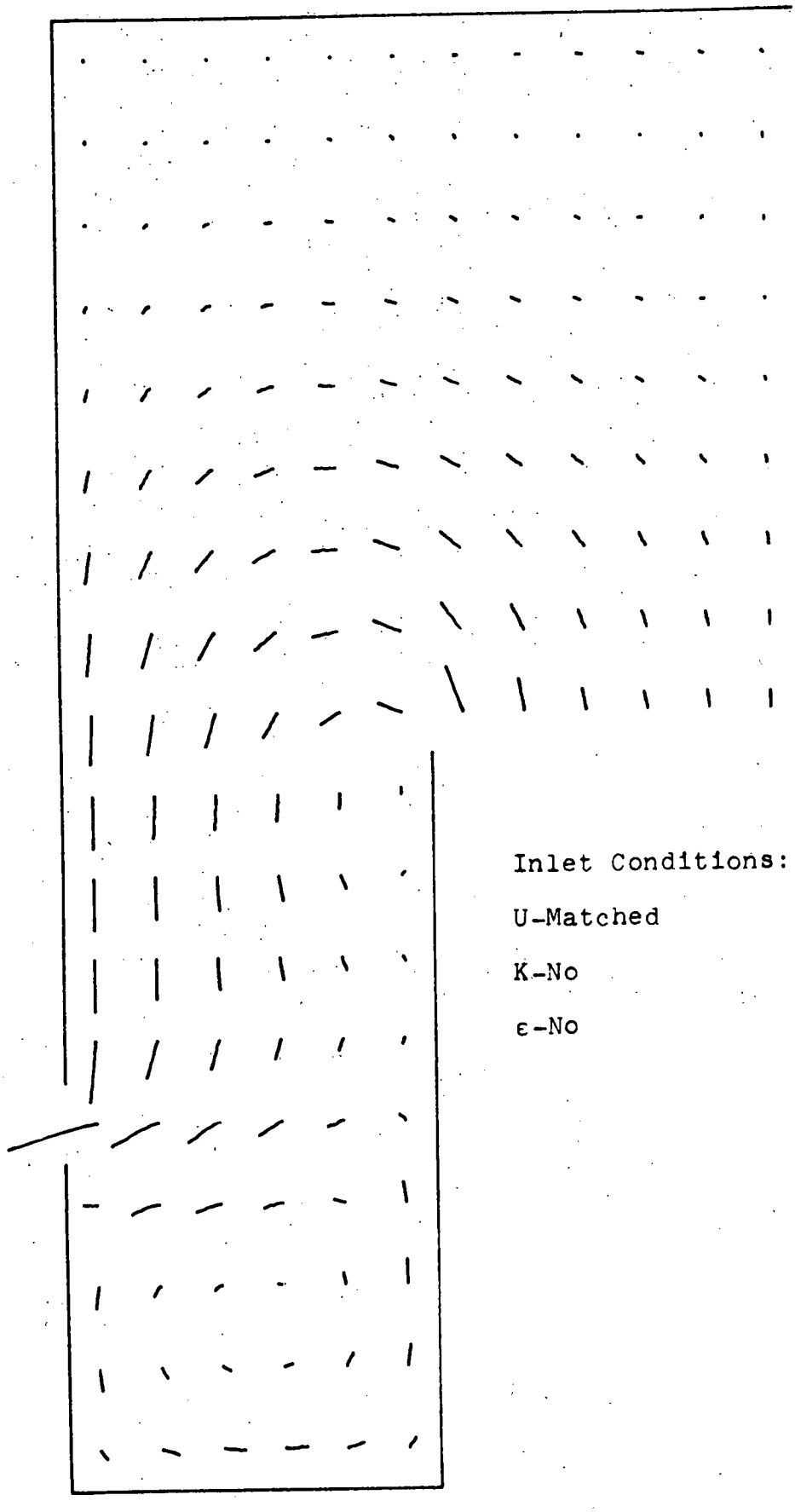

Fig. H.2 TEACH-T Prediction, CRBR Geometry, Re=35000
Distorted Inlet Velocity Distribution

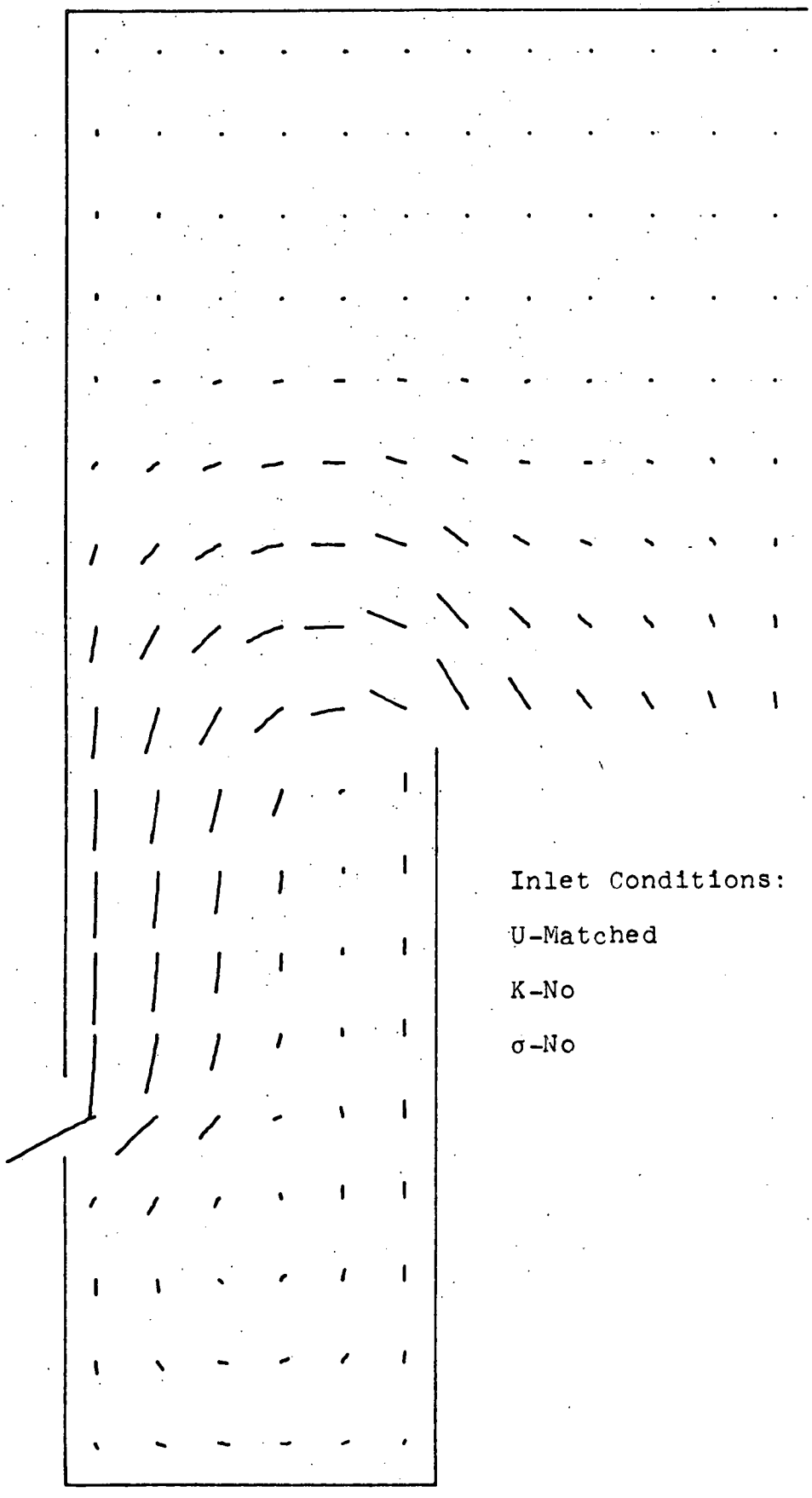

Fig. H.3 VARR-II Prediction, CRBR Geometry, Re=35000
Distorted Inlet Velocity Distribution

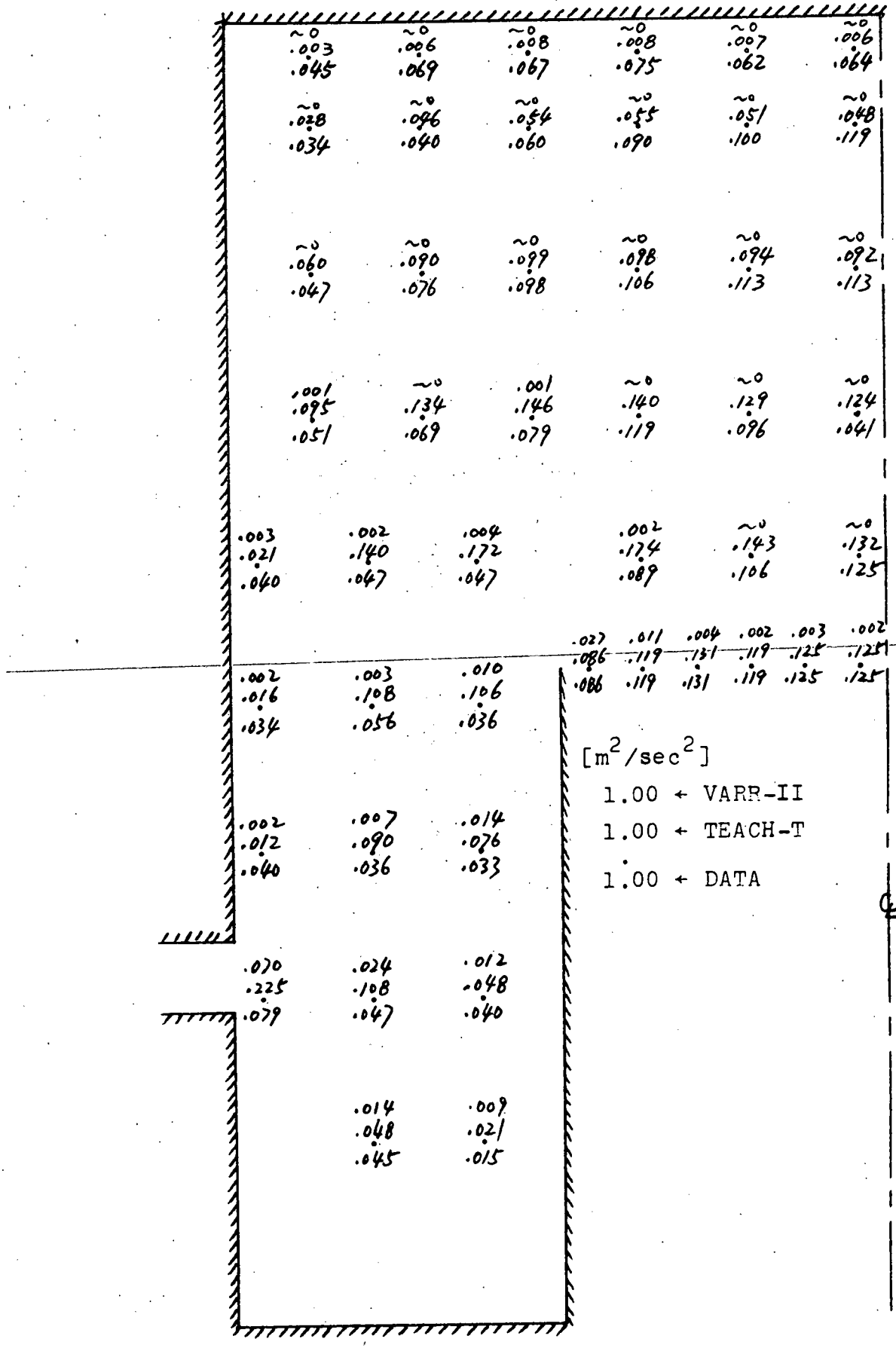

Fig. H.4 Compared Calculated and Measured Turbulent Kinetic Energy Fields, CRBR Geometry, Distorted Inlet Velocity Distribution

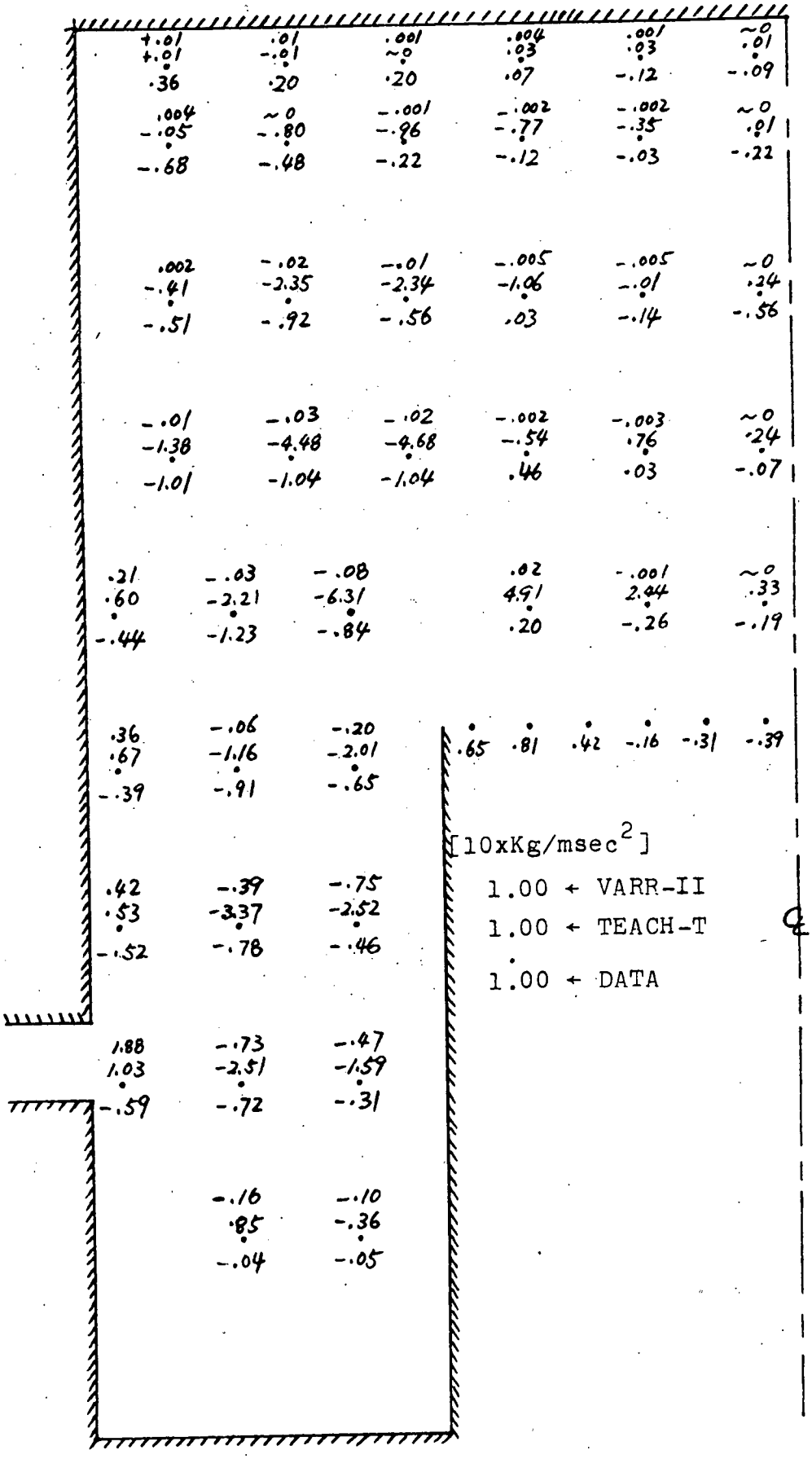

Fig. H.5 Compared Calculated and Measured Reynolds Stress Fields, CRBR Geometry, Distorted Inlet Velocity Distribution

APPENDIX I

DATA OF SENSITIVITY ANALYSIS

The results of sensitivity analysis of five free parameters in TEACH-T model for case of FFTF geometry with normal inlet velocity distribution are shown in Figs. I.1 through I.24. The resulting best set of parameters is applied to distorted inlet velocity distribution case with different combination of inlet turbulent kinetic energy dissipation rates. They are shown in Figs. I.25 through I.33. Finally, the results of sensitivity analysis of two parameters, σ_K and σ_ε, for the distorted inlet velocity distribution case are shown in Figs. I.34 through I.40.

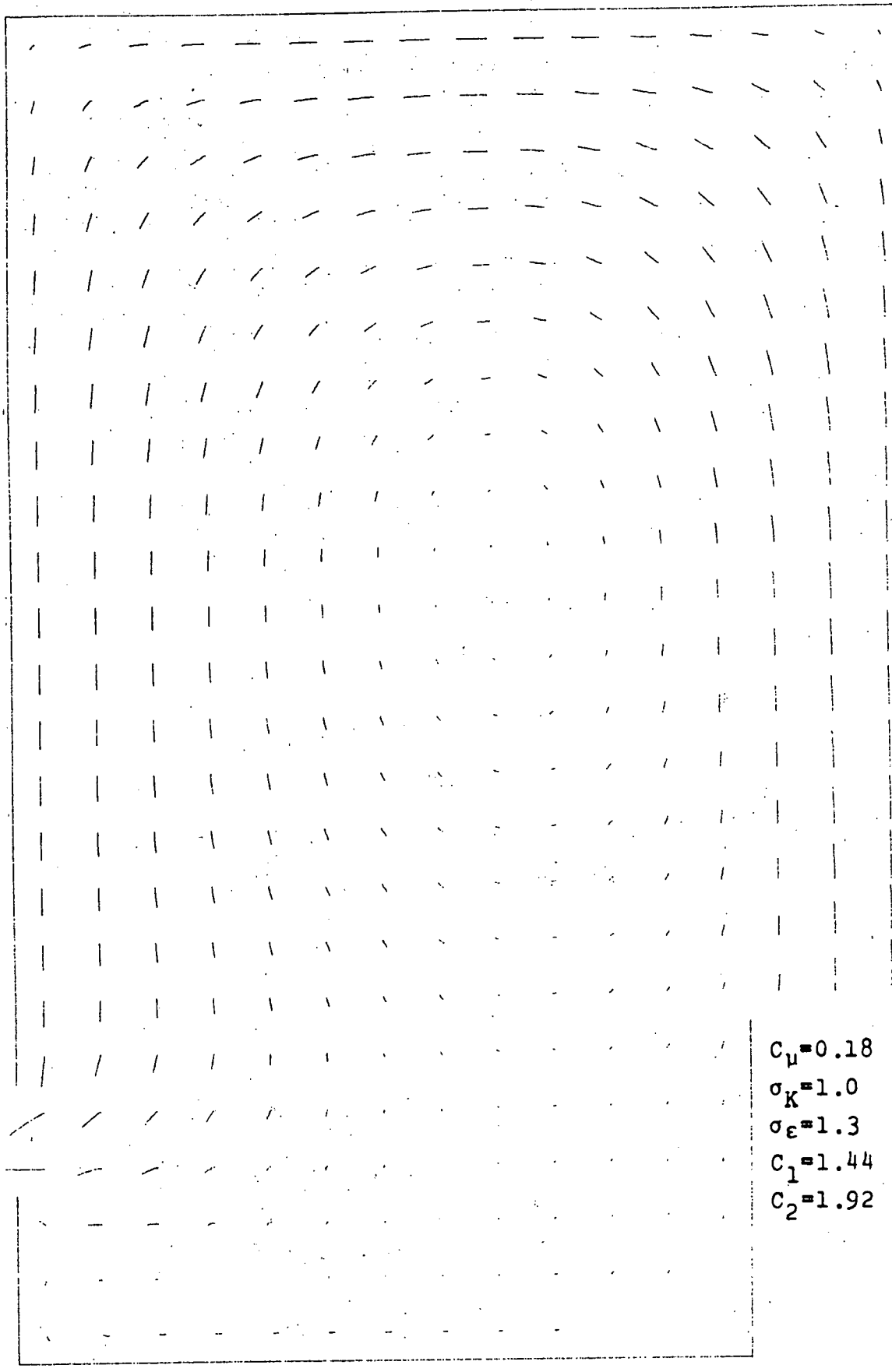

Fig. I.1 TEACH-T Prediction with C_μ = 0.18, FFTF Geometry, Re=70000, Normal Inlet Velocity Distribution

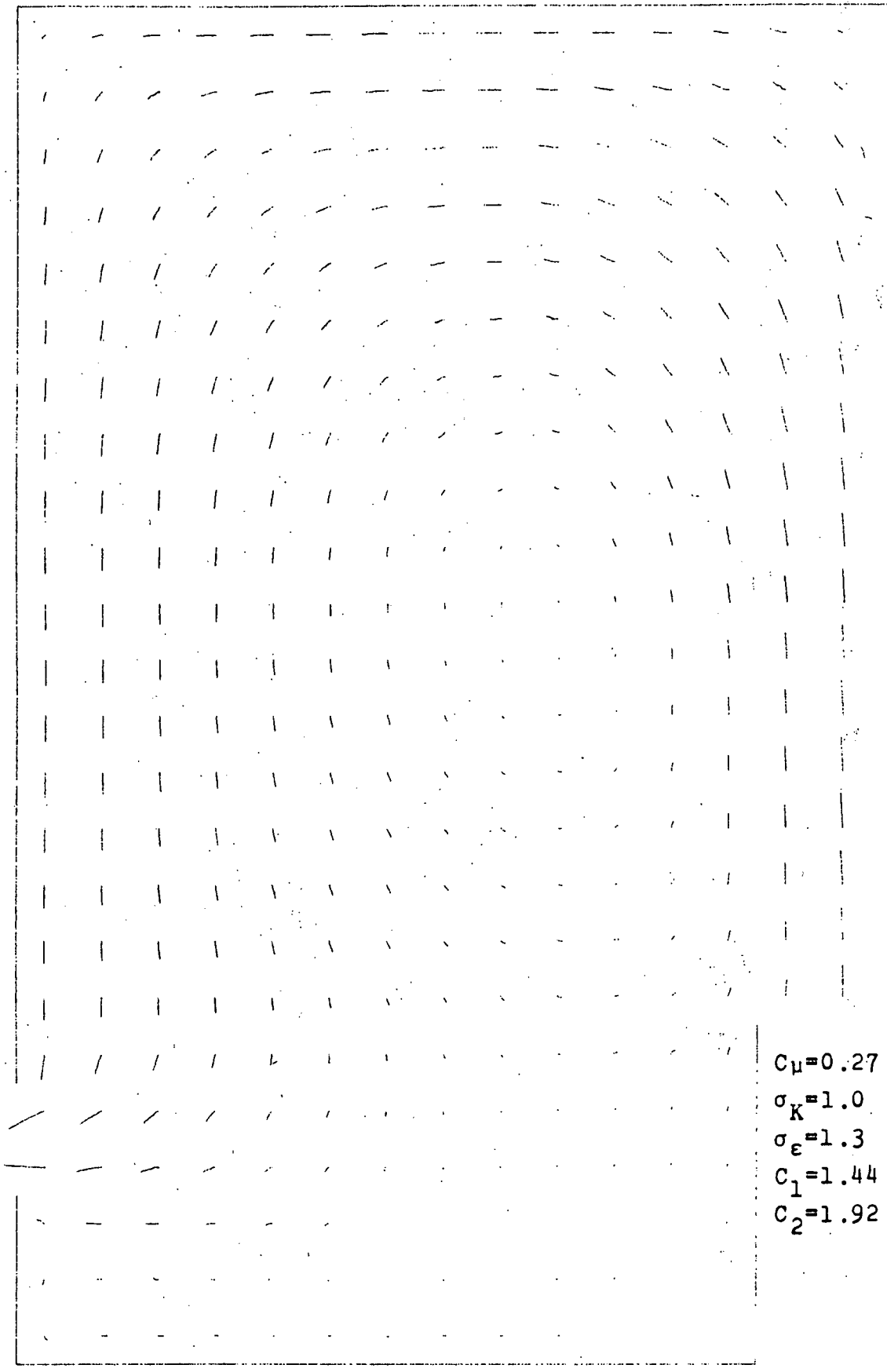

Fig. I.2 TEACH-T Prediction with C_μ = 0.27, FFTF Geometry, Re=70000, Normal Inlet Velocity Distribution

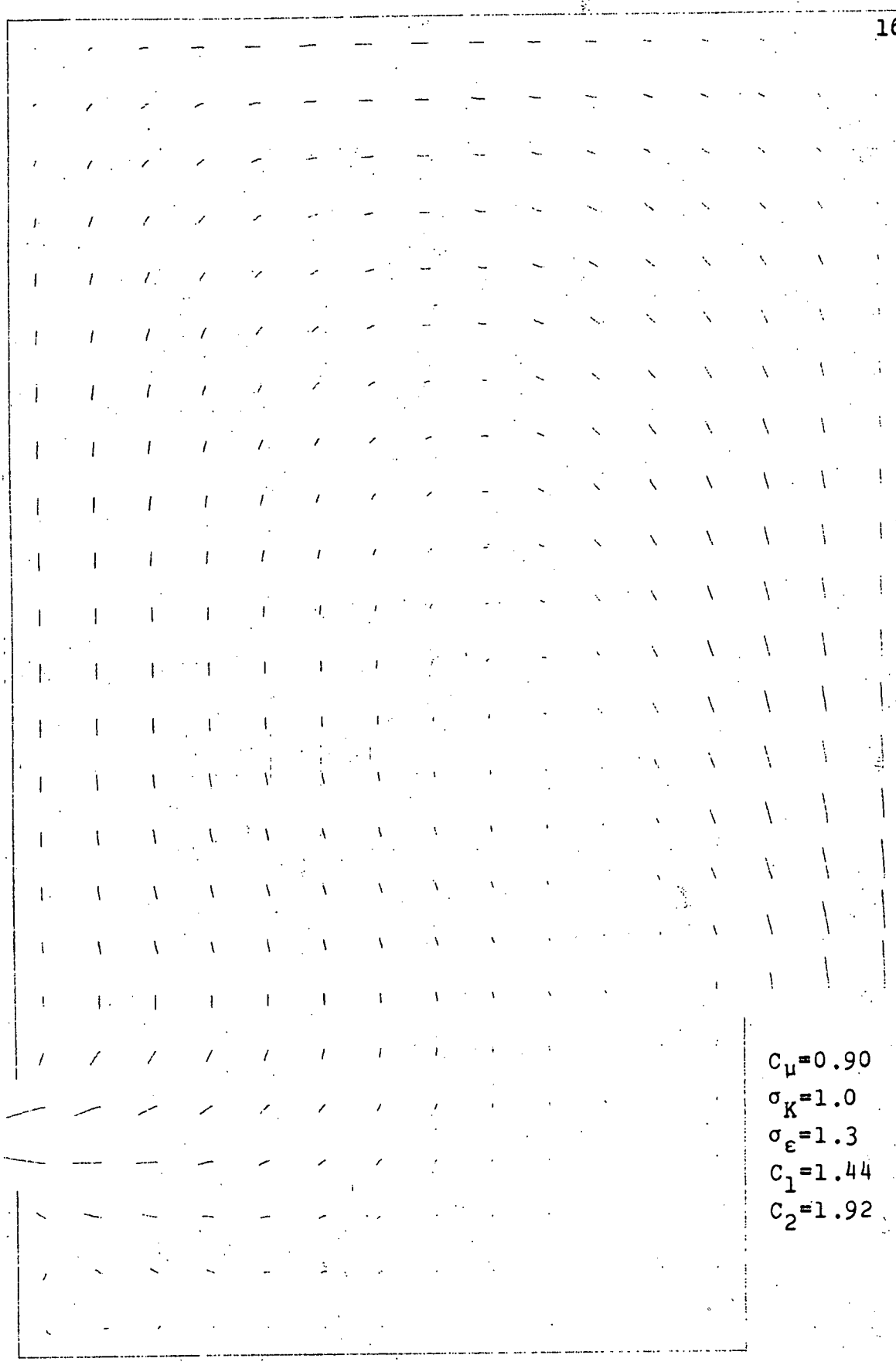

Fig. I.3 TEACH-T Prediction with C_μ = 0.90, FFTF Geometry, Re=70000, Normal Inlet Velocity Distribution

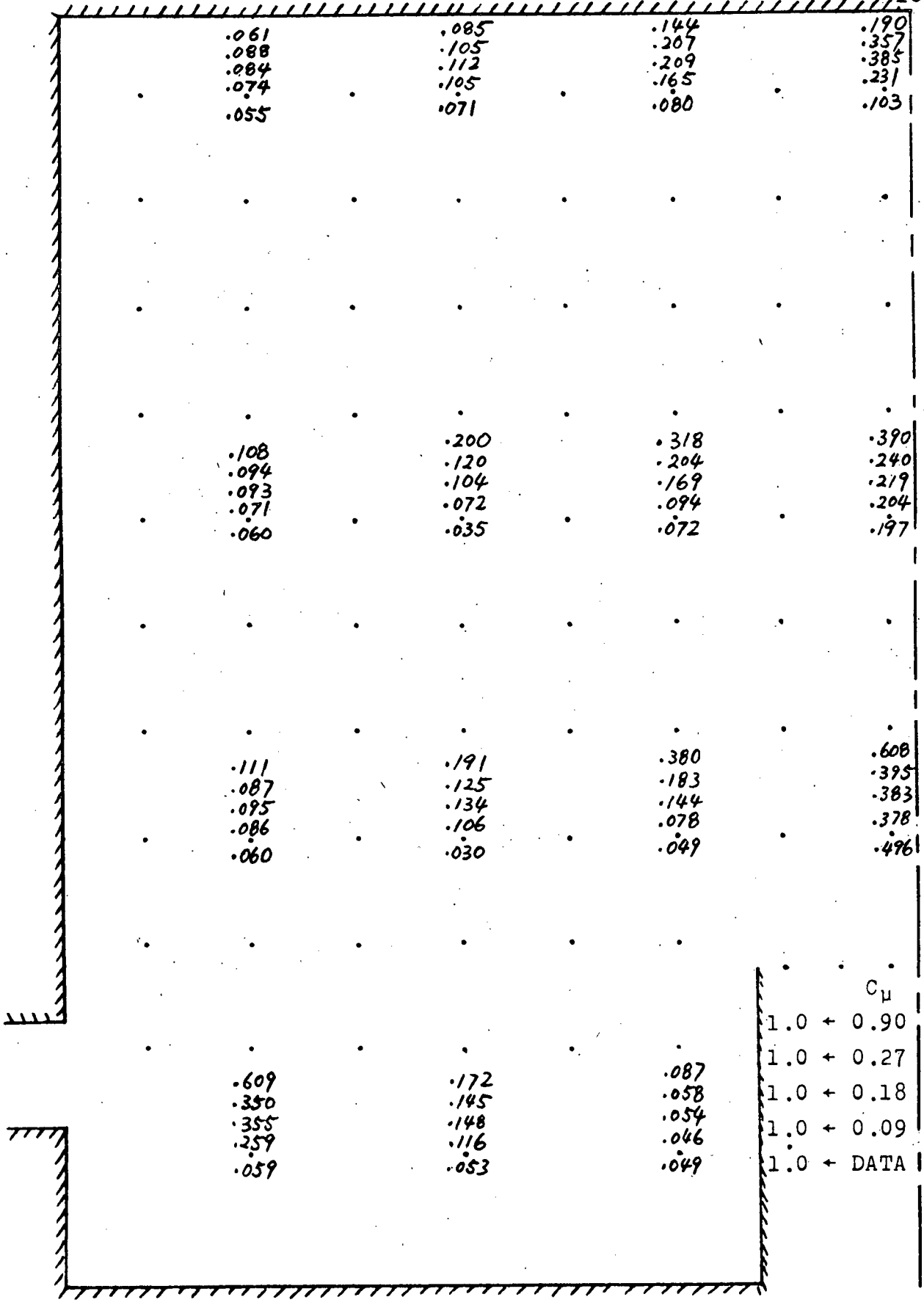

Fig. I.4 Compared Calculated and Measured Turbulent Kinetic Energy Fields, FFTF Geometry, Re=70000, Normal Inlet Velocity Distribution

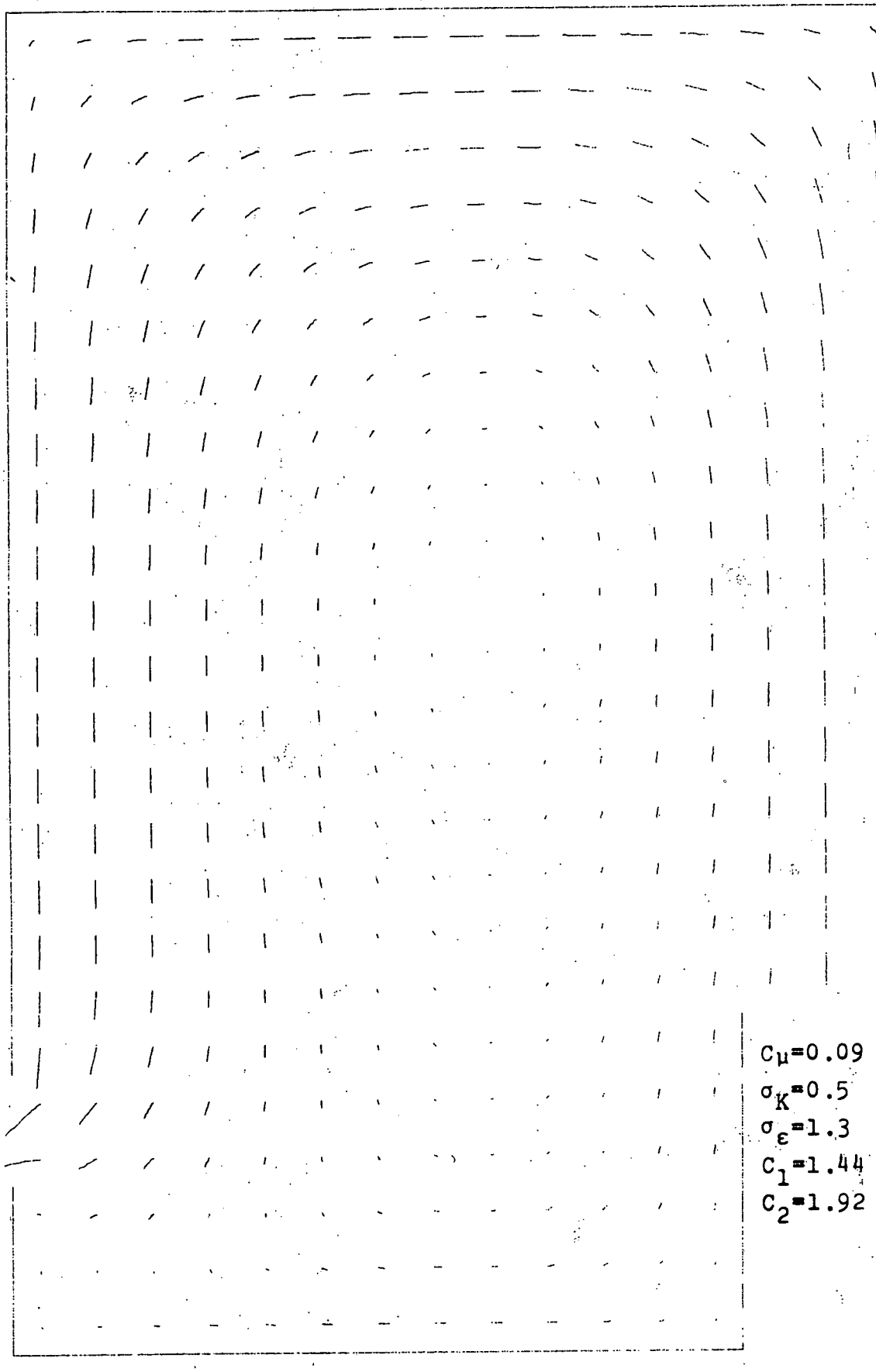

Fig. I.5 TEACH-T Prediction with σ_K = 0.5, FFTF Geometry, Re=70000, Normal Inlet Velocity Distribution

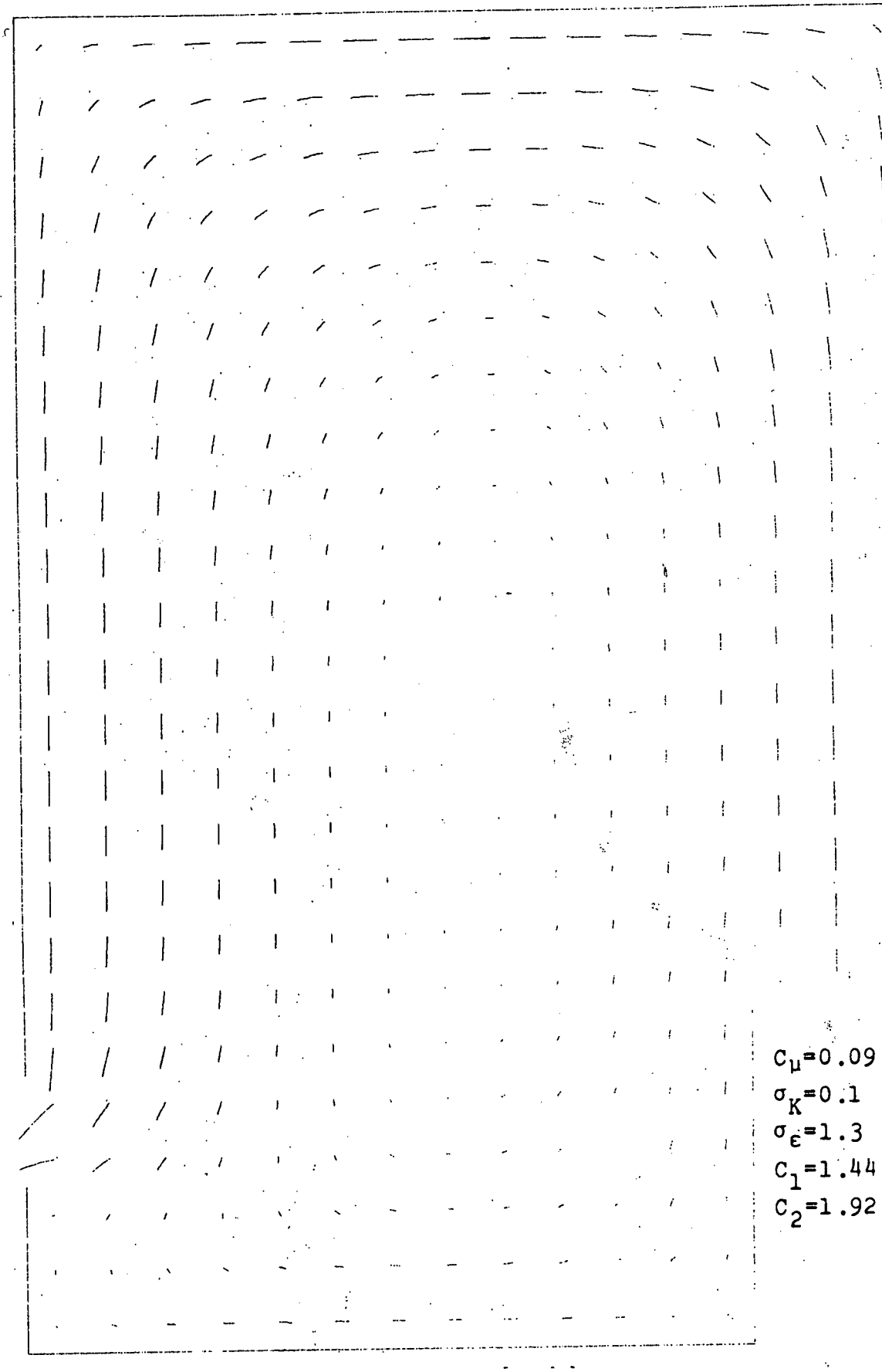

Fig. I.6 TEACH-T prediction with σ_K = 0.1, FFTF Geometry, Re=70000, Normal Inlet Velocity Distribution

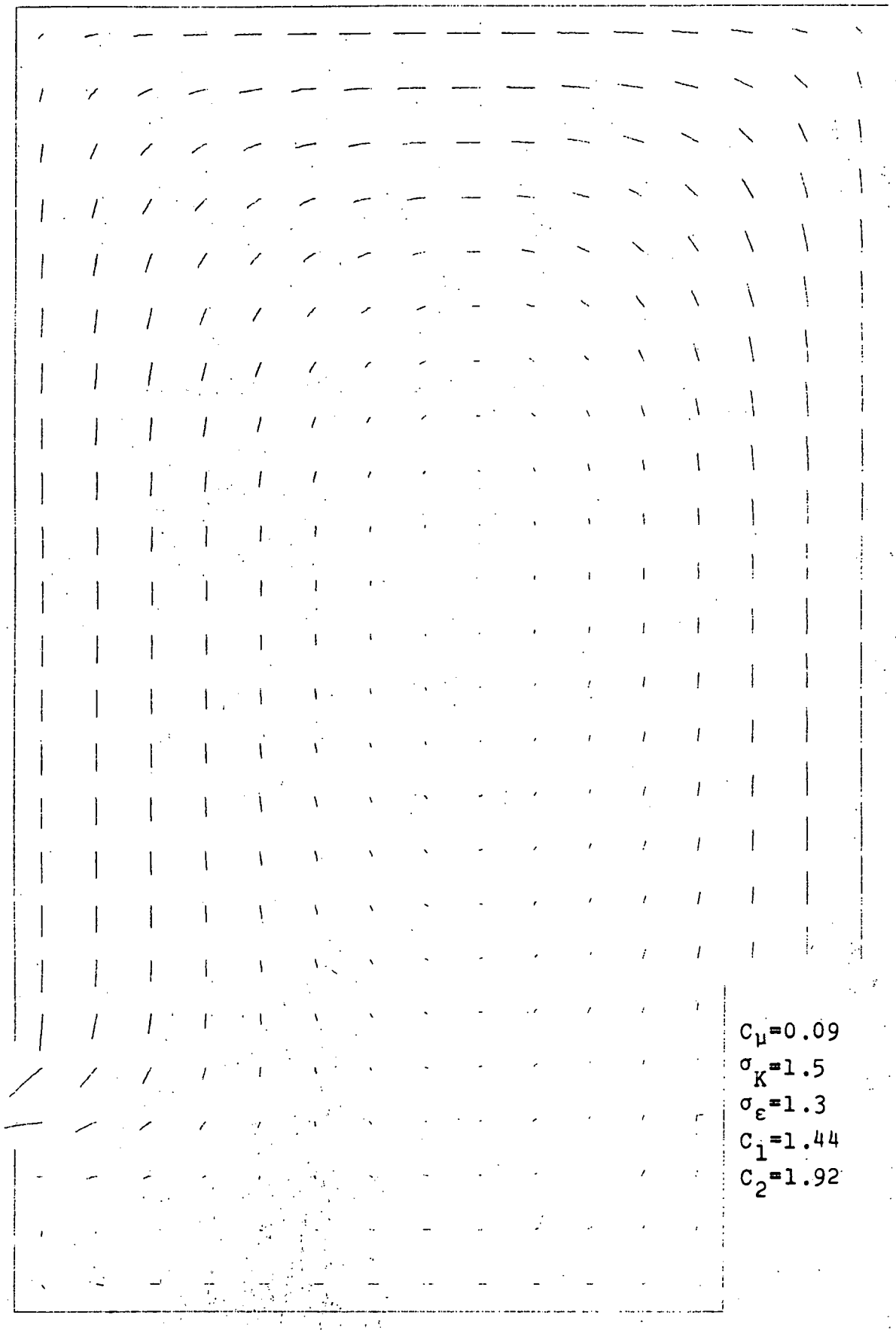

Fig. I.7 TEACH-T Prediction with σ_K = 1.5, FFTF Geometry, Re=70000, Normal Inlet Velocity Distribution

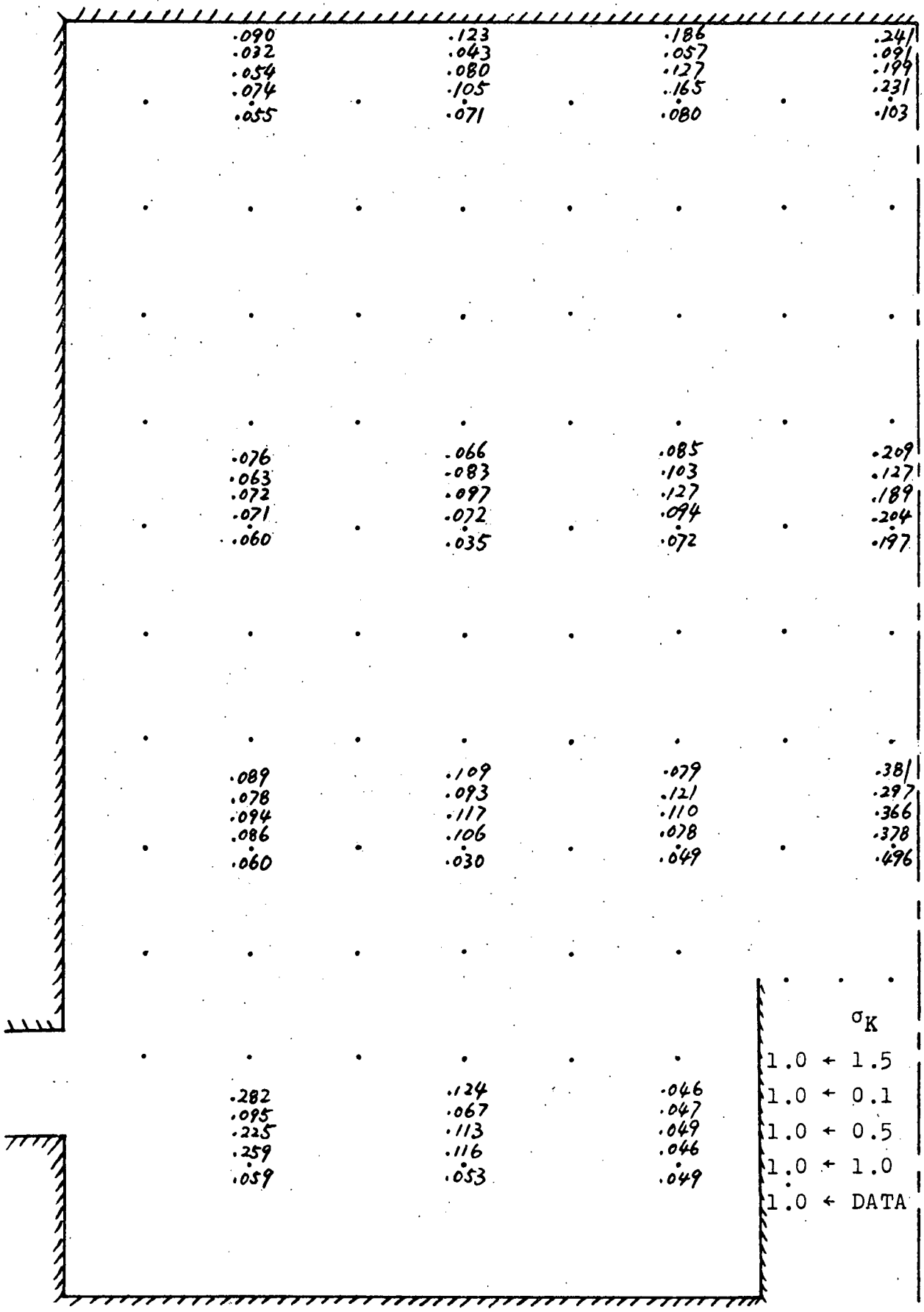

Fig. I.8 Compared Calculated and Measured Turbulent Kinetic Energy Fields, FFTF Geometry, Re=70000, Normal Inlet Velocity Distribution

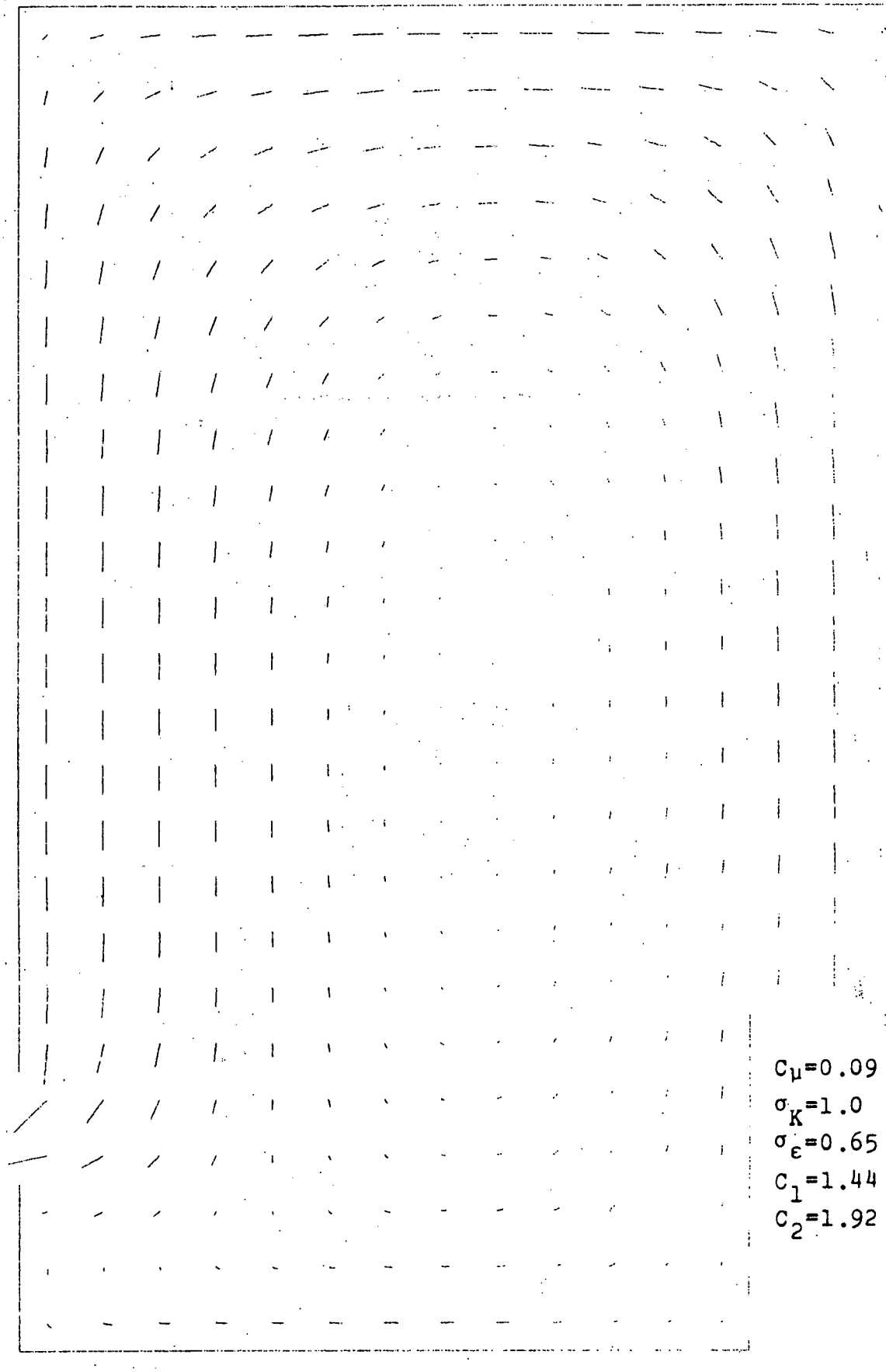

Fig. I.9 TEACH-T Prediction with σ_ε = 0.65, FFTF Geometry, Re=70000, Normal Inlet Velocity Distribution

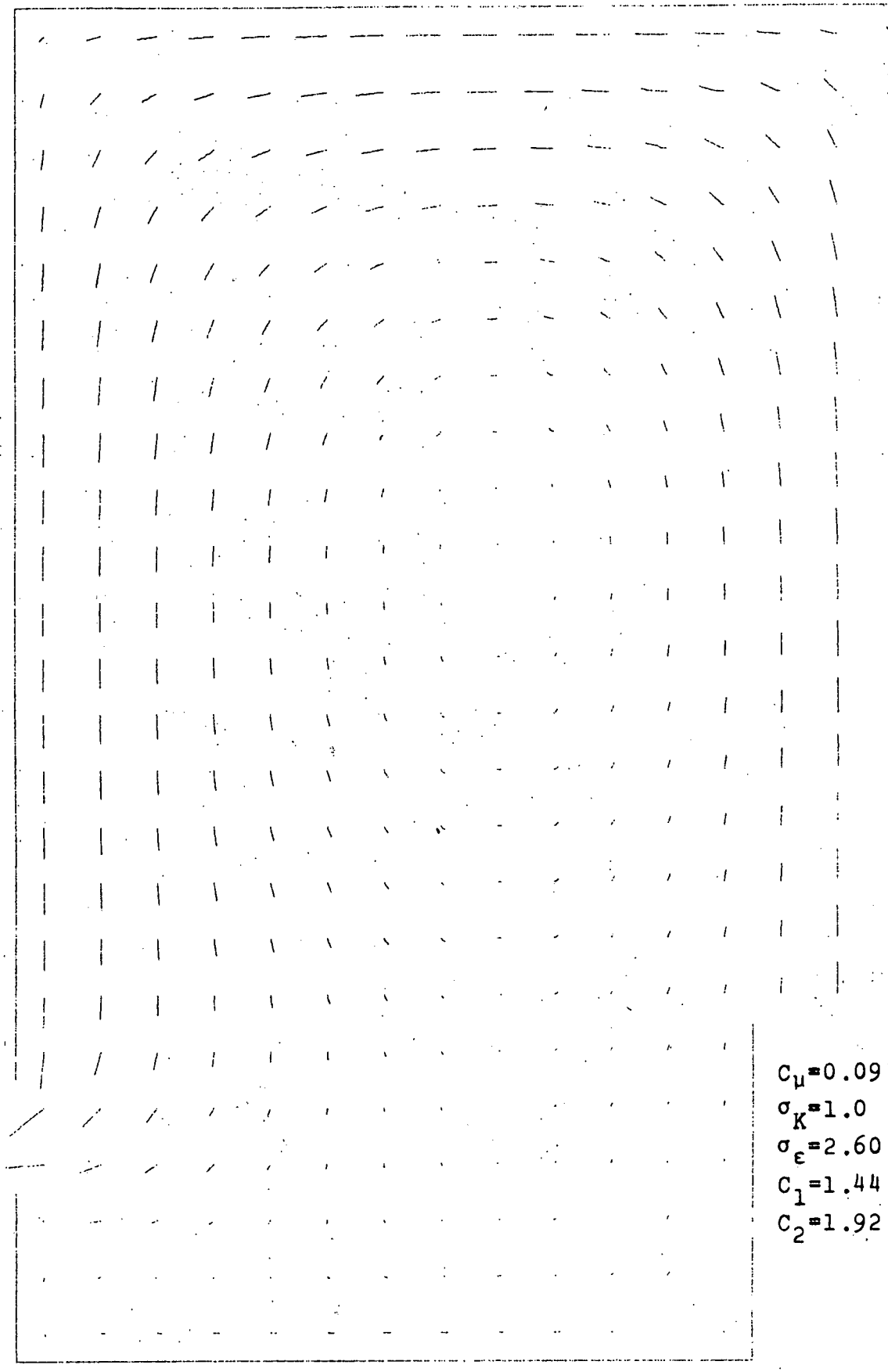

Fig. I.10 TEACH-T Prediction with σ_ε = 2.60, FFTF Geometry, Re=70000, Normal Inlet Velocity Distribution

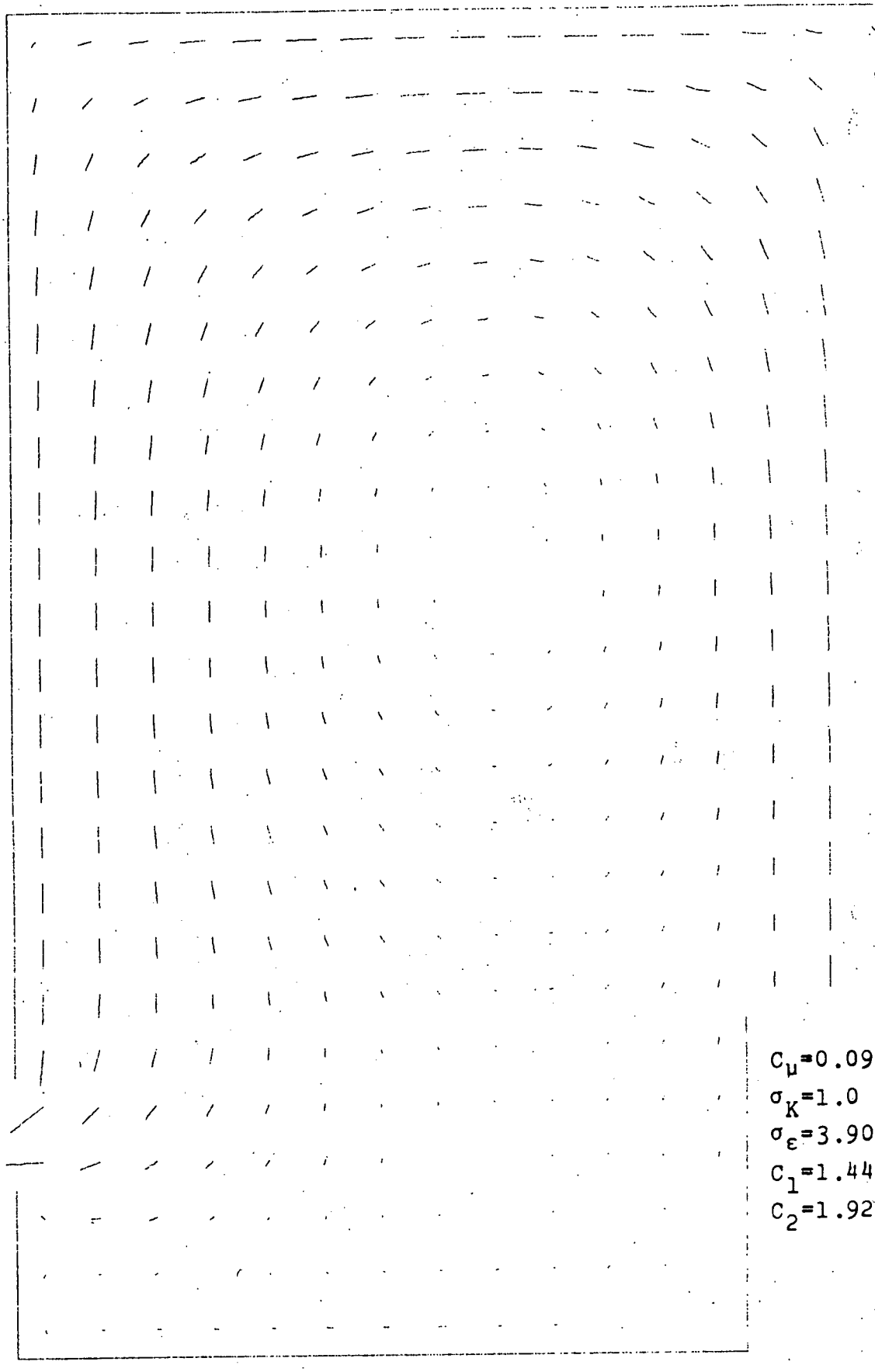

Fig. I.11 TEACH-T Prediction with σ_ε = 3.90, FFTF Geometry Re=70000, Normal Inlet Velocity Distribution

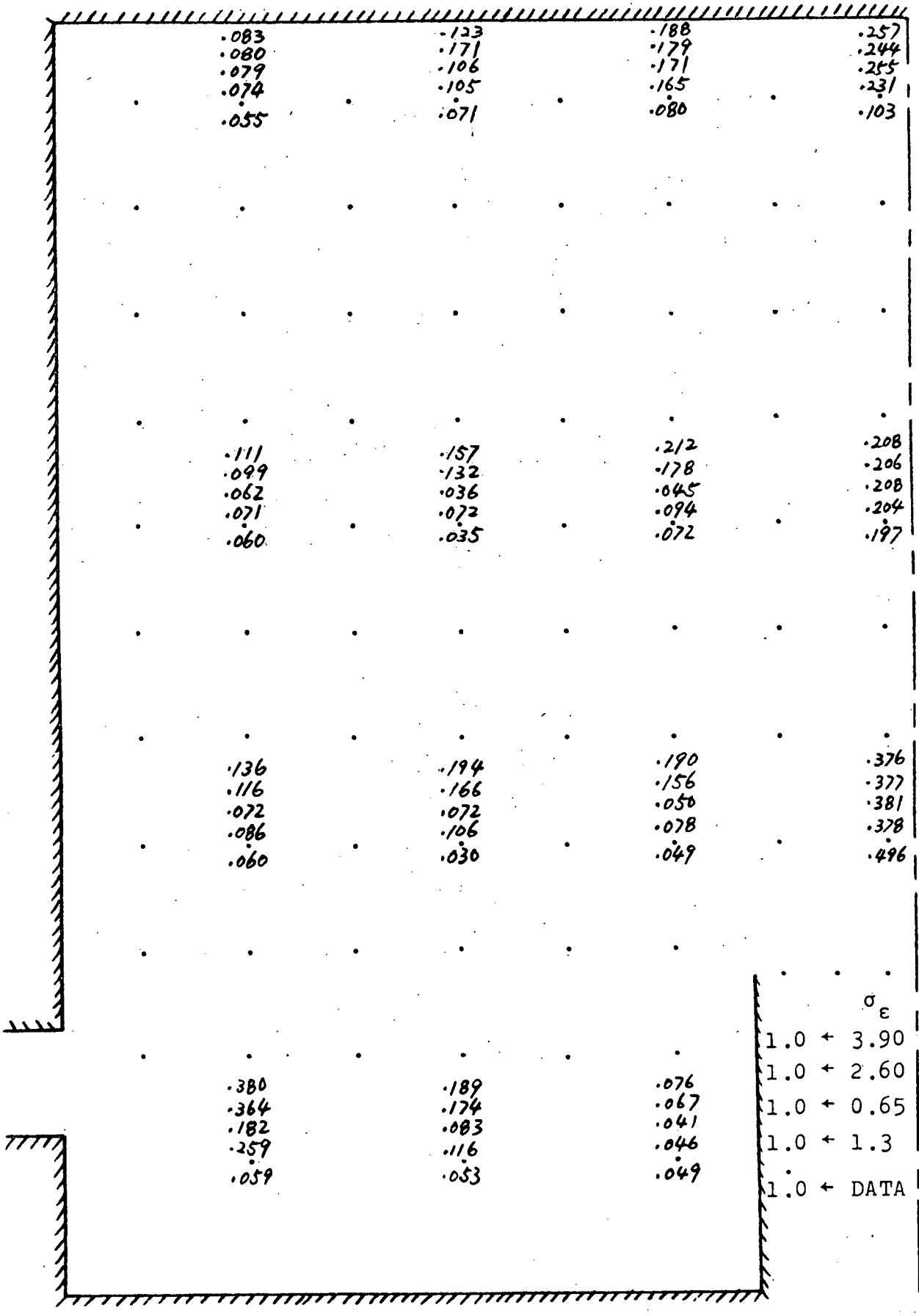

Fig. I.12 Compared Calculated and Measured Turbulent Kinetic Energy Fields, FFTF Geometry, Re=70000, Normal Inlet Velocity Distribution

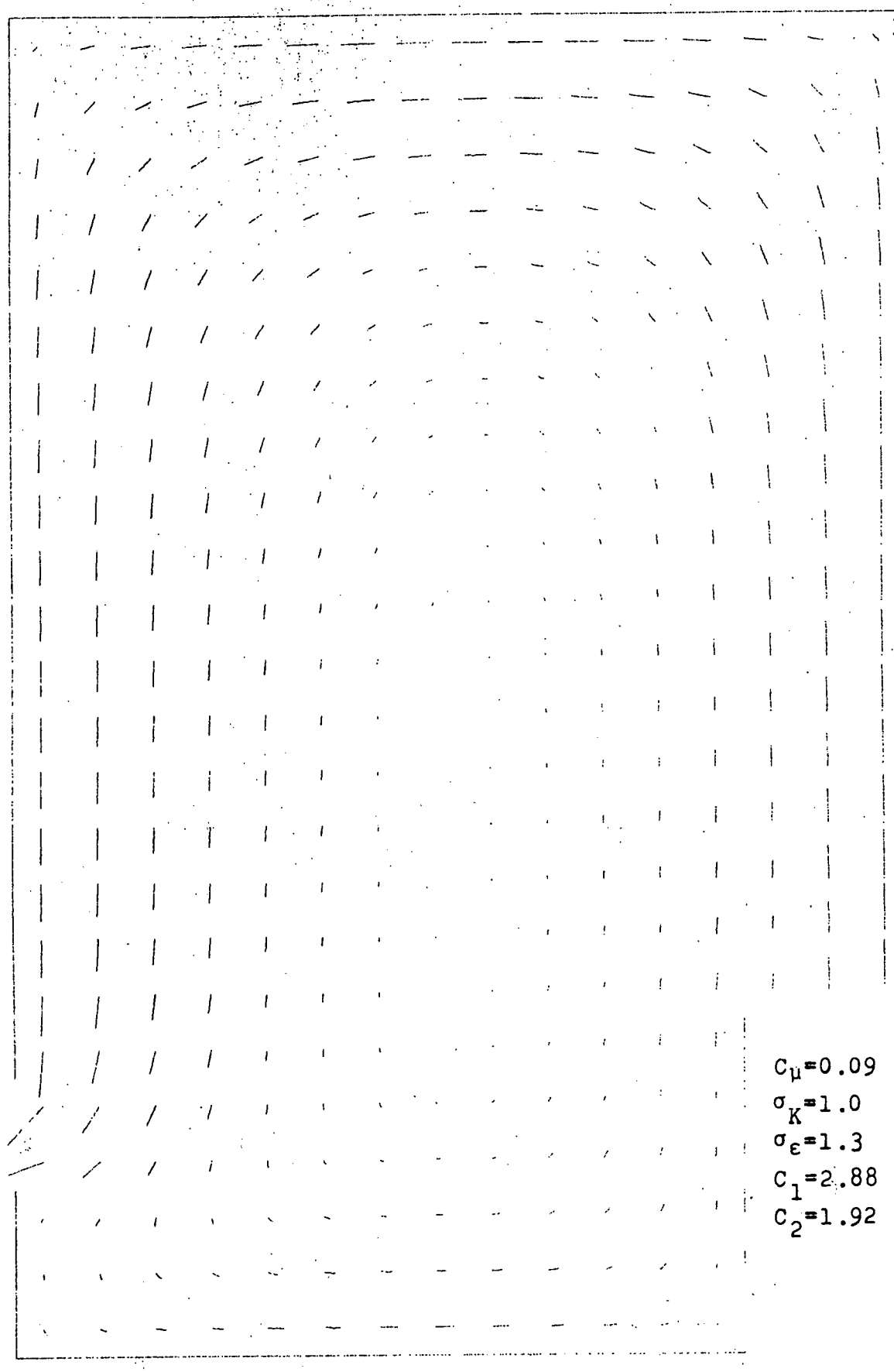

Fig. I.13 TEACH-T prediction with C_1 = 2.88, FFTF Geometry, Re=70000, Normal Inlet Velocity Distribution

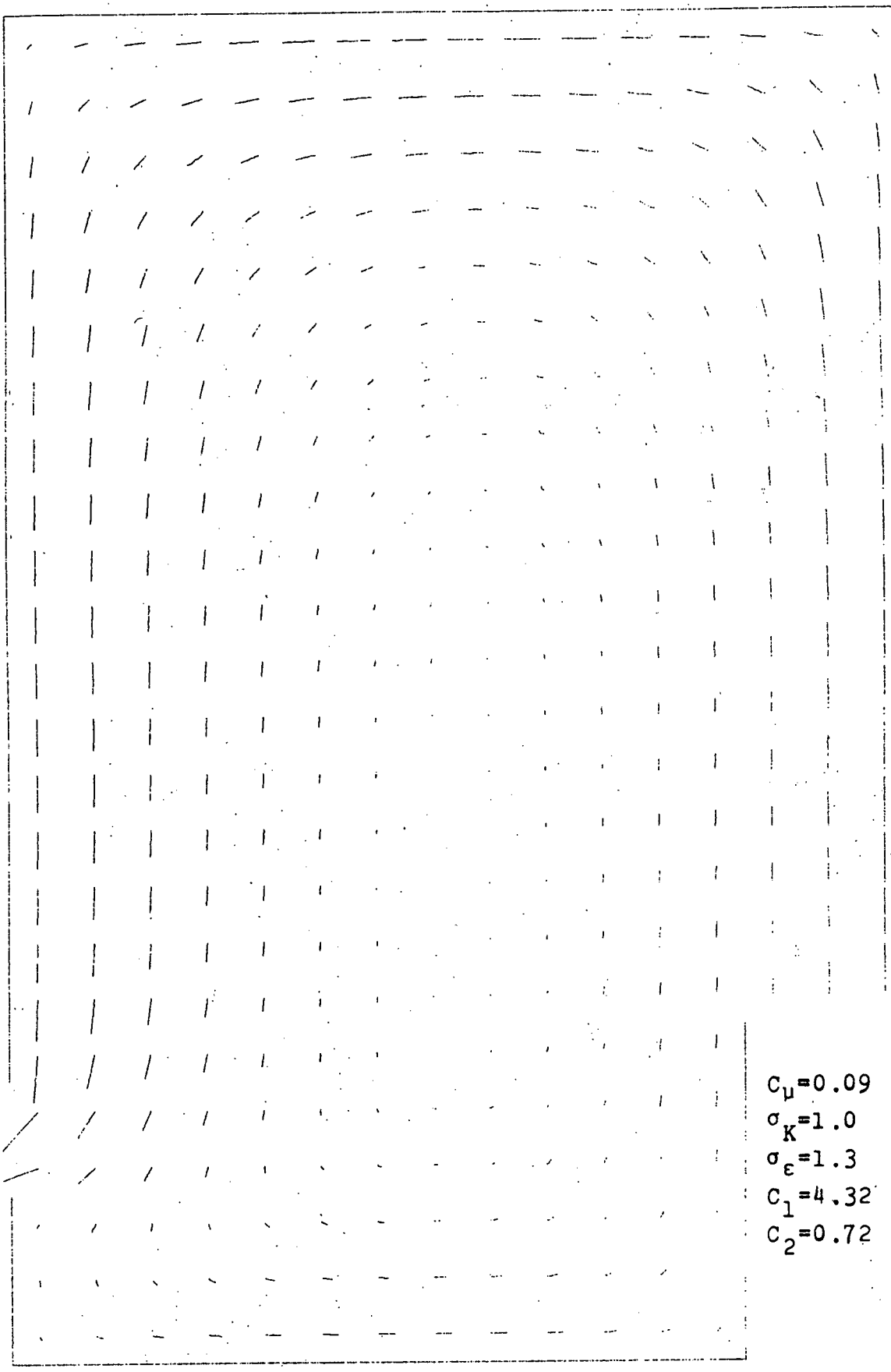

Fig. I.14 TEACH-T Prediction with C_1 = 4.32, FFTF Geometry, Re=70000, Normal Inlet Velocity Distribution

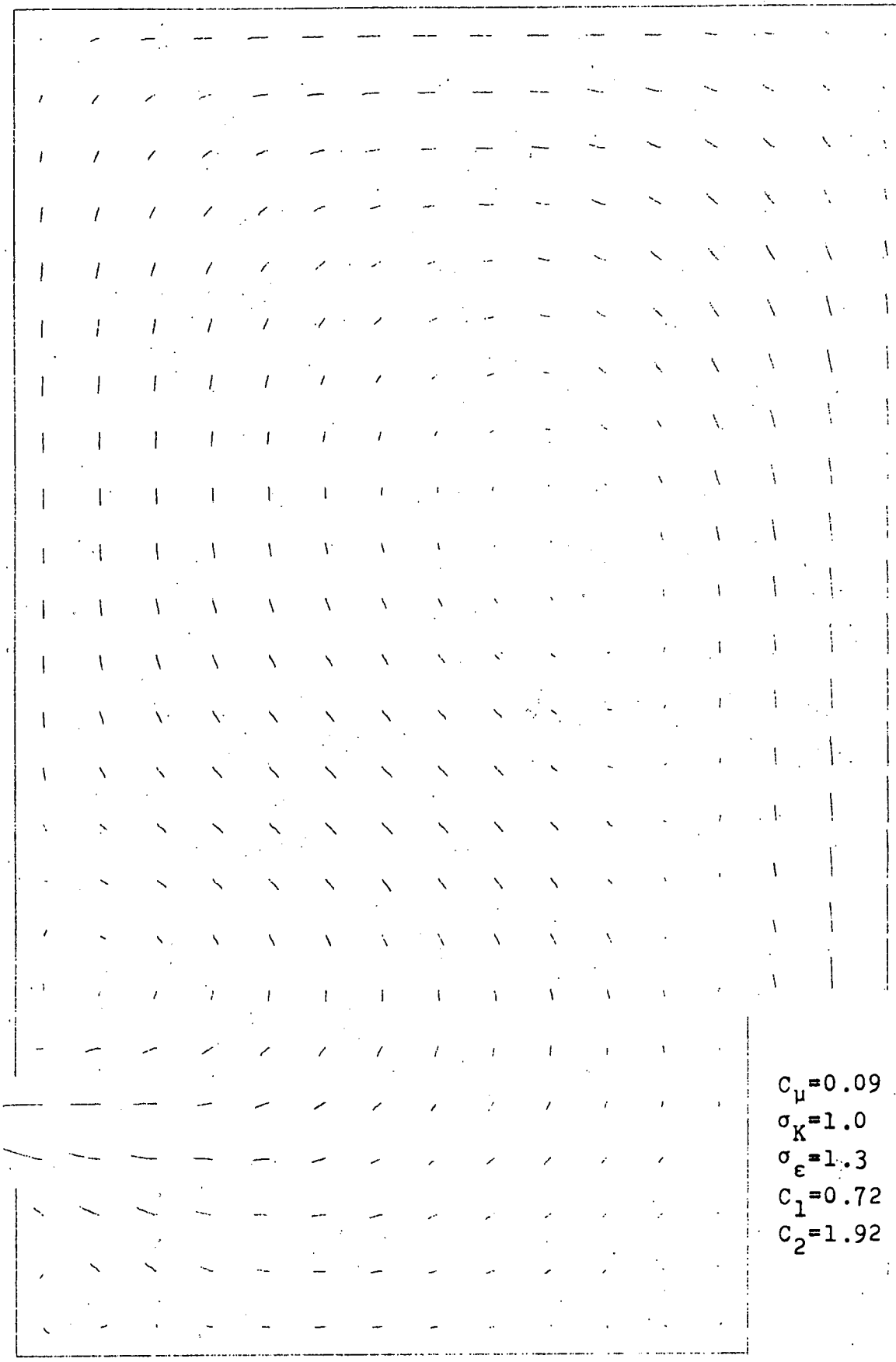

Fig. I.15 TEACH-T Prediction with C_1 = 0.72, FFTF Geometry, Re=70000, Normal Inlet Velocity Distribution

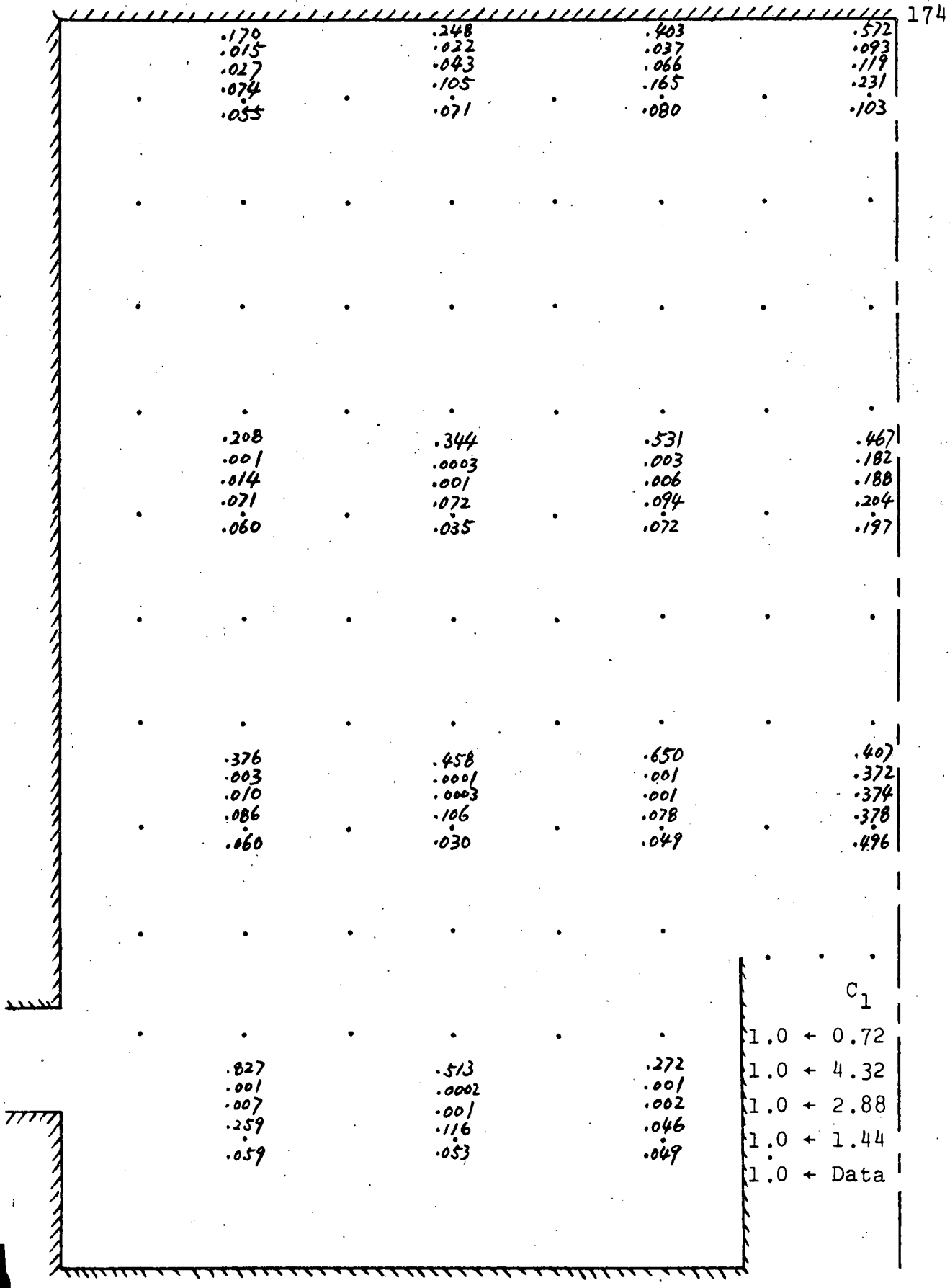

Fig. I.16 Compared Calcualted and Measured Turbulent Kinetic Energy Fields, FFTF Geometry, Re=70000, Normal Inlet Velocity Distribution

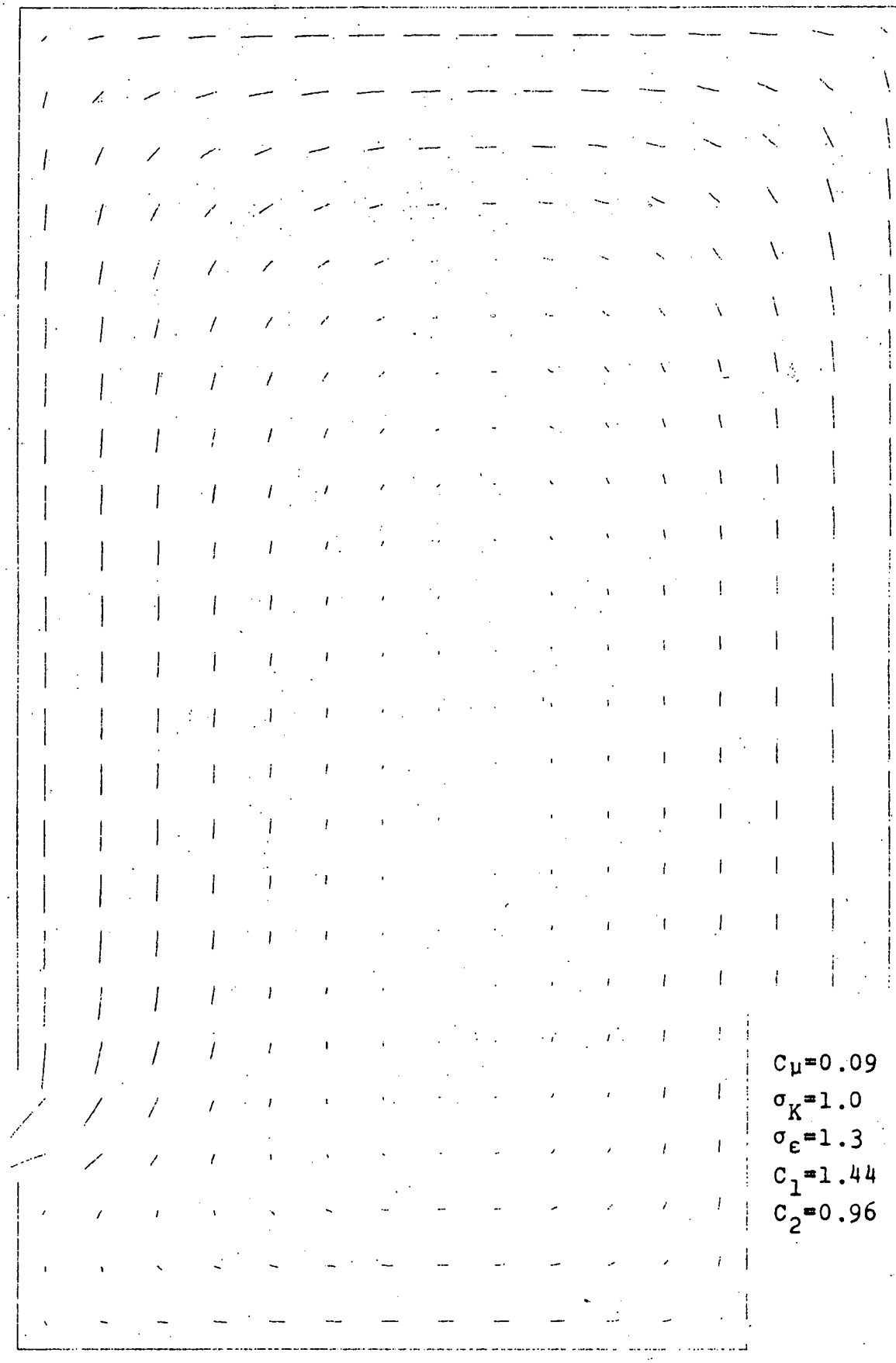

Fig. I.17 TEACH-T prediction with C_2 = 0.96, FFTF Geometry, Re=70000, Normal Inlet Velocity Distribution

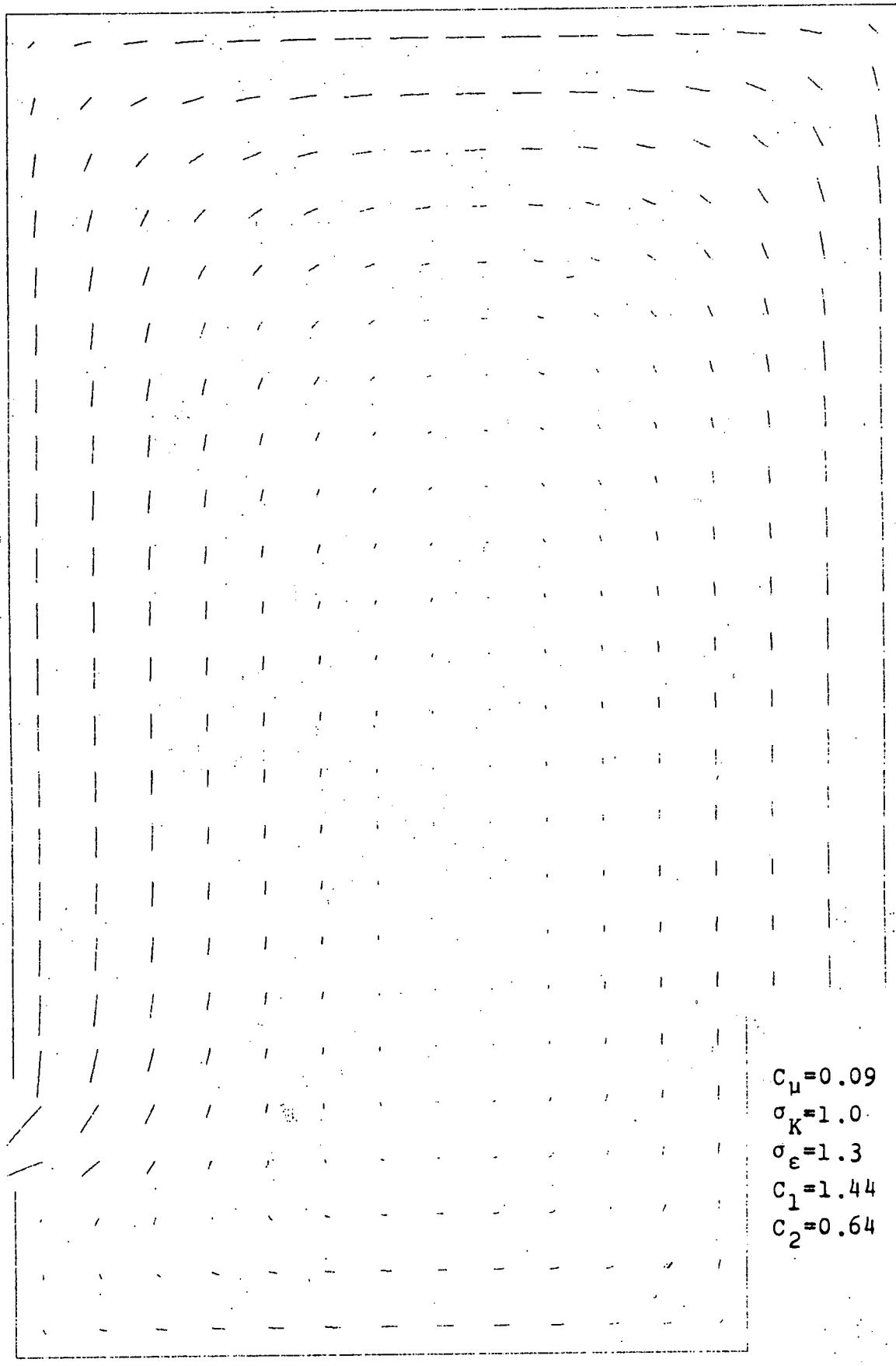

Fig. I.18 TEACH-T Prediction with C_2 = 0.64, FFTF Geometry, Re=70000, Normal Inlet Velocity Distribution

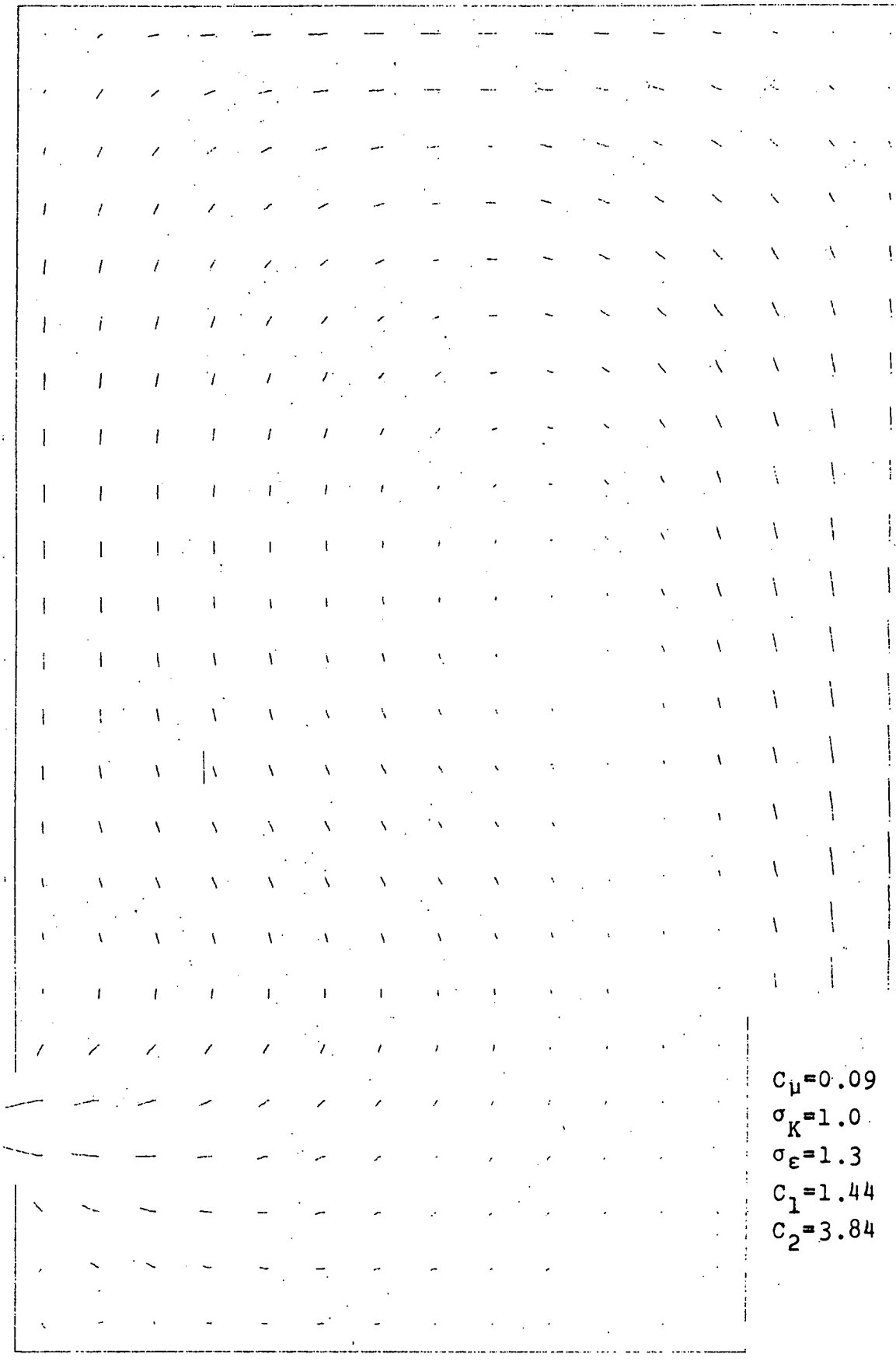

Fig. I.19 TEACH-T Prediction with C_2 = 3.84, FFTF Geometry, Re=70000, Normal Inlet Velocity Distribution

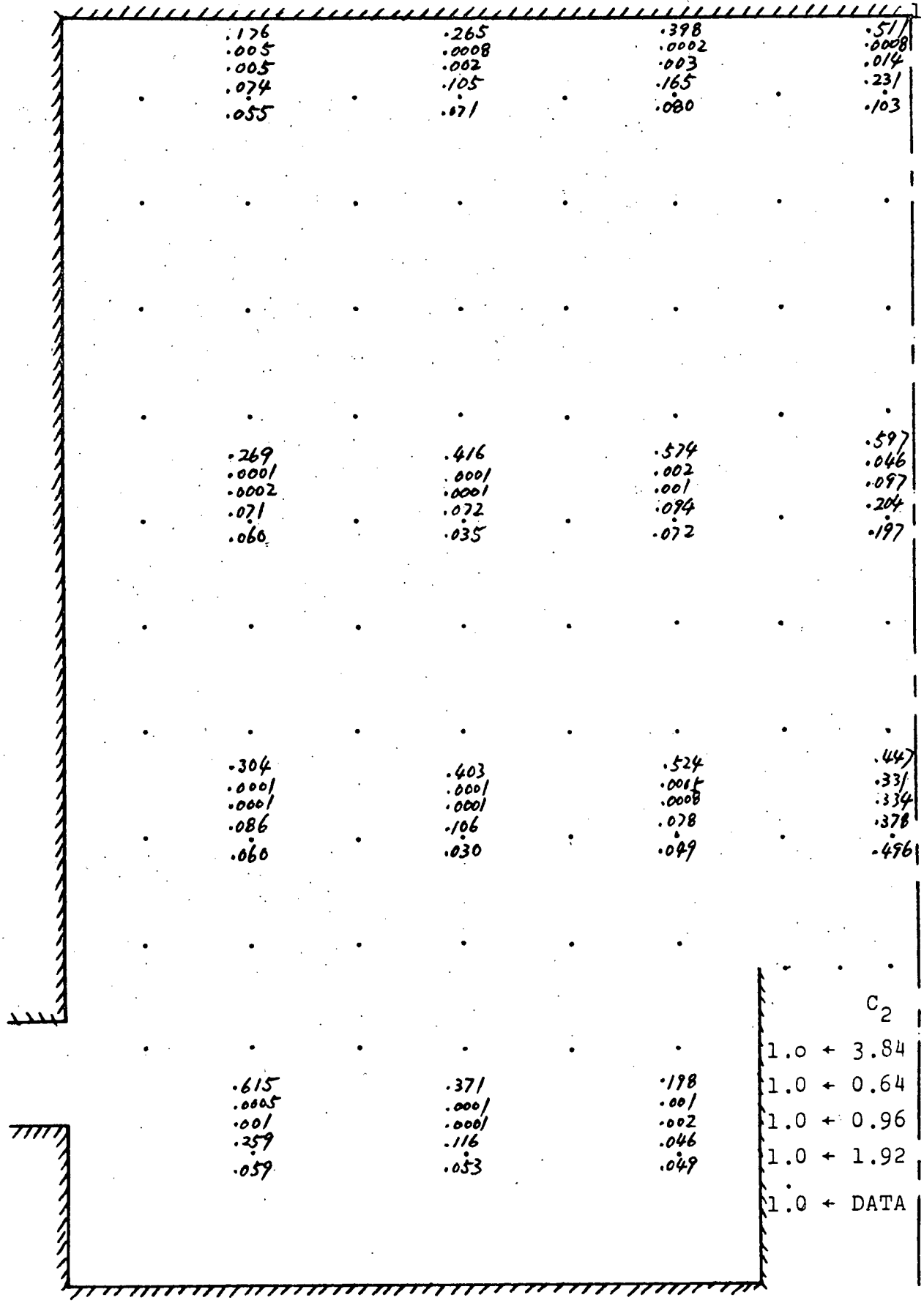

Fig. I.20 Compared Calculated and Measured Turbulent Kinetic Energy Fields, FFTF Geometry, Re=70000, Normal Inlet Velocity Distribution

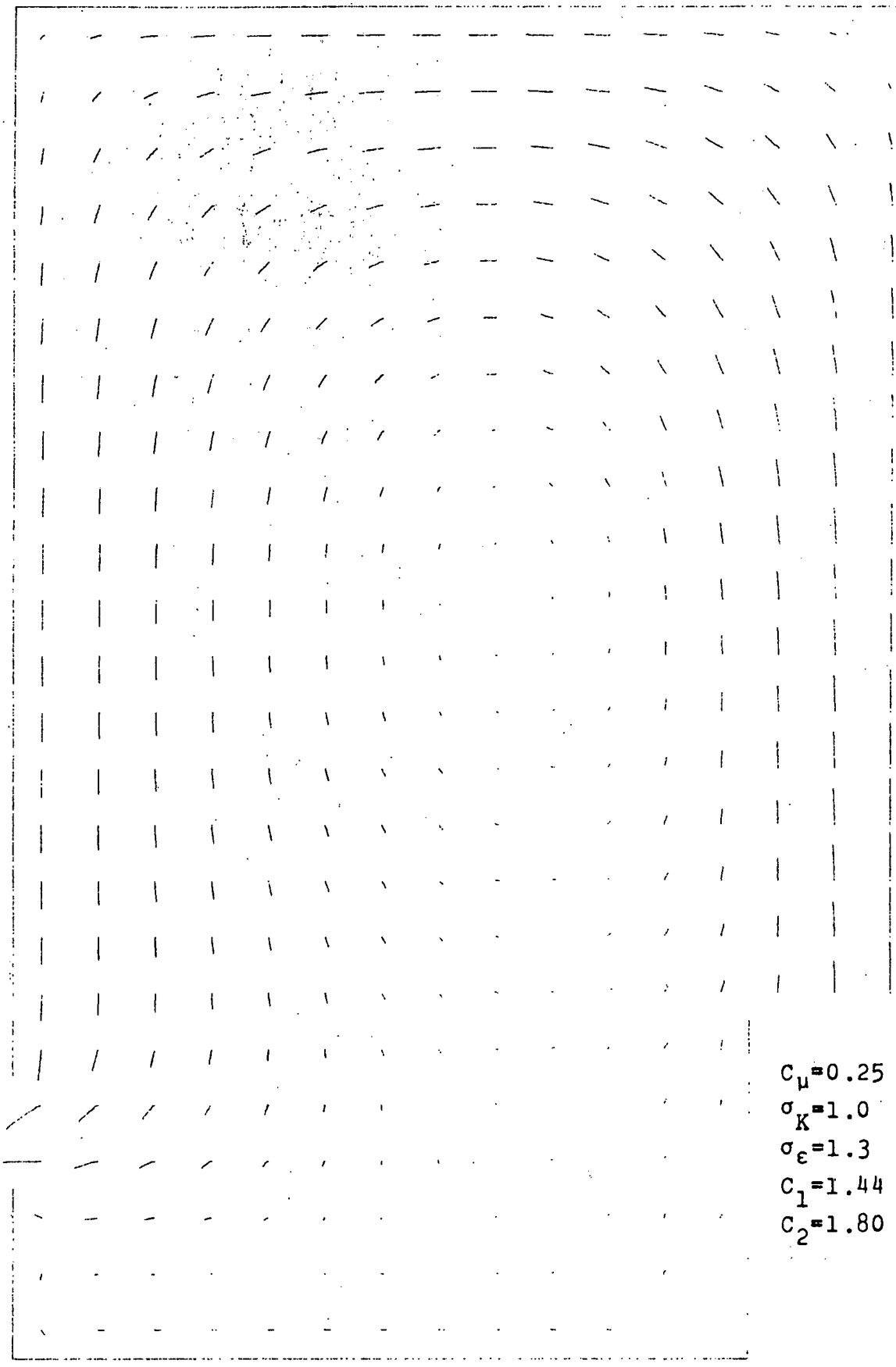

Fig. I.21 TEACH-T prediction with C_μ = 0.25, C_2 = 1.80, FFTF Geometry, Re=70000, Normal Inlet Velocity Distribution

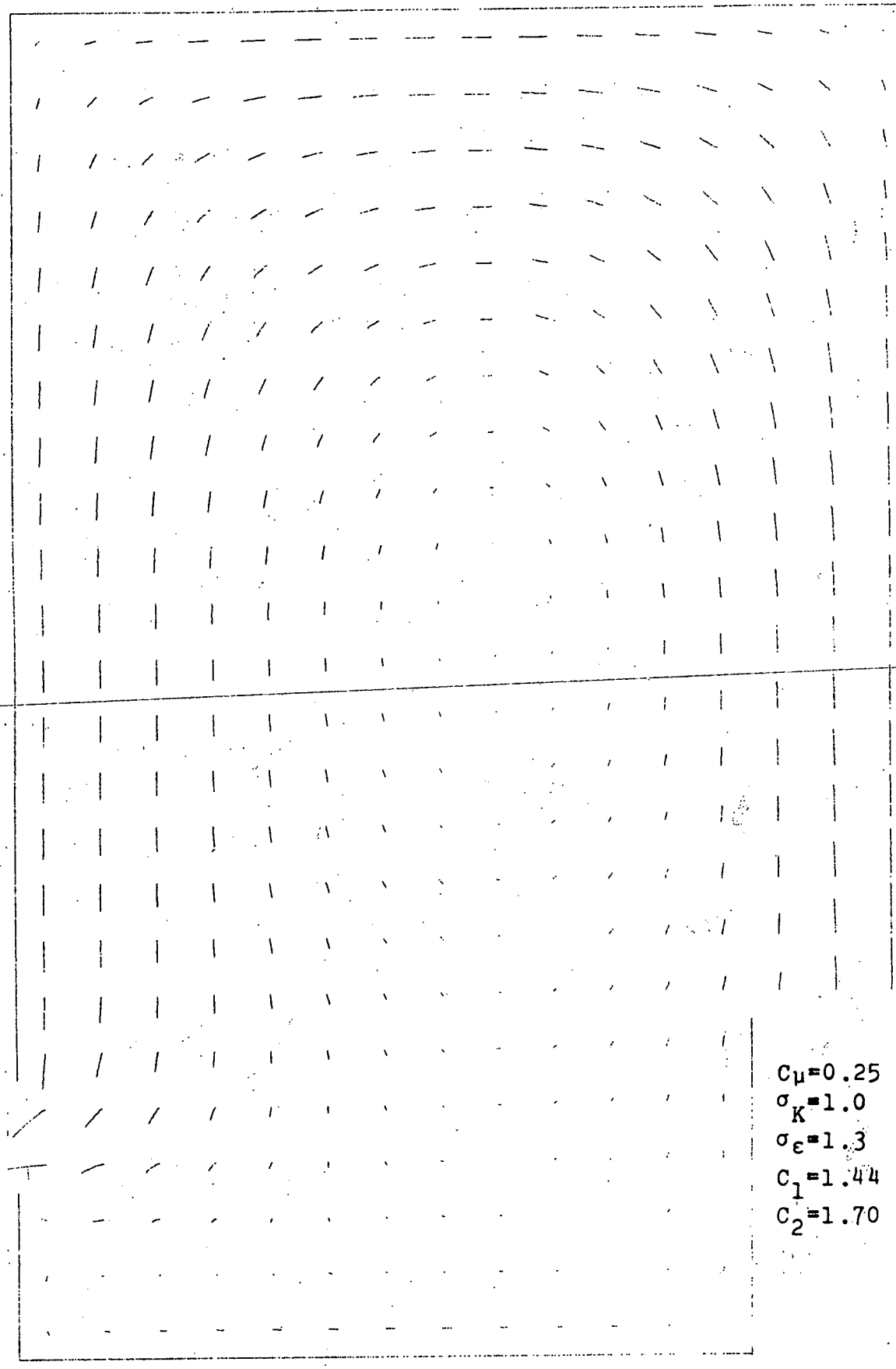

Fig. I.22 TEACH-T Prediction with C_μ = 0.25, C_2 = 1.70, FFTF Geometry, Re=70000, Normal Inlet Velocity Distribution

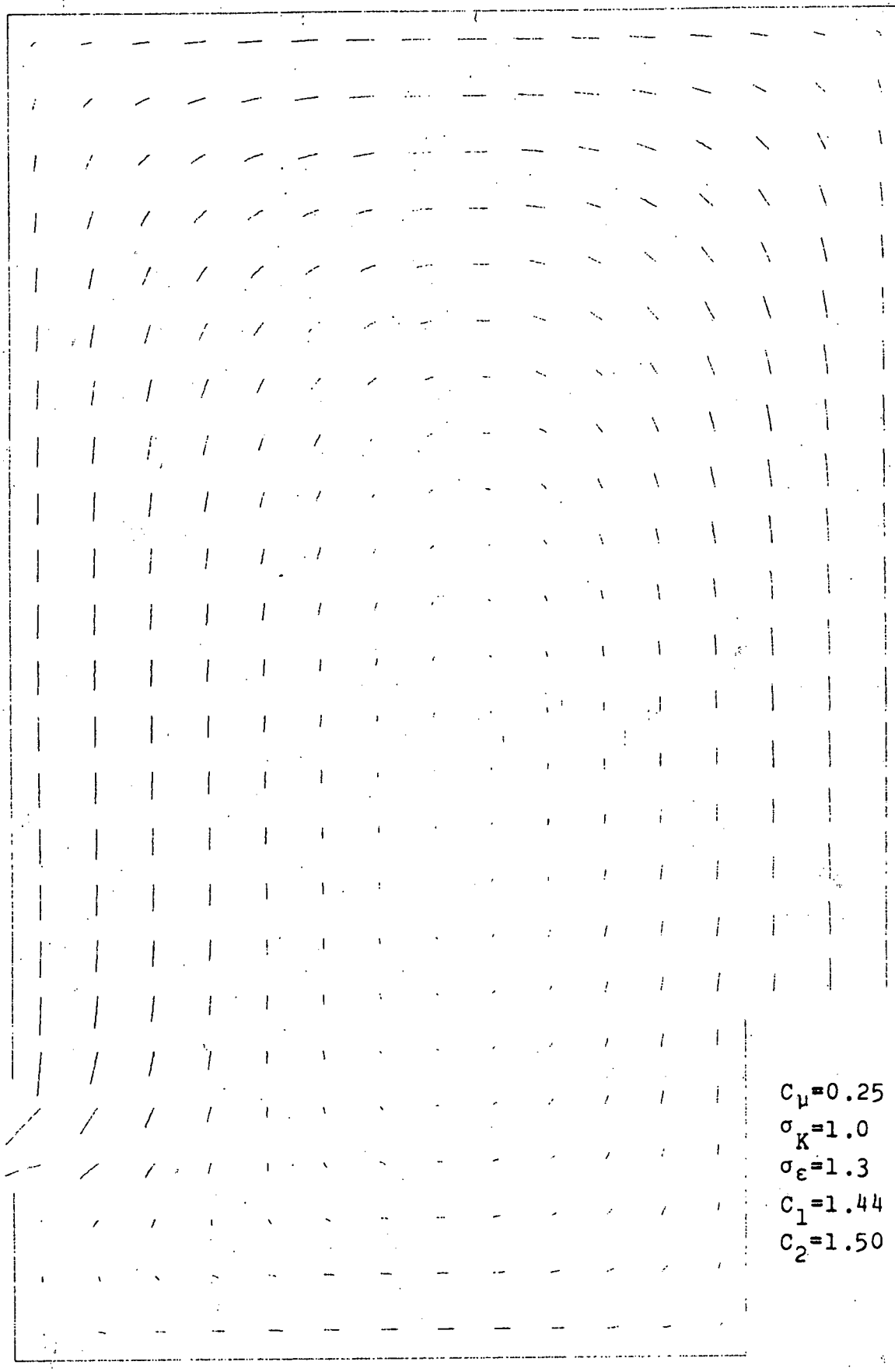

Fig. I.23 TEACH-T Prediction with C_μ = 0.25, C_2 = 1.50, FFTF Geometry, Re=70000, Normal Inlet Velocity Distribution

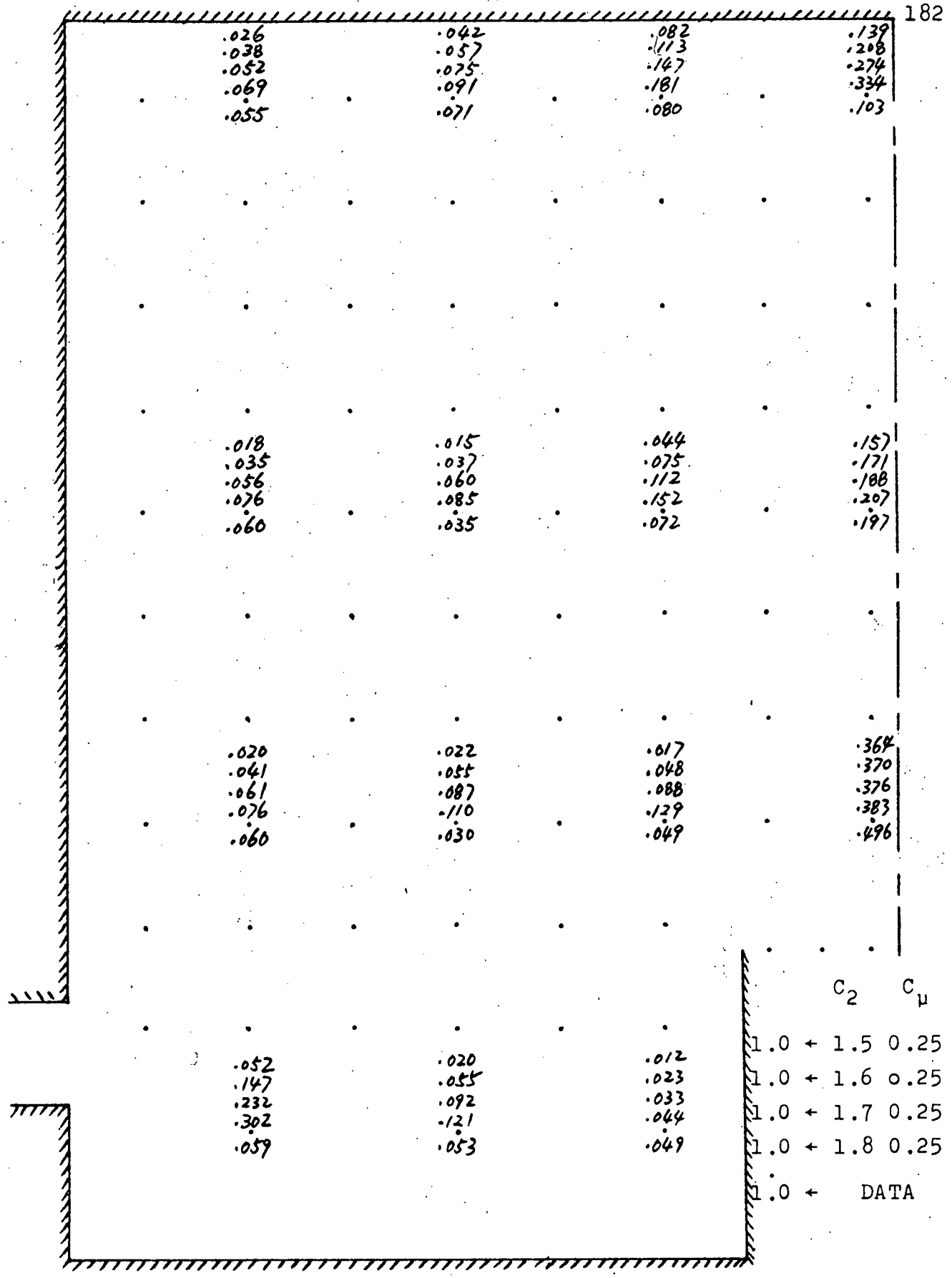

Fig. I.24 Compared Calculated and Measured Turbulent Kinetic Energy Fields, FFTF Geometry, Re=70000, Normal Inlet Velocity Distribution

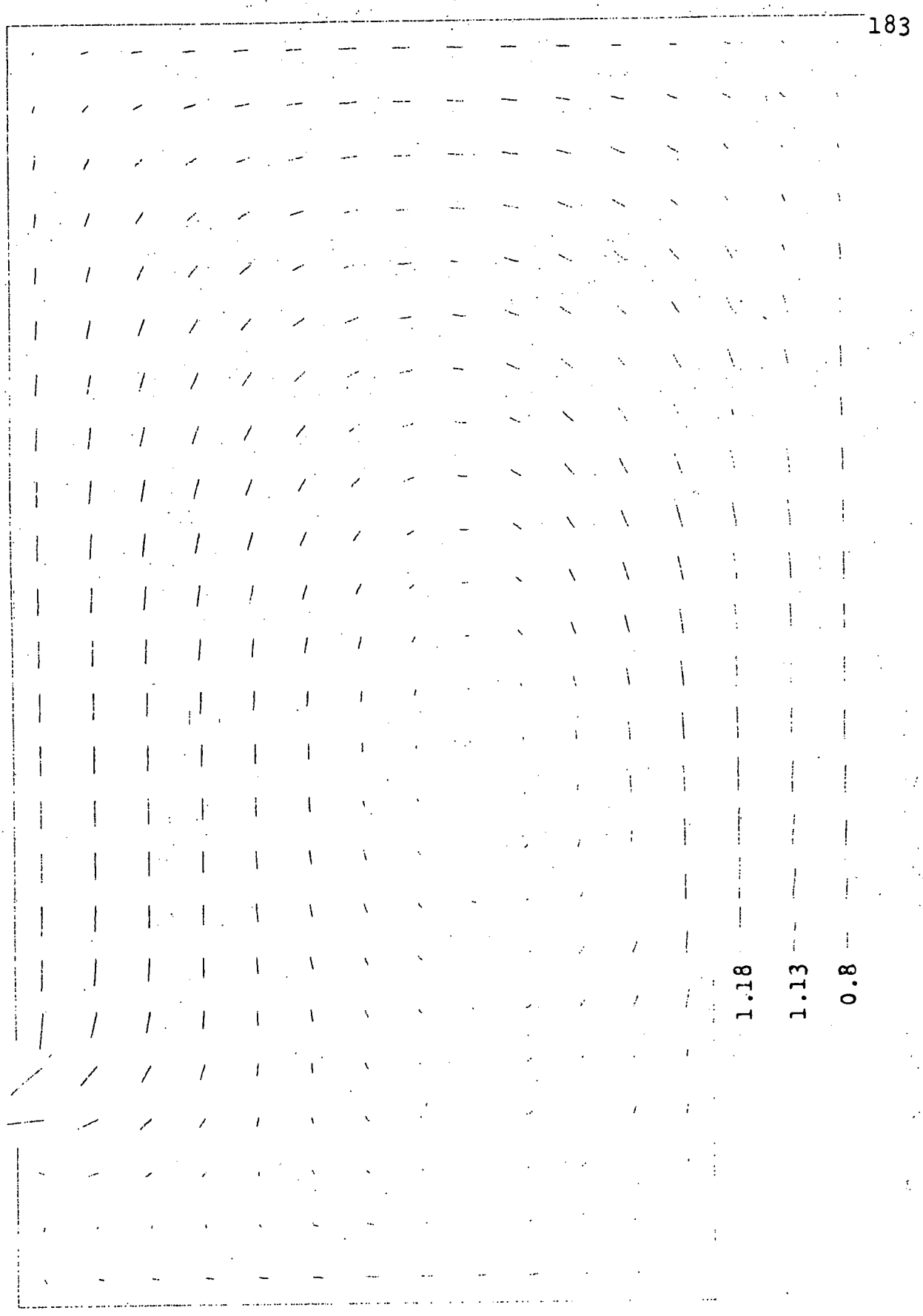

Fig. I.25 TEACH-T Prediction with Inlet Turbulent Energy Dissipation Rates, 0.8, 1.13, and 1.18, FFTF Geometry, Re=70,000, Distorted Inlet Velocity Distribution

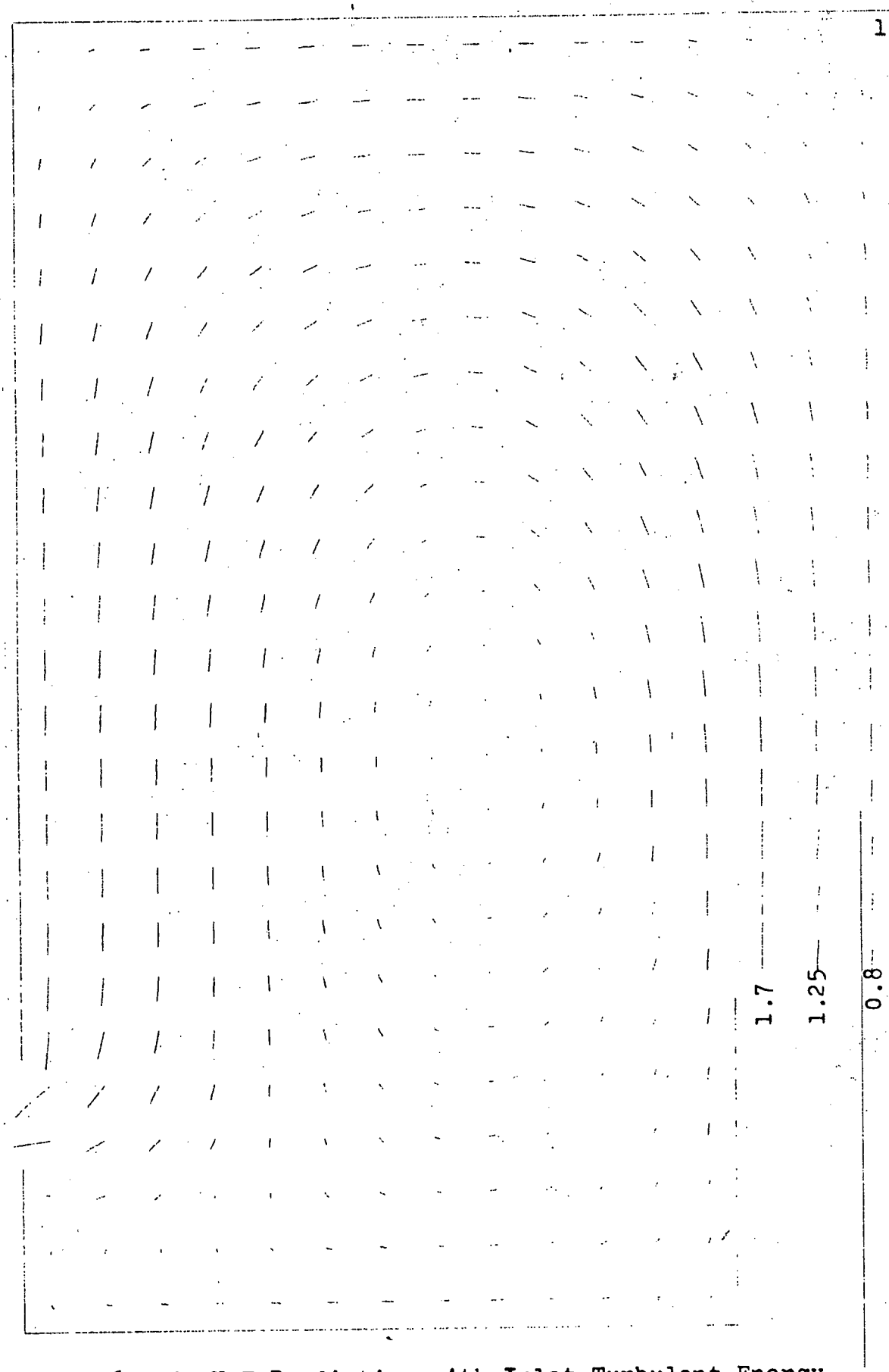

Fig. I.26 TEACH-T Prediction with Inlet Turbulent Energy Dissipation Rates, 0.8, 1.25, and 1.7, FFTF Geometry, Re=70,000, Distorted Inlet Velocity Distribution

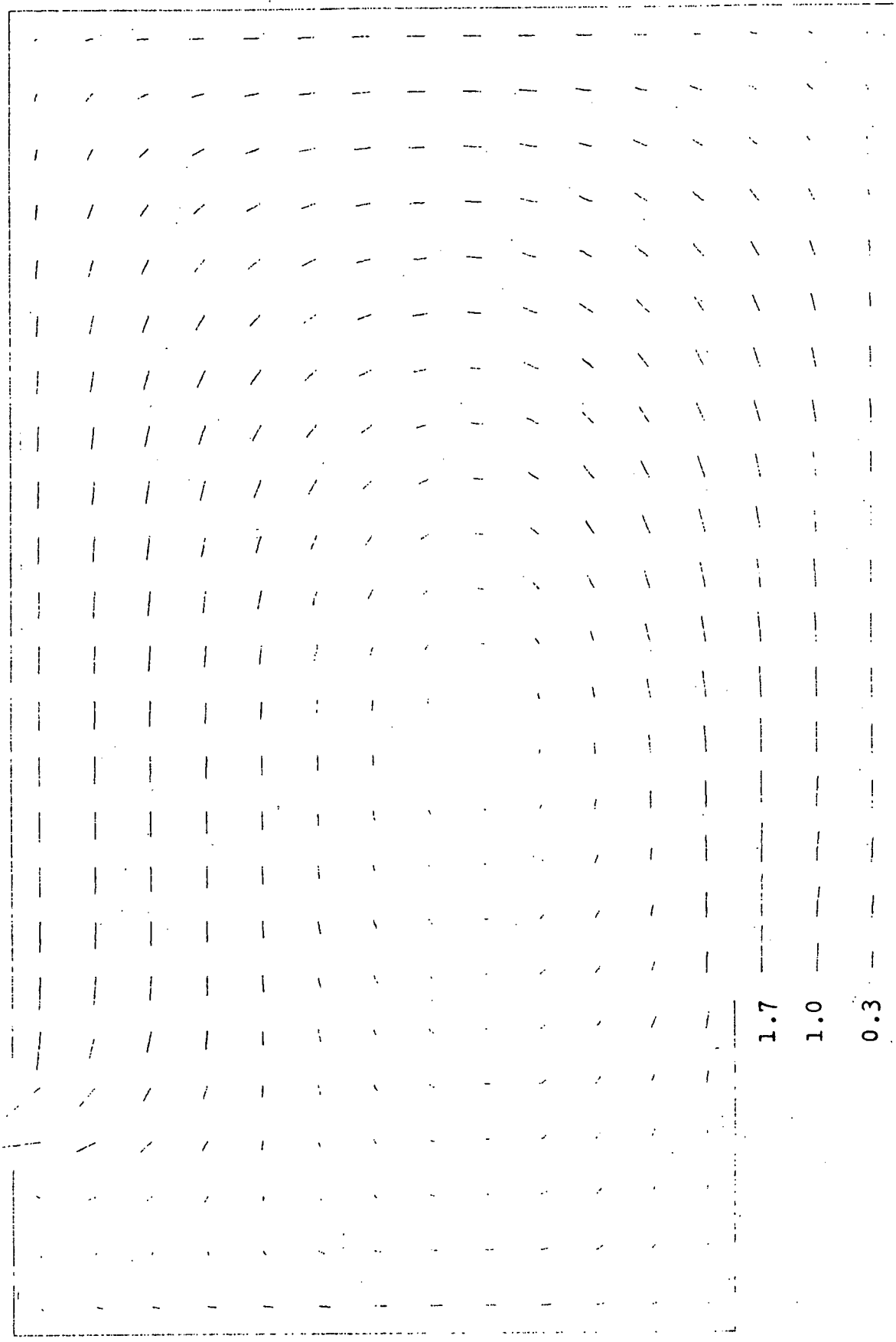

Fig. I.27 TEACH-T Prediction with Inlet Turbulent Energy Dissipation Rates, 0.3, 1.0, and 1.7, FFTF Geometry, Re=70,000, Distorted Inlet Velocity Distribution

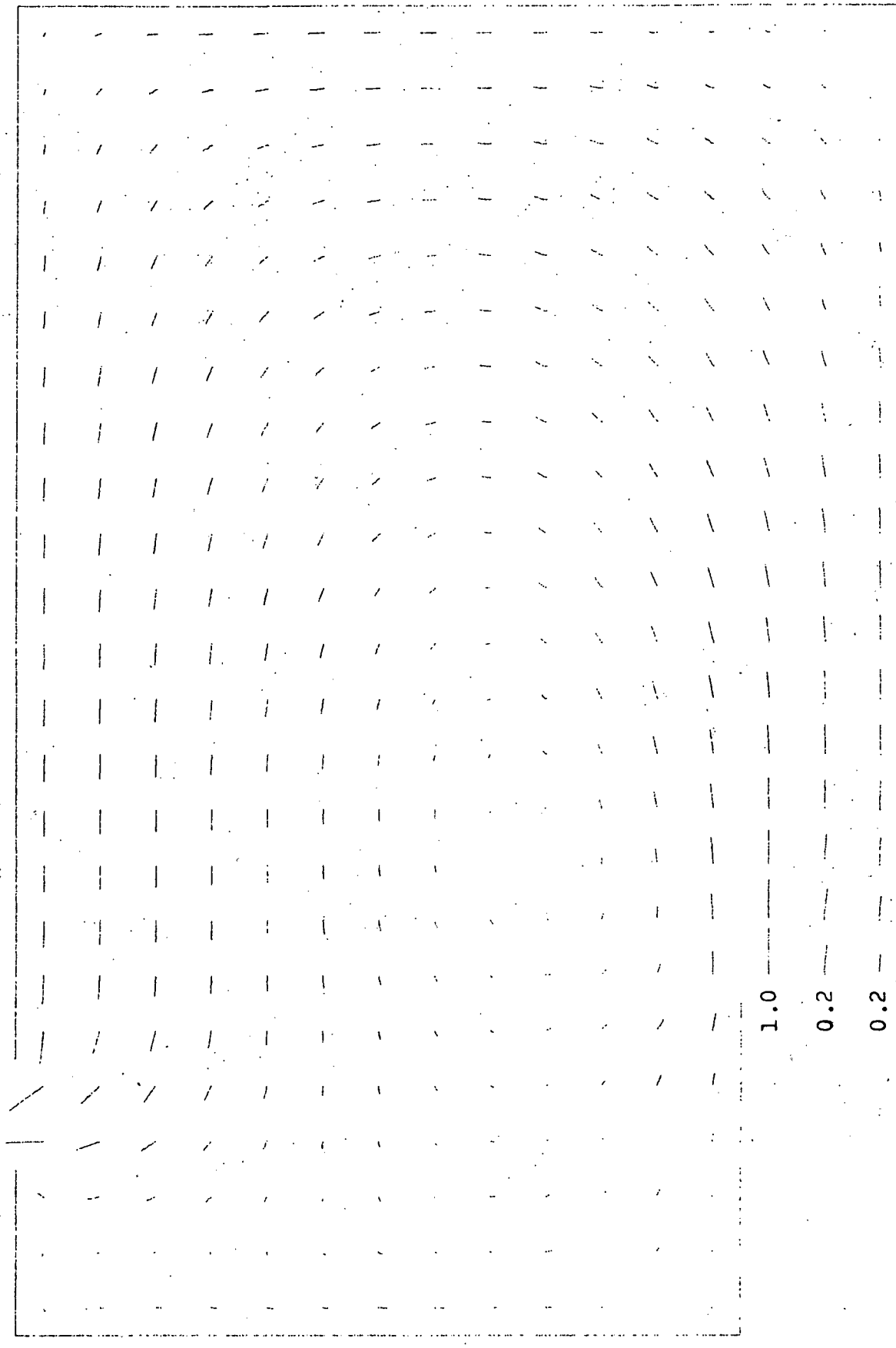

Fig. I.28 TEACH-T Prediction with Inlet Turbulent Energy Dissipation Rates, 0.2, 0.2, and 1.0, FFTF Geometry, Re=70,000, Distorted Inlet Velocity Distribution

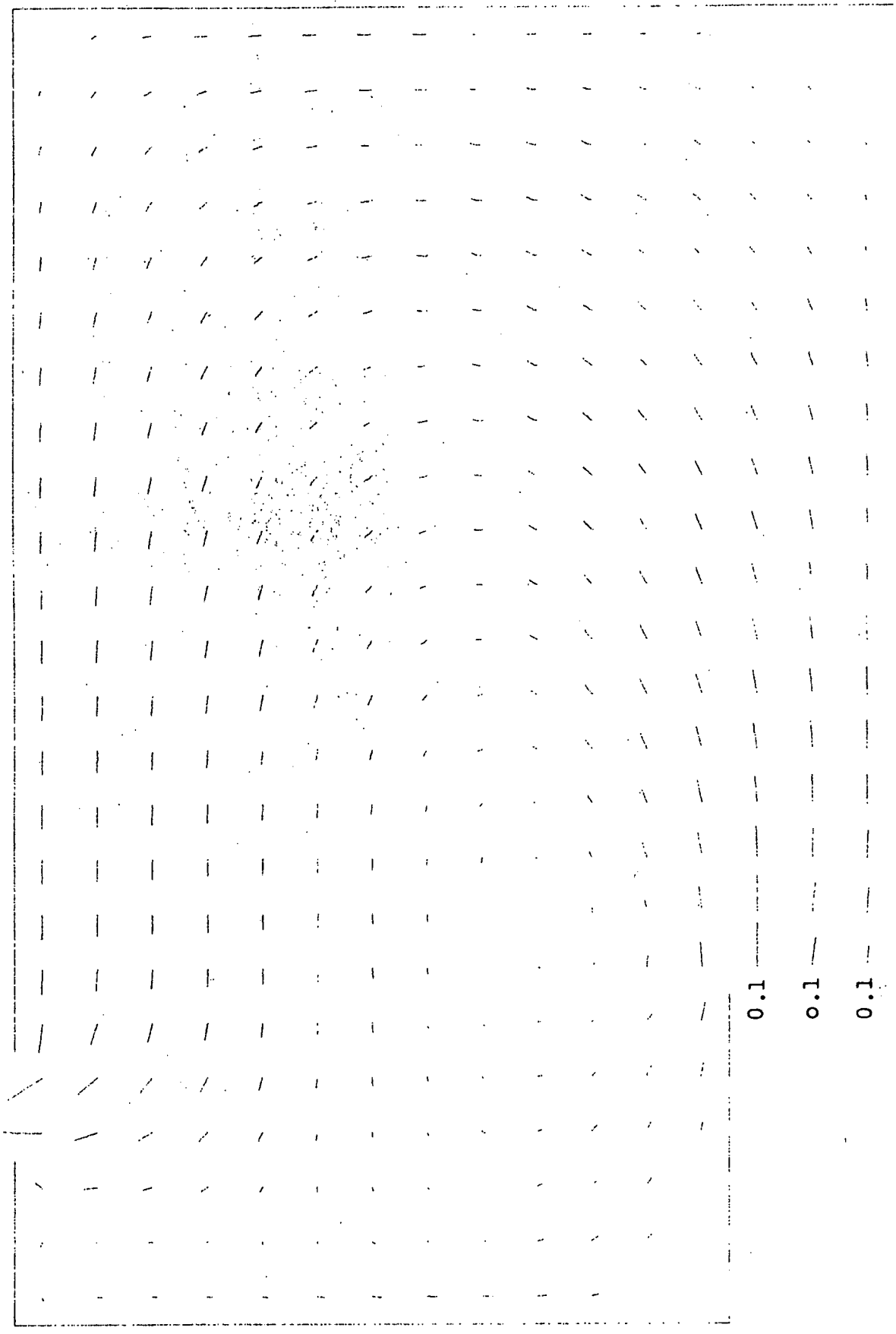

Fig. I.29 TEACH-T Prediction with Inlet Turbulent Energy Dissipation Rates, 0.1, 0.1, and 0.1, FFTF Geometry, Re=70,000, Distorted Inlet Velocity Distribution

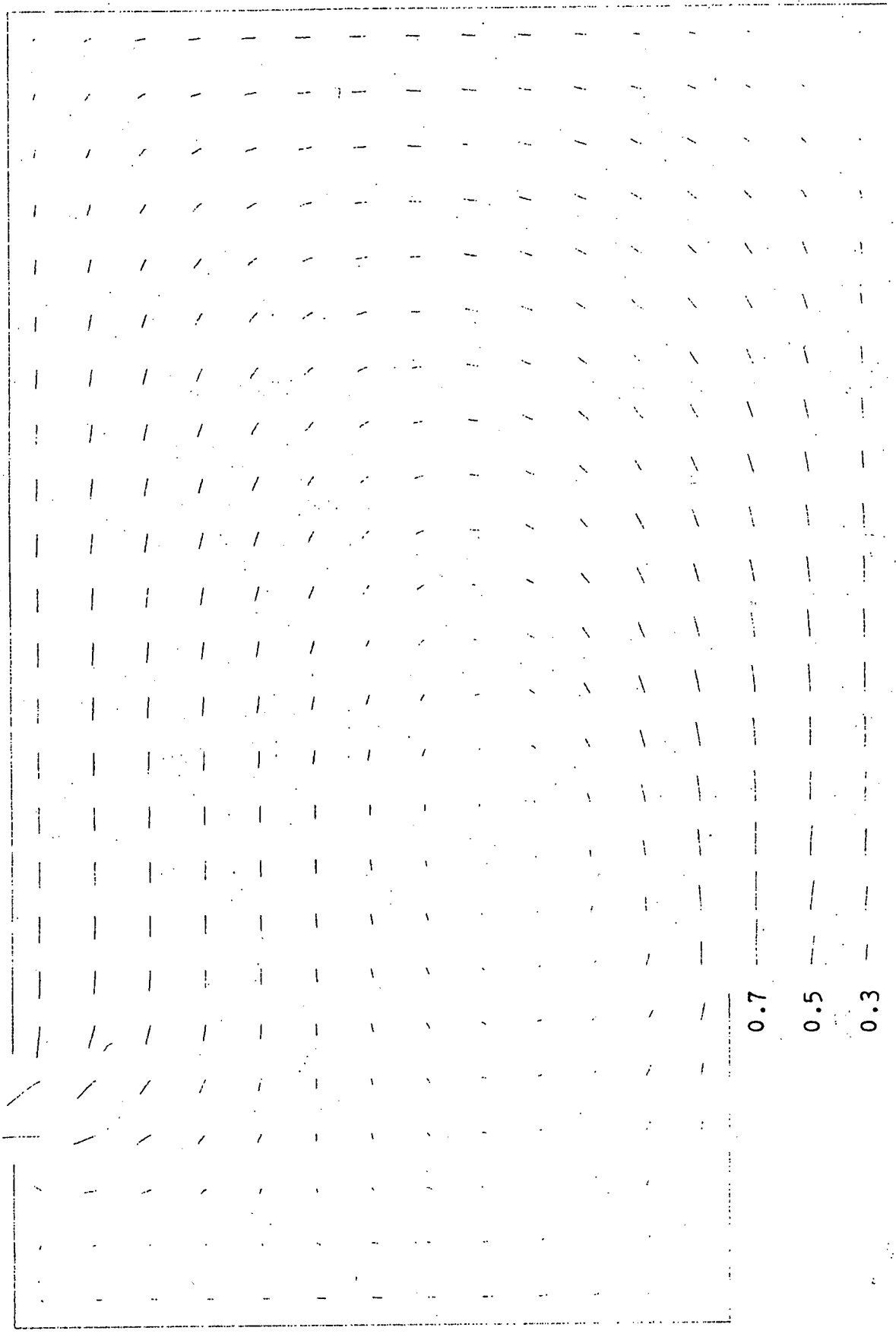

Fig. I.30 TEACH-T Prediction with Inlet Turbulent Energy Dissipation Rates, 0.3, 0.5, and 0.7, FFTF Geometry, Re=70,000, Distorted Inlet Velocity Distribution

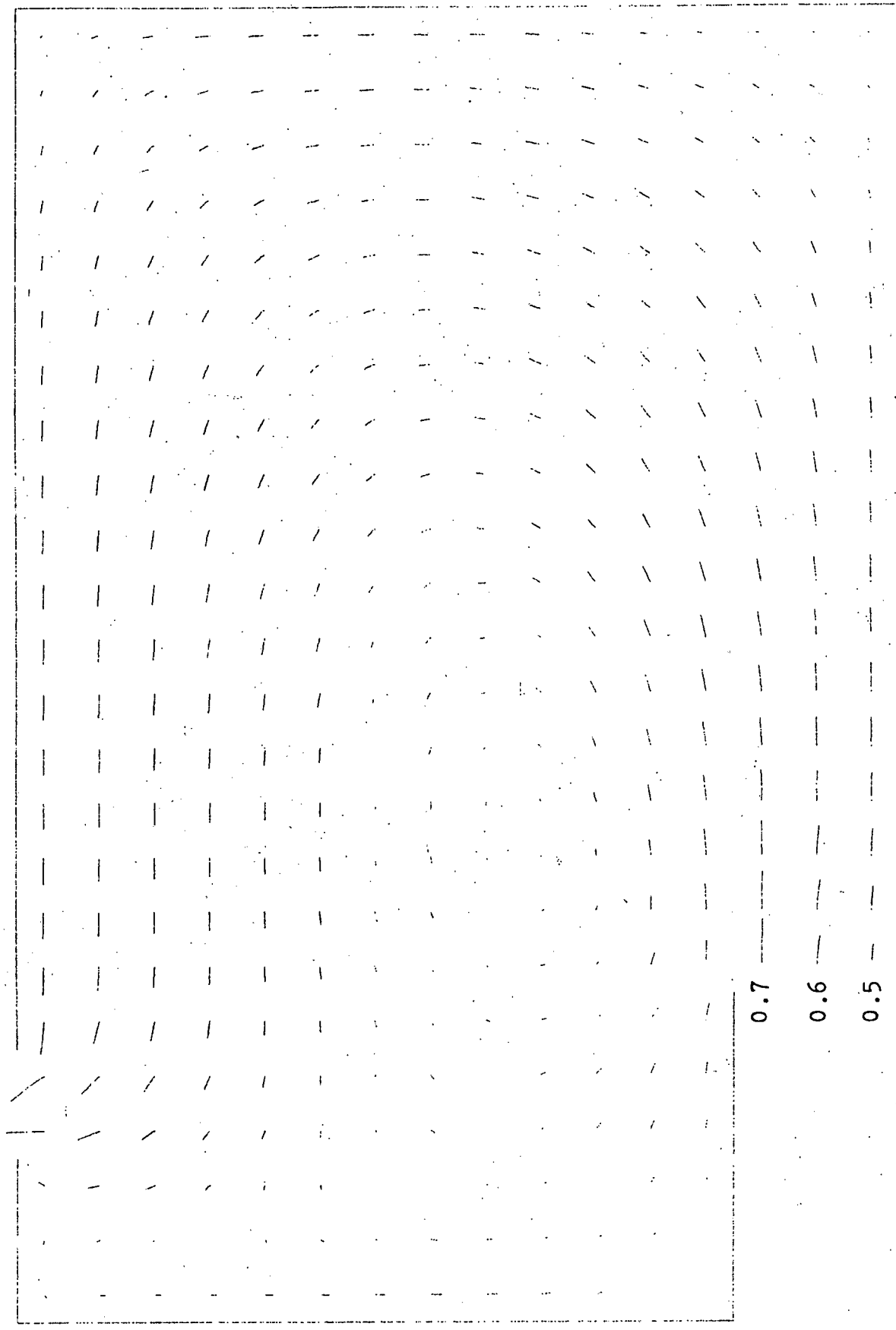

Fig. I.31 TEACH-T Prediction with Inlet Turbulent Energy Dissipation Rates, 0.5, 0.6, and 0.7, FFTF Geometry, Re=70,000, Distorted Inlet Velocity Distribution

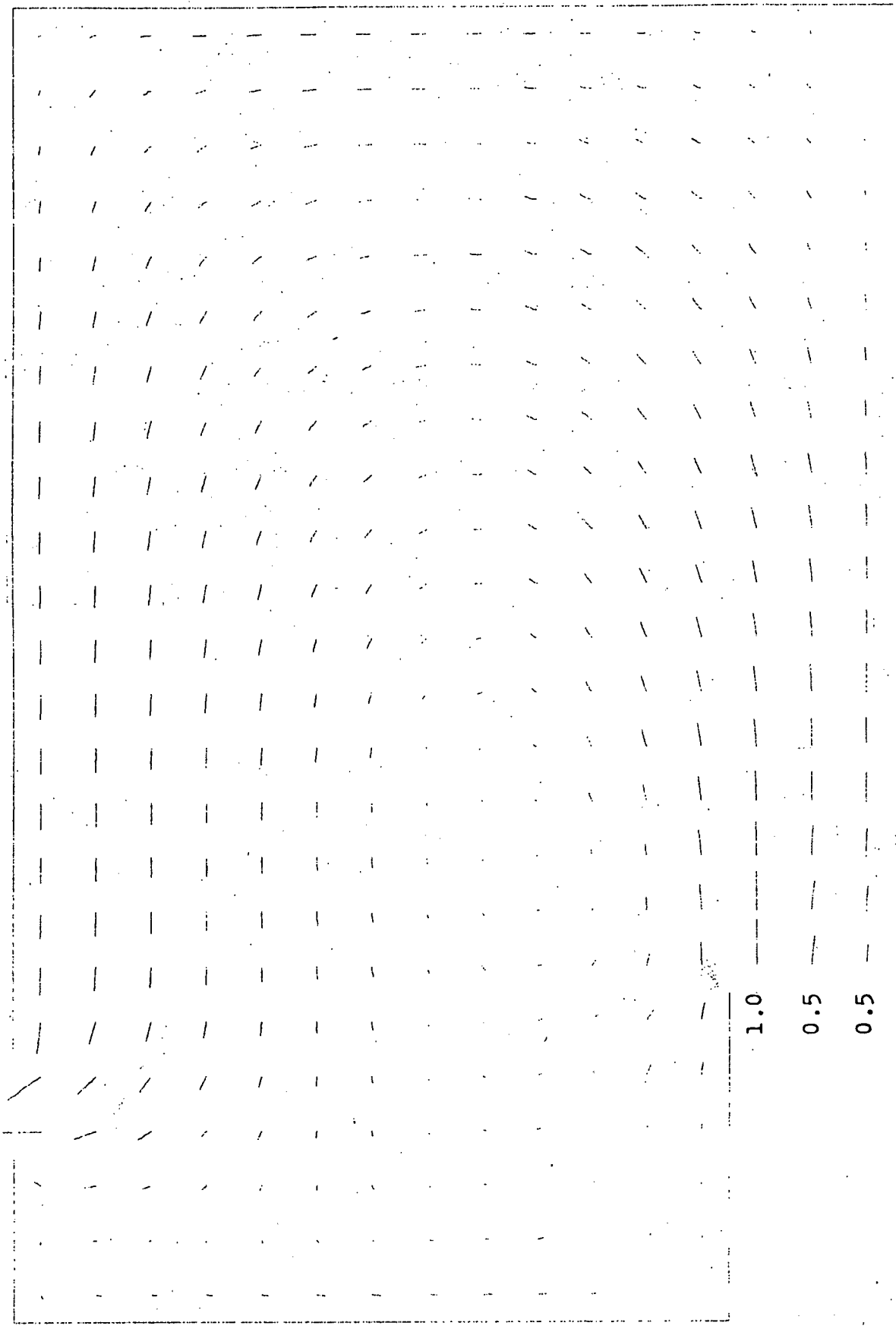

Fig. I.32 TEACH-T Prediction with Inlet Turbulent Energy Dissipation Rates, 0.5, 0.5, and 1.0, FFTF Geometry, Re=70,000, Distorted Inlet Velocity Distribution

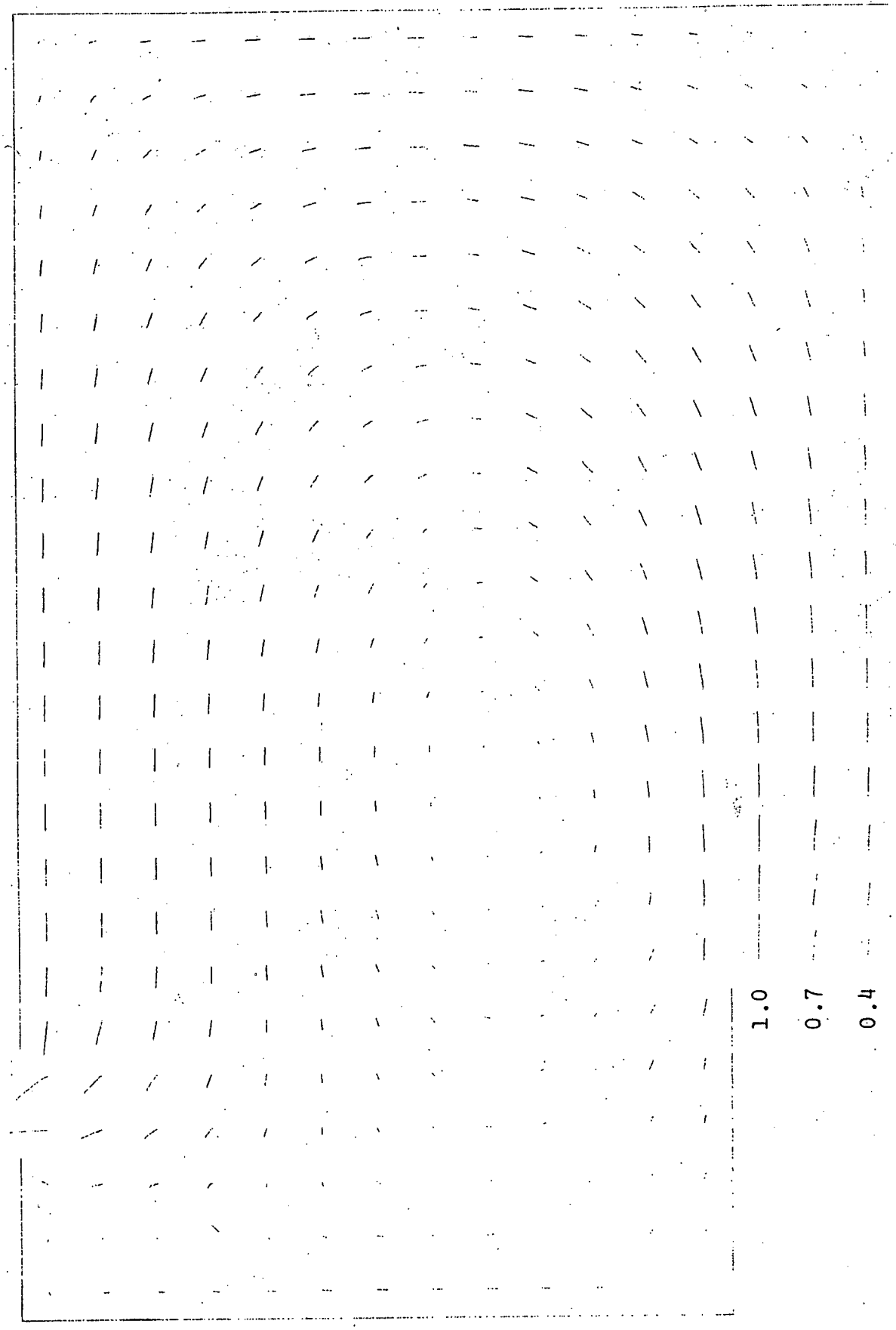

Fig. I.33 TEACH-T Prediction with Inlet Turbulent Energy Dissipation Rates, 0.4, 0.7, and 1.0, FFTF Geometry, Re=70,000, Distorted Inlet Velocity Distribution

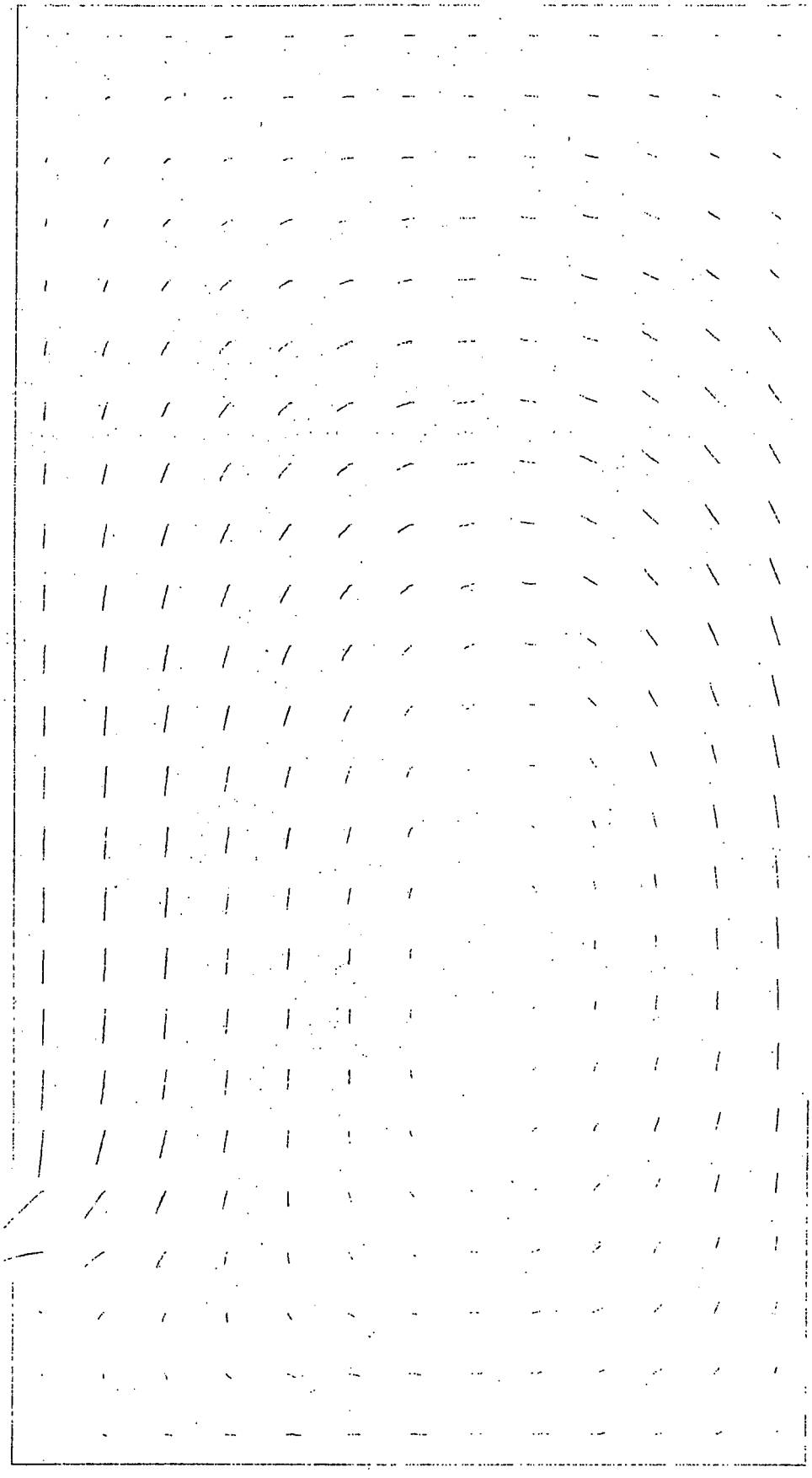

Fig. I.34 TEACH-T Prediction with σ_K=0.1, FFTF Geometry, Re=70,000, Distorted Inlet Velocity Distribution

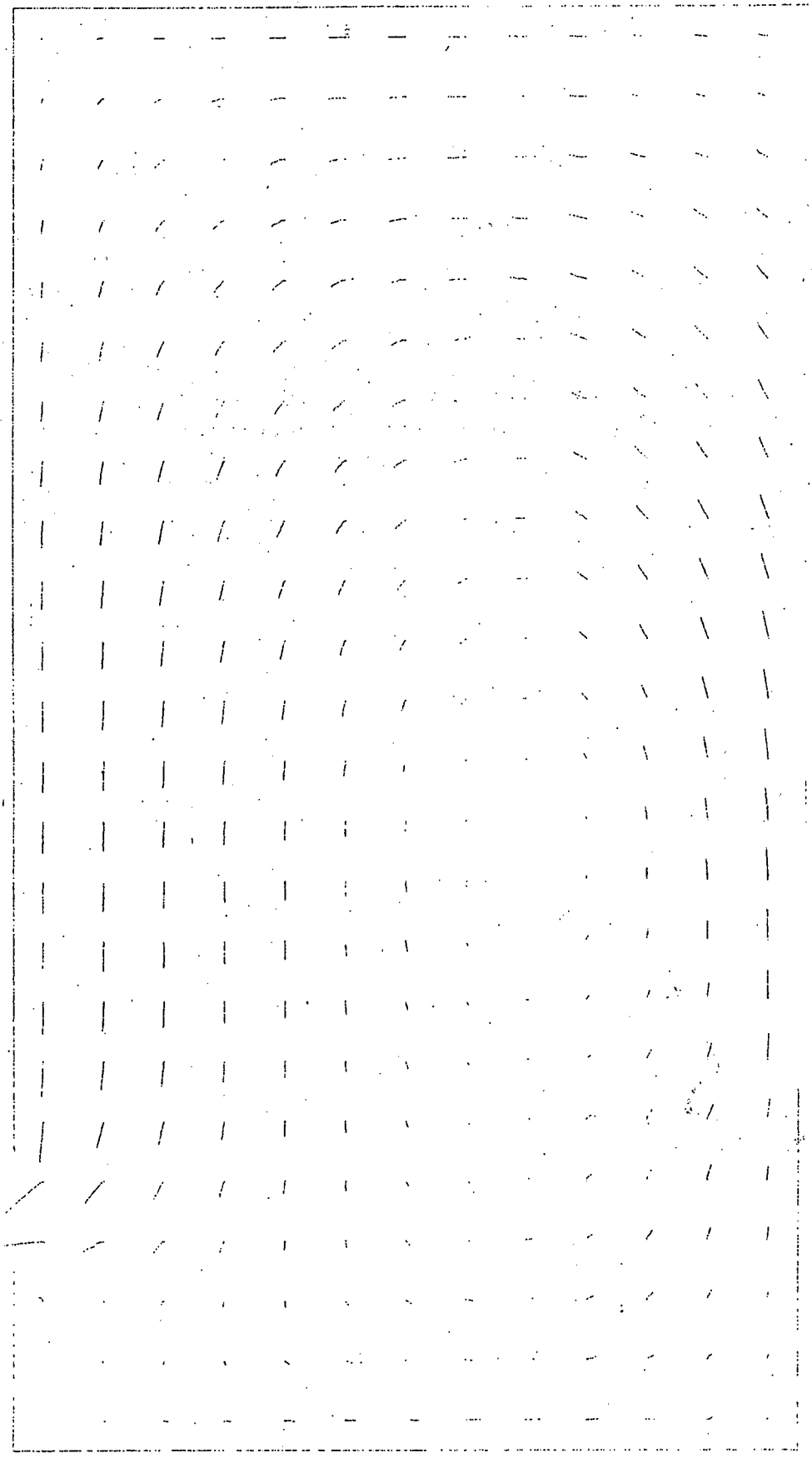

Fig. I.35 TEACH-T Prediction with σ_K=0.5, FFTF Geometry, Re=70,000, Distorted Inlet Velocity Distribution

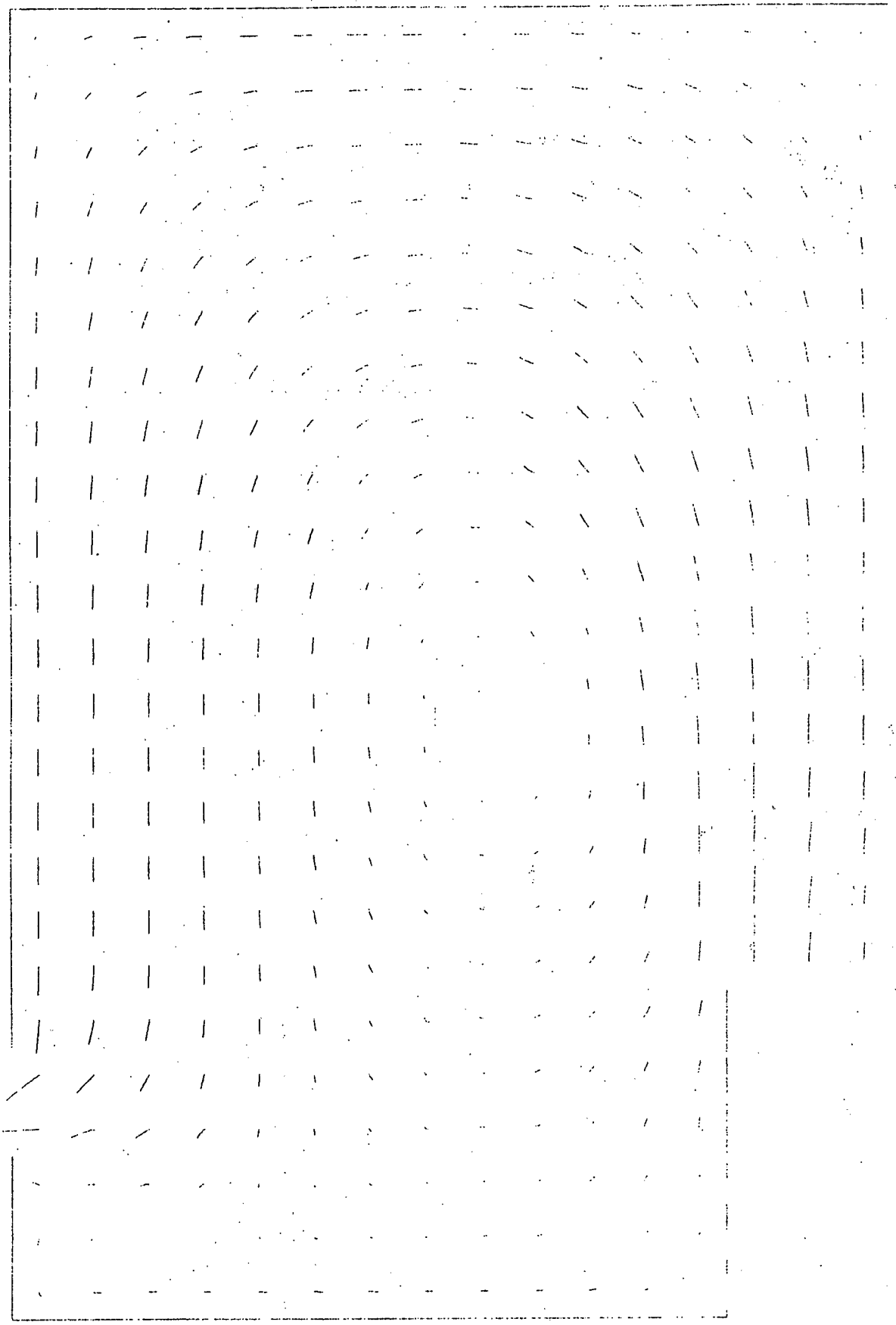

Fig. I.36 TEACH-T Prediction with σ_K=2.0, FFTF Geometry, Re=70,000, Distorted Inlet Velocity Distribution

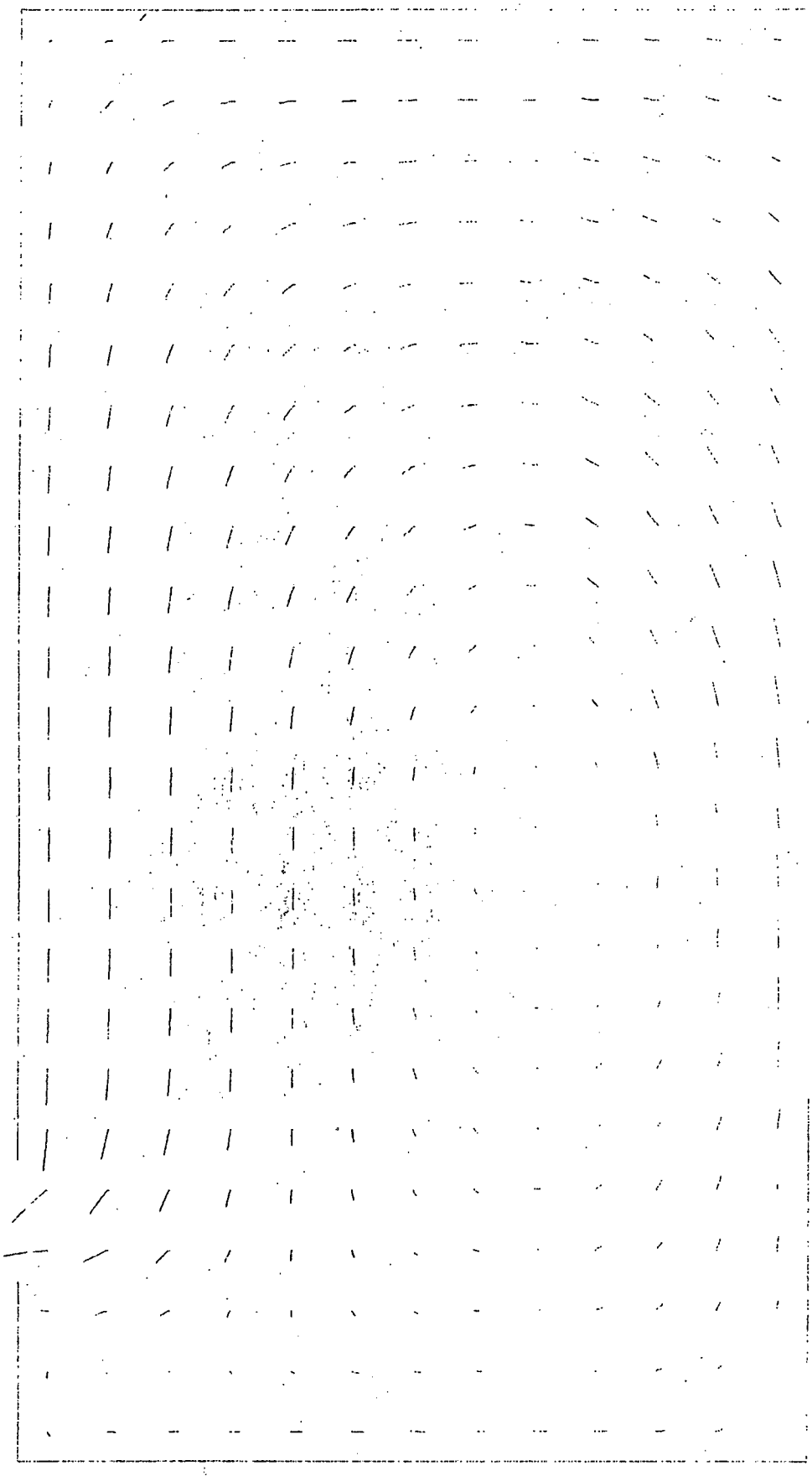

Fig. I.37 TEACH-T Prediction with σ_ε=0.65, FFTF Geometry, Re=70,000, Distorted Inlet Velocity Distribution

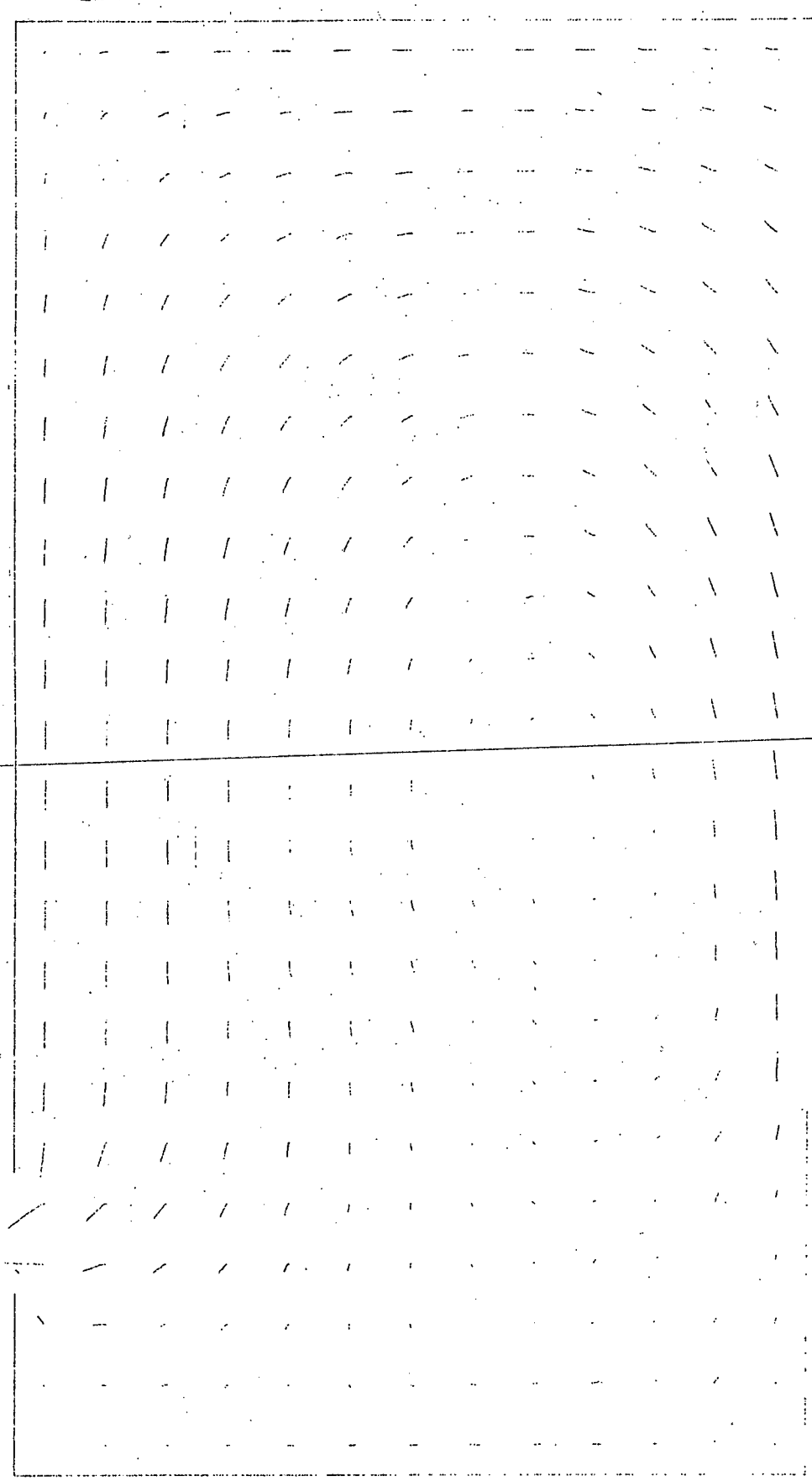

Fig. I.38 TEACH-T Prediction with $\sigma_\varepsilon = 2.6$, FFTF Geometry, Re=70,000, Distorted Inlet Velocity Distribution

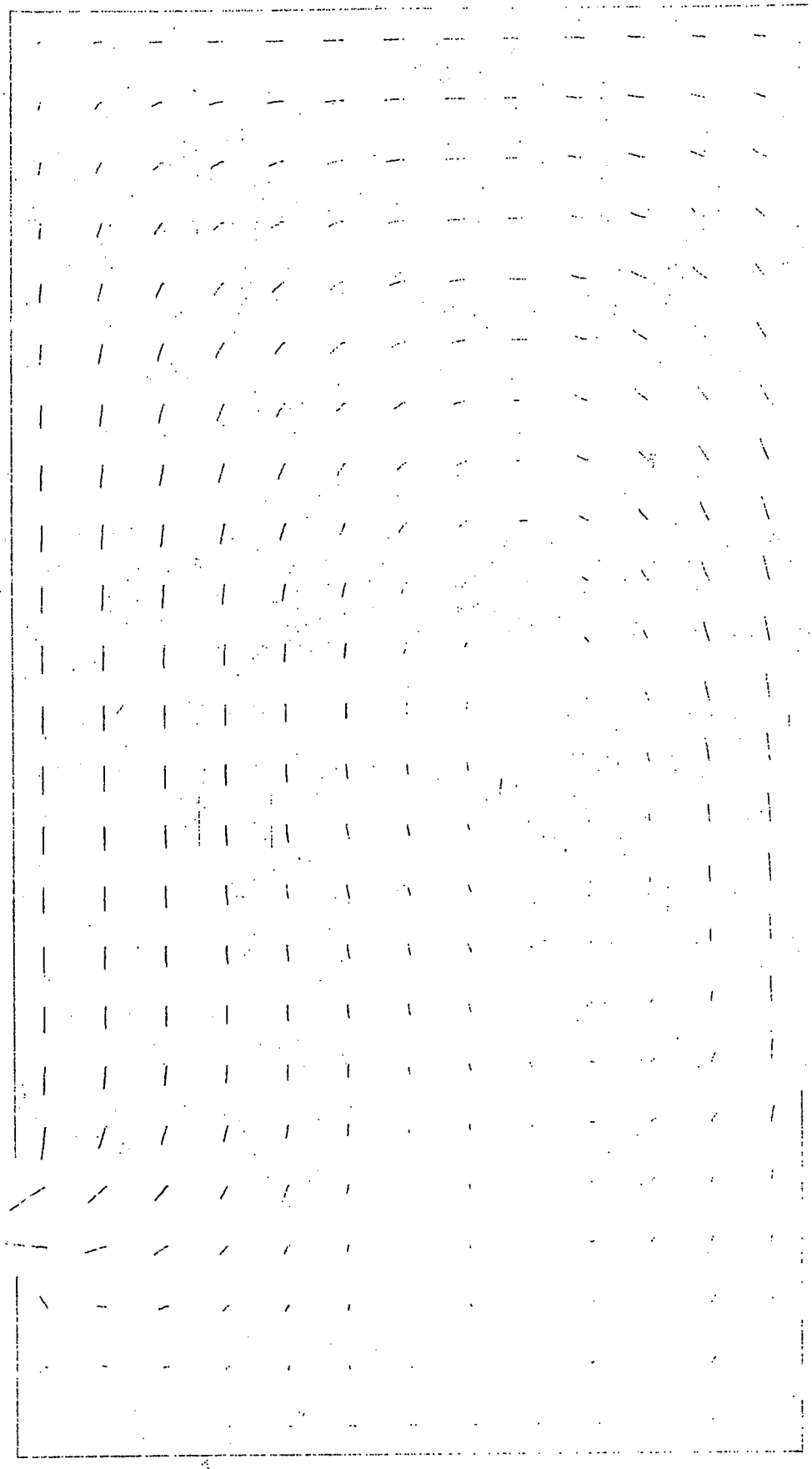

Fig. I.39 TEACH-T Prediction with σ_ε=3.9, FFTF GEometry, Re=70,000, Distorted Inlet Velocity Distribution

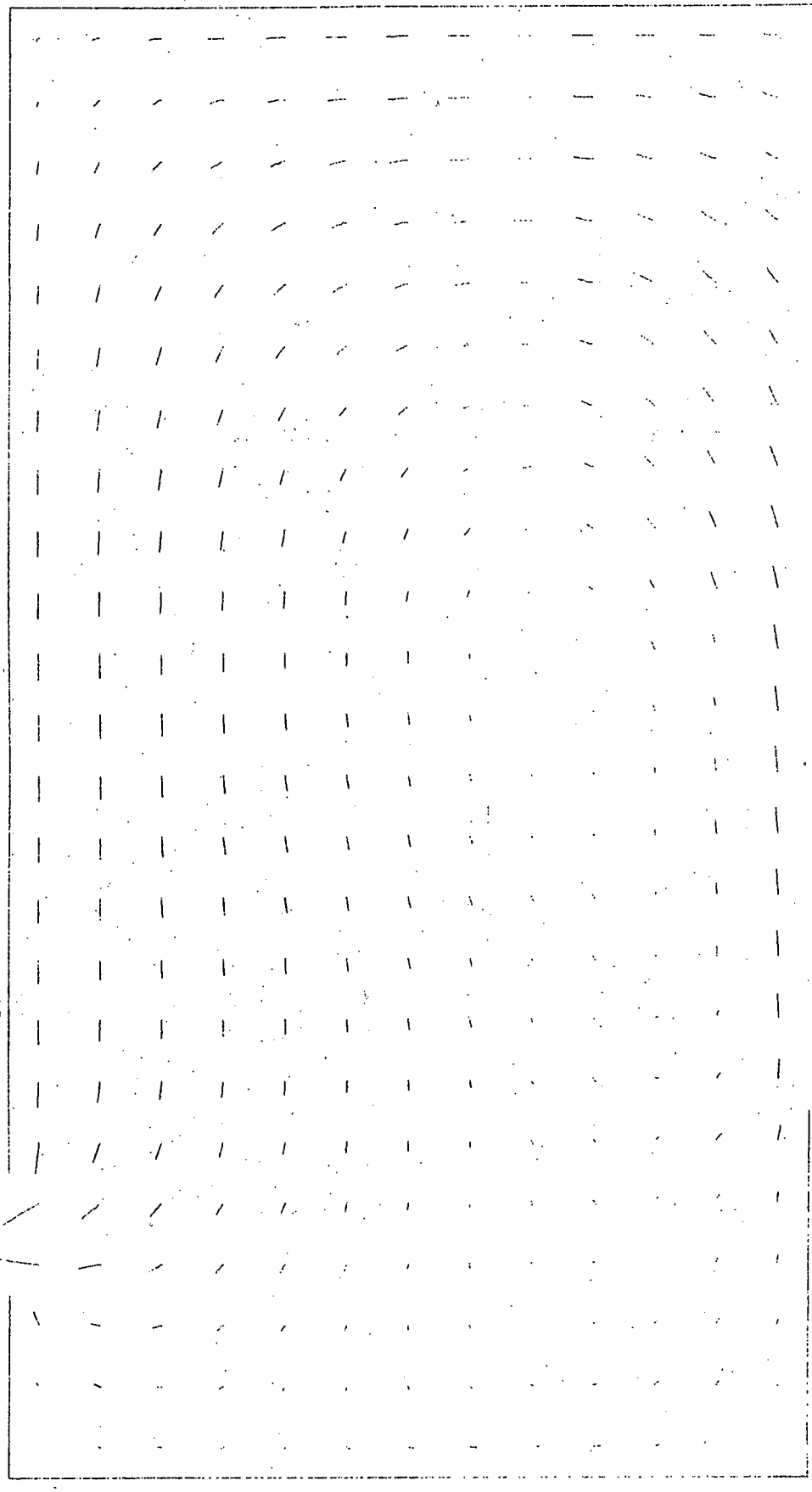

Fig. I.40 TEACH-T Prediction with σ_ε =13.0, FFTF Geometry, Re=70,000, Distorted Inlet Velocity Distribution

BIOGRAPHICAL NOTE

The author was born and raised in Taiwan, Republic of China. He received his Bachelor's degree in Nuclear Engineering from the National Tsing-Hua University in June 1971. After one year of military service in the Chinese Air Force, he came to the United States and entered the Nuclear Engineering Department at M.I.T. where he received his Master's degree in February 1975.

The author is a member of Sigma Xi, the American Nuclear Society, the American Society of Mechanical Engineers, and the American Society of Engineering Education.

The author is married to the former E-Hua Chou. The author's publications include:

1. Chen, Y.B., K. Ip, N.E. Todreas, "Velocity Measurement in Edge Channels of Wire-Wrapped LMFBR Fuel Assemblies," Trans. Amer. Nucl. Soc., 19, 458, 1974.
2. Chen, Y.B., M.W. Golay, "Validation of Turbulence Models for LMFBR Outlet Plenum Flows," ASME/AIChE National Heat Transfer Conference, Salt Lake City, Utah, 1977.